# PHOTODEGRADATION OF A PERSISTENT ORGANIC POLLUTANT USING MWCNT-TITANIA COMPOSITE PHOTOCATALYST

**TAN TONG LING**

**INSTITUTE OF GRADUATE STUDIES**
**UNIVERSITY OF MALAYA**
**KUALA LUMPUR**

**2017**

# PHOTODEGRADATION OF A PERSISTENT ORGANIC POLLUTANT USING MWCNT-TITANIA COMPOSITE PHOTOCATALYST

**TAN TONG LING**

**THESIS SUBMITTED IN FULFILMENT OF THE REQUIREMENTS FOR THE DEGREE OF DOCTOR OF PHILOSOPHY**

**INSTITUTE OF GRADUATE STUDIES**
**UNIVERSITY OF MALAYA**
**KUALA LUMPUR**

**2017**

## UNIVERSITY OF MALAYA
## ORIGINAL LITERARY WORK DECLARATION

Name of Candidate: TAN TONG LING (I.C/Passport No: 891222-23-5166)

Matric No: HHC120013

Name of Degree: DOCTOR OF PHILOSOPHY

Title of Project Paper/Research Report/Dissertation/Thesis ("this Work"):

PHOTODEGRADATION OF A PERSISTENT ORGANIC POLLUTANT
USING MWCNT-TITANIA COMPOSITE PHOTOCATALYST

Field of Study: ENVIRONMENTAL CHEMISTRY

I do solemnly and sincerely declare that:

(1) I am the sole author/writer of this Work;
(2) This Work is original;
(3) Any use of any work in which copyright exists was done by way of fair dealing and for permitted purposes and any excerpt or extract from, or reference to or reproduction of any copyright work has been disclosed expressly and sufficiently and the title of the Work and its authorship have been acknowledged in this Work;
(4) I do not have any actual knowledge nor do I ought reasonably to know that the making of this work constitutes an infringement of any copyright work;
(5) I hereby assign all and every rights in the copyright to this Work to the University of Malaya ("UM"), who henceforth shall be owner of the copyright in this Work and that any reproduction or use in any form or by any means whatsoever is prohibited without the written consent of UM having been first had and obtained;
(6) I am fully aware that if in the course of making this Work I have infringed any copyright whether intentionally or otherwise, I may be subject to legal action or any other action as may be determined by UM.

Candidate's Signature Date:

Subscribed and solemnly declared before,

Witness's Signature Date:

Name:

Designation:

# ABSTRACT

Persistent Organic Pollutants (POPs), particularly phthalate esters (PAEs) have been recognized as an endrocrine disrupting compound (EDC). It is a significant emerging priority contaminant that could easily be released into the environment. Hence, the health issues of PAEs exposure have raised public concern because of there are hepatoxic, teratogenic and carcinogenic in nature. In this study, a simple one-pot sol-gel technique was adopted to fabricate $TiO_2$ nanoparticles (15 nm) and MWCNTs/$TiO_2$ nanocomposites. The $TiO_2$ nanoparticles were first incorporated into the MWCNTs surfaces via hydrolysis of titanium isopropoxide (TTIP), ethanol and acetic acid at a volume ratio of 2:3:1 and were crystallized into anatase nanoparticles after annealing at 450 ºC. The experimental results revealed that the photocatalytic activity of MWCNTs/$TiO_2$ nanocomposites was strongly influenced by the synthesis parameters (MWCNTs/$TiO_2$ ratio, calcination temperature and pH). The optimum synthesis conditions for MWCNTs/$TiO_2$ nanocomposites were achieved with 10 wt % MWCNTs at pH 9 under calcination temperature of 450 °C. The photocatalytic degradation of the synthesized $TiO_2$ and MWCNTs/$TiO_2$ was evaluated using dimethyl phthalate esters (DMPEs) as a model compound of PAEs. The photocatalytic degradation rate of DMPEs for both MWCNTs/$TiO_2$ nanocomposites and $TiO_2$ nanoparticles under 96 W UV irradiation were carried out at the same time. The results show that the MWCNTs/$TiO_2$ nanocomposites (97%) exhibit high photocatalytic degradation rate, and it was much faster than $TiO_2$ (71 %). It is obvious that the nanocomposites have induced synergy effects on the photocatalytic performance of $TiO_2$ nanoparticles by decreasing the band gap energy of the nanocomposite. The formation of Ti-O-C bonds between the carboxylic acid groups of MWCNTs and the hydroxyl groups existent at the surface of $TiO_2$ during an esterification reactions, contribute to a synergetic effect due to the creation of an electronic interphase interaction between MWCNTs and $TiO_2$ phases. The ideal efficiency for removal of DMPEs was obtained when the dosage for MWCNTs/$TiO_2$ nanocomposites was 0.5 g/L, the initial concentration and pH of DMPEs was 1 ppm and 6, respectively. The irradiation time to achieve highly degradation was 3 h. The photoproducts from PAEs degradation were elucidated through UHPLC-Orbitrap-MS/MS analysis. A total of eighteen products were identified and were used to propose a primary degradation mechanism of DMPEs. The MWCNTS/$TiO_2$ nanocomposites is a promising catalyst for photocatalytic degradation. Basically, the functional groups present at the surface of MWCNTs promote the anchoring of the $TiO_2$ nanoparticles as well as avoiding agglomeration and subsequently increasing the surface area of the resulting MWCNTs/$TiO_2$ composite. In addition, this strong interface interaction also favours electron transfer pathways, thus the probability for electron/hole recombination is reduced.

# ABSTRAK

Pencemar organic degil (POPs), terutamanya ester phthalate (PAEs) telah diiktiraf sebagai “endocrine disrupting compounds” (EDC). Ia adalah pencemar keutamaan yang besar yang dengan mudah boleh dilepaskan ke dalam alam sekitar. Oleh itu, isu-isu kesihatan pendedahan PAEs telah menimbulkan kebimbangan orang ramai disebabkan ciri-ciri PAEs yang bersifat hepatoksik, teratogenik dan karsinogenik secara alam semula jadi. Dalam kajian ini, teknik sol-gel mudah diguna pakai untuk menyediakan nanopartikel $TiO_2$ (15 nm) dan nanokomposit nanotiub karbon-nano (MWCNTs)/$TiO_2$. Nanopartikel $TiO_2$ terdahulu dimasukkan ke dalam MWCNTs permukaan melalui hidrolisis titanium isopropoxide (TTIP), etanol dan asid asetik pada nisbah jumlah 2: 3: 1 dan seterusnya menghablur membentuk anatase $TiO_2$ nanopartikel pada suhu 450 °C. Keputusan eksperimen menunjukkan bahawa aktiviti foto pemangkinan daripada nanokomposit MWCNTs / $TiO_2$ kuat dipengaruhi oleh parameter sintesis (nisbah MWCNTs/$TiO_2$, suhu pengkalsinan dan pH). Syarat-syarat sintesis optimum untuk MWCNTs / $TiO_2$ nanocomposites telah dicapai dengan 10 wt% MWCNTs pada pH 9 di bawah suhu pengkalsinan 450 °C. Kemusnahan photocatalytic $TiO_2$ yang disintesis dan MWCNTs / $TiO_2$ telah dinilai menggunakan ester dimetil phthalate (DMPEs) sebagai sebatian model PAEs. Kadar kemerosotan foto pemangkinan bagi DMPEs untuk kedua-dua nanokomposit MWCNTs / $TiO_2$ dan nanopartikel $TiO_2$ di bawah sinaran berkuasa 96 W UV telah dijalankan pada masa yang sama. Keputusan menunjukkan bahawa nanokomposit MWCNTs/$TiO_2$ (97%) menunjukkan kadar degradasi foto pemangkinan tinggi, dan ia adalah lebih cepat daripada $TiO_2$ (71%). Ia adalah jelas bahawa nanokomposit telah mendorong kesan sinergi kepada prestasi foto pemangkinan nanopartikel $TiO_2$ dengan mengurangkan sela tenaga nanokomposit. Pembentukan ikatan Ti-O-C antara kumpulan asid karboksilik daripada MWCNTs dan kumpulan hidroksil wujud di permukaan $TiO_2$ semasa tindak balas pengesteran, menyumbang kepada kesan sinergi kerana pembentukan interaksi interfasa elektronik antara MWCNTs dan fasa $TiO_2$. Kecekapan ideal untuk penyingkiran DMPEs diperolehi apabila dos untuk nanokomposit MWCNTs/$TiO_2$ adalah 0.5 g / L, kepekatan awal DMPEs dan pH DMPEs adalah 1 ppm dan 6 masing-masing. Masa penyinaran untuk mencapai maximum degradasi adalah 3 h. Fotoproduk dari degradasi PAEs telah dijelaskan melalui analisis UHPLC-Orbitrap-MS / MS. Sebanyak sembilan belas produk telah dikenal pasti dan ion dan serpihan puncak molekul dibandingkan dengan data UHPLC / Orbitrap / perpustakaan MS. Keputusan yang diperolehi telah digunakan untuk mencadangkan satu mekanisme degradasi utama DMPEs. Nanokomposit MWCNTs / $TiO_2$ adalah pemangkin menjanjikan untuk kemerosotan photocatalytic. Pada asasnya, kumpulan berfungsi yang hadir pada permukaan MWCNTs menggalakkan “anchoring” nanopartikel $TiO_2$ serta mengelakkan penumpuan dan seterusnya meningkatkan kawasan permukaan yang terhasil MWCNTs/ $TiO_2$ komposit. Di samping itu, interaksi antara muka yang kukuh ini juga membantu laluan pemindahan elektron, oleh itu kebarangkalian untuk elektron / lubang penggabungan semula dikurangkan.

# ACKNOWLEDGEMENTS

Embarking on a PhD journey is the beginning of a challenging and stimulating experience which, to a large extent, is dependent on the support of the people you encounter along the way. This research work was carried out in the Nanotechnology and Catalysis Research Centre (NANOCAT), University of Malaya. I would like to express my deepest gratitude to all those people who have helped and encouraged me in the successful completion of my doctoral study.

First and foremost, I would like to give my sincere thanks to my supervisors, Prof Sharifah Bee Abd Hamid and Dr. Lai Chin Wei, for their guidance, kindness, stimulating discussion, continued advice permanent support during these three years, as well as the time and patience they spent in reading and correcting my thesis chapters. With their enormous help and supervisions, I have obtained a lot of precious research experience such as scientific thinking, knowledge in chemistry and materials, as well as laboratory techniques. It was truly a great pleasure and privilege to study under their mentorships.

I would also like to express my sincere gratitude to Dr. Lee Kian Mun, he is such a virtuous, kind and generous mentor who provided me with guidance, encouragement and support for my study. I respect and appreciate him pretty much.

Besides that, I would also like to acknowledge to all the academic and technical staffs of NANOCAT for their advice and assistance. Also, my heartfelt go to all my colleagues for all the help, discussion, and sharing.

In particular, I wish to thank the Bright Sparks Scholarship, under the University of Malaya, which sponsored me at all stages of my doctoral studies with the benefits and incentives provided.

Last but not least, my parents are always there for me especially their support and unconditional love in all my pursuits, for which my mere expression of gratitude does never suffice.

# TABLE OF CONTENTS

Abstract ..... iii

Abstrak ..... v

Acknowledgements ..... vii

Table of Contents ..... ix

List of Figures ..... xv

List of Tables ..... xx

List of Symbols and Abbreviations ..... xxii

List of Appendices ..... xxv

**CHAPTER 1: INTRODUCTION ..... 1**

1.1 Introduction ..... 1

1.2 Problem Statement ..... 9

1.3 Motivations ..... 10

1.4 Objectives of Study ..... 12

1.5 Outline of Research Work ..... 12

- 1.5.1 Synthesis of MWCNTs/$TiO_2$ nanocomposites ..... 13
- 1.5.2 Characterizations of the photocatalyst ..... 14
- 1.5.3 Photocatalytic reaction of DMPEs ..... 15
- 1.5.4 Possible photocatalytic degradation mechanism of DMPEs ..... 15

1.6 Outline of Thesis ..... 15

**CHAPTER 2: LITERATURE REVIEW ..... 17**

2.1 Phthalate esters (PAEs) ..... 18

- 2.1.1 Properties and Classification of PAEs ..... 19

2.1.2 Occurrence of Phthalate esters in the environment ..... 22

2.1.3 Application ..... 23

2.1.4 Toxicity/Health Hazards ..... 25

2.2 Removal of Phthalate esters (PAEs) ..... 26

2.2.1 Physical/Chemical treatments ..... 27

2.2.2 Biological treatments ..... 28

2.2.3 Advanced Oxidation Process (AOPs) ..... 29

2.2.3.1 Ozonation ..... 30

2.2.3.2 Fenton and photo-Fenton process ..... 31

2.2.3.3 Heterogeneous photocatalysis ..... 32

2.3 Bulk Properties of Titanium dioxide ..... 39

2.3.1 Basic principle of $TiO_2$ photocatalysis ..... 42

2.3.2 Limitations of $TiO_2$ nanoparticles ..... 44

2.3.3 Modifications of $TiO_2$ nanoparticles ..... 45

2.3.3.1 Activated carbon/$TiO_2$ composites ..... 47

2.3.3.2 Fullerenes ($C_{60}$)/$TiO_2$ composite ..... 49

2.3.3.3 Graphene/$TiO_2$ composite ..... 50

2.3.3.4 CNTs/$TiO_2$ nanocomposites ..... 53

2.3.4 Synthesis of CNTs/$TiO_2$ ..... 58

2.3.4.1 Simple mixing ..... 59

2.3.4.2 Chemical Vapor Deposition (CVD) ..... 59

2.3.4.3 Electrodeposition ..... 60

2.3.4.4 Hydrothermal ..... 61

2.3.4.5 Sol-gel ..... 61

**CHAPTER 3: RESEARCH METHODOLOGY ........................................................ 67**

3.1 Materials Synthesis .................................................................................... 67

3.1.1 Raw Materials and Chemicals Selection ................................................. 67

3.2 Pre-treatment of Pristine MWCNTs ............................................................ 70

3.3 Preparation of catalysts ............................................................................. 71

3.3.1 Synthesis procedures of $TiO_2$ nanoparticles ........................................... 71

3.3.2 Synthesis procedures of MWCNTs-$TiO_2$ nanocomposites ...................... 72

3.4 Photocatalytic activity Evaluation Test for Dimethyl Phthalate Esters ................. 73

3.4.1 Measurement of DMPEs concentrations ................................................. 74

3.4.2 Reaction kinetic study ............................................................................. 75

3.4.3 Parameter studies in photodegradation of DMPEs .................................. 75

3.4.3.1 Effect of catalyst dosage ......................................................... 76

3.4.3.2 Effect of initial concentration of DMPEs ................................. 76

3.4.3.3 Effect of solution pH ............................................................... 77

3.4.3.4 Effect of irradiation time ......................................................... 77

3.4.3.5 Effect of $H_2O_2$ dosage ............................................................ 78

3.4.3.6 Catalyst reusability study ........................................................ 78

3.5 Analytical and Characterization Techniques ............................................. 78

3.5.1 Field Emission Scanning Electron Microscopy (FESEM) ....................... 79

3.5.2 High Resolution Transmission Electron Microscopy (HRTEM) ............ 80

3.5.3 Energy dispersive X-ray Spectroscopy (EDX) ....................................... 82

3.5.4 X-ray diffraction (XRD) ......................................................................... 83

3.5.5 Raman Spectroscopy .............................................................................. 84

3.5.6 Nitrogen adsorption-desorption measurement ........................................ 86

3.5.7 Fourier transformed infrared (FT-IR) spectroscopy ................................ 87

3.5.8 Thermo gravimetric (TGA) analysis ...................................................... 88

3.5.9 Ultraviolet-Visible Spectroscopy (UV-Vis) ........ 88

3.5.9.1 UV-Vis Absorption Spectroscopy ........ 88

3.5.9.2 UV-Vis Diffuse Reflectance Spectroscopy (UV-Vis DRS) ........ 89

3.5.10 Photoluminescence (PL) analysis ........ 90

3.5.11 X-ray photoelectron spectroscopy (XPS) ........ 91

3.5.12 High Performance Liquid Chromatography (HPLC) Analysis ........ 92

3.5.13 Ultra High Performance Liquid Chromatography Coupled With High Resolution Orbitrap Mass Spectrometry (UHPLC/ Orbitrap/MS) ........ 93

3.5.14 Total Organic Carbon (TOC) analysis ........ 94

## CHAPTER 4: RESULTS AND DISCUSSION ........ 95

4.1 Pristine MWCNTs Vs Purified MWCNTs ........ 96

4.1.1 Characterizations of pristine MWCNTs Vs. purified MWCNTs ........ 96

4.1.1.1 Surface Morphology and Elemental Analysis ........ 96

4.1.1.2 FT-IR spectra ........ 100

4.1.1.3 Raman analysis ........ 101

4.1.1.4 Summary ........ 103

4.2 $TiO_2$ Nanoparticles ........ 105

4.2.1 Characterizations of $TiO_2$ Nanoparticles ........ 105

4.2.1.1 Formation of $TiO_2$ Nanoparticles ........ 106

4.2.1.2 Surface Morphology and Elemental Analysis ........ 107

4.2.1.3 Phase Structure and Raman analysis ........ 110

4.2.1.4 Optical properties ........ 111

4.2.1.5 Summary ........ 113

4.3 The Effect of MWCNTs loading ........ 114

4.3.1 Characterizations of MWCNTs/$TiO_2$ nanocomposites ........ 114

4.3.1.1 Surface Morphology and Elemental Analysis ........................ 115

4.3.1.2 Phase Structure and Crystalinity ........................................... 121

4.3.1.3 Raman Analysis .................................................................... 124

4.3.1.4 Light absorption and photoluminesce (PL) properties .......... 127

4.3.1.5 Summary ............................................................................... 136

4.4 Effect of pH ............................................................................................. 137

4.4.1 Phase Structure and Crystallinity analysis ........................................... 137

4.4.2 Morphological Studies ......................................................................... 140

4.4.3 Raman Analysis ................................................................................... 143

4.4.4 Light absorption and photoluminesce (PL) properties ......................... 144

4.4.5 Photocatalytic activity On DMPEs ...................................................... 147

4.4.6 Summary .............................................................................................. 150

4.5 Effect of Calcination Temperatures ........................................................ 151

4.5.1 Characterizations of MWCNTs/$TiO_2$ nanocomposites ......................... 151

4.5.1.1 Phase Structure and Crystallinity analysis ............................ 151

4.5.1.2 Morphological Studies .......................................................... 155

4.5.1.3 Raman analysis ..................................................................... 158

4.5.1.4 Light absorption and photoluminesce (PL) properties .......... 160

4.5.1.5 Photocatalytic activity On DMPEs ....................................... 163

4.5.1.6 Summary ............................................................................... 167

4.6 Chemical State Analysis by XPS ............................................................ 168

4.7 Parameter studies in photocatalytic degradation process ........................ 174

4.7.1 Effect of irradiation time ...................................................................... 174

4.7.2 Effect of pH ......................................................................................... 176

4.7.3 Effect of Initial DMPEs Concentration ................................................ 178

4.7.4 Effect of Catalyst Dosage .................................................................... 180

4.7.5 Effect of $H_2O_2$ amount ........ 182

4.7.6 Reusability of MWCNTs/$TiO_2$ nanocomposites ........ 184

4.8 Photocatalytic Degradation Intermediates and DMPEs Degradation Mechanisms… ........ 187

4.9 Mineralization of DMPEs ........ 196

**CHAPTER 5: CONCLUSION & FUTURE WORK RECOMMENDATIONS ... 197**

5.1 Conclusion ........ 197

5.2 Suggestions and Recommendations ........ 201

References ........ 204

List of Publications and Papers Presented ........ 219

Appendix ........ 225

# LIST OF FIGURES

Figure 1.1: Global plastisizer consumption in 2014 .......................................................4

Figure 1.2: Global plasticizers markets, 2014-2020 ........................................................5

Figure 2.1: Regional demand for plasticizers ..............................................................19

Figure 2.2: General chemical structures of Phthalate esters (R and R’ represent alkyl side-chain)..........................................................................................................20

Figure 2.3 : Formation of phthalate esters via the esterification process........................20

Figure 2.4: Treatment methods described for the degradation of PAEs.........................27

Figure 2.5: Schematic representation of $E_g$ values (in eV) and position of band edges of various semiconductors. ..........................................................................33

Figure 2.6: Crystal structure of (a) rutile, (b) anatase and (c) brookite. .........................40

Figure 2.7: A schematic diagram illustrating the mechanism of photocatalysis on $TiO_2$ nanoparticles ..........................................................................................44

Figure 2.8: A schematic diagram of the pore distribution of an activated carbon support ..............................................................................................................47

Figure 2.9: Representative of fullerenes [$C_{60}$] molecules ..............................................49

Figure 2.10: Schematic diagram of graphene with a hexagonal packed structure..........51

Figure 2.11: Schematic representation of SWCNTs and MWCNTs .............................57

Figure 3.1: Overview of research methodology............................................................69

Figure 3.2: Experiment set up for the Pre-treatment of pristine MWCNTs....................71

Figure 3.3: A schematic representation on the preparation of $TiO_2$ coated on MWCNTs ..............................................................................................................73

Figure 3.4: A custom-made photocatalytic reactor for the photodegradation of DMPEs ..............................................................................................................74

Figure 3.5: Schematic of Field emission scanning electron microscope ........................80

Figure 3.6: Schematic of High resolution transmission electron microscope................82

Figure 3.7: Schematic of Bragg spectrometer ........ 84

Figure 3.8: Schematic of Renishaw Raman-spectrometer ........ 86

Figure 3.9: Schematic of FTIR Spectroscopy ........ 88

Figure 3.10: Picture of integrating sphere attached on DRS ........ 90

Figure 3.11: Emission luminescence of semiconductor ........ 91

Figure 3.12: Schematic of HPLC system ........ 93

Figure 4.1: FESEM images of Pristine MWCNTs (a) low magnification and (b) high magnification, Purified MWCNTs with (c) low magnification and (d) high magnification, and (e) TEM image of Purified MWCNTs ........ 98

Figure 4.2: Pre-treatment oxidation of MWCNTs at 100 °C for 2h ........ 99

Figure 4.3: FTIR spectra for the (a) Pristine MWCNTs and (b) Purified MWCNTs ... 101

Figure 4.4: Raman spectra for the (a) Pristine MWCNTs and (b) Purified MWCNTs ........ 103

Figure 4.5: FESEM images of $TiO_2$ nanoparticles with (a) low magnification and (b) high magnification, and (c) HRTEM image of $TiO_2$ nanoparticles ........ 108

Figure 4.6: (a) Elemental mapping and (b) EDX spectrum and composition of $TiO_2$ nanoparticles (calcined in air at 450 °C for 2h) ........ 109

Figure 4.7: XRD spectra of $TiO_2$ nanoparticles calcined in air at 450 °C for 2 h ........ 110

Figure 4.8: Raman spectra of $TiO_2$ nanoparticles calcined in air at 450 °C for 2 h ...... 111

Figure 4.9: UV-vis diffuse reflectance spectra (Inset is a variation of $(\alpha h\nu)^2$ versus photon energy (hν) of $TiO_{2)}$ ........ 112

Figure 4.10: FESEM images of (a) 3 wt%, (b) 5 wt%, (c) 10 wt % and (d) 15 wt % of MWCNT/$TiO_2$ nanocomposites ........ 117

Figure 4.11: HRTEM images of (a) 3 wt%, (b) 5 wt%, (c) 10 wt % and (d) 15 wt % of MWCNT/$TiO_2$ nanocomposites, (e) high resolution of 10 wt % of MWCNT/$TiO_2$ and (f) lattice fringe of MWCNT/$TiO_2$ nanocomposites ........ 119

Figure 4.12: Elemental mapping of (a) 3 wt% and (b) 15 wt% of MWCNTs/ $TiO_2$ nanocomposites ........ 121

Figure 4.13: XRD spectra of (a) $TiO_2$ nanoparticles, (b) 3 wt%, (c) 5 wt%, (d) 10 wt% and (e) 15 wt% of MWCNTs/ $TiO_2$ nanocomposites ........ 122

Figure 4.14: Raman spectra of (a) $TiO_2$, (b) 3 wt%, (c) 5 wt%, (d) 10 wt% and (e) 15 wt% of MWCNTs/ $TiO_2$ nanocomposites ........ 126

Figure 4.15: Raman shifts of the D band and G band of (a) 3 wt%, (b) 5 wt%, (c) 10 wt% and (d) 15 wt% of MWCNTs/ $TiO_2$ nanocomposites ........ 127

Figure 4.16: UV spectra of (a) $TiO_2$ nanoparticles, (b) Purified MWCNTs, (c) 3 wt%, (d) 5 wt%, (e) 10 wt% and (f) 15 wt% of MWCNTs/ $TiO_2$ nanocomposites ........ 129

Figure 4.17: PL spectra of (a) $TiO_2$, (b) Purified MWCNTs, (c) 3 wt%, (d) 5 wt%, (e) 10 wt% and (f)15 wt% of MWCNTs/ $TiO_2$ nanocomposites ........ 131

Figure 4.18: UV-visible spectrum of DMPEs ........ 132

Figure 4.19: Photocatalytic activity of a) $TiO_2$, b-e) 3, 5, 10, 15 wt% of MWCNTs / $TiO_2$ to degradation DMPEs ........ 134

Figure 4.20: First-order kinetics for DMPEs photodegradation using of a) $TiO_2$, b-e) 3, 5, 10, 15 wt% of MWCNTs/$TiO_2$ nanocomposites ........ 135

Figure 4.21: XRD spectra of of MWCNTs/ $TiO_2$ nanocomposites at (a) pH 3, (b) pH 5, (c) pH 7, (d) pH 9 and (e) pH 11 ........ 139

Figure 4.22: FESEM images of MWCNT/$TiO_2$ nanocomposites at (a) pH 3, (b) pH 5, (c) pH 7, (d) pH 9 and (e) pH 11 ........ 142

Figure 4.23: Raman spectra of MWCNT/$TiO_2$ nanocomposites at (a) pH 3, (b) pH 5, (c) pH 7, (d) pH 9 and (e) pH 11 ........ 144

Figure 4.24: UV spectra of MWCNT/$TiO_2$ nanocomposites at (a) pH 3, (b) pH 5, (c) pH 7, (d) pH 9 and (e) pH 11 ........ 145

Figure 4.25: PL spectra of MWCNT/$TiO_2$ nanocomposites ........ 147

Figure 4.26: Photocatalytic activity of MWCNTs / $TiO_2$ at (a-e) pH 3, 5, 7, 9 and 11 for degradation of DMPEs ........ 148

Figure 4.27: First-order kinetics for DMPEs photodegradation using MWCNTs/$TiO_2$ with different pH solution (a-e) pH 3, 5, 7, 9 and 11 ........ 149

Figure 4.28: XRD spectra of MWCNTs/ $TiO_2$ nanocomposites calcined at (a) 350 °C, (b) 450 °C, (c) 550 °C, (d) 650 °C and (e) 750 °C ........ 153

Figure 4.29: FESEM images of MWCNTs/ $TiO_2$ nanocomposites calcined at (a) 350 °C, (b) 450 °C, (c) 550 °C, (d) 650 °C and (e) 750 °C ..................................................... 157

Figure 4.30: Raman spectra of MWCNTs/ $TiO_2$ nanocomposites calcined at(a) 350 °C, (b) 450 °C, (c) 550 °C, (d) 650 °C and (e) 750 °C ..................................................... 159

Figure 4.31: TGA curves of (a) Purified MWCNTs and (b)10 wt % MWCNTs/$TiO_2$ nanocomposites ........................................................................................................ 160

Figure 4.32:UV spectra of MWCNTs/ $TiO_2$ nanocomposites calcined at (a) 350 °C, (b) 450 °C, (c) 550 °C, (d) 650 °C and (e) 750 °C .......................................................... 161

Figure 4.33: PL spectra of MWCNTs/ $TiO_2$ nanocomposites calcined at (a) 350 °C, (b) 450 °C, (c) 550 °C, (d) 650 °C and (e) 750 °C .......................................................... 163

Figure 4.34: Photocatalytic activity of MWCNTs / $TiO_2$ calcined at (a) 350 °C, (b) 450 °C, (c) 550 °C, (d) 650 °C and (e) 750 °C ................................................................ 165

Figure 4.35: First-order kinetics for DMPEs photodegradation using MWCNTs/$TiO_2$ calcined at (a) 350 °C, (b) 450 °C, (c) 550 °C, (d) 650 °C and (e) 750 °C................... 166

Figure 4.36: XPS survey spectra of 10 wt % MWCNTs/$TiO_2$ nanocomposites synthesized at pH 9 and calcined at 450 °C, $TiO_2$ and purified MWCNTs.................. 169

Figure 4.37: The XPS narrow scan of $TiO_2$ (a) Ti 2p and ........................................... 170

Figure 4.38: The XPS narrow scan of MWCNTs (a) C 1s and (b) O 1s ...................... 171

Figure 4.39: The XPS narrow scan of MWCNTs/$TiO_2$ nanocomposites (a) Ti 2p, (b) O 1s and (c) C 1s.............................................................................................................. 173

Figure 4.40: Effect of irradiation time of (a) photolysis, (b) dark adsorption, (c) nanocomposites photocatalysis with $TiO_2$ nanoparticles and (d) photocatalysis with MWCNTs/$TiO_2$ on the photocatalytic degradation of DMPEs ................................... 176

Figure 4.41: Effect of pH (a) pH =2, (b) pH =4, (c) pH =6, (d) pH =8 and (e) pH =10 on the photocatalytic degradation of DMPEs ................................................................. 178

Figure 4.42: Effect of initial DMPEs concentrations (a) 1 mg/L, (b) 1.5 mg/L, (c) 2 mg/L, (d) 2.5 mg/L and (e ) 3 mg/L on the photocatalytic degradation of DMPEs ..... 180

Figure 4.43: Effect of MWCNTs/$TiO_2$ dosage (a) 0.1 g/L, (b) 0.3 g/L, (c) 0.5 g/L and (d) 0.7 g/L on the photocatalytic degradation of DMPEs................................................. 182

Figure 4.44: Effect of $H_2O_2$ amount (a) 5 mg/L, (b) 10 mg/L, (c) 15 mg/L and (d) 20 mg/L on the photocatalytic degradation of DMPEs (MWCNTs/$TiO_2$ dosage= 0.5 g/L, [DMPEs] = 1 mg/L, pH =6) .......... 184

Figure 4.45: Reusability data over 10 wt % MWCNTs/$TiO_2$ nanocomposites in the degradation of 1mg/L DMPEs, over 0.5g/L catalyst, for 3 h irradiation under 96 W UV irradiation .......... 185

Figure 4.46: Photocatalytic mechanism of MWCNTs/$TiO_2$ nanocomposites .......... 187

Figure 4.47: HPLC chromatogram of DMPEs at (a) 0 h, (b) 15 mins, (c) 30 mins, (d) 45 mins, (e) 60 mins, (f) 120 mins, and (g) 180 mins irradiation time .......... 190

Figure 4.48: Proposed degradation pathways of DMPEs in photocatalytic reaction. The identified products are shown with solid arrows while the dotted black arrows are undefined pathways. .......... 195

Figure 4.49: Percentage removal of TOC of DMPEs by MWCNTs/$TiO_2$ nanocomposites .......... 196

# LIST OF TABLES

Table 1.1: Examples of the Initial Twelve Targeted POPs .......... 1

Table 1.2: Common properties of PAEs (Cao, 2010) .......... 4

Table 2.1: Physical properties of phthalate esters (PAEs) .......... 21

Table 2.2: Examples of blacklisted water priority pollutants, PAEs .......... 24

Table 2.3: Comparing the advantages and disadvantages of water treatment methods .. 36

Table 2.4: Photodegradation of PAEs under different treatment conditions .......... 37

Table 2.5: The basic properties for anatase, rutile and brookite $TiO_2$ .......... 39

Table 2.6: Physical properties of different carbonaceous materials .......... 54

Table 2.7: Comparing the advantageous and disadvantageous of carbonaceous materials .......... 55

Table 2.8: Characteristics and textural properties of SWCNTs and MWCNTs .......... 57

Table 2.9: Comparison of the most widely used synthesis methods for preparing CNTs/$TiO_2$ composite .......... 63

Table 2.10: Representative summary of CNT/$TiO_2$ composite synthesis routes .......... 64

Table 3.1: List of raw materials and chemicals used in the synthesis of .......... 68

Table 4.1: EDX elemental analysis (Weight %) of Pristine MWCNTs and .......... 100

Table 4.2: Elemental composition of (a) 3 wt %, (b) 5 wt %, (c) 10 wt % and (d) 15 wt % of MWCNTs/ $TiO_2$ nanocomposites .......... 120

Table 4.3: Effect of various MWCNTs content on crystallite size, BET surface area and band gap energy of MWCNTs/ $TiO_2$ nanocomposites .......... 124

Table 4.4: $I_D/I_G$ ratio of (3-15) wt% of MWCNTs/$TiO_2$ .......... 127

Table 4.5: Rate constants for catalytic photodegradation of DMPEs .......... 135

Table 4.6: Effect of various pH on crystallite size, BET surface area and band gap energy of MWCNTs/ $TiO_2$ nanocomposites .......... 140

Table 4.7: $I_D/I_G$ ratio of pH (3-11) of MWCNTs/$TiO_2$ .......... 144

Table 4.8: Rate constants for catalytic photodegradation of DMPEs using MWCNTs/$TiO_2$ nanocomposites ... 150

Table 4.9: Effect of various calcination temperatures on crystallite size, phase composition, surface area, and band gap energy of MWCNTs/ $TiO_2$ nanocomposites 155

Table 4.10: Rate constants for catalytic photodegradation of DMPEs ... 166

Table 4.11: Effect of irradiation time on the photocatalytic degradation of DMPEs ... 176

Table 4.12: Effect of pH value on the photocatalytic degradation of DMPEs ... 178

Table 4.13: Effect of initial DMPEs concentrations on the photocatalytic degradation of DMPEs ... 180

Table 4.14: Effect of MWCNTs/$TiO_2$ dosage on the photocatalytic degradation of DMPEs ... 182

Table 4.15: Photodegradation of DMPEs in solution at different $H_2O_2$ concentrations within 120 min ... 184

Table 4.16: Possible products of the degradation of DMPEs ... 193

# LIST OF SYMBOLS AND ABBREVIATIONS

| | | |
|---|---|---|
| POPs | : | Persistent organic pollutants |
| UNEP | : | United Nations Environment Programme |
| NIP | : | National Implementation Plan |
| EDCs | : | Endocrine Disrupting Chemicals |
| PAEs | : | Phthalate Esters |
| HAA | : | Hormonally Active Agents |
| DMPEs | : | Dimethyl Phthalate Esters |
| USEPA | : | United States Environmental Protection Agency |
| AOPs | : | Advanced Oxidation Processes |
| $TiO_2$ | : | Titania |
| MWCNTs | : | Multiwalled Carbon Nanotubes |
| UHPLC-Orbitrap/MS/MS | : | Ultra-high Performance Liquid Chromatography-Orbitrap Mass spectrometry |
| TTIP | : | Titanium isopropoxide |
| FESEM | : | Field Emission Scanning Electron Microscopy |
| HRTEM | : | High Performance Transmission Electron Microscopy |
| EDX | : | Energy Dispersive X-ray Spectroscopy |
| XRD | : | X-ray diffraction |
| BET | : | Brunauer-Emmett-Teller |
| FTIR | : | Fourier Transformed Infra-red Spectroscopy |
| UV-vis DRS | : | UV-vis Diffuse Reflectance Spectroscopy |
| PL | : | Photoluminesce |
| TGA | : | Thermogravimetric |
| XPS | : | X-ray Photoelectron Spectroscopy |

PCO : Photocatalytic Oxidation
HPLC : High Performance Liquid Chromatography
WHO : World Health Organization
EU : European Union
ROW : Rest of World
DEP : Diethyl Phthalate
DBP : Dibutyl phthalate
BBP : Butylbenzyl Phthalate
DEHP : Bis(2-ethylhexyl) phthalate
PVC : Poly (vinyl chloride)
DINP : Diisononyl phthalate
DOM : Dissolved Organic Matters
LD : Lethal dose
PMEs : Phthalate Monoesters
PA : Phthalic acid
$CO_2$ : Carbon Dioxide
$CH_4$ : Methane
•OH : Hydroxyl radical
$O_3$ : Ozonation
$H_2O_2$ : Hydrogen Peroxide
UV : Ultraviolet
IUPAC : International Union of Pure and Applied Chemistry
VB : Valence band
CB : Conduction band
nm : Nanometer

Ev : Electron volt

$O_2^{\bullet-}$ : Superoxide radical anion

MOCVD : Metal Organic Chemical Vapour Deposition

$C_{60}$ : Fullerenes

OD : Zero dimensional

GO : Graphene oxide

CVD : Chemical Vapor Deposition

$TiCl_4$ : Titanium tetrachloride

$TiOSO_4$ : Titanium Oxysulfate

Rpm : Revolutions per minute

TOC : Total Organic Carbon

FWHM : Full Width Half Maximum

# LIST OF APPENDICES

Appendix A: HPLC-Orbitrap-MS chromatogram of photoproducts from DMPEs degradation……………………………………………………………................225

# CHAPTER 1: INTRODUCTION

This present chapter comprises of the concise introduction regarding the dimethyl phthalate esters issues in which the research topic is concerned, problem statement, motivations, objectives, and outline of the research works.

## 1.1 Introduction

In the last four decades, the larger classes of chemical receiving comparatively little attention are the Persistent Organic Pollutants (POPs) due to the impact of chemical pollution has focused on the conventional “priority” pollutants. POPs are man-made chemical substances that are toxic, highly persistent, accumulate in fatty tissue, magnify in the food chain and pose a global threat to all living beings (Hung et al., 2016, Lee et al., 2014, Nadal et al., 2015). Initially, there are twelve targeted POPs and so called as the “dirty dozen” which are grouped according to their use and origin. These initial twelve targeted POPs include eight pesticides, two industrial chemicals and two unintended industrial by-products by the United Nations Environment Programme (UNEP) as shown in Table 1.1. POPs manage to sustain in the environment for years and it still can be found in the environment even their usage have been banned in the early 1970s because of the longer half-lives and persistent in nature in a given environmental media (Sajid et al., 2016, Xu et al., 2013b).

**Table 1.1:** Examples of the Initial Twelve Targeted POPs (Rigét et al., 2015)

| **Persistent Organic Pollutants (POPs)** | **Examples** |
|---|---|
| Pesticides | Aldrin, Dieldrin, Chlordane, Dichlorodiphenyl trichloroethane (DDT), Endrin, Heptachlor, Mirex and Toxaphene |
| Industrial chemicals | Polychlorinated biphenyls (PCBs) and Hexachlorocyclohexane (HCB) |
| Unintended by-product | Dibenzodioxins and Dibenzofurans |

These groups of chemicals have long been used in large amount throughout the world; quantities of many are on par with agrochemicals and they have been released into the environment on a large scale. Most importantly, the exposure to POPs can cause serious health impacts, including cancers and tumors at multiple sites, birth defects, neurobehavioral impairment, reproductive deficits and sex-linked disorders. Human, organism at the top of food chains, usually accumulate the highest body burden over their lifetime (Hansen et al., 2015, Sajid et al., 2016).

In response to this global problem, the Stockholm Convention on POPs was adopted on May 2001 in Stockholm, Sweden and came into force in 2004 under the UNEP with the participation of 171 countries. This Stockholm Convention is an internationally environmental treaty to protect human health and the environment from potentially harmful effects of POPs (Bao et al., 2012, Hansen et al., 2015). The evidence of detrimental effects on living organisms at the level of entire populations of some POPs demonstrated that almost 45,000 people in an Indian state, Kerela had been reported to suffer from different diseases (Sajid et al., 2016, Sharma et al., 2014). Besides, the estimation of 40,000 new cancer cases is detected every year and one in four Malaysian can be expected to get cancer in his or her lifetime. As reported, Malaysia became a signatory to the Stockholm Convention on POPs on 16 May 2002 for the development of a National Implementation Plan (NIP) for POPs management. However, the awareness among Malaysian public regarding POPs is still low due to their lack of understanding about the environment issues (Pariatamby and Kee, 2016).

Apart from the list of twelve POPs identified by Stockholm Convention, increasing concerns are given to emerging pollutants which are not currently covered under the listed chemicals in Stockholm Convention on POPs. They are persistent in nature, bioaccumulative, have a high potential being transported long-range in the environment, and pose a serious threat to wildlife and human health (Deblonde et al., 2011, Sauvé and Desrosiers, 2014). Meanwhile, some emerging POPs acts as endocrine disrupters which mimicking endogenous hormones and disrupting hormone secretion or metabolism. Endocrine disrupting chemicals (EDCs) could be defined as a mixture that affects the function of the endocrine system and causes adverse health effect in an organism (Bao et al., 2012, Sin et al., 2011, Thomaidi et al., 2015). For example, the incidence of genital malfunctions, such as cryptorchidism and penile malformations in baby boy has increased over past decades. EDCs were disposed or discharged into the environment on a continual basis via domestic/industrial sewage systems and wet-weather runoff. Enormous examples of endocrine disruption in wildlife are mostly involving animals that live in or closely related to the aquatic environment. The best evidence shows that exposure to EDCs affects the reproductive health and immune function of wildlife populations, resulting in increased susceptibility to infectious disease of vertebrates, especially marine mammals. Undoubtedly, this trace amount (parts per trillion) of EDCs present is adequate to initiate an estrogenic activity. The estrogenic activity can be defined as chemicals that mimic or antagonize the actions of naturally occurring estrogens (Caserta et al., 2013, Frye et al., 2012). Thus, a representative example of a class of emerging pollutants concern in environmental and wastewater is phthalate esters since they are abundant in the environment (Gao and Wen, 2016).

Phthalate esters (PAEs) or IUPAC name as dialkyl or alkyl aryl esters of 1,2-benzenedi-carboxylic acid are basically diesters of phthalic anhydride. It can be synthesized through an esterification reaction between phthalic anhydride and oxo alcohols (Cao, 2010). PAEs are liquids at typical environmental temperatures and mostly soluble in organic solvents. The common properties of PAEs are listed in Table 1.2.

**Table 1.2:** Common properties of PAEs (Cao, 2010)

| **Properties** | |
|---|---|
| Abbreviations | PAEs |
| Appearance | Colorless or yellowish oil like liquids |
| Melting point | Between 5.5 °C and -58 °C |
| Boiling point | Between 230 °C and 486 °C |
| Water solubility | Low |
| Soluble in common organic solvents | Benzene, toluene, xylene, diethyl ether, chloroform, and petroleum ether |

According to the worldwide production of PAEs, more than six million tons of PAEs per year has been produced, and such large productions are causing significant human diseases and pollution (Liu et al., 2013). The global plasticizer consumption in 2014 is shown in Figure 1.1**.**

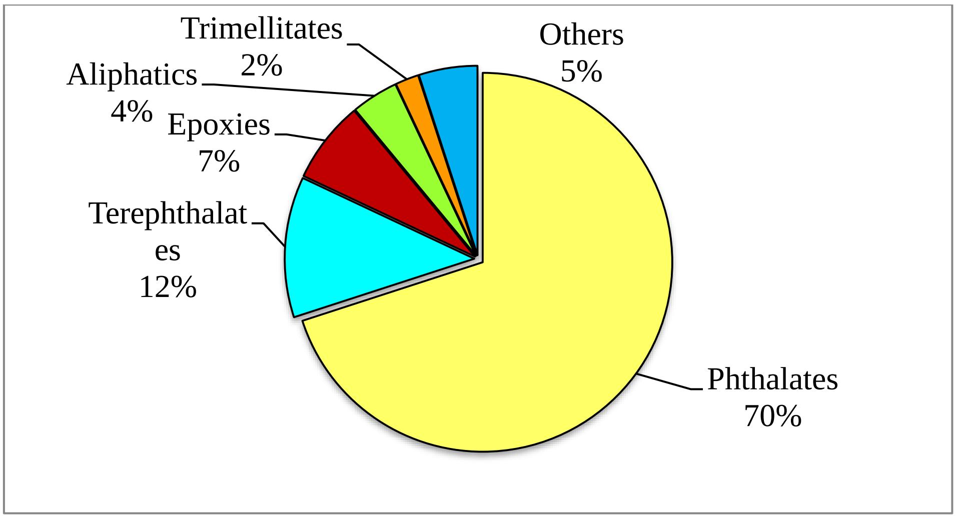

**Figure 1.1:** Global plastisizer consumption in 2014 (Tullo, 2015)

Besides, the rapidly growing demands for PAEs are expected to be the major drivers of the plasticizers market. The historic data of 2014 along with a forecast from 2015 to 2020 based on both volumes (kilo tons) and revenue (USD million) for the plasticizers market on a global level had been reported by Zion research. It was noted that the global plasticizer market accounted for USD 15.35 Billion in 2014 and is estimated to reach USD 19.82 Billion by 2020 (Market Research Store, 2016).

**Figure 1.2:** Global plasticizers markets, 2014-2020 (Market Research Store, 2016)

PAEs have been widely applied in industrial, cosmetic, pharmaceutical and consumer products primarily for their uses as plasticizers for the production of polyvinyl chloride resins, skin moisturizers, skin softeners, anti-brittleness and anti-cracking agents in nail polishes, pharmaceutical tablets and capsules, children’s toys and food product containers (Gao and Wen, 2016, Hansen et al., 2015, Hubinger, 2009). PAEs were reported to be hormonally active agents (HAA) whose exposure may pose a strong threat to the ecosystem and humans (Kamrin, 2009, Liang et al., 2008). They have indicated that PAEs induce testicular atrophy and malfunctions, reduce sperm counts and decrease survival of offspring by mimicking or antagonizing the actions of endogenous steroid hormones (Fisher, 2004, Maqbool et al., 2016, Liu et al., 2013, Ren et al., 2011, Xu et al., 2009a).

DMPEs are among the most frequently identified PAEs in the environment because of its common usage and its refractory biodegradability. For instance, DMPE acts as a major plasticizer and bind non-covalently to the polymers; it can easily be leached out and released from the polymeric products such as lunch boxes, spoon and forks to the hot soup or heated food which may cause acute toxicity when orally ingested daily (Cheung et al., 2007, Osman et al., 2013, Yuan et al., 2008b). Furthermore, functional disturbances in the nervous system and liver of animals can be caused by the long-term exposure to DMPEs. Therefore, DMPEs has been listed as Priority Persistent Organic Pollutants by the United States Environmental Protection Agency (USEPA) and other European countries (Ding et al., 2008, Osman et al., 2013, Xu et al., 2009b, Zeng et al., 2008, Zhang et al., 2015).

Basically, there are various types of physical, biological, and chemical treatment processes that had been carried out for mitigating DMPEs. However, activated sludge or charcoal system that being used by conventional water and wastewater treatment plants are ineffective and non-destructive to remove DMPEs. Most of these DMPEs remain soluble in the effluent (Amin et al., 2014, Ding et al., 2008, Xu et al., 2009a, Yuan et al., 2008b). Due to environmental healthy, appropriate treatment technologies are necessary to be identified to remediate the pollution of DMPEs from waters and wastewater. In recent years, advanced oxidation processes (AOPs) such as UV/$H_2O_2$, Fenton/UV and ozonation are among the most common method for DMPEs removal from wastewater. Heterogeneous catalytic system, a kind of AOPs, particularly semiconductor photocatalysis is one of the highly advanced promising technologies for the elimination of a wide range of recalcitrant organic pollutants resistant to conventional methods without high temperature and pressure and low negative effect on water quality (Ding et al., 2008, Wu et al., 2011, Xu et al., 2009a, Yuan et al., 2008b).

Moreover, the pollutants from the complex molecules can be broken down into simple and non-toxic substances during the photocatalytic oxidation treatment, thus, no second treatment is involved for processing the sludge. Furthermore, the catalyst remains unchanged and can be reused which results in a significantly lower operating expense.

Among all kinds of semiconductor photocatalysts (i.e. $WO_3$, $Fe_2O_3$, $CeO_2$, ZnO and ZnS), nanoscale anatase titania ($TiO_2$) has received considerable attention because it is an inexpensive, thermal stability, non-toxicity, chemical inertness and easily attainable catalyst. They have reported that ZnO is unstable in water and will form $Zn(OH)_2$ on the particle surface while metal sulfides are toxic and not stable enough for catalysis in aqueous media. However, the photocatalytic efficiency of $TiO_2$ is hindered by the wide band gap energy of $TiO_2$ (3.2 eV for anatase phase and 3.0 eV for rutile phase), which may induce the fast recombination of electron-hole pairs. This extensively restricts the effectiveness of photo conversion by $TiO_2$ (Chen and Oh, 2010, Gui et al., 2014a, Hamid et al., 2014, Teh and Mohamed, 2011, Xie et al., 2009).

Generally, a good photocatalyst must has large specific surface area with high photo active efficiency under UV illumination as it is capable of conducting electrons and adsorbing organic pollutants (Chen et al., 2009, Hamid et al., 2014, Wu et al., 2013). Several attempts such as metal / non-metal doping, coupling with semiconductors and dyes sensitization have been implemented to improve the photocatalytic activity of $TiO_2$ by reducing the electron-hole recombination rate, increasing the adsorption capacity under UV illumination and modification of $TiO_2$ surface for organic pollutants removal(Gao et al., 2008, Jiang et al., 2011).

In the present study, the nanocomposites of carbonaceous materials with $TiO_2$ nanoparticles have become the major interest of researchers because of their unique properties in terms of physical, structural, chemical, thermal, mechanical, electrical and optical applications. Among the carbonaceous materials, multiwalled carbon nanotubes (MWCNTs) shows the good intrinsic properties as a good adsorbent and dispersing agent which may create more active sites for photon absorption from illumination (Jiang et al., 2011, Ling Tan et al., 2015, Wang et al., 2009, Wu et al., 2013). Besides, the unique properties of MWCNTs such as high electrical conductivity, high surface area and good support for $TiO_2$ nanoparticles make it a promising material for the fabrication of MWCNTs/$TiO_2$ nanocomposites for degradation of DMPEs. In this manner, MWCNTs plays an essential role as a good electron acceptor for photo excitation $TiO_2$ through the facilitating for the separation of electron-hole pairs and modification of the optical band gap which may lead to the enhancement in the efficiency of $TiO_2$ (Su et al., 2013). The electrons are transferred away from the $TiO_2$ after the photo excitation, leaving holes on the surface of the $TiO_2$. Thus, the photoreaction can be triggered by these electrons by the formation of very reactive radicals such as superoxide radical ions and hydroxyl radicals (Gui et al., 2014b). In photocatalytic system, MWCNTs/$TiO_2$ nanocomposites showed higher photocatalytic activity than $TiO_2$ due to the heterojunction between $TiO_2$ and MWCNTs that could separate electron and holes and thereby retard the recombination of photogenerated electrons and holes (Aazam, 2014, Tseng et al., 2010, Xie et al., 2009). The heterojunction between MWCNTs and $TiO_2$ indicates the interaction between these two composites via the lattice fringe measurements.

Therefore, in this research, a modified sol-gel method was used to synthesize MWCNTs/$TiO_2$ nanocomposites. The effects of the MWCNTs loading, pH of the solution, and calcination temperature were investigated. The morphological and the optical properties of MWCNTs/$TiO_2$ nanocomposites were studied. Their applications in DMPEs removal was also studied in detailed.

## 1.2 Problem Statement

$TiO_2$, a well-known environmentally benign photocatalyst, has been applied for environmental remediation such as air purification, water purification, and hazardous waste remediation due to its high activity, strong oxidizing power, non-toxicity, low cost and good physical-chemical stability (Chen et al., 2003, Gupta and Tripathi, 2011, Jiang et al., 2011, Pelaez et al., 2012). However, vast applications of bulk $TiO_2$ as photocatalytic materials are restricted by its relatively low specific surface area (30 $m^2/g$). Therefore, it is important to maximize the specific surface area of $TiO_2$ in order to improve photon absorption and photocatalytic performance. In addition, technical limitations for adopting this technology are separation of the catalyst, its reuse and its low quantum efficiency. Recent advances in $TiO_2$ nanomaterials with sizes smaller than 100 nm have provided the opportunities to address the water quality issues due to their structure. $TiO_2$ nanoparticles, having high absorption, interaction, and reaction capabilities, can behave as colloid by mixing mixed with aqueous suspensions and they can penetrate deeper and thus can treat wastewater which is generally not possible by conventional technologies (Chen et al., 2014).

Another limitation of $TiO_2$ which need to be overcome is the their rapid recombination rate of photogenerated electron-hole pairs due to its relatively wide band gap energy, which resulting in lower photodegradation efficiency (Chen et al., 2003, Gao et al., 2008, Jiang et al., 2011, Pelaez et al., 2012, Wu et al., 2013). In $TiO_2$, the longer electron transporting time are caused by the presence of defects or trapping sites, more grain boundaries, and disordered contact area between two particles, which leads to more recombination losses and scattering problems of photo-induced electrons. This drawback cannot be overcome by only $TiO_2$ nanoparticles itself. Thus, production of high efficient photocatalytic system by using $TiO_2$ nanoparticles is challenging unless several issues pointed out are addressed. Considerable efforts have been exerted to improve the rapid recombination of photo-generated charge carriers by coupling MWCNTs with $TiO_2$ nanoparticles. The synergistic effects of the coupling of $TiO_2$ and MWCNTs are able to enhance the overall efficiency of the photocatalytic process. The separation of the photo-generated electron-hole pairs is favored by the conductive structure of the MWCNTs through the formation of heterojunctions at the MWCNTs/$TiO_2$ nanocomposites interface (Aazam, 2014, Djokić et al., 2014, Tseng et al., 2010, Xie et al., 2009). Therefore, in the present study, considerable efforts have been devoted to the synthesis of MWCNTs/$TiO_2$ nanocomposites. A few factors that influent the synthesis of MWCNTs/$TiO_2$ such as the effects of MWCNTs loading, pH of the solution and calcination temperatures on the formation of MWCNTs/$TiO_2$ nanocomposites were studied.

## 1.3 Motivations

The toxicity of Dimethyl phthalate esters (DMPEs), impacts and pollution have long been recognized from various reports described earlier. Thus, a few problem statements have been addressed: what type of material is suitable to degrade DMPEs; why it is being selected; what is the interaction between the material and DMPEs that can prevent the DMPEs pollution issues; and what are the possible intermediate products formed after the reaction. In this work, photocatalysis using $TiO_2$ was studied for DMPEs mitigation. However, two major challenges associated with $TiO_2$ photocatalysis are to decrease the recombination rate and lower the band gap energy. Thus, to resolve the problems of the unmodified $TiO_2$ listed above, continuous efforts have been conducted by coupling $TiO_2$ nanoparticles with carbon nanomaterials. In this case, the $TiO_2$ nanoparticles with carbon nanomaterials must fulfill several basic requirements for better charge separation efficiency, such as the carbon nanomaterials can act as effective electron transfer unit and can prompt electron transfer from the conduction band of the $TiO_2$ nanoparticles towards the carbon surface due to their lower Fermi level (Aazam, 2014, Djokić et al., 2014). In the present study, MWCNTs was selected as a suitable carbon nanomaterial to be coupled with $TiO_2$ nanoparticles due to modification of MWCNTs with strong acids to form surface groups such as carboxylic acids which can induce stronger $TiO_2$ anchoring by improving surface contact between the carbon-phase and $TiO_2$ nanoparticles. This stronger interface interaction also favors electron transfer pathways, thus the probability for electron/hole recombination is reduced. The role of MWCNTs in photocatalysis is mainly as support for $TiO_2$ to form composite catalysts due to their large specific surface area and high quality active sites for stronger adsorption on MWCNTs/$TiO_2$ nanocomposites for the DMPEs (Tseng et al., 2010, Xie et al., 2009). Apart from that, in the case where the MWCNTs/$TiO_2$ nanocomposites are applied, the strong interaction and intimate contact between the $TiO_2$ nanoparticles and the surface of the MWCNTs could form a barrier junction which enhances the transmission stability of promoted electron between the MWCNTs and the conduction band of $TiO_2$. Herein, the MWCNTs coupled with $TiO_2$ nanoparticles was the ideal compound for DMPEs removal.

In particular for the photodegradation of DMPEs, the degraded products were analysed by ultra-high performance liquid chromatography-Orbitrap mass spectrometry (UHPLC-Orbitrap/MS/MS) for the first time, and the possible degradation pathways are proposed. The unique Orbitrap mass analyzers equipped with a quadrupole mass filter, linear ion trap and Orbitrap mass analyzers provide the high-resolution, accurate-mass performance and identify the compounds more quickly. This study will give a better understanding of the transfer, transform, and degradation of DMPEs which could provide further insight into the mechanisms occurring under oxidative and reductive conditions.

## 1.4 Objectives of Study

The objectives of this study are listed as follow:

- To synthesize MWCNTs/$TiO_2$ nanocomposites using a simple modified sol-gel technique.
- To study the synthesis parameters (effect of concentration, calcination temperature and pH) towards the photocatalytic activity of MWCNTs/ $TiO_2$ nanocomposites.
- To investigate the structural, morphological and optical properties of the MWCNTs/ $TiO_2$ nanocomposites.
- To evaluate the photocatalytic activity of the synthesized MWCNTs/$TiO_2$ nanocomposites for effective degradation of DMPEs.
- To identify the degraded products and hence, propose the degradation mechanism of DMPEs.

## 1.5 Outline of Research Work

Primarily, this research study could be divided into four main sections which included the synthesis of MWCNTs/$TiO_2$ nanocomposites, characterizations of the photocatalyst, photocatalytic reaction of DMPEs and possible photocatalytic degradation mechanism of DMPEs. These four well-organized work scopes will be examined thoroughly in order to achieve the objectives mentioned in Section 1.4.

### 1.5.1 Synthesis of MWCNTs/$TiO_2$ nanocomposites

In this section, MWCNTs/$TiO_2$ nanocomposites were successfully synthesized using modified sol-gel method with titanium isopropoxide (TTIP) and purified MWCNTs as the starting precursors. Prior to purification, the pristine MWCNTs were treated with concentrated nitric acid in order to remove the carbonaceous impurities as well as the residual metal-oxide particles before applying in the synthesis of MWCNTs/$TiO_2$ nanocomposites. Under such conditions, the remaining metal oxide particles were removed and the holes were formed in the sidewalls followed by an oxidative etching along the walls with the concomitant release of carbon dioxide. The oxygen-containing groups mainly hydroxyl and carboxyl groups were introduced onto the ends and sidewalls of the MWCNTs (Tessonnier et al., 2009, Su et al., 2013). During the sol gel techniques, the mixture of solution was underwent vigorous stirring for 2 hour, washing with ethanol, drying in oven and further heat-treatment in order to convert the amorphous structure of the composite into crystalline phase by an annealing step at temperatures higher than 300 °C, leading in most cases to a collapse of the pore system and an increase in the particle size. The sol-gel synthesis of MWCNTs/$TiO_2$ nanocomposites was carried out with different weight percent of MWCNTs, pH of solution and calcination temperature, in order to study the structural, morphological and optical properties of the MWCNTs/$TiO_2$ nanocomposites and then, were applied to photocatalytically degrade DMPEs. The procedures used to prepare the samples are described in details in Chapter 3- Research Methodology while the parameter studies on MWCNTs/$TiO_2$ are discussed in Chapter 4.

### 1.5.2 Characterizations of the photocatalyst

The second section is associated with various characterization techniques that were used to investigate the chemical and physical properties of the MWCNTs, $TiO_2$, and MWCNTs/$TiO_2$ nanocomposites prepared via a simple modified sol-gel technique. The surface morphologies of the prepared samples were observed by Field Emission Scanning Electron Microscopy (FESEM) and High Resolution Transmission Electron Microscopy (HRTEM). Additionally, the elemental analysis was carried out with Energy Dispersive X-ray Spectroscopy (EDX) analysis. The phase composition of the samples was determined by X-ray diffraction (XRD) and Raman Spectroscopy techniques. Moreover, the graphitic structure of carbon bond and defects was obtained by Raman Spectroscopy technique. Brunauer-Emmett-Teller (BET) analysis was used to determine the surface areas of the prepared samples. Fourier Transformed Infra-red Spectroscopy (FTIR) was used to determine the chemical bondings and functional groups of pristine MWCNTs and purified MWCNTs. The optical properties and electron hole/pairs recombination of the MWCNTs/$TiO_2$ nanocomposites were studied by UV-vis Diffuse Reflectance Spectroscopy (UV-vis DRS) and Photoluminesce (PL) measurements, respectively. Thermogravimetric (TGA) analysis was used to study the thermal stability and the oxidation weight loss conditions of the samples. The elemental composition, chemical and oxidation state of the sample surface was identified by X-ray Photoelectron Spectroscopy (XPS). The fundamental principles and the operating parameters for sample characterization are described in details in Chapter 3-Research Methodology.

### 1.5.3 Photocatalytic reaction of DMPEs

In this section, the synthesized MWCNTs/$TiO_2$ nanocomposites were applied in the Photocatalytic Oxidation (PCO) process of Dimethyl Phthalate Esters (DMPEs). Photocatalytic degradation of DMPEs was evaluated under irradiation of a 96 W UV lamp in a custom made photoreactor with five cylindrical quartz vessels (150 mL). In this part, the effect of reaction parameter i.e. irradiation time, initial concentrations of DMPEs, catalyst dosages, pH of the solution and $H_2O_2$ dosages were carried out in order to investigate the photocatalytic efficiency of DMPEs. The concentration of DMPEs in the test solution with $\lambda_{max} = 204$ nm was determined via UV-Vis spectrophotometer.

### 1.5.4 Possible photocatalytic degradation mechanism of DMPEs

The degraded products of DMPEs were identified by using High Performance Liquid Chromatography (HPLC). The retention time of the primary intermediates of DMPEs degradation was showed by HPLC chromatogram. Subsequently, the identification for each unknown intermediate product was further investigated through Ultra High Performance Liquid Chromatography coupled with high resolution Orbitrap Mass Spectrometry (UHPLC-Orbitrap/MS/MS) to propose the possible degradation mechanism of DMPEs.

## 1.6 Outline of Thesis

The outline of this thesis is well-structured into five chapters successively. The Chapter 1 in this thesis associated with the brief introduction of this research work, problem statement, motivations, research objectives, the outline of research work in conjunction with thesis overview. The Chapter two in this thesis is related to the review on properties, classification, application, toxicity and health hazards of PAEs as well as the treatment technologies used for PAEs removal. The last section of this chapter two gives the properties, limitations, and modifications of $TiO_2$. The specifications of the raw materials, research methodology and the characterizations involved are presented in Chapter 3. The Chapter 4 in this thesis presented the characterization results of the prepared samples along with the discussion and the performance evaluation of MWCNTs/$TiO_2$ in the photodegradation of DMPEs. Lastly, the conclusions, suggestions as well as recommendations for future work are summarized in Chapter 5.

# CHAPTER 2: LITERATURE REVIEW

Nowadays, widespread concerns continue to be raised about the impacts of exposure to emerging persistent organic pollutants (POPs) with endocrine disrupting activities that exert hormonal imbalance. These emerging POPs are globally concerned pollutants due to their widespread occurrence, long-term persistence, strong resistance, and potentially pose a great threat to human beings and ecosystems. Since emerging POPs such as phthalate esters (PAEs) has become a class of concerning water pollutants, thus, there is a strong need to look for alternative and faster treatment processes for such pollutants. Advanced oxidation processes (AOPs) employing semiconductor photocatalysis is one of the most promising prospects for efficient degradation of PAEs. To bring this technology to the point of commercial readiness and viability in terms of performance and cost, substantial research on the development of photocatalytic oxidation on PAEs is necessary to be carried out.

Recent studies have indicated that $TiO_2$ had emerged as the leading candidate in the photocatalytic degradation of organic pollutants. Lately, interesting and unique features of carbonaceous materials-based $TiO_2$ photocatalyst system have gained much attention and became favorite research matter among various groups of scientists. The relationship between the carbonaceous materials on $TiO_2$ photocatalyst as well as their photocatalytic performance on PAEs was still as a matter of debate and remains unclear. It was noted that the properties of this carbonaceous materials-based $TiO_2$ photocatalyst primarily depend on the nature of the preparation method and the synergies effects between the carbonaceous materials and $TiO_2$. Therefore the development of efficient carbonaceous materials-based $TiO_2$ photocatalyst remains to be determined. In the subsequent section, the historical overview, basic principle, material selection and work done by various researchers with regards to the carbonaceous materials-based $TiO_2$ photocatalyst as well as their photocatalytic application in the degradation of environmental pollutants will be reviewed in detail.

This chapter is divided into three sections. The first section gives the review on properties, classification, application, toxicity and health hazards of PAEs. The second section provides the review on the methods used for PAEs removal. The last section gives the properties, limitations, and modifications of $TiO_2$.

## 2.1 Phthalate esters (PAEs)

Nowadays, water quality has become a critical environmental and public health issue which contributing to the death of 2 million people a year. There are currently more than 0.78 billion people around the world who do not have access to safe water resources resulting in a major water-related problem of diarrhea. It is reckoned that in the year of 2025, there will be at least 3 billion people will live in an area where they are unable to meet the basic water needs due to the presence of hazardous environmental contaminants especially organic and inorganic pollutants in everyday of life. One of the major water pollutions is the PAEs from different sources (eg., plasticizers for plastics, nail polish, cosmetics, perfumes, insect repellents, fishing lures, adhesive and paint industry) which are considered a wide variety of emerging persistent organic pollutants (POPs) introduced into the surface marine waters, freshwaters or wastewater treatment systems (Deblonde et al., 2011, Gao and Wen, 2016). As a result, PAEs have become ubiquitous environmental pollutants and are found in food, atmosphere, natural waters, soils and aquatic organisms. In addition, PAEs are relatively stable in the natural environment and the estimation for their hydrolysis half-life is to be about 20 years. The concentration of PAEs in surface water has been reported in the ranges of ng/L. In 1995, the World Health Organization (WHO) promulgated chemicals that can disrupt human endocrine function and must be controlled, and PAEs are included in the list of priority monitoring pollutants (Zeng et al., 2008). Despite their low concentration present in the aquatic environment, PAEs have been listed as hazardous pollutants by both the USEPA and the European Union (EU) due to the fact that even a trace amount of them is found to be potentially harmful to human and the environment. Up to now, the global production of PAEs is estimated to be several million tons and will continue to increase. As shown in Figure 2.1, 95 % of all plasticizer used was in polyvinyl chloride (PVC) of which 87 % were phthalates of various types. In addition, the Asia Pacific market holds the majority of the demand for the plastisizer market, closely followed by North America, Europe and Rest of World (ROW).

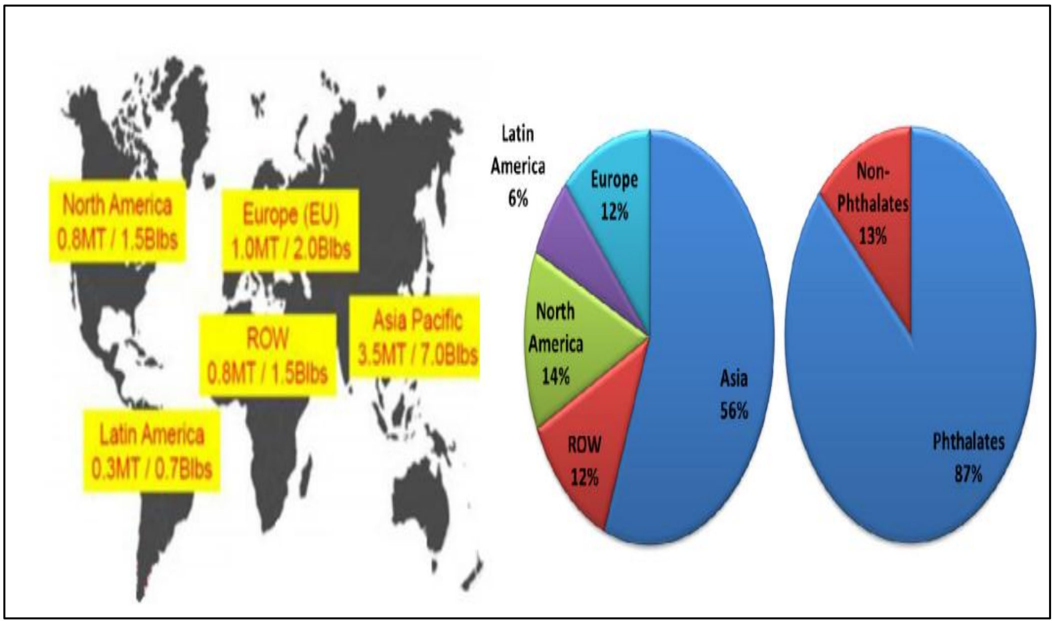

**Figure 2.1:** Regional demand for plasticizers (Minnesota Corn Research & Promotion Council, 2014)

### 2.1.1 Properties and Classification of PAEs

Basically, Phthalate esters (PAEs) or phthalates are dialkyl or alkyl aryl esters of 1, 2-benzendicarboxylic acid (phthalic acid). The chemical structure of PAEs as shown in Figure 2.2 are described as a planar aromatic ring with the two slightly mobile side chain that comprised of chemical groups, including alkyl, benzyl, phenyl, cycloalkyl, or alkoxy (Cheung et al., 2007, Huang and Chien, 2013, Xu et al., 2015, Wu et al., 2011, Yuan et al., 2008b).

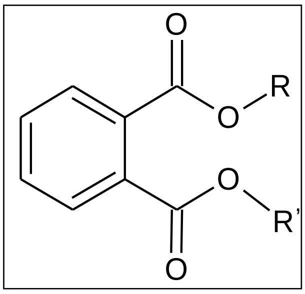

**Figure 2.2:** General chemical structures of Phthalate esters (R and R' represent alkyl side-chain)

The desired phthalate esters are prepared by the reaction of the phthalic acid with a specific alcohol as shown in Figure 2.3.

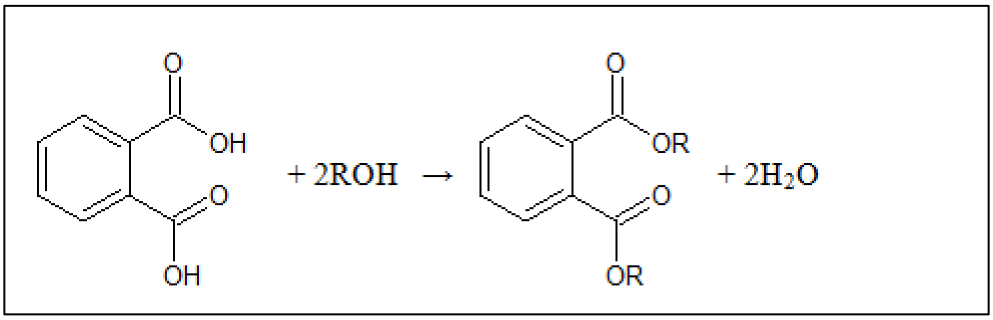

**Figure 2.3 :** Formation of phthalate esters via the esterification process

Normally, PAEs are colorless or yellowish oil like liquids and almost odorless at ambient temperature. PAEs have a melting point below -25 ºC and the boiling point ranges from 230 ºC to 486 ºC. Mostly, PAEs have low water solubility and high octanol partition coefficient ($K_{OA}$) values, thus, they become concentrated in suspended matter and sediment. In addition, PAEs become more viscous and oily as the size of the alkyl side-chain increased. PAEs have basically low volatility which decreased with the increasing of the side chain of the ester. Accordingly, dimethyl phthalate (DMP) is the most hydrophilic and water soluble of the esters while the $C_{10}$, $C_{11}$, and $C_{13}$ esters are the most hydrophobic and least water soluble due to effects of alkyl chain length (Cheung et al., 2007, Huang and Chien, 2013, Xu et al., 2015, Su et al., 2013, Yuan et al., 2008b).

Mainly, most of the PAEs are soluble in organic solvents such as benzene, toluene, diethyl ether and chloroform. Indeed, the longer the alkyl side-chain or degree of branching, the more persistent the compound and tend to have longer half-lives in a given environmental media. The physical properties of some relevant phthalates such as dimethyl phthalate (DMP), diethyl phthalate (DEP), dibutyl phthalate (DBP), butylbenzyl phthalate (BBP) and bis(2-ethylhexyl) phthalate (DEHP) are summarized in Table 2.1.

**Table 2.1:** Physical properties of phthalate esters (PAEs) (Rivera-Utrilla et al., 2012)

| **Phthalate esters** | **Abbreviation** | **Formula** | **CAS. No.** | **Molecular Weight (g/mol)** | **Melting point (°C)** | **Special gravity (20°C)** | **LD50 (median dose), mg/kg** |
|---|---|---|---|---|---|---|---|
| Dimethyl phthalate | DMP | $C_{10}H_{10}O_4$ | 131-11-3 | 194.2 | 2 | 1.192 | 5200 [rabbit, oral] |
| Diethyl phthalate | DEP | $C_{12}H_{14}O_4$ | 84-66-2 | 222.2 | -4 | 1.118 | 1000 [rabbit, oral] |
| Dibutyl phthalate | DBP | $C_{16}H_{22}O_4$ | 84-74-2 | 278.4 | -35 | 1.042 | 3474 [mouse, oral] |
| Butyl benzyl phthalate | BBP | $C_{19}H_{20}O_4$ | 85-68-7 | 312.4 | -35 | 1.111 | 4170 [mouse, oral] |
| Bis(2-ethylhexyl) phthalate | DEHP | $C_{24}H_{38}O_4$ | 117-81-7 | 390.6 | -47 | 0.986 | 33900 [rabbit, oral] |

### 2.1.2 Occurrence of Phthalate esters in the environment

Due to the lack of toxicological data for phthalate esters (PAEs) before use, scientists have been working towards better understanding of their environmental occurrences to wildlife and humans. The toxicity of PAEs has led to a dramatic increase in awareness about the occurrence of PAEs in the environment. A systematic search for reports in the past 20 years using keywords containing phthalates has been performed and the result indicating that the number of related reports on PAEs increased with each progressive years. Remarkably, the number of PAEs in 2014 is reported to be 12 times greater than in 1995 and this demonstrates the sharp increase of PAEs in the environment as reported in scientific literature (Gao and Wen, 2016).

The majority of PAEs exists in the environment are caused by the slow release of phthalates from cosmetics, personal care products, and plasticizers during the manufacturing, storage, use, and disposal process. It is noteworthy that the PAEs are refractory to the environmental microorganisms and the wide distribution of PAEs in an aqueous system like rivers, lakes, and ground waters. In addition, a noticeable influence on the ecological environment is caused by the accumulation of persistent toxic PAEs in natural waters (Cheung et al., 2007).

Chemically, phthalates are ubiquitous because they are not covalently bound to polymer matrixes and thus it can leach, migrate, and evaporate into food stuff and being discharged into the environment during their production and use and after their disposal. Due to the low solubility of PAEs, PAEs tend to be concentrated from wastewater into sewage sludge. Studies have reported that the presence of phthalates was observed in the rivers and small streams in the Han River basin, Korea and the detection of PAEs in freshwater fish species are obtained (Rivera-Utrilla et al., 2012). As a result, the accumulation of PAEs in the environment is actually a threat to our ecosystem and human health. Thus, there is a need to ensure the sludge is free from these contaminants (Cheung et al., 2007, Huang and Chien, 2013, Xu et al., 2015, Wu et al., 2011, Yuan et al., 2008b).

### 2.1.3 Application

Phthalate esters (PAEs) have been widely applied in numerous industrial and consumer products, primarily as plasticizers in poly (vinyl chloride) (PVC) products. Generally, PAEs can be used as plasticizers, heat transfer fluids and carriers due to the low melting point and high boiling point. In addition, it can also be found as a common additive in paints, lubricants, adhesives, insecticides, and packaging. The examples of low molecular weight of phthalates such as dimethyl phthalate (DMP), diethyl phthalate (DEP) and dibutyl phthalate (DBP) are widely used in cosmetics and personal care products. For instance, DMP and DEP allow perfume fragrances to evaporate more slowly, lengthening the duration of the scent, and a small amount of DBP gives nail polish a chip-resistant property. Additionally, the examples of high molecular weight of phthalates consist of di (2-ethylhexyl) phthalate (DEHP), diisononyl phthalate (DINP) and BBP, they are widely utilized as plasticizers in the polymer industry in order to improve flexibility, workability, and general handling properties. Estimated over 470 million pounds of phthalates are produced in large volume per year (Matsumoto et al., 2008).

Although PAEs have been commercially used for over 50 years, some parties have expressed concern about PAEs and have advocated for their elimination from the consumer products. Policies and regulations restricting the use of phthalates have been developed in various jurisdictions. Studies have reported that some of the PAEs are blacklisted as priority water pollutants by the United States Environmental Protection

Agency (USEPA) and the Chinese Environmental Monitoring Center (Huang and Chien, 2013, Xu et al., 2015, Wu et al., 2011, Yuan et al., 2008a). Among these phthalates, DMP, DBP, and DOP are blacklisted as priority detection pollutants for water in China. Besides, DnBP and DEHP have been banned by the European Union (EU), US and Japan for use in cosmetic and personal care products. Furthermore, bis(2-ethylhexyl) phthalate (DEHP) that is widely applied in the manufacture of plastic products is also listed on Health Canada’s Cosmetic Ingredient Hotlist as prohibited ingredient and should not be included in cosmetic products. Moreover, in May 2011, the Taiwan Food and Drug Administration reported that DEHP as a food additive is illegally added to foods and beverages and the presence of DEHP in foods and drinks can lead to kidney damage and fertility problems if it is consumed regularly. Therefore, all contaminated products are destroyed by the Taiwanese government and this outbreak event is also known as the “2011 Taiwan Food Scandal”. The examples of PAEs that have been listed in the blacklist of water priority pollutants, by the USEPA, EU, China and other countries are summarized in Table 2.2.

**Table 2.2:** Examples of blacklisted water priority pollutants, PAEs

| Blacklisted PAEs | Country | References |
|---|---|---|
| Dimethyl phthalate (DMP)<br>Di-n-butyl phthalate (DnBP)<br>Di-n-octyl phthalate (DnOP) | China | (Zhang et al., 2014b)<br>(Zhang et al., 2015)<br>(Hu et al., 2014) |
| Di(2-ethylhexyl) phthalate (DEHP)<br>Dibutyl phthalate (DBP) | European Union<br>United States<br>Japan | (Gao and Wen, 2016)<br>(Bui et al., 2016) |
| Di(2-ethylhexyl) phthalate (DEHP) | Canada<br>Taiwan | (Guo et al., 2014)<br>(Al-Saleh and Elkhatib, 2016) |

### 2.1.4 Toxicity/Health Hazards

Due to the low solubility properties of PAEs, phthalates tend to be concentrated from wastewater into sewage sludge and the release of phthalates into the environment from the sources of industrial, municipal solid waste, land application of sewage sludge and so forth. Phthalates become the concern of Environmental Protection Agency (EPA) due to their toxicity and impact on human health and the environment.

The exposure of human upon PAEs is through ingestion, inhalation, and dermal exposure for their whole lifetime, and they could accumulate in human through the food chain in water and soil. Generally, PAEs are reported to be endocrine disruptors or hormonally active agents (HAA) whose exposure may pose a strong threat to the ecosystem and can lead to adverse effects on human health even in a low concentration. Lethal dose (LD) 50 values of 1-30 g/kg bodyweight or with even higher concentrations were exhibited by phthalates with low acute toxicity. To this regard, it has been known that PAEs have potential to cause teratogenicity, mutagenicity and carcinogenicity when to interfere with biological processes in humans and wildlife. As a result, the developmental malformation is increased and the abalone embryo hatchability can be significantly reduced by PAEs (Bui et al., 2016, Guo and Kannan, 2012).

Some laboratory experimental on studying the toxicity of PAEs in the animal has been carried out and it can be concluded that PAEs are animal carcinogens and can cause fetal death, malformations, testicular injury, liver injury, anti-androgenic activity, teratogenicity and reproductive toxicity. In addition, some case studies showed that phthalate esters are known to be toxic to the developing male reproductive system, and have been found to cause irritation of eyes, nose and throat by low molecular weight phthalates. Therefore, EPA tends to take action upon the manufacturing, processing, distribution in commerce, and use of these phthalates. Furthermore, PAEs have been listed as priority pollutants compiled by both the USA Environmental Protection Agency (USEPA) and the EU, and in the list of priority pollutants in Chinese waters (Cheung et al., 2007, Sun et al., 2013, Wu et al., 2011).

## 2.2 Removal of Phthalate esters (PAEs)

Phthalate esters are one of the most frequent emerged persistent organic pollutants (POPs) in the environment and thus, a better understanding of their occurrence in the environment and during wastewater treatment process is important in order to remove these pollutants. As mentioned earlier in Section 2.1.2, large amounts of PAEs are leached from plastics dumped at municipal landfills and thus, the removal of PAEs from water and sediments have been carried out by numerous studies. However, the occurrence of PAEs in polluted wastewater has rendered existing conventional wastewater treatment plant ineffective to meet the environmental standards. The conventional water treatment processes like activated sludge, nanofiltration, reverse osmosis membranes are not able to address adequately the removal of a complex and complicated polluted toxic PAEs. Significantly, much of them can pass through conventional water treatment due to the occurrence of these substances in micro- or even in nanograms per liter. Generally, the treatments technologies of PAEs can be classified into three types, including physical/ chemical treatments, biological treatments and advanced oxidation processes (AOPs) (Figure 2.4) (Rivera-Utrilla et al., 2012). Nevertheless, these technologies will have their respective limitations in PAEs removal as described in the following section.

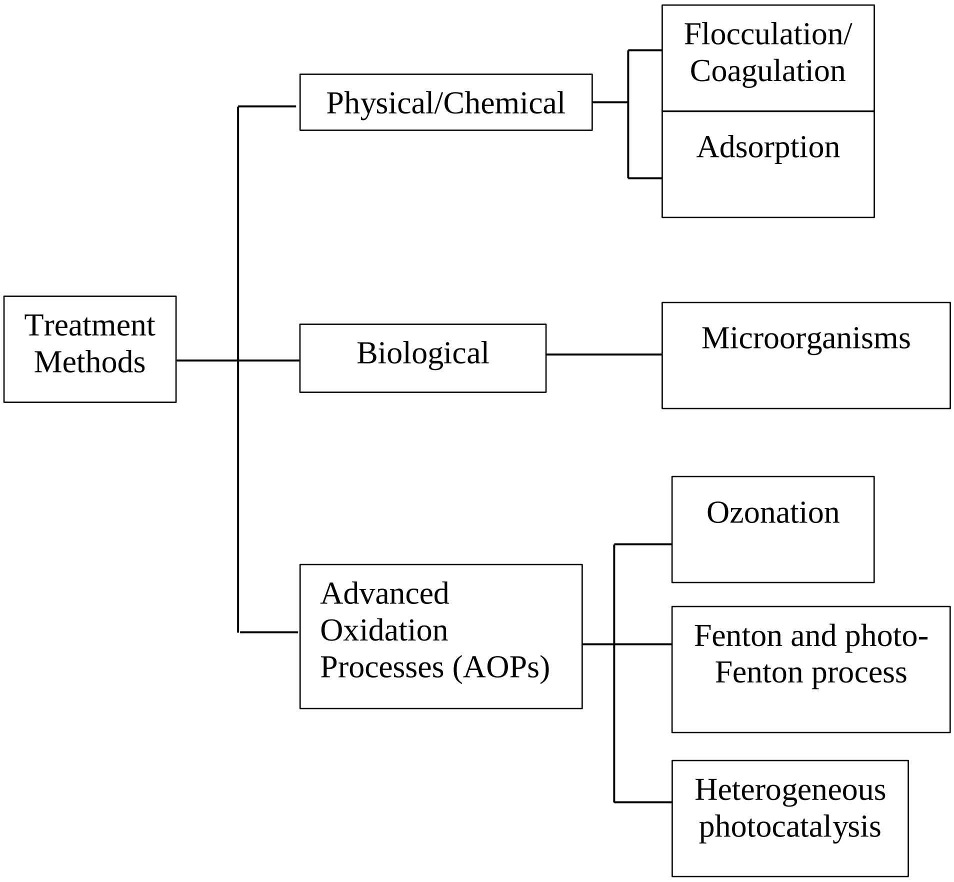

**Figure 2.4:** Treatment methods described for the degradation of PAEs

### 2.2.1 Physical/Chemical treatments

Generally, the physical and chemical processes include flocculation, coagulation and adsorption for the reduction of suspended solids, colloid particles, floating material, color and toxic compounds. Flocculation or coagulation is widely used to produce a fast-settling floc that can be removed by the addition of floc-forming chemical reagents into water or wastewater and the combination with non-settleable colloid solids and slow-settling suspended solids. The previous report investigated that the removal of dissolved organic matters (DOM) and PAESs from landfill leachate via a flocculation process by using coagulants such as ferric chloride, aluminum sulfate and poly aluminum chloride. The feasibility of removing PAEs from fresh and partially stabilized landfill leachates are evaluated by coagulation and flocculation process and found that the removal of the PAEs in the leachate are less than 30%. One of the drawbacks of flocculation and coagulation process is a lot of chemicals will be utilized and the generated sludge may contain hazardous materials, thus, sludge disposal may remain as a problem (Choi et al., 2006, Zhang and Wang, 2009).

Besides flocculation/coagulation process, adsorption process had proven to be one of the effective, reliable and non-destructive techniques for PAEs removal. The adsorption of PAEs in aqueous solution is carried out by using activated carbon as an effective adsorbent due to its large surface area, chemical nature and phenolic group content. In addition, the adsorption capacity is not influenced by any presence of electrolyte and it is likely to occur at acidic pH. However, the disadvantage of this method is that the pollutants may only transfer to the adsorbent which needs to be regenerated frequently, thus, additional costs are needed (Choi et al., 2006, Rivera-Utrilla et al., 2012).

### 2.2.2 Biological treatments

Generally, the biological treatments on organic pollutants are carried out under both aerobic and anaerobic conditions. The primary photoproducts of biodegradation pathway of Phthalate esters (PAEs) consist mainly of phthalate monoesters (PMEs), phthalic acid (PA) and ultimate biodegradation of PA to carbon dioxide ($CO_2$) and/or methane ($CH_4$).

Under aerobic conditions, the biodegradation of PAEs can be degraded by phthalate-degrading bacteria isolates such as *Pseudomonas* sp., *Sphingomonas* sp., *Arthrobacter* sp., and *Acinetobacter* sp. It has been reported that PA can be degraded aerobically via hydroxylation and decarboxylation to give protocatechuic acid, which can be further degraded into carbon dioxide. In addition, the aerobic biodegradation process of PAEs is affected by various environmental conditions, including microbial populations, temperature and pH. In particular, the biodegradability of PAEs increases with the decreased length of the phthalate ester alkyl chains. Furthermore, the enhancement of biodegradability can be achieved with the supplementation of a simple carbon source as co-metabolic substrate (Cases et al., 2011, Gao and Wen, 2016).

Abundant data from the literature demonstrated that biodegradation of PAEs using microorganisms, bacteria and fungi becoming the main degradation mechanism for their degradation in aquatic and terrestrial systems, including soils, surface waters and sediments. Previous studies indicated that the hydrolysis and photolysis of the organic compound are slow as compared with the biological pathway. PAEs can be degraded by microorganism under various conditions, however, it is a long time-consuming process and long chain PAEs cannot readily be biodegraded. Besides, this method is not applicable for removing higher concentrations of pollutant that present in the wastewater (Oloibiri et al., 2015, Rivera-Utrilla et al., 2012).

### 2.2.3 Advanced Oxidation Process (AOPs)

Advanced oxidation processes (AOPs) for PAEs treatment have received an enormous deal of attention in recent years. Complex organic compounds that are difficult to biologically degrade into simpler by-products could be achieved using AOPs. During AOPs process, hydroxyl and free radicals are being generated that could enhance the degradation process and complete the conversion of the target pollutant species into $CO_2$, $H_2O$ and mineral acids. Due to the ability of AOPs to convert contaminants into less harmful chemicals, AOPs have been proposed as a potential alternative approach for the treatment of bio-recalcitrant organic pollutants. In addition, AOPs are able to mineralize a wide range of organic pollutants, thus allowing a better compliance with specific treatment to generate highly reactive hydroxyl radical (•OH) to attack the organic molecules rapidly and non-selectivity (Cesaro and Belgiorno, 2016).

AOPs include different combination of Ozonation ($O_3$) such as ozone combined with hydrogen peroxide ($O_3/H_2O_2$) and UV irradiation ($O_3$/UV) or both ($O_3/H_2O_2$/UV) and ozone combined with catalyst ($O_3$/catalysts), Fenton and photo-Fenton process ($Fe^{2+}/H_2O_2$ and $Fe^{2+}/H_2O_2$/UV) and photocatalysis (Atalay and Ersöz, 2016, Oturan and Aaron, 2014).

#### 2.2.3.1 Ozonation

Ozone is an environmentally friendly oxidant and the by-product is not produced in the oxidation process. It can be widely applied in the purification of drinking water, treatment of wastewater and process water and the sterilization of water in artificial pools. There are two possible oxidizing reactions may occur in an ozonation process. The first reaction involves the reaction between ozone and the dissolved compounds while the second reaction involves the reaction between the generation of hydroxyl radical in ozone decomposition and the dissolved compounds. In particular, ozone is combined with $H_2O_2$ and UV light in order to increase the efficiency of the ozonation process by generating more hydroxyl radicals in the treatment system as shown in Equation (2.8-2.9).

$$H_2O_2 + 2O_3 \rightarrow 2{\bullet}OH + 3O_2 \qquad \textbf{(2.8)}$$

$$O_3 + h\nu + H_2O \rightarrow 2{\bullet}OH + O_2 \qquad \textbf{(2.9)}$$

The interaction between ozone and $H_2O_2$ may generate hydroxyl radicals. Besides, hydroxyl radicals can also be generated by photolysis of ozone in the presence of water.

However, the practical applications can be limited by this high energy cost of direct ozonation (Liu et al., 2013, Medellin-Castillo et al., 2013).

### 2.2.3.2 Fenton and photo-Fenton process

Fenton is a process employs iron salt with hydrogen peroxide while Photo-Fenton is a reaction with the combination of Fenton reagent with UV light. The presence of UV light irradiation in the reaction will enhance the efficiency of the Fenton process. The advantage of using Fenton reagent is that no energy input is required to activate hydrogen peroxide. Generally, the iron catalyzed the decomposition of $H_2O_2$ may generate hydroxyl radical in the Fenton process as shown in the Equation (2.10-2.16) and the processing mechanism is quite complex as reported in the literature.

$$Fe^{2+} + H_2O_2 \rightarrow \bullet OH + Fe^{3+} + OH^{-} \quad \textbf{(2.10)}$$

$$Fe^{3+} + H_2O_2 \rightarrow HO_2^{\bullet} + Fe^{2+} + H^{+} \quad \textbf{(2.11)}$$

$$\bullet OH + H_2O_2 \rightarrow HO_2^{\bullet} + H_2O \quad \textbf{(2.12)}$$

$$\bullet OH + Fe^{2+} \rightarrow Fe^{3+} + OH^{-} \quad \textbf{(2.13)}$$

$$Fe^{3+} + HO_2^{\bullet} \rightarrow Fe^{2+} + O_2H^{+} \quad \textbf{(2.14)}$$

$$Fe^{2+} + HO_2^{\bullet} + H^{+} \rightarrow Fe^{3+} + H_2O_2 \quad \textbf{(2.15)}$$

$$2HO_2^{\bullet} \rightarrow H_2O_2^{\bullet} + O_2 \quad \textbf{(2.16)}$$

The photo-Fenton process is an efficient and inexpensive method of wastewater and soil treatment. The UV irradiation used in this process in order to recycle of the ferrous catalyst by the reduction of $Fe^{3+}$ and increase the rate of organic pollutant degradation. Basically, more hydroxyl radicals are produced in the photo-Fenton process than the conventional Fenton method, thus, the degradation rate of organic pollutants are promoted (Chu et al., 2012).

However, Fenton and the photo-Fenton process cannot proceed at pH>10 and NaOH is added to the reaction samples before Chemical oxygen demand (COD) analysis. Moreover, the photo-treatment time needed for the photo-Fenton process is extremely low in order to prevent high electricity consumption and it strongly depends on the operating pH value and the concentrations of $H_2O_2$ and iron added. As reported in the literature, the photo-Fenton process can efficiently degrade one of the PAEs compounds, Diethyl phthalate (DEP), a maximum percentage degradation of 75.8 % of DEPs are obtained after 120 min at pH 3. The formation of hydroxyl radical in the photo-Fenton process is shown in the following Equation (2.17-2.18) (Song et al., 2016, Xu et al., 2007).

$$H_2O_2 + UV \rightarrow OH\bullet + OH\bullet \qquad \textbf{(2.17)}$$

$$Fe^{3+} + H_2O + UV \rightarrow OH\bullet + Fe^{2+} + H^+ \qquad \textbf{(2.18)}$$

#### 2.2.3.3 Heterogeneous photocatalysis

Heterogeneous photocatalysis is one of the advanced oxidation technology which has been the subject of a huge amount of studies for air and water purification treatment. It can be carried out in various media, including gas phase, pure organic liquid phases or aqueous solutions. Among these AOPs, heterogeneous photocatalysis employing semiconductor catalysts has demonstrated its efficiency in degrading a wide range of ambiguous refractory organics into readily biodegradable compounds and substantially, mineralization to innocuous carbon dioxide and water (Herrmann, 1999, Ibhadon and Fitzpatrick, 2013).

Taking into account the advance photocatalysis processes involved photodegradation under UV irradiation, the materials used as photocatalysts must satisfy several functional requirements with respect to band gap energy, morphology, surface area, stability and reusability (Khan et al., 2015). Besides, light harvesting ability of a photocatalyst is an important criterion to produce maximum photo-induced charge carriers. The basic parameter that governs the light-harvesting ability of the photocatalyst is its electronic structure, which determines its band-gap energy (Chan et al., 2011). Figure 2.5 illustrates the $E_g$ values and the positions of band edges of various semiconductors.

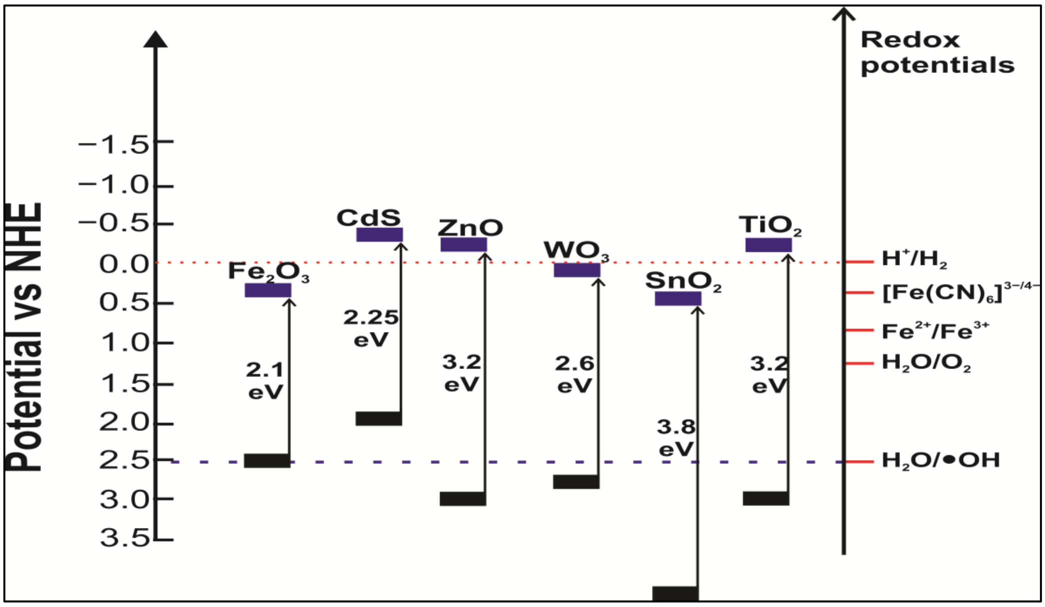

**Figure 2.5:** Schematic representation of $E_g$ values (in eV) and position of band edges of various semiconductors (Bessegato et al., 2014).

Among the advanced semiconducting materials (i.e. $WO_3$, $Fe_2O_3$, $CeO_2$, ZnO, and ZnS) being reported for electronics, magnetic, optical and photocatalytic applications; $TiO_2$ is the most widely used photocatalyst for the removal of organic pollutants from drinking water treatment, industrial and aqueous systems in environment clean-up. The extensive use of $TiO_2$ in photocatalytic building materials is attributed to the following characteristics: (a) relatively inexpensive, non-toxic and chemically stable; (b) high photocatalytic activity compared with other metal oxide photocatalysts and (c) the photogenerated holes are highly oxidizing (Fujishima et al., 2000).

From literature, binary metal sulfides semiconductors such as CdS, CdSe or ZnS are regarded as toxic and insufficiently stable for catalysis in aqueous media due to photoanodic corrosion. Photo-corrosion occurs when the anion from the catalyst itself is oxidized by photogenerated holes instead of water. Besides, the band gap (3.2 eV) and band-edge positions of ZnO are similar to those of $TiO_2$ and it was reported that ZnO has a higher electron mobility than $TiO_2$. However, ZnO is unstable in water due to incongruous dissolution and will form $Zn(OH)_2$ on the ZnO particle surfaces and thus lead to catalyst inactivation. Moreover, ZnO suffer from photo corrosion induced by self-oxidation and they can react with the photogenerated holes giving the following reactions as shown in Equation 2.17:

$$ZnO + 2h^+ \rightarrow Zn^{2+} + \frac{1}{2} O_2 \tag{2.17}$$

The $Zn^{2+}$ released by photo-corrosion may produce a new poisoning effect on the environment, bringing about further pollution. As a result, the utilization of ZnO in environmental purification is greatly limited by these disadvantages. Thus, $TiO_2$ proves to be more a suitable benchmark photocatalyst for photodegradation of organic pollutants due to its high photoactivity, resistance to photo corrosion and it was used in this present study for the degradation of PAEs under UV irradiation. $TiO_2$ showed the good performances under UV irradiation due to the contemporary presence of the anatase phase and possess a good mechanical resistance in acidic and oxidative environments. However, there are some drawbacks of using $TiO_2$ as a heterogeneous catalyst where the catalyst is difficult to be separated from the reaction media and inadequacy for continuous processing and thus, the applications of $TiO_2$ as a heterogenous catalyst in large scale industries is limited (Bagheri et al., 2014, Fujishima et al., 2000).

Generally, the removal percentage of PAEs by AOPs has ranged from 0.0 to 99.9% depending on the type of PAE and its chemical and physical characteristics. Although some treatments, such as direct UV radiation and single $H_2O_2$, there was no PAE degradation. However, with the combination of $TiO_2$-UV/$O_2$ treatment has proven effective; reducing DMP by 68% after 120 min (Jing et al., 2011, Yuan et al., 2008b). Hence, $TiO_2$ is expected to play an important role in helping material scientists, chemists and engineers in exploring the distinctive correlation of the physiochemical properties with photocatalytic performance (Bagheri et al., 2014, Fujishima et al., 2000, Nakata and Fujishima, 2012, Schneider et al., 2014). The comparison between the advantages and disadvantages of physical/chemical treatment, biological treatment, and advanced oxidation processes are summarized in Table 2.3. Ozone is a robust oxidizing agent but it lead to a very limited mineralization of organic pollutants. On the other hand, photocatalysis uses semiconductor material has shown to be adequate for converting photon energy into chemical energy to destruct a wide variety of organic pollutants. Table 2.4 summarizes the target PAEs, light sources, catalysts and the influences of various operational parameters on the photodegradation of PAEs based on the recently published work. The progress of the scientific research on the properties, limitations and modifications of $TiO_2$ will be reviewed in the following section.

**Table 2.3:** Comparing the advantages and disadvantages of water treatment methods

| **Treatment** | **Advantage** | **Disadvantage** |
|---|---|---|
| Physical/Chemical | | |
| • Flocculation/Coagulation | •High efficient of processing | •Excessive sludge<br>•Large amount of chemicals will be utilized |
| • Adsorption | •Effective, reliable and non-destructive techniques | •Regeneration of adsorbent<br>•Additional costs |
| Biological | •High reliability of the method<br>•High load operation can be processed | •High level sludge<br>•Long time-consuming process |
| Advanced oxidation processes | | |
| • Ozonation | •Environmentally friendly oxidant<br>•By-product is not produced | •High energy cost of direct ozonation |
| • Fenton/photo-fenton | •Efficient<br>•Treatment process is simple and easy to manage | •High operating costs over the use of the Fenton's reagent |
| • Heterogenous photocatalysis | •Low operational and installation cost<br>•Sludge treatment costs do not occur | •Catalyst is difficult to be separated from the reaction media<br>•Inadequacy for continuous processing |

**Table 2.4:** Summary of PAEs removal by photocatalytic reaction under various operational parameters

| Type of PAEs | Catalyst | Initial [PAEs], mg/L | Light source | Irradiation time, (h) | Catalyst dosage, (g/L) | $O_2$ flow/ $H_2O_2$/ $O_3$ | Removal effciency , (%) | References |
|---|---|---|---|---|---|---|---|---|
| DMP | SDS-organic layered double hydroxides(LHDs)/$TiO_2$ composites | 10 | UV lamp | 8 | 2 | NA | 90 | (Park and Youn, 2012) |
| DMP | Magnetic hybrid photocatalyst (phthalocyanine/anatase/silica/ magnetite, CuPc/TSM,VSTM) | 10 | Xenon lamp | 6 | 1.2 | $O_2$ flow=500 ml/min | 42.4 | (Chang and Man, 2014) |
| DMP | $V_2O_5/MoO_3$ | 40 | Xenon lamp | 5 | 0.17 | NA | 80 | (Chuai et al., 2015) |
| DEP | UV/$H_2O_2$<br>$O_3/H_2O_2$<br>$O_3$/activated carbon | 10 | Mercury lamp | 1 | 1 | $H_2O_2$=0.60 mM<br>$O_3$=1 x 10 $^{-4}$M | 21<br>43<br>54 | (Medellin-Castillo et al., 2013) |
| DEP | $CuFe_2O_4$<br>$CuFe_2O_4$/MWCNTs | 5 | NA | 0.5 | 0.2 | NA | 10<br>30 | (Zhang et al., 2016) |
| DEP | Immobilized PANI/CNT/$TIO_2$ | 1 | Simulated sunlight | 2 | NA | NA | 41.5-59.0 | (Hung et al., 2017) |

**Table 2.4 (to be continued)**

| | | | | | | | | |
|---|---|---|---|---|---|---|---|---|
| DBP | $Co_3(BTC)_2\cdot 12H_2O$ (Co-BTC)<br>Co-BTC + Peroxymonosulfate (PMS) | 11.8 | NA | 1 | 0.3 | NA | < 10<br>43.9 | (Li et al., 2016) |
| BBP | P25<br>$TiO_2$ film<br>P-$TiO_2$ film | 20 | Xenon lamp | 3 | NA | NA | 17<br>28<br>98 | (Mohamed and Aazam, 2013) |

## 2.3 Bulk Properties of Titanium dioxide

Titanium dioxide is a polymorphic compound with the molecular formula of $TiO_2$. It is also known as titanium (IV) oxide or titania, the naturally occurring oxide of titanium and appear as an opaque white pigment in color. $TiO_2$ exist primarily in three different polymorphous structures: anatase, rutile and brookite. Both anatase (a=b=3.782Å, c=9.502Å) and rutile (a=b=4.584Å, c=2.953Å) structures are stable compound and tetragonal in shape while brookite (a=9.166Å, b=5.436Å, c=5.135Å) structure are unstable at room temperature and orthorhombic in shape (Reyes-Coronado et al., 2008, Zhang et al., 2014a). The comparison between anatase, rutile and brookite properties can be summarized in Table 2.5.

**Table 2.5:** The basic properties for anatase, rutile and brookite $TiO_2$ (Luttrell et al., 2014, Nakata and Fujishima, 2012)

| **Property** | **Anatase** | **Rutile** | **Brookite** |
|---|---|---|---|
| Crystal structure | Tetragonal | Tetragonal | Orthorhombic |
| Density (g/cm$^3$) | 3.90 | 4.27 | 4.13 |
| Entropy $S_{298.16}$ | 11.93 | 12.01 | - |
| Cell parameter a, Å | 3.782 | 4.584 | 9.166 |
| Cell parameter c, Å | 9.502 | 2.953 | 5.135 |
| Atoms per unit call (Z) | 4 | 2 | 8 |
| Band gap energy (eV) | ~3.2 | ~3.0 | ~3.3 |
| Wavelength (nm) | ~387 | ~413 | ~375 |

Basically, the structure anatase and rutile can be described in terms of the spatial arrangement of $TiO_6$ octahedra in which each $Ti^{4+}$ ion is coordinated to six $O^{2-}$ ions. The differences between these two polymorphous structures are the distortion of each ortahedron and the assembly pattern of chains. The octahedron in anatase is significantly distorted so that its symmetry is lower than orthorhombic. Whereby, $TiO_6$ octahedron in rutile is not regular, showing a slight orthorhombic distortion. The Ti-Ti distances in anatase are greater (3.79 and 3.04 Å vs 3.57 and 2.96Å in rutile) whereas the Ti-O distances are shorter than in rutile (1.937 and 1.966 Å in anatase vs 1.946 and 1.983 Å in rutile). Even though both anatase and rutile are the same tetragonal system but anatase has a longer vertical axis of the crystals than rutile. In the brookite phase, all bond lengths and bond angles slightly differ from each other due to stronger distortions in $TiO_2$ brookite, thus leading to the formal loss of local symmetry (Figure 2.6) (Reyes-Coronado et al., 2008, Zhang et al., 2014a).

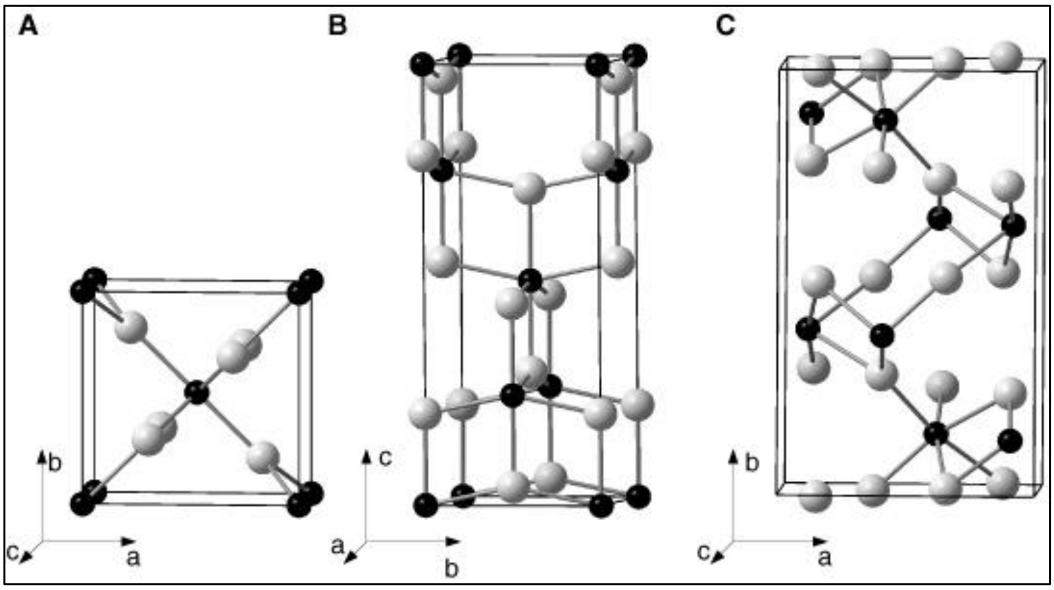

**Figure 2.6:** Crystal structure of (a) rutile, (b) anatase and (c) brookite (Rebecca et al., 2005).

Due to difficulty in synthesis, brookite is rarely reported as a photocatalyst. Anatase and rutile type of $TiO_2$ are most common to be used in photocatalytic applications. Both have an indirect band gap, which is 3.2 eV for anatase and 3.0 eV for rutile, corresponding to UV light absorption. Despite the larger band gap of anatase of 3.2 eV, compared to rutile, the photocatalytic performance of anatase basically is considered superior to that of more stable rutile due to its better electronic and surface chemistry properties. The larger band gap of anatase $TiO_2$ reduces the light that can be absorbed which may raise the valence band maximum to higher energy levels relative to redox potentials of adsorbed molecules. Thus, the oxidation 'power' of electrons is increased and the electron is facilitated transfer from the $TiO_2$ to adsorbed molecules. Moreover, anatase is the most active phase for photocatalysis which is ascribed to the higher density of localised states and consequent surface-adsorbed hydroxyl radicals and slower charge carrier recombination in anatase relative to rutile. As a result, higher levels of radicals adsorbed on the anatase surface give rise to significantly higher photoactivity than rutile (Odling and Robertson, 2015). In addition, the lifetime of photogenerated electrons and holes in anatase is about an order of magnitude larger than that of photogenerated electron and holes in rutile, hence, the chance of photoexcited electrons and holes in anatase participating in surface chemical reactions are greatly enhanced. Furthermore, anatase $TiO_2$ has inherent surface band bending that forms spontaneously in a deeper region with a steeper potential compared with the rutile phase, therefore surface hole trapping dominates due to the spatial charge separation is achieved by the transfer of photogenerated holes towards the surface of the particle via the strong upward band bending (Hanaor and Sorrell, 2011, Silva and Faria, 2009). On the other hand, the higher rate of electron-hole recombination in rutile is due to the larger grain size and lower specific surface areas which resulting in the lower capacity for adsorbing species. Therefore, the $TiO_2$ photocatalytic system is considered as a promising technology for the AOPs for water treatment. However, various investigations have established that $TiO_2$ is much more effective as a photocatalyst in the form of nanoparticles than in bulk powder. An exponential growth of research activities had been seen in nanoscience and nanotechnology in the past decades, there has been a tremendous growth in the application of $TiO_2$ nanoparticles for tackling the environmental challenges. The intrigue of nanotechnology is the ability to control the manipulation of nanoscale (approximately 1 nm to 100 nm) structured materials and integrate them into large material components. The merits of using $TiO_2$ photocatalyst in their nano range far outweigh their use in their bulk form.

In particular, compared to the bulk $TiO_2$, $TiO_2$ nanoparticles has a highly specific surface area (large surface area-to-volume ratio), which promotes efficient charge separation and charge trapping of ions on the $TiO_2$ surfaces. Moreover, the oxidative power of the $TiO_2$ nanoparticles with the opacity of the aqueous phase are increased as compared to the bulk-size $TiO_2$. Also, the surface energy per nanoparticle increases significantly in the nano range which directly results in an increase in contaminant removal even at low concentrations. As a result, $TiO_2$ nanoparticles enables an improvement in the adsorption capacity of the contaminants which may enhance the photocatalytic activities during the water treatment process by maximizing the active surface area of $TiO_2$ with nanoscale (Chen and Selloni, 2014, De Angelis et al., 2014).

### 2.3.1 Basic principle of $TiO_2$ photocatalysis

According to International Union of Pure and Applied Chemistry (IUPAC) compendium of chemical terminology, a catalytic reaction involving light absorption by a catalyst can be defined as photocatalysis (Serpone and Emeline, 2002). The photocatalytic properties of $TiO_2$ nanoparticles are derived from the illumination with photons having energy greater than the band gap energy, the photons will excite the electrons from the valence band (VB) into the conduction band (CB), resulting in the formation of photogenerated charge carriers (hole and electron). The photogenerated holes in the valence band will react with adsorbed water molecules, forming hydroxyl radicals (•OH). •OH produced has the second highest oxidation potential which can non-selectively oxidize almost all electron rich organic molecules and eventually converting them into $CO_2$ and water. Therefore, the organic pollutants which are adsorbed on the surface of the catalyst will be oxidized by •OH. In the meantime, electrons in the conduction band will typically participate in reduction processes, which typically react with molecular oxygen to produce superoxide radical anion ($O_2^{\bullet-}$). The presence of molecular oxygen plays a substantial role in the photoinduced processes on the irradiated $TiO_2$ surface, as effective charge carriers, separation is enabled. In addition, $O_2^{\bullet-}$ may not only take place in the further oxidation process but also prevents the electron-hole recombination, hence electron neutrality within the $TiO_2$ is maintained. Therefore, both •OH and $O_2^{\bullet-}$ play such an important roles in the photocatalytic reaction mechanism. The Equation (2.1-2.7) represents the mechanism of the photocatalytic degradation by $TiO_2$ (Bagheri et al., 2014, Fujishima et al., 2000, Schneider et al., 2014).

$$TiO_2 + h\nu \rightarrow e_{CB}^- + h_{VB}^+ \qquad \textbf{(2.1)}$$

$$H_2O + h^+_{vb} \rightarrow \bullet OH + H^+ \qquad \textbf{(2.2)}$$

$$O_2 + e^-_{cb} \rightarrow O_2^{\bullet-} \qquad \textbf{(2.3)}$$

$$\bullet OH + \text{Organic Pollutant} \rightarrow CO_2 + H_2O \qquad \textbf{(2.4)}$$

It is essential for effective photocatalytic degradation of organic pollutants that the oxidation of pollutant and the reduction process of oxygen occur simultaneously in order to prevent the accumulation of electron in the conduction band and hence, the rate of recombination of $e_{CB}^-$ and $h_{VB}^+$ is reduced. A schematic diagram illustrating the mechanism of photocatalysis on $TiO_2$ nanoparticles is shown in Figure 2.7. In applying $TiO_2$ nanoparticles for the AOPs for water treatment, $TiO_2$ nanoparticles have a very fast response and has a great advantage in good photo-efficiency even in weak light. Nonetheless, its practical exploitation has been restricted by the major drawbacks of $TiO_2$ nanoparticles, as we will discuss in the following section.

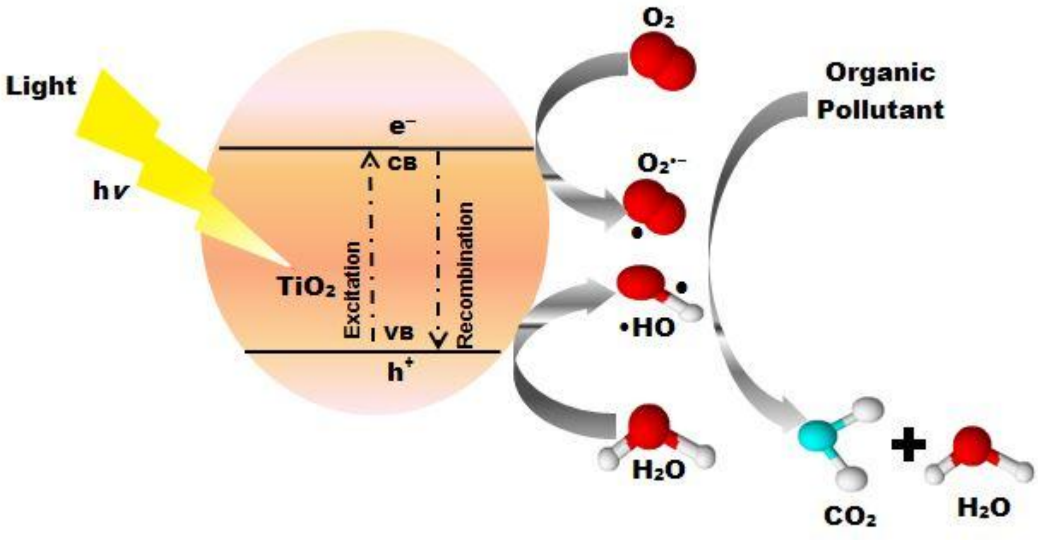

**Figure 2.7:** A schematic diagram illustrating the mechanism of photocatalysis on $TiO_2$ nanoparticles

### 2.3.2 Limitations of $TiO_2$ nanoparticles

In particular, from several points of view, $TiO_2$ nanoparticles turned out to be an ideal photocatalyst to break down organic compounds. It is relatively inexpensive, highly stable for chemical properties, and the photogenerated holes are highly oxidizing. However, an obvious hindrance to the widespread use of $TiO_2$ nanoparticles as a photocatalyst is its poor visible light response, the rapid recombination rate of charge carriers, low adsorption capacity to hydrophobic contaminants, high aggregation tendency and difficulty of separation and recovery, which decreases the quantum efficiency of the overall reaction. The main limitations of $TiO_2$ nanoparticles are that $TiO_2$ (anatase) has a wide band gap, $Eg \approx 3{,}2eV$, as it can only be activated by ultraviolet (UV) light irradiation with a wavelength of 387 nm. Moreover, recombination of photogenerated charge carriers is also the major limitation in $TiO_2$ nanoparticles photocatalysis as it reduces the low quantum efficiency (i.e., low electron transfer rate) of $TiO_2$ nanoparticles resulting in low photoreaction rates. Besides, the photocatalytic degradation mainly occurs on the surface of $TiO_2$ nanoparticles, but $TiO_2$

nanoparticles have a poor affinity towards the organic pollutants particularly the hydrophobic organic pollutants. Thus, the low adsorption ability of organic pollutants on $TiO_2$ surface resulting in slow photocatalytic degradation rates of $TiO_2$ nanoparticles. Consequently, how to concentrate the organic pollutants around the $TiO_2$ nanoparticles requires consideration. In addition, the $TiO_2$ nanoparticles may undergo aggregation due to the instability of the nanosized particle during the photocatalytic degradation process, which may hamper the light incidence on the active centers and subsequently the catalytic activity of $TiO_2$ nanoparticles are reduced (Chen and Mao, 2006, Gupta and Tripathi, 2011).

These drawbacks cannot be overcome by only modifying the size and morphology of $TiO_2$ nanoparticles itself as described in the previous section. Therefore, considerable efforts have been exerted to minimize the recombination losses of charge carriers and extend the absorption of the wavelength range into the visible light region by anchoring the $TiO_2$ nanoparticles onto carbonaceous materials. Researchers have been working on enhancing the photocatalytic activity of the hybrid composites between $TiO_2$ nanoparticles and a range of carbonaceous materials (to be discussed next), exposing more active crystal facets, and forming heterojunction structures to delay the intrinsically fast charge recombination. As a result, hybrid composites between $TiO_2$ nanoparticles and carbonaceous materials can improve the photocatalytic efficiency, visible light absorption, stability and reproducibility, and to improve the recycle and reuse abilities of $TiO_2$ nanoparticles (Jo and Kim, 2012, Leary and Westwood, 2011).

### 2.3.3 Modifications of $TiO_2$ nanoparticles

As discussed earlier, one of the major drawbacks of $TiO_2$ nanoparticles is the formation of recombination sites for photogenerated charge carriers and thus lowering the quantum efficiency. Thus, to solve the limitations of $TiO_2$ nanoparticles, carbonaceous materials are considered to be suitable as a support for $TiO_2$ nanoparticles owing to their excellent thermal, optical, mechanical, electrical, chemical resistance, and surface properties, resulting in a rapid charge transfer on hybrid composites between $TiO_2$ and carbon. The hybrid composites between $TiO_2$ nanoparticles and carbonaceous materials provide high surface area and a strong adsorption affinity towards the pollutants to be degraded. Furthermore, the hybrid carbonaceous /$TiO_2$ composites sufficiently bond either physically or chemically to the $TiO_2$ without reducing the $TiO_2$ nanoparticle’s photocatalytic activity. Therefore, the photocatalytic activity of $TiO_2$ nanoparticles can be enhanced by coupling with carbonaceous materials to suppress recombination rate and thus increasing quantum yield. In the past decades, conventional carbonaceous materials such as carbon black, graphite and graphitized nanomaterials have long been applied in heterogenous catalysis. Now, a significant of the review concerns the role of novel nanostructured carbonaceous materials such as activated carbon, fullerenes, graphene and carbon nanotubes (CNTs) for the enhancement of $TiO_2$ photocatalysis. In the present study, CNTs is used as a one-dimensional photocatalyst for contributing to the routes of enhancing $TiO_2$ photocatalytic activities, e.g., $TiO_2$ is an n-type semiconductor, but with the presence of CNTs, photoinduced electrons may migrate freely in the direction to the CNTs surfaces where CNTs can act as extremely effective electron sinks, which might have a lower Fermi level like a metal for suppressing the electron-hole pairs recombination. The general principles of carbonaceous materials (i.e., activated carbon, fullerenes, graphene and carbon nanotubes) are briefly introduced in the following section, with reference to further literature (Bergmann and Machado, 2015, Leary and Westwood, 2011, Tiwari et al., 2008).

#### 2.3.3.1 Activated carbon/$TiO_2$ composites

Activated carbon (AC) or known as activated charcoal exhibit a porous amorphous structure with porosity that has been extensively used as a support for $TiO_2$ photocatalysis. AC typically exhibits a heterogeneous pore structure, in which micro- (<1 nm), meso- (1-25 nm) and macro- (>25 nm) pore ranges are present but the relative proportions vary considerably according to their raw material (Figure 2.8). AC is manufactured from various carbonaceous raw materials such as coal, coconut shells, wood, peat and petroleum based residues (Chen et al., 2002). Basically, micropores structure of an AC plays an effective role in adsorption while mesopores structure is used for transportation and macropores structure of an AC is used as an entrance of adsorbed pollutant into AC (Hsieh and Teng, 2000).

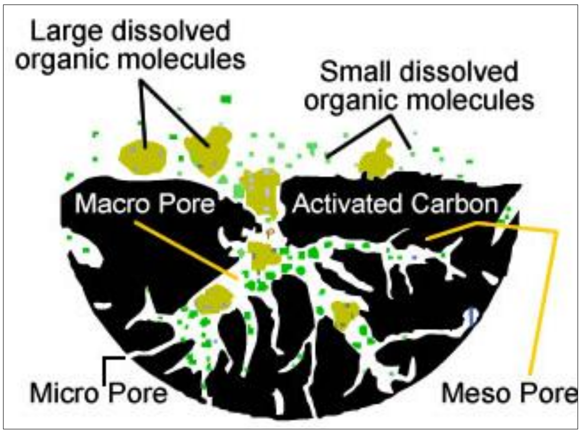

**Figure 2.8:** A schematic diagram of the pore distribution of an activated carbon support (Begg Cousland Envirotec Limited, 2015-2016)

The fundamental benefit of AC is that it possesses a large specific surface area, high adsorption capacity, and suitable pore structure over which $TiO_2$ may be distributed and immobilized (typically 900-1200 $m^2/g$). In this respect, the resulting AC/$TiO_2$ composites are widely reported for the photodegradation of organic pollutants, attributed to the porosity of the AC providing high adsorption capacity of the pollutants on the $TiO_2$ surface. The adsorption on the surface is due to Van der Waals or London dispersion forces. This force is strong over short distances, equal between all carbon atoms and not dependent on external parameters such as pressure or temperature. Therefore, the adsorbed pollutants will be held most strongly where they are surrounded by the most carbon atoms (Çeçen and Aktaş, 2011, Yang, 2003).

In addition, it has been shown that a synergistic effect between the mixture AC and $TiO_2$ via metal organic chemical vapour deposition (MOCVD) technique where the $TiO_2$ strongly adhered on the porous surface of an AC. The synergistic effect due to the porosity of the AC support can be explained as an enhanced adsorption of the organic pollutant onto the AC phase followed by a transfer through an interphase to the $TiO_2$ phase, giving a complete photodegradation process. In addition, the use of AC photocatalyst support will provide help to molecules of pollutant closer to the active site of $TiO_2$ for a quick and effective photodegradation process. Meanwhile, the immobilization of $TiO_2$ onto the AC can compromise for the loss of photocatalytic ability of $TiO_2$ due to the difficulty to effectively dispersion in water for complete interaction with pollutants. Besides having good properties as a catalyst support, AC is receiving considerable attention with commercial potential owing to the properties of inert, cheap and easy to manufacture. However, it has been reported the pores (micropores) in the AC is very small, and the diffusion rate of the adsorbed pollutant in the micropores towards the surface of $TiO_2$ is slow. Thus, the small pores are rarely infiltrated, with the $TiO_2$ remaining on the outer macropores which may lead to a lower $TiO_2$ photocatalytic efficiency. Moreover, the use of AC as a support for tuning the band gap of $TiO_2$ remains un-tackled due to no chemically interaction between AC and $TiO_2$ unless additional constituents are added to the system (Bergmann and Machado, 2015, Puma et al., 2008, Xing et al., 2016).

### 2.3.3.2 Fullerenes ($C_{60}$)/$TiO_2$ composite

Fullerenes ($C_{60}$) are a class of carbon allotropes and play a role as a photocatalyst supporting materials. It is a carbon-based zero dimensional (OD) materials with $sp^2$ hybridization (Figure 2.9). The $C_{60}$ molecule has approximately 7 Å of inner diameter and is composed of 12 pentagons and 20 hexagons of carbon atoms. $C_{60}$ having similar structure as graphite which is composed of a sheet of linked hexagonal rings, but they contain pentagonal rings that prevent the sheet from being planar (Dai et al., 2012). The specific surface area of $C_{60}$ molecule obtained experimentally varies from approximately 1.1-176 $m^2/g$ due to the different methods of synthesis (Politakos et al., 2013). It has attracted considerable attention for environmental application because of their delocalized conjugated structures and electron-accepting ability. The remarkable properties of $C_{60}$ as the inner and outer surface are covered with homogeneous $\pi$ electrons and thus, a strong interaction with organic molecules such as endocrine disrupting chemicals via $\pi$–$\pi$ stacking is allowed. However, their application in $TiO_2$ photocatalysis is much less well explored, with only a few handfuls of studies readily available in the published literature (Shpilevsky et al., 2011).

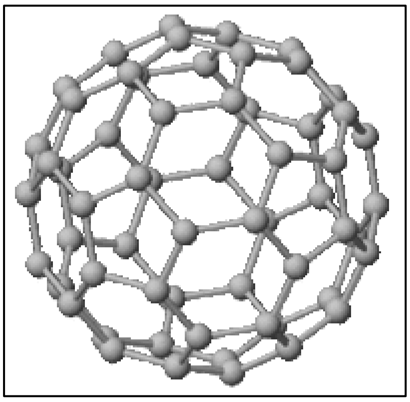

**Figure 2.9:** Representative of fullerenes [$C_{60}$] molecules (Smart Economy, 2008)

There are distinct adsorption sites in $C_{60}$ clusters that can contribute significantly to the overall adsorption. The adsorptive activity of $C_{60}$ for organic pollutants such as organometallic compounds, polycyclic aromatic hydrocarbon and organochlorine compounds has been carried out and in comparison with activated carbon. As a result, the adsorption behavior of activated carbon was found to be lower to that of $C_{60}$. $C_{60}$ has a higher electron-accepting ability that capable of accepting up to six electrons, which showed the minimization of electron/hole recombination and enhanced the photocatalytic activity. It can be deduced that $C_{60}$ efficiently provoke a rapid photoinduced charge separation and a relatively slow charge recombination via the combination of $TiO_2$ and $C_{60}$. $C_{60}$ has a closed-shell configuration consisting of 30 bonding molecular orbitals with 60 $\pi$-electrons, and is suitable for efficient electron transfer reduction because of the uptake or release of electrons results in minimal structural and solvation change upon electron transfer. In addition, $C_{60}$ is one of the promising carbon materials because of its band gap energy, about 1.6 to 1.9 eV, hence, it has a strong absorption in the ultraviolet region (Bergmann and Machado, 2015, Leary and Westwood, 2011). However, $C_{60}$ has poor light-harvesting capability and thus, a low incident photo-to-photocurrent efficiency is exhibited. Furthermore, $C_{60}$ is only adsorbed on the surface of $TiO_2$ through electrostatic forces, thus, a close contact between the $C_{60}$ and the $TiO_2$ matrix cannot be guaranteed and the synergistic behavior of $C_{60}$/ $TiO_2$ composite is often not presented (Ghosh and Oh, 2012). Among the same types of carbon supports, the investigation on the role of graphene as an important component for graphene/$TiO_2$ composite will be described in the following section.

#### 2.3.3.3 Graphene/$TiO_2$ composite

Graphene, as a new allotrope of carbon supporting materials and have been exhaustively studied since their discovery due to their unique physical-chemical properties. It is a flat monolayer of carbon atoms tightly packed into two dimensional (2D) honeycomb lattice materials with a unique $sp^2$ hybrid carbon network (Figure

2.10). Graphene can be obtained through the oxidation and exfoliation of graphite to produce graphene oxide (GO), followed by a chemical reduction to give graphene. In addition, it is naturally found as the building block of graphite, where the lamellar graphite structure is strongly hold by the π-stacking of graphene sheets, with an interlayer spacing of 3.34 Å between the sheets. Each carbon atom in the lattice has π orbitals that contribute to a delocalized network of electrons which is responsible for the electron conduction of graphene and the weak interaction among graphene layers or between the graphene and the substrate (An and Yu, 2011, Bergmann and Machado, 2015, Leary and Westwood, 2011, Perreault et al., 2015).

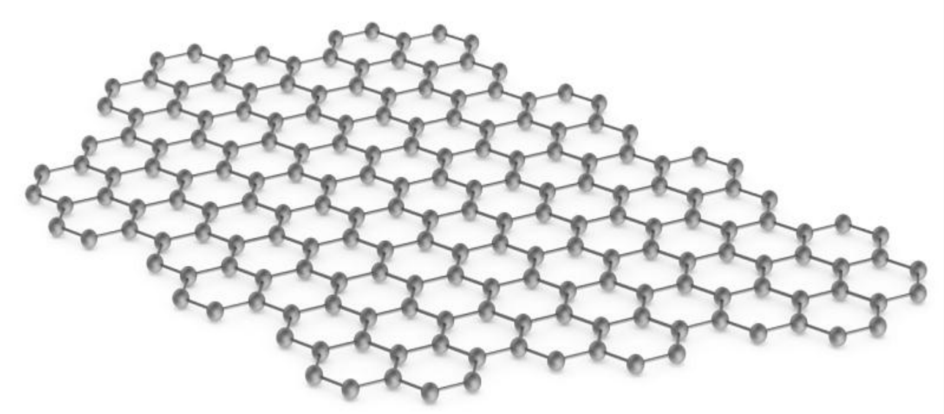

**Figure 2.10:** Schematic diagram of graphene with a hexagonal packed structure (Geim, 2012)

Graphene acts as one of the most exciting discovered carbonaceous materials and has attracted immense attention due to a large theoretical specific surface area (2630 $m^2/g$) and high intrinsic electron mobility. The high electron mobility in graphene as 10 000 $cm^2 V^{-1} s$-$^1$ to 50 000 $cm^2 V^{-1} s^{-1}$ at room temperature possesses promising electronic properties. Nonetheless, the large numbers of π electrons delocalized make graphene highly attractive as a high surface area 2D photocatalyst support for $TiO_2$. It can interact with pollutant molecules via π-π conjugation, which enhances the adsorption of pollutants by graphene/$TiO_2$ composite and thereby the efficiency of photocatalyst degradation is improved. Also, because of the extremely high conductivity and zero band gap of graphene, the conduction band of $TiO_2$ is higher than the Fermi level of graphene, the photogenerated electrons are readily transferred from the $TiO_2$ to graphene by passing through the interface between them. This facilitates the charge transfer and reduces the recombination of photogenerated electrons and holes, which enhances the photocatalytic quantum efficiency of graphene/$TiO_2$ composite. Meanwhile, graphene also helps to disperse $TiO_2$ by decreasing agglomeration and promoting the contact between $TiO_2$ and pollutants (An and Yu, 2011, Huang et al., 2012).

In spite of the fact that high quality graphene can be produced via micromechanical exfoliation and chemical vapor deposition, the insufficient functional groups present on graphene sheets can cause the difficulties of dispersion and interaction with $TiO_2$ photocatalyst, which could reduce its compatibility and surface active sites. In addition, graphene has already been applied as one of the most promising materials in graphene/$TiO_2$ composite, however, the single-layer graphene sheets have a certain tendency to form aggregates in solution by strong van der Waals interactions which may greatly lower its high specific surface area. As a result, the surface area of graphene could be reduced by the defects of wrinkling and folding of graphene sheets and the presence of curled sheets. By the way, the agglomeration of graphene can be reduced to some extent by chemical functionalization. However, impurities are often introduced into the graphene/$TiO_2$ composite during the chemical surface modification and the presence of foreign stabilizers is undesirable and very difficult to eliminate in the further process. Besides, from an experiment point of view, at the moment large scale production of single- or few-layer graphene is difficult and expensive (An and Yu, 2011, Bergmann and Machado, 2015, Leary and Westwood, 2011, Perreault et al., 2015).

The limited performance of graphene in environmental applications can be, in part, attributed to their low dispersion ability and aggregation problems (Chabot et al., 2014, Perreault et al., 2015). Therefore, the unique properties of carbon nanotubes (as discussed in the next section) have opened new possibilities to improve the performance of numerous environmental processes and overcome this limitation.

#### 2.3.3.4 CNTs/$TiO_2$ nanocomposites

Carbon nanotubes (CNTs) are carbon allotropes with the carbon atom in $sp^2$ hybridization rolled up become tubular structure or known as one dimensional (1D) materials. Different from other carbon materials, CNTs can be envisioned as cylinders composed of rolled up graphite planes with diameters in nanometer scale and have an aspect ratio greater than 1000. CNTs are a unique nanostructure with remarkable structural, chemical, thermal, catalytic, adsorption, transport and electrical properties that have attracted significant attraction in a variety of scientific fields. The structural properties of CNTs show a strong interaction with organic molecules via noncovalent forces such as hydrogen bonding, π-π stacking, electrostatic forces, van der Waals forces, and hydrophobic interactions (Dai et al., 2012). Furthermore, the strong $sp^2$ carbon-carbon bonds structure provides CNTs with extremely high mechanical values. In addition to the exceptional mechanical properties associated with CNTs, they also possess good candidates for adsorption kinetics study. The adsorption capacity of CNTs is very fast, which is mainly due to the highly accessible adsorption sites and the short intraparticle diffusion distance, which is related to their large specific surface area. Moreover, CNTs possess good structural integrity and chemical inertness support with relatively high oxidation stability which could endow CNTs more excellent performances as support for photocatalytic active materials (De Volder et al., 2013, Eatemadi et al., 2014). The oxygen functional groups such as hydroxyl and carboxyl are introduced onto the CNTs surface during the synthesis and purification process. These functional groups can influence the maximum adsorption capacity of CNTs and make them more hydrophilic and suitable for the adsorption. Up to now, CNTs can be easily scaled-up to batch-scale production by chemical vapor deposition (CVD) method due to simplicity and economy. Furthermore, CNTs may acts as effective electron sinks with a high electrical conductivity and high electron storage capacity which can store up to 1 electron per 32 carbon atoms during photoexcitation, and transfer the electron away from the $TiO_2$ particles after photoexcitation (An and Yu, 2011, Bergmann and Machado, 2015, Leary and Westwood, 2011, Perreault et al., 2015).

However, excessive use of acids and chemicals at high concentration in the chemical functionalization techniques may result in damage to CNT structure. In particular, due to similarities between the chemical structure of $C_{60}$, graphene, and CNTs, all can act as an electron reservoir to trap photoexcited electrons from $TiO_2$ nanoparticles, thereby the lifespan of electron-hole pairs is improved, which is regarded as the most important factor contributing to the enhancement of photoactivity of carbonaceous/$TiO_2$ composite (Dai et al., 2012, Ghosh and Oh, 2012). Table 2.6 summarizes the physical properties of different carbonaceous materials.

**Table 2.6:** Physical properties of different carbonaceous materials (Chen et al., 2001)

| **Properties** | **AC** | **$C_{60}$** | **Graphene** | **CNTs** |
|---|---|---|---|---|
| Dimensional | Three | Zero | Two | One |
| Surface area | 900-1200 | 1.1-176 | 2630 | 200-900 |
| Specific gravity ($g/cm^3$) | 1.4-1.5 | 1.7 | ~1 | 0.8-1.8 |
| Electron mobility ($cm^2V^{-1}s^{-1}$) | - | 0.5-6 | 10 000-50 000 | $10^4$-$10^5$ |
| Tensile strength (GPa) | - | - | 125 | 50-200 |

Hence, the choice of whether to use CNTs as a carbon-based composite will be determined by the cost, properties, and environmental applications of each material. As been discussed previously, environmental applications based on CNTs offer more realistic possibilities and have many advantages over other carbon materials in terms of structural, electrical properties and CNT's lower production costs. Table 2.7 summarizes the advantages and disadvantages of carbonaceous materials.

**Table 2.7:** Comparing the advantageous and disadvantageous of carbonaceous materials

| Carbonaceous materials | Advantage | Disadvantage |
|---|---|---|
| Activated carbon | •Inert<br>•Cheap<br>•Easy to manufacture<br>•Large specific surface area<br>•High adsorption capacity<br>•Exhibits a heterogeneous pore structure | •Difficulty to effectively dispersion in water for complete interaction with pollutants<br>•Diffusion rate of the adsorbed pollutant in the micropores towards the the surface of $TiO_2$ is slow |
| $C_{60}$ | •Delocalized conjugated structures<br>•Inner and outer surface are covered with homogeneous $\pi$ electrons<br>•Higher electron-accepting ability | •Poor light-harvesting capability<br>•Low incident photo-to-photocurrent efficiency |
| Graphene | •Large theoretical specific surface area<br>•High intrinsic electron mobility<br>•Large numbers of $\pi$ electrons delocalized | •Insufficient functional groups present on graphene sheets<br>•Difficulties of dispersion and interaction with $TiO_2$ photocatalyst<br>•Graphene sheets tend to aggregates and restack<br>•High production cost |

**Table 2.7 (to be continued)**

| | | |
|---|---|---|
| CNTs | •High aspect ratio<br>•High mechanical values<br>•Strong interaction with organic molecules via noncovalent forces<br>•High oxidation stability<br>•High electrical conductivity<br>•High electron storage capacity<br>•Lower production cost | •High concentration of acid used in functionalization may result in damage to CNTs structure |

Based on the above discussion, it is clear that CNTs remains a unique material with properties that could lead to significant development as CNTs/$TiO_2$ composite. The CNTs/$TiO_2$ composite basically exhibit four positive factors that can potentially enhance the photocatalytic activity (provision of highly adsorptive active sites, minimization of electron-hole recombination, effective electron sinks, and band gap tuning). There are two main types of CNTs which are single walled carbon nanotubes (SWCNTs) and multi walled carbon nanotubes (MWCNTs) that differ in the arrangement of their graphene cylinders (Figure 2.11). SWCNTs consist of a single layer of graphene cylinders; while MWCNTs consist of multiple layers of graphite rolled into form a tube shape (De Volder et al., 2013).

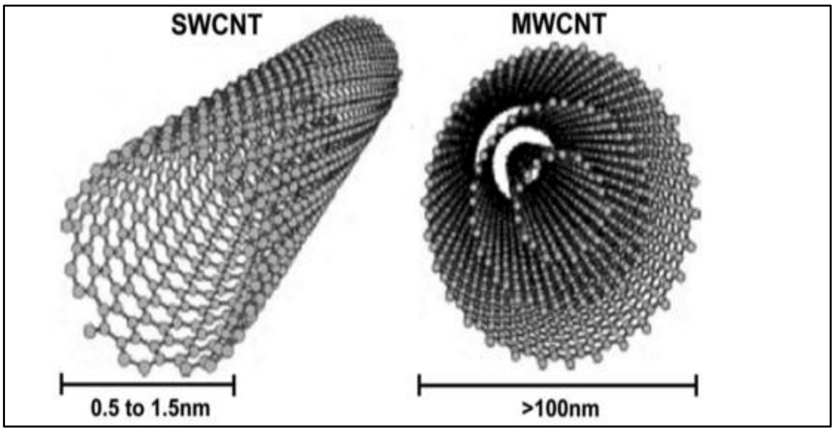

**Figure 2.11:** Schematic representation of SWCNTs and MWCNTs (Martins-Júnior et al., 2013)

As reported, the total specific surface area of SWCNTs is in the range of 400-900 $m^2/g$ while for MWCNTs between 200-400 $m^2/g$, and this provides CNTs with more reactive surface areas (Dai et al., 2012, Leary and Westwood, 2011). However, SWCNTs are still very expensive to produce as compared to MWCNTs due to their synthesis is extremely complicated and the yields are small, hence; MWCNTs favor to be utilized as MWCNTs/$TiO_2$ composite for the photocatalytic degradation of organic compounds. The properties of SWCNTs and MWCNTs are summarized in Table 2.8. In addition, nano-scaled composite materials of MWCNTs have been utilized due to its high chemical inert nature, non-swelling effect and rigidity (Bergmann and Machado, 2015, Leary and Westwood, 2011, Hamid et al., 2014).

**Table 2.8:** Characteristics and textural properties of SWCNTs and MWCNTs (Ong et al., 2010)

| **Properties** | **SWCNTs** | **MWCNTs** |
|---|---|---|
| Layer of graphite | Single layer | Multiple layers |
| Specific gravity, $g/cm^3$ | 0.8 | 1.8 |
| Elastic Modulus, TPa | ~1 | ~0.3-1 |
| Strength, GPa | 50-500 | 10-60 |
| Thermal conductivity, $W\ m^{-1}\ K^{-1}$ | 3000 | 3000 |
| Total specific surface area, $m^2/g$ | 400-900 | 200-400 |
| Cost | High | Low |

The use of MWCNTs in photocatalysis is mainly as support for photocatalytically active materials to form MWCNTs/$TiO_2$ composite photocatalyst. Indeed, the combination of MWCNTs with $TiO_2$ has attracted much attention, since MWCNTs take an important role in the way they link to $TiO_2$ nanoparticles and consequently, in the electronic and photocatalytic performance of the MWCNTs/$TiO_2$ composite. A good dispersion of $TiO_2$ nanoparticles in the MWCNTs/$TiO_2$ composite attributed to the functionalization of MWCNTs with nitric acids leads to the creation of large amounts of carboxylic acid and phenol groups at the surface of the MWCNTs. Basically, the functional groups present at the surface of MWCNTs promote the anchoring of the $TiO_2$ nanoparticles as well as avoiding agglomeration and subsequently increasing the surface area of the resulting MWCNTs/$TiO_2$ composite. In addition, this strong interface interaction also favors electron transfer pathways, thus the probability for electron/hole recombination is reduced. The formation of Ti-O-C bonds between the carboxylic acid groups of MWCNTs and the hydroxyl groups existent at the surface of $TiO_2$ during an esterification reactions, contribute to a synergetic effect due to the creation of an electronic interphase interaction between MWCNTs and $TiO_2$ phases (Bergmann and Machado, 2015, Dai et al., 2012, Ghosh and Oh, 2012). The success of incorporating the CNTs surface with $TiO_2$ nanoparticles depends on the preparation technique. The uniformity of the $TiO_2$ varies according to the preparation method and the surface reactions of CNTs with $TiO_2$ nanoparticles.

### 2.3.4 Synthesis of CNTs/$TiO_2$

Over the past few years, various synthesis methods to form CNTs/$TiO_2$ composite have been explored. The incorporation of the MWCNTs can control the physiochemical properties of $TiO_2$ nanoparticle photocatalyst to meet the specific requirement for a given application purpose. To date, there are several synthesis methods that can be utilized to produce MWCNTs/$TiO_2$ composite photocatalyst. The techniques included are liquid phase deposition method, simple mixing, ultrasonic irradiation, chemical vapor deposition, electrodeposition, hydrothermal, solvothermal and sol-gel method. In the following section, the most commonly techniques such as simple mixing, chemical vapor deposition, electrodeposition, hydrothermal and sol-gel methods are briefly reviewed.

#### 2.3.4.1 Simple mixing

Simple mixing has been reported as one of the most fundamental routes for the synthesis of carbon based $TiO_2$ nanocomposites. Under simple mixing method, a certain amount of $TiO_2$ powder and CNTs were dispersed and mixed in water under slow stirring rate at room temperature. This method usually performed in solution and water is to be used as the solvent. In respect to this method, it is simple and less time-consuming; however, it has been criticized for the low level of interaction where there is no intimate contact or chemical bonding between CNTs and $TiO_2$. The type of bonding exists between CNTs and $TiO_2$ in this method is physisorption and $TiO_2$ may detach from CNTs surface through mechanical process such as sonication. Thus, this implies that the attachment of $TiO_2$ onto the surface of CNTs is through van der Waals interactions. Significantly, the interaction between CNTs and $TiO_2$ is one of the key factors for controlling electron transfer and photocatalytic activity in CNTs/$TiO_2$ nanocomposite structure (Barberio et al., 2014, Xu et al., 2010).

#### 2.3.4.2 Chemical Vapor Deposition (CVD)

Chemical vapor deposition (CVD) techniques are among the most common methods to synthesis CNT/$TiO_2$ composite that utilize the growth of a solid material from gas phase through chemical reaction at the surface of a substrate. Due to the high purity of reagent used in this method, it can provide $TiO_2$ with a good control of the size, shape, purity, composition and easy scalability. In contrast to high pressure or high temperature synthesis, medium temperature at around 600-800 °C and a slightly reduced atmospheric pressure is required by this technique. Uniform coating of $TiO_2$ on CNTs can be achieved by this technique but when it scales down to few nanometers, uniformity and defect-free coatings are difficult to be achieved due to the fast deposition. Furthermore, this technique is not simple and specialized equipment is needed. (Chen et al., 2015; Darbari et al., 2011; Shitole et al, 2013; Zhu et a., 2012).

#### 2.3.4.3 Electrodeposition

Electrodeposition is one of the powerful techniques for the deposition of $TiO_2$ nanoparticles via reduction of metal complexes by electrons. In the early stages of electrodeposition, the limiting step corresponds to electron transfer from work electrode for metallic ions in solution. The size and the coverage of $TiO_2$ nanoparticles on the sidewalls of CNTs can be controlled by electrodeposition parameters, including concentration of the metal salt, nucleation potential and deposition time. The main advantage of this technique is that the electrodeposited nanoparticles show higher purity as well as a good adhesion to the surface of CNTs. In detail, a strong adhesion could be provided via a simple van der Waals interaction between the CNTs and the $TiO_2$ nanoparticles. For instance, the deposition of $TiO_2$ can be carried out by using $TiCl_3$ as a precursor and electrolyte through galvanostatic oxidation with 1 $mA/cm^2$ at pH 2.5 with $HCl/Na_2CO_3$. As a result, it has been reported that this technique occurs to the same extent on both the sidewalls of the tubes and the tips. However, electrodeposition technique is difficult to produce bulk quantities of samples and this becoming the major drawback of this method (Benneti et al, 2016; Daniele et al., 2016; Zhao et al., 2010).

### 2.3.4.4 Hydrothermal

Hydrothermal techniques have been employed in the synthesis of carbon-$TiO_2$ nanomaterials in recent years. It is usually performed in Teflon-sealed autoclave under controlled temperature and/or pressure. It is worth mentioning that the titanium precursors using for hydrothermal processes are mainly titanium tetrachloride ($TiCl_4$) and titanium oxysulfate ($TiOSO_4$). Typically, the final materials obtained are mostly amorphous $TiO_2$ with seeds of anatase regardless the chosen conditions and chemistry. Thus, a further heat treatment that occurs at 300-500 °C in air is required to fully crystallize the $TiO_2$ coating on CNTs and avoid the burnout of the CNTs.

In a typical hydrothermal synthesis of MWCNTs/$TiO_2$ nanocomposites, the pristine or acid-treated CNTs were added to the aqueous solution of the titanium precursor and treated in an autoclave at temperature between 100-200 °C to produce crystalline films of $TiO_2$. As a result, a dense coating of spherical or slightly elongated nanoparticles are obtained. In contrast with others methods, the advantages of the composites prepared by hydrothermal methods are found to give better results, including reduce agglomeration among particles, narrow particle size distribution, and control phase homogeneity and particle morphology. However, this method requires long preparation times (several hours or a day) and acquires hydrothermal temperature and pressure (Dai et al., 2013; Shitole et al, 2013; Yu et al., 2011; Zhu et al., 2012).

### 2.3.4.5 Sol-gel

Sol-gel is a versatile technique that involves the transition of a liquid colloidal sol, followed by hydrolysis and polymerization of the precursors which are usually metal alkoxides into a solid gel phase. Typically, sol-gel method is the most common technique to synthesize $TiO_2$ on the CNTs surface because this method is cheap, easy to control the chemical composition, does not require complicated equipment and occur at ambient temperature that can produce materials with high purity and homogeneity. However, the major drawback of this synthesis is that the final product normally consists of an amorphous phase rather than the defined crystals and hence, crystallization and post annealing steps are required. Moreover, this method usually leads to heterogeneous, non-uniform coating and random aggregation of $TiO_2$ onto the CNTs surface.

Significantly, the selection of precursor is crucial for sol-gel method due to the reason that homogeneous nucleation or heterogeneous on CNTs are influenced by the reactivity of the precursor with the solvent. The most common titanium precursor used is titanium isopropoxide since it readily dissolves in alcohol and is not overly sensitive. Furthermore, the growth rate of nanoparticles is also affected where the fast condensation rates resulting in a large particle-size distribution. Therefore, acids or bases are added for altering the reaction rate. The previous report has shown that the MWCNTs/$TiO_2$ nanocomposites prepared by the sol-gel method have higher photocatalytic activity than the simple physical mixture of MWCNTs/$TiO_2$ with the same CNTs content. Besides, it is also demonstrated that fine and well dispersion of $TiO_2$ nanoparticles on CNTs surface prepared by sol-gel method shows higher photocatalytic activity as opposed to those produced by hydrothermal route (Soroodan Miandoab & Fatemi, 2015; Tseng et al., 2010; Wongaree et al., 2015; Wu et al., 2013). The comparison between the unique features of simple mixing, chemical vapor deposition, electrodeposition, hydrothermal and sol-gel methods is summarized in Table 2.9. Basically, the combination of MWCNTs with $TiO_2$ will increase the photocatalytic degradation rate when compared with $TiO_2$ nanoparticles. Most organic compounds can be photocatalytically degraded within minutes to a few hours under UV or near UV-visible irradiation, while lower rates and longer time was needed for visible light. Synthesis routes covers the range of techniques are summarized in Table 2.10.

**Table 2.9:** Comparison of the most widely used synthesis methods for preparing CNTs/$TiO_2$ composite

| **Synthesis method** | **Advantage** | **Disadvantage** |
|---|---|---|
| Simple mixing | •Simple<br>•Less time-consuming | •No intimate contact or chemical bonding between CNTs and $TiO_2$ nanoparticles |
| CVD | •Short processing time<br>•Provide $TiO_2$ with a good control of size, the shape and purity<br>•Uniform coating of $TiO_2$ on CNTs | •High deposition temperature is required<br>•This technique is not simple and specialized equipment is needed |
| Electrodeposition | •Electrodeposited $TiO_2$ nanoparticles show higher purity as well as good adhesion to the surface of CNTs | •Difficult to produce bulk quantities of CNTs/$TiO_2$ sample |
| Hydrothermal | •Reduce agglomeration among $TiO_2$ nanoparticles<br>•Control phase homogeneity and particle morphology | •Long preparation time is required<br>•Hydrothermal temperature and pressure is acquired |
| Sol-gel | •Simple<br>•Cheap<br>•Occur at ambient temperature<br>•Fine and well-dispersion of $TiO_2$ nanoparticles on CNTs surface | •Hydrolysis rate is difficult to be controlled |

**Table 2.10:** Representative summary of CNT/$TiO_2$ composite synthesis routes

| **Synthesis routes** | **Precursors** | **Details** | **Remarks** | **Reference** |
|---|---|---|---|---|
| Simple mixing | MWCNTs<br>Commercial P25 | • Purification of MWCNTs using $HNO_3$<br>• Dispersed in anhydrous ethanol solution | • Less individual interfacial between MWCNTs and $TiO_2$<br>• Simple mixing cannot combine P25 and MWCNTs effectively | Xu et al., 2010 |
| | MWCNTs<br>Titanium sulfate | • MWCNTs was treated using $HNO_3/H_2SO_4$ mixture<br>• Acid-treated MWCNTs were dispersed in water and introduced into titanium sulfate solution | • Unable to create effective interfacial contact between $TiO_2$ and CNTs | Yu et al., 2011 |
| | SWCNTs (Arry-nano)<br>$TiO_2$ | • CNT/$TiO_2$ composite were prepared with a the sequence of mixing and heating process<br>• Dispersed in dichlorobenzene | • No observe formation of chemical bonds and the CNTs are wrapped around $TiO_2$ anatase grains | Marianna Barberio et al., 2014 |
| Chemical vapor deposition | CNTs<br>Titanium tetrachloride | • CVD growth of CNTs was carried out using the supported Ni as the catalyst<br>• CVD deposition of a $TiO_2$ layer on the CNTs | • The conformal coverage of $TiO_2$ nanoparticles on the CNTs walls | Darbari et al., 2011 |

**Table 2.10 (to be continued)**

| | | | | |
|---|---|---|---|---|
| | CNTs<br>Commercial anatase $TiO_2$ | • CVD growth of CNTs was carried out using the supported Fe as the catalyst and a mixture of $C_2H_4$ and $H_2$<br>• CNTs directly grown on $TiO_2$ | • CNTs were found to be uniformly grown in $TiO_2$ particles without altering the crystalline structure | Chen et al., 2015 |
| Electrodeposition | CNT $TiO_2$ | • The electrodeposition of $TiO_2$ was performed in a three-electrode cell with resin as a working electrode, Pt wire and Ag/AgCl were used as counter and reference electrodes<br>• KCl solution as the electrolyte | • CNTs were coated with a uniform layer of highly crystalline anatase $TiO_2$ nanoparticles | Zhao et al., 2010 |
| Hydrothermal | MWCNTs<br>Titanium sulfate | • MWCNTs was treated using $HNO_3/H_2SO_4$ mixture<br>• Hydrothermal treatment at 160 °C for 5 h | • A very uniform of $TiO_2$ nanoparticles deposits on the MWCNTs | Yu et al., 2011 |
| | MWCNTs<br>Titanium isopropoxide | • Purification and functionalization of MWCNTs using HCl and $HNO_3$<br>• Hydrothermal treatment at 140 °C for 24 h | • Favors a decrease in agglomeration among particles and controlled particle morphology | Shitole et al., 2013 |

**Table 2.10 (to be continued)**

| | | | | |
|---|---|---|---|---|
| | SWCNTs<br>Titanium sulfate | - SWCNTs were treated in the boiled nitrate solution<br>- Hydrothermal treatment at 140 °C for 24 h | - Well-dispersed SWCNTs and $TiO_2$ nanoparticles have intimate contact, which inhibit growth of the $TiO_2$ grain | Dai et al., 2013 |
| Sol-gel | MWCNTs<br>Titanium tetrachloride | - Addition of HCl; stirring for 24 h; calcination at 350 °C | - Homogeneous distribution of $TiO_2$ on the CNTs<br>- CNTs were covered with $TiO_2$ particles | Kim et al., 2008 |
| | MWCNTs<br>Titanium isopropoxide | - CNT/$TiO_2$ composite were prepared with the aiding of benzyl alcohol as a linking agent | - Homogeneous coating of $TiO_2$ sols over the CNTs | Soroodan Miandoab & Fatemi, 2015 |
| | MWCNTs<br>Titanium isopropoxide<br>Titanium butoxide | - MWCNTs was treated using $HNO_3/H_2SO_4$ mixture<br>- Titanium precursor, ethanol, $H_2O$, and HCl was mixed and stirred at ambient temperature | - Dispersion of $TiO_2$ nanoparticles on the surface of CNTs | Wongaree et al., 2015 |

# CHAPTER 3: RESEARCH METHODOLOGY

This chapter fully describes the details of the whole experiment work conducted and is divided into five segments. The first segment provides the details on the materials and chemicals involved in the studies. The second segment shows the experimental set-up and procedures used for the pre-treatment of pristine MWCNTs. The third segment imparts the investigations and experimental procedure implicated in the synthesis of $TiO_2$ nanoparticles and MWCNTs/$TiO_2$ nanocomposites. The following segment describes the photocatalytic activity and evaluation testing for $TiO_2$ nanoparticles and MWCNTs/$TiO_2$ nanocomposites on Dimethyl phthalate esters respectively. Finally, the last segment discusses on the characterization techniques acquired in the analysis.

## 3.1 Materials Synthesis

### 3.1.1 Raw Materials and Chemicals Selection

Materials and chemical selections are significantly essential in determining the morphology structure as well as the functional properties of the MWCNTs/$TiO_2$ nanocomposites. In this study, the raw materials and chemicals used in the pre-treatment of pristine MWCNTs are multiwalled carbon nanotubes, nitric acid and sodium bicarbonate. The raw materials and chemicals used in the synthesis of MWCNTs/$TiO_2$ are titanium isopropoxide, sodium dodecylbenzesulfonate, glacial acetic acid, absolute ethanol and diluted ammonia solution. Dimethyl phthalate esters was used as a model of organic pollutant in this research studies. Besides, the mobile solvents used in the high performance liquid chromatogram analysis are acetonitrile and Millipore Milli-Q water. All the chemicals and reagents were used as received as tabulated in Table 3.1. Deionized water was used throughout this study.

**Table 3.1:** List of raw materials and chemicals used in the synthesis of $MWCNTs/TiO_2$ nanocomposites and photodegradation of DMPEs

| **Materials/ Chemicals** | **Manufacturer** | **Specifications** |
|---|---|---|
| Multi-walled Carbon nanotubes (MWCNTs) | Bayer Material Science AG (Germany) | Chemical Formula: MWCNTs<br>Purity > 95%<br>Function = Pre-treatment of MWCNTs |
| Nitric Acid | Merck | Chemical Formula: $HNO_3$<br>Molar Mass = 63.01 g/mol<br>Purity = 65%<br>Function = Pre-treatment of MWCNTs |
| Sodium Bicarbonate | Sigma-Aldrich | Chemical Formula: $NaHCO_3$<br>Molar Mass = 84.01 g/mol<br>Purity ≥ 99 %<br>Function = Remove $NO_x$ gas produced from the reaction of Pre-treatment of MWCNTs |
| Titanium Isopropoxide | Sigma-Aldrich | Chemical Formula: $Ti[OCH(CH_3)_2]_4$<br>Molar Mass = 284.22 g/mol<br>Purity = 97%<br>Function = Synthesis of $TiO_2$ nanoparticles |
| Sodium Dodecylsulfate | Merck | Chemical Formula: $C_{12}H_{25}OSO_2ONa$<br>Molar Mass = 288.37 g/mol<br>Purity ≥ 98%<br>Function = Dispersing agent |
| Glacial Acetic Acid | Fisher Scientific | Chemical Formula: $CH_3CO_2H$<br>Molar Mass =60.05 g/mol<br>Purity ≥ 99.7 %<br>Function = To restrain the hydrolysis process |
| Absolute Ethanol | Fisher Scientific | Chemical Formula: $C_2H_5OH$<br>Molar Mass = 46.04 g/mol<br>Purity > 99.8%<br>Function = Solvent used for the synthesis of $TiO_2$ nanoparticles |
| Diluted Ammonia Solution | Fisher Scientific | Chemical Formula:$NH_4OH$<br>Molar Mass =35.04 g/mol<br>Purity =EMSURE® grade<br>Function= Adjustment of pH |
| Dimethyl Phthalate Esters | Sigma-Aldrich | Chemical Formula: $C_6H_4$-1,2- $(CO_2CH_3)_2$<br>Molar Mass = 194.18 g/mol<br>Purity > 99%<br>Function = Model organic compound |
| Acetonitrile | Merck | Chemical Formula: $CH_3CN$<br>Molar Mass = 41.05 g/mol<br>Purity ≥ 99.9 %<br>Function = Solvent used for HPLC |

The overview of the research methodology is displayed in Figure 3.1.

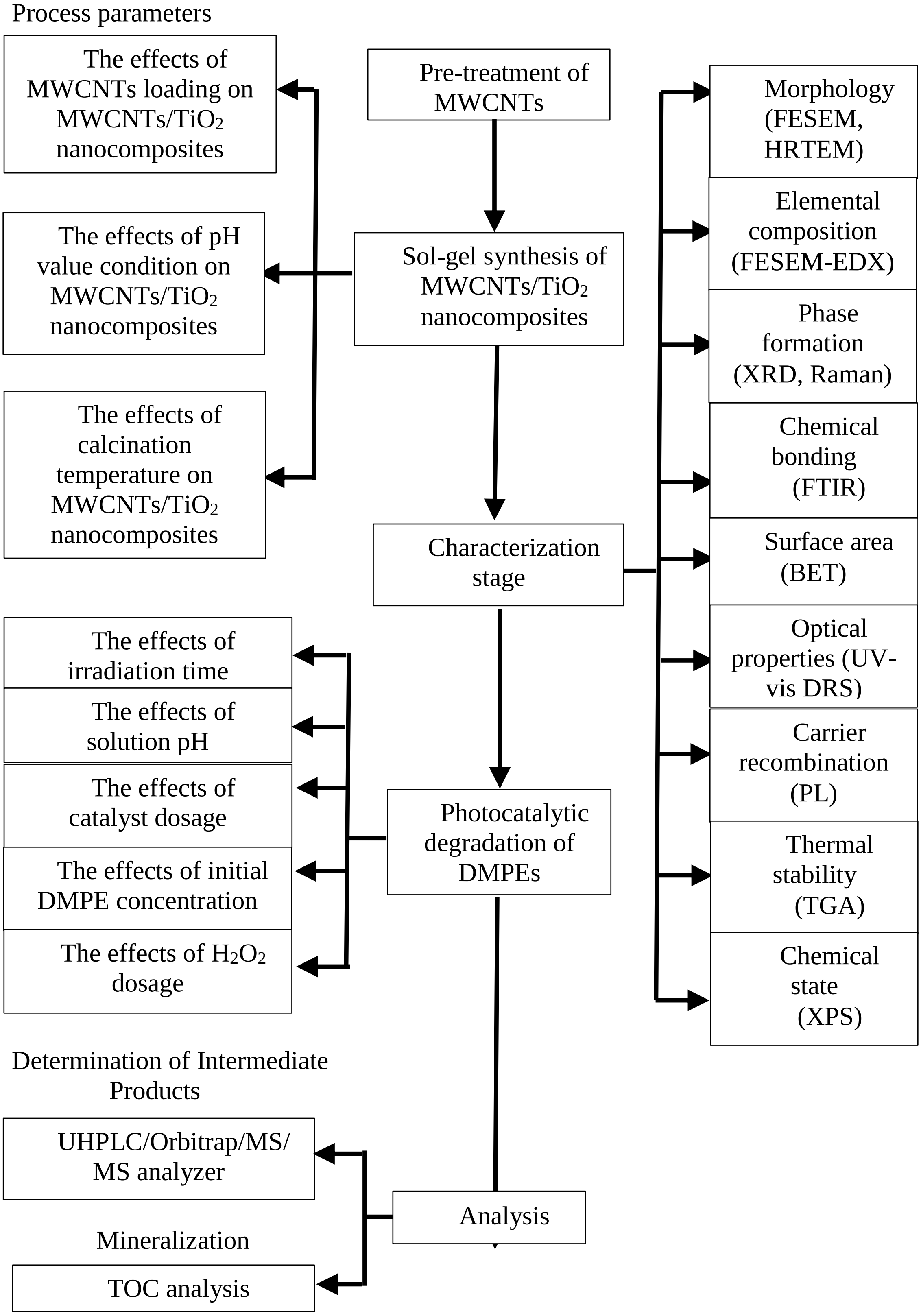

**Figure 3.1:** Overview of research methodology

## 3.2 Pre-treatment of Pristine MWCNTs

Pristine multi-walled carbon nanotubes (MWCNTs) supplied from Bayer Material Science is grown by catalytic chemical vapor deposition (CCVD) in a fluidized bed reactor. Stepwise purification of pristine MWCNTs was chemically performed as steps elimination of metal impurities and amorphous graphitic platelets. In this study, pristine MWCNTs were purified by an appropriate amount of concentrated nitric acid in a 1000 ml round bottom flask equipped with a condenser and the dispersion was refluxed under magnetic stirring at 100 °C for 2 hours as shown in Figure 3.2. The ratio of nitric acid to carbon sample was set to 500 ml for 10g. Refluxing a reaction mixture is a simple and efficient way to maintain a constant reaction temperature. After treatment, the solution was cooled to room temperature, washed with distilled water and vacuum-filtered. The resulting sample was washed up to neutral pH, and the sample was oven dried overnight at 100 °C. In such conditions, the remaining metal catalysts are removed and the holes are formed in the sidewalls followed by an oxidative etching along the walls with the concomitant release of carbon dioxide. The oxygen-containing groups mainly hydroxyl and carboxyl groups are introduced onto the ends and sidewalls of the MWCNTs (Tessonnier et al., 2009). The resulting purified MWCNTs from the procedure above were subjected to different characterization tools *i.e.* FESEM and TEM for morphological studies, FESEM-EDX for elemental composition analysis, FTIR for chemical bonding analysis, TGA for thermal stability and also Raman Spectroscopy for obtaining graphitic structure of carbon defects.

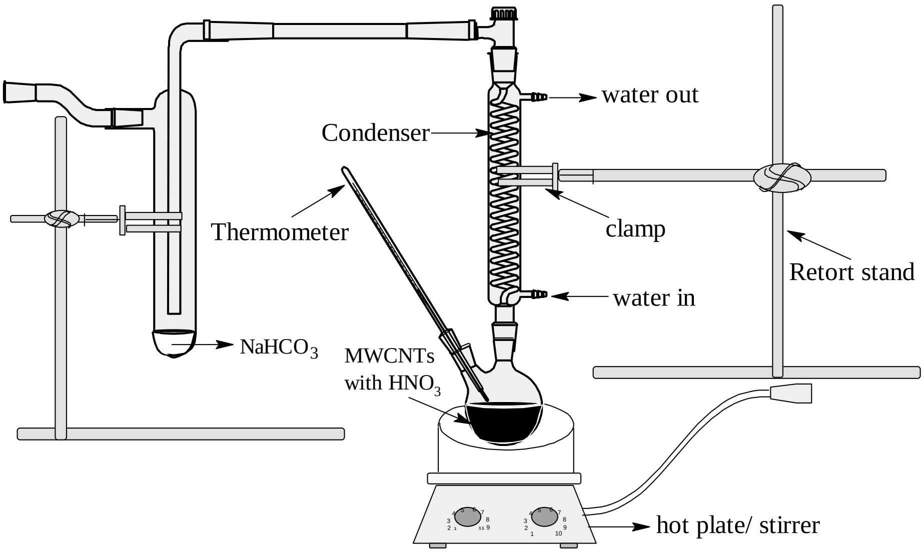

**Figure 3.2:** Experiment set up for the Pre-treatment of pristine MWCNTs

## 3.3 Preparation of catalysts

$TiO_2$ nanoparticles and MWCNTs/$TiO_2$ nanocomposites were prepared via a simple modified sol-gel method, respectively. The details of the synthesis methods are described as below.

### 3.3.1 Synthesis procedures of $TiO_2$ nanoparticles

Titanium precursor, titanium isopropoxide was first dissolved in ethanol solution for 30 mins under constant stirring at 350 revolutions per minute (rpm) [Solution A]. Next, a mixture of water, ethanol and acetic acid were undergoing constant stirring at 350 rpm for 30 minutes [Solution B]. Then, the solution B was added dropwise at 1 mL/min into the solution A under vigorous stirring at 28 °C for 2 hours. The sample was centrifuged at 4000 rpm and rinsed with ethanol. After that, the resulting sample was oven-dried at 80 °C and then calcined in air at 450 °C for 2h. Drying process is used to remove the organic solvent while calcination process is used to convert the amorphous structure of $TiO_2$ nanoparticles to crystalline phase. This is important because the photocatalytic activity of crystalline phase such as anatase is much more effective compared to amorphous structure.

### 3.3.2 Synthesis procedures of MWCNTs-$TiO_2$ nanocomposites

An appropriate amount of purified MWCNTs (3 wt %, 5 wt %, 10 wt % and 15 wt %) was added with SDS in an aqueous solution and agitated for 24 hours. The above mentioned solution was then dispersed in ethanol and stirred for another 30 minutes to achieve homogeneity [Solution A]. A mixture of titanium tetraisopropoxide (TTIP), ethanol and acetic acid at a volume ratio of 2:3:1 was undergoing constant stirring at 350 rpm for 30 minutes to form a clear solution [Solution B]. Then, the solution B was added dropwise into the solution A under vigorous stirring at 28 °C for 2 hours. Diluted ammonia solution was then added dropwise at 1 mL/min into the mixture solution in order to hydrolyze and to form a well-uniform $TiO_2$ coated on the surface of MWCNTs (Gao, Chen & Puma, 2009; Hamid et al., 2014). Numerous runs with different pH (3, 5, 7, 9 and 11) were adjusted to study the effect of pH for MWCNTs/$TiO_2$. The samples were separated by centrifuging and rinsed with ethanol to remove the adsorbed impurities. The resulting sample was oven-dried at 80 °C and then calcined in air at various temperatures (350 °C, 450 °C, 550 °C, 650 °C and 750 °C). Calcination process is used to convert the amorphous structure of MWCNs/$TiO_2$ nanocomposites to crystalline phase. A schematic representation on the preparation of $TiO_2$ coated on MWCNTs was shown in Figure 3.3.

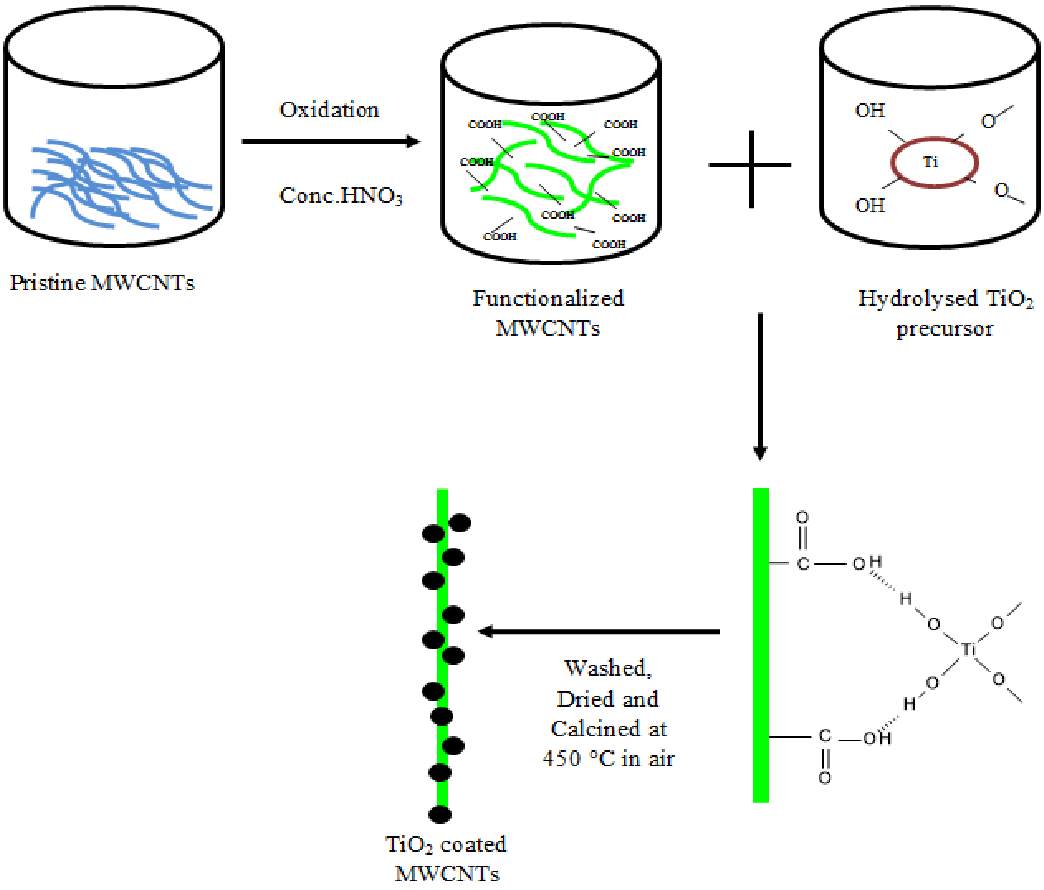

**Figure 3.3:** A schematic representation on the preparation of $TiO_2$ coated on MWCNTs

## 3.4 Photocatalytic activity Evaluation Test for Dimethyl Phthalate Esters

Photocatalytic degradation of DMPEs was evaluated under exposure of a 96 W UV-C lamp in a custom-made photoreactor as shown in Figure 3.4. UV light, however, has sufficient energy of radiation to disrupt and break the covalent bonds of organic molecules. This property may be employed to advantage in inducing degradation of organic pollutants. Typically, an appropriate amount of MWCNTs/$TiO_2$ photocatalysts was added into a 100 mL of DMPEs solution. The operating conditions used are described in Section 3.4.3. The solution was stirred in darkness at 350 rpm for 30 minutes to reach adsorption-desorption before UV lamp was switched on to initiate the photodegradation of DMPEs. The test samples were withdrawn at regular time intervals and then filtered through 0.22 µm Nylon membrane filters (Thermo Scientific) to remove the catalyst particles from the test solution before being analyzed by using a UV-Vis spectrophotometer. Furthermore, the photocatalytic degradation of DMPEs using either $TiO_2$ or MWCNTs alone was also studied. In addition, various experimental conditions such as photolysis, adsorption and photocatalysis process were also carried out by $TiO_2$ and MWCNTs/$TiO_2$ on the preliminary study of photocatalytic efficiency of DMPEs. This study is mainly focus on the photocatalytic activity of MWCNTs/$TiO_2$ in which the degradation efficiency for DMPEs has been increased greatly with the incorporation of MWCNTs.

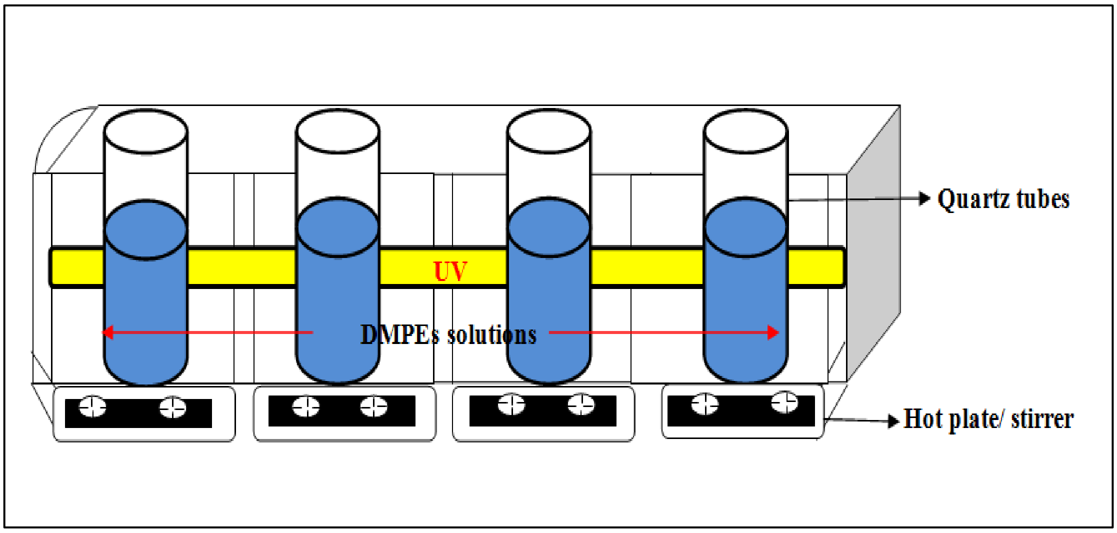

**Figure 3.4:** A custom-made photocatalytic reactor for the photodegradation of DMPEs

### 3.4.1 Measurement of DMPEs concentrations

The concentration of DMPEs in the test samples was determined by UV-Vis spectrophotometer (Shidmadzu UV-2500). A series of five different standard DMPEs solutions (1 ppm, 1.5 ppm, 2 ppm, 2.5 ppm and 3 ppm) were prepared. The absorbance of the standard samples was scanned in the wavelength range of 200 to 800 nm to determine the maximal absorbance of DMPEs. The calibration curves of standard DMPEs solutions were used to estimate the degradation efficiency of DMPEs. The degradation efficiency of DMPEs (%) was calculated based on the Equation 3.1:

$$\text{DMPEs Removal or Degradation Efficiency (\%)} = \frac{C_0 - C_t}{C_0} \times 100 \quad \textbf{(3.1)}$$

where $C_0$ is the initial concentration and $C_t$ is the concentration of DMPEs (ppm or mg/L) after different light irradiation time (min), respectively.

### 3.4.2 Reaction kinetic study

The photocatalytic degradation kinetics of DMPEs with the presence of MWCNTs/$TiO_2$ and $TiO_2$ was studied. The concentration of DMPEs was withdrawn and measured continuously (each 15 min) as a function of time. Then, the results collected were analyzed by the first order kinetic model (Equation 3.2):

$$\ln (C_0/C) = kt \quad \textbf{(3.2)}$$

where $C_0$ is the initial concentration and $C$ is the concentration (ppm or mg/L) at time $t$. The plots of the concentration data gave a straight line.

### 3.4.3 Parameter studies in photodegradation of DMPEs

The efficiency of the photodegradation process depends strongly on the experimental conditions. Taking into account the role of the different parameters should be of great importance to have a better understanding on the photocatalytic process and a great opportunity for its application for the degradation of DMPEs. Various reaction parameters such as catalyst dosage, initial DMPEs concentration, pH, irradiation time, and $H_2O_2$ dosage are the significant factors in the photocatalytic degradation process. In this research, the photocatalytic degradation of DMPEs with MWCNTs/$TiO_2$ nanocomposites was evaluated according to the reaction parameters described as below.

### 3.4.3.1 Effect of catalyst dosage

In this study, numerous runs with different catalyst dosages ranged from 0.1 to 0.7 g/L were conducted to study the dosage of catalysts on DMPEs. Most of the research works reported recently are limited to the removal of DMPEs at higher concentration; however, the concentrations of PAEs in highly industrialized Klang Valley, Malaysia have found varying concentrations of PAEs ranging from 0.1 to 64.3 µg/L in the river water (Sin et al., 2011). In this research works, higher concentration of DMPEs, 1 mg/L, was chosen. According to the parameters reported in literature, the other operating parameters were fixed at pH 6 of solution pH and 3 h of reaction time before each of the parameter was selected (Zhu and Jiang, 2014). The solution was stirred in darkness for 30 minutes to reach adsorption-desorption before UV lamp was switched on to initiate the photodegradation of DMPEs. The test samples were withdrawn at regular time intervals and then filtered through 0.22 µm Nylon membrane filters to remove the catalyst particles from the test solution. The dosage of catalyst *i.e.* 0.5 g/L, which was able to give the highest degradation efficiency as described in Section 4.7.4, was used in the subsequent sections.

### 3.4.3.2 Effect of initial concentration of DMPEs

In this study, different DMPEs concentrations ranged from 1 to 3 mg/L were conducted to study the effect of initial concentration of DMPEs. At the same time, the dosage of MWCNTs/$TiO_2$ dosage was fixed at 0.5 g/L, solution pH of 6 and 3 h of reaction time. The solution was stirred in darkness for 30 minutes to reach adsorption-desorption before UV lamp was switched on to initiate the photodegradation of DMPEs. The test samples were withdrawn at regular time intervals and then filtered through 0.22 µm Nylon membrane filters to remove the catalyst particles from the test solution. The initial concentration of DMPEs *i.e.* 1 mg/L as described in Section 4.7.3, which was able to give the highest degradation efficiency, was used in the subsequent sections.

#### 3.4.3.3 Effect of solution pH

In this study, numerous runs with pH ranged from pH 2 to pH 10 were conducted to study the effect of the solution pH on DMPEs. At the same time, the dosage of MWCNTs/$TiO_2$ dosage was fixed at 0.5 g/L, the initial concentration of DMPEs was fixed at 1 mg/L and 3 h of reaction time. The solution was stirred in darkness for 30 minutes to reach adsorption-desorption before UV lamp was switched on to initiate the photodegradation of DMPEs. The test samples were withdrawn at regular time intervals and then filtered through 0.22 µm Nylon membrane filters to remove the catalyst particles from the test solution. The solution pH *i.e.* pH 6, which was able to give the highest degradation efficiency as described in Section 4.7.2, was used in the subsequent sections.

#### 3.4.3.4 Effect of irradiation time

In this study, numerous runs with different irradiation time ranged from 1 to 4 h were conducted to study the effect of irradiation time on DMPEs. At the same time, the initial concentration of DMPEs was fixed at 1 mg/L, the dosage of MWCNTs/$TiO_2$ dosage was fixed at 0.5 g/L and solution pH of 6. The solution was stirred in darkness at 350 rpm for 30 minutes to reach adsorption-desorption before UV lamp was switched on to initiate the photodegradation of DMPEs. The test samples were withdrawn at regular time intervals and then filtered through 0.22 µm Nylon membrane filters to remove the catalyst particles from the test solution. The irradiation time *i.e.* 3 h, which was able to give the highest degradation efficiency as described in Section 4.7.1.

#### 3.4.3.5 Effect of $H_2O_2$ dosage

In this study, numerous runs with different $H_2O_2$ dosages ranged from 5 mg/L to 20 mg/L were added into DMPEs solution to study the effect of the addition amount of $H_2O_2$ on DMPEs. At the same time, the dosage of MWCNTs/$TiO_2$ dosage was fixed at 0.5 g/L, the initial concentration of DMPEs was fixed at 1 mg/L, solution pH of 6 and 3 h of reaction time. The solution was stirred in darkness for 30 minutes to reach adsorption-desorption before UV lamp was switched on to initiate the photodegradation of DMPEs. The test samples were withdrawn at regular time intervals and then filtered through 0.22 µm Nylon membrane filters to remove the catalyst particles from the test solution. The amount of $H_2O_2$ *i.e.* 15 mg/L, was able to give the highest degradation efficiency in this study.

#### 3.4.3.6 Catalyst reusability study

Considering the potentially of using MWCNTs/$TiO_2$ nanocomposites for environmental application, the reusability of MWCNTs/$TiO_2$ nanocomposites was examined by evaluating its catalytic performance. After the photocatalytic degradation reaction, MWCNTs/$TiO_2$ nanocomposites catalysts were collected using centrifugal method. The catalyst was washed three times with distilled water and subsequently dried in an oven at 80 °C for 24 h. Then, the MWCNTs/$TiO_2$ nanocomposites catalysts were reused for the degradation of DMPEs in order to perform photocatalytic degradation process. The degradation efficiency of DMPEs within 3 h for UV irradiation was investigated up to five catalytic cycles.

## 3.5 Analytical and Characterization Techniques

In this section, the synthesized MWCNTs/$TiO_2$ were subjected to characterization tests to comprehend properties such as morphological studies, elemental composition, phase structure and crystallinity, surface area, thermal stability, chemical bonding, chemical state and optical properties by utilizing appropriate instrument tools. The catalysts were characterized using FESEM, HRTEM, EDX, XRD, Raman Spectroscopy, BET surface analyzer, FT-IR, TGA, UV-Vis DRS, PL analysis and also XPS analysis. In addition, the fundamental principles and the operating parameters for sample characterizations were specified and described in details. Moreover, the identification of possible intermediate products generated during the phodegradation and mineralization process of DMPEs was performed by employing a UHPLC/Orbitrap/MS/MS analyzer and TOC analysis.

### 3.5.1 Field Emission Scanning Electron Microscopy (FESEM)

Field Emission Scanning Electron microscope (FESEM) is a non-destructive technique and often the first analytical instrument used by the investigators to visualize the surface morphology of a material with a highly magnified optical image. In this study, the sample preparation for FESEM analysis was initiated by the sample was spread evenly on the top of a carbon conductive tape which was attached to an aluminum sample stub. The surface morphology and particle size of the aprepared samples were determined by using a FESEM operating at 5.00 kV and high vacuum with a magnification of 30, 50, 70 and 100 kX, using a Quanta FEG 450. The FEI Quanta 450 is a high resolution FESEM and this instrument is easy-to-use and flexible user interface with auto navigation montage, double-click stage–movements and provide better resolution for analysis. In FESEM, the optical image is produced from the four main components which included an electron gun, a demagnification unit, a scan unit and a detection unit (Figure 3.5). Electrons are liberated by the electron gun, which is the field emission source and accelerated in a high electrical field gradient. The entire electron beam enters the demagnification unit, consisting of several electron lenses, and the specimen is bombarded by the narrow scan beam which is produced by the focusing of the primary electrons and the reflection of the electronic lenses. Furthermore, the electron beam from gun to specimen must be under vacuum in order to prevent the collision between electrons and air molecules. Moreover, the secondary electrons are emitted from the striking of the electrons on the specimen and these electrons are picked up, amplified and converted into electrical signal by the main detector system. This signal produces the screen image that can be seen on a monitor. Nevertheless, all the samples were dried prior to the analysis (Yao & Kimura, 2007).

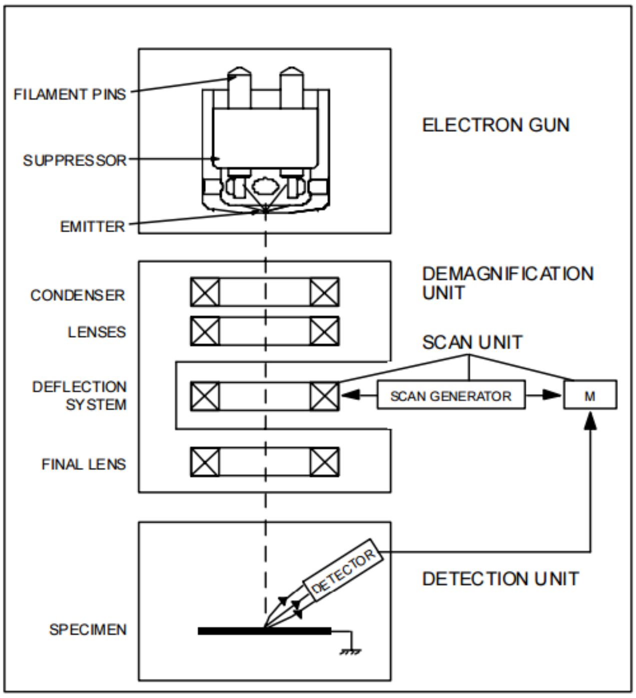

**Figure 3.5:** Schematic of Field emission scanning electron microscope (FEI Company, 2003)

### 3.5.2 High Resolution Transmission Electron Microscopy (HRTEM)

High-resolution transmission electron microscopy (HRTEM) is a high-resolution analytical instrument with a $LaB_6$ electron gun and Gatan GIF camera with 1.6 eV energy resolutions that mainly used for advanced microstructural and allowed lattice fringe imaging that can be directly related to the nanomaterials structure. The sample preparation for HRTEM analysis was initiated with a small amount of sample in the powder form was dispersed in ethanol solution and sonicated for a few minutes. Then, a drop of the suspension solution was placed on Cu grids covered with amorphous carbon film. Significantly, the prepared sample must be dried before being examined by the microscope. In this study, HRTEM were performed on a JEOL, JEM-2010 electron microscope with an accelerating voltage of 200 kV. Several images of representative area of the sample were taken at different magnifications. The basic principle of HRTEM on imaging and analyzing the structure of materials was known by the transmission of a high electron beam through the sample. HRTEM comprises varieties of components which included an electron source, electron beam, electromagnetic lenses, vacuum chamber, two condensers, specimen holder and fluorescent screen (Figure 3.6). A stream of electrons is produced by an electron source which is accelerated towards the specimen using a positive electrical potential. This stream is then focused into monochromatic beam using the condenser lenses. The specimen is then strike by this beam and some portion of the beam is focused into an image using the objective lenses. The function of a fluorescent screen is to produce the image. Additionally, it was observed that the thicker or denser region is represented by the darker areas of the image while the thinner or less dense area is represented by the lighter areas of the image (Tonejc, 1999).

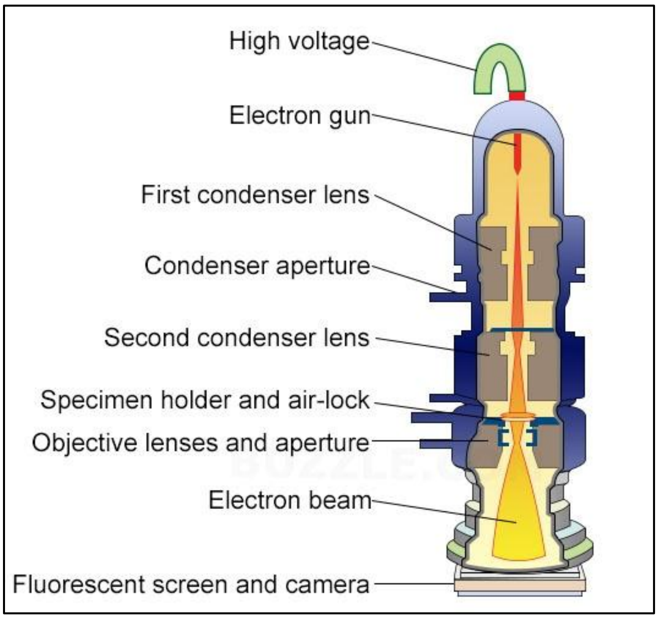

**Figure 3.6:** Schematic of High resolution transmission electron microscope (Buzzle, 2016)

### 3.5.3 Energy dispersive X-ray Spectroscopy (EDX)

FESEM coupled with Energy Dispersive X-Ray Spectroscopy (EDS or EDX) is a chemical microanalysis technique used for qualitative, quantitative and elemental mapping analysis. In this study, the sample preparation for EDX analysis was initiated by the sample was spread evenly on the top of a carbon conductive tape which was attached to an aluminum sample stub. It used Mn Kα as the energy source which was operated at 15 kV of accelerating voltage using Octane Silicon Drift Detector (SDD). The elemental composition and elemental mapping of the samples were determined by INCA Energy 400 software with the images captured by FEI Quanta 450 microscope instrument. Basically, the working principle of EDX indicates when the surface of the sample is bombarded by an electron beam, electrons are ejected from the atom comprising the sample's surface and cause the emissions of characteristics X-ray from that point of the material. When an incident x-ray strikes the detector, it will generate a charge pulse which is proportional to the x-ray energy. The relative abundance of emitted x-rays versus their energy was measured through the EDS- x-ray detector. The elemental composition of the sample can be determined through the evaluation of the spectrum of x-ray energy versus counts.

### 3.5.4 X-ray diffraction (XRD)

Powder X-ray diffraction is the most widely technique used for analyzing the phase structure and crystallite size of the prepared samples. In this study, the sample preparation for XRD analysis was initiated by grinding the measured samples into fine powder and placed in the sample holder. The sample was flattened and smoothened before putting it into the sample chamber of the diffractometer. The XRD analysis was operated at 40 kV and 30 mA with a scanning rate of 0.01°/s (Cu Kα radiation = 1.5406 Å) on a Bruker axs D8 Advance diffractometer from 10° to 80° with the integrated software, X'Pert HighScore for data acquisition. The diffraction peaks present in the XRD spectrum were matched with Powder Diffraction File (PDF) database, distributed by the International Centre for Diffraction Data (ICDD) for evaluating and identifying the phases of the sample. The basic principle of XRD is based on when an X-ray beam strikes a sample; part of the beam will be transmitted, absorbed by the sample, refracted and scattered and part of it will get diffracted to produce diffraction patterns. These patterns will be indexed in order to get information on the phase of the sample (Figure 3.7). The distance between the planes of the atoms that constitute the samples can be measured by applying Bragg's Law (Equation 3.3) when an X-ray beam hits the sample and the beam is diffracted.

$$n\lambda = 2d \sin\theta \qquad \textbf{(3.3)}$$

where the integer n is the order of the diffracted beam, $\lambda$ is the wavelength of the incident X-ray beam, d is the distance between adjacent planes of atoms (the d-spacings), and $\theta$ is the angle of incidence of the X-ray beam.

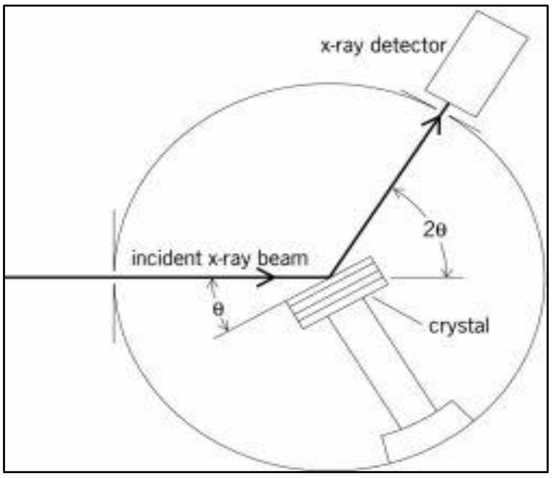

**Figure 3.7:** Schematic of Bragg spectrometer (Farlex, 2013-2016)

The average crystallite size of the samples was calculated by Scherer's equation a shown in Equation 3.4 (Talat-Mehrabad et al., 2016).

$$D = \frac{k\,\lambda}{\beta \cos\theta} \tag{3.4}$$

where D is the average size of crystallite, k is a constant of 0.9, λ is the wavelength (nm) of characteristics X-ray applies, β is the full width at half maximum (FWHM) of selected peak (in radians) and θ is Bragg angle.

The phase composition (rutile and anatase content) of the prepared samples after being subjected to various heat treatments were calculated based on the following Equation 3.5 (Hamad et al., 2015).

$$X\mathrm{R} = 1 - [1 + 1.26\,(I\mathrm{R}/I\mathrm{A})]^{-1} \tag{3.5}$$

where $X$R is the weight fraction of rutile in the mixture, and $I$R and $I$A are the peak intensities of the rutile (1 1 0) and anatase (1 0 1) diffractions, respectively.

### 3.5.5 Raman Spectroscopy

Raman spectroscopy is a very useful and ideal technique for obtaining graphitic structure of carbon bond and defects and can be used for sample phase identification. In this study, the sample preparation for Raman analysis was initiated with a small amount of sample in the powder form was placed on the top of the glass slide before putting it into microscope. Raman spectroscopy analyses were performed using a Renishaw in Via (United Kingdom) and its Windows-based Raman Environment (Wire™) software with a 514.5 nm Argon ion laser as an excitation source. The in Via means that a Raman spectrometer coupled to a microscope. It was operated at a low power level of 20 mW in order to prevent any heating effect due to laser irradiation. A Raman system normally consists of four major components which included the excitation source (laser), sample illumination system and light collection optics, wavelength selector and lastly the detector (Figure 3.8). The basic principle of Raman analysis is based on inelastic scattering of monochromatic light from a laser source. The meaning of inelastic scattering can be explained by the frequency of photons in monochromatic light changes upon the interaction with a sample. A specific area of sample is illuminated with a laser beam and the scattered light is collected and is sent through interference filter to obtain the Raman spectrum. The Raman scattered light can be detected by a Charge-Coupled Devices (CCD). The intensity of the inelastic light versus the frequency is plotted, representing the energy levels of different functional group vibrations in a Raman spectrum. Data acquisition was then obtained from computer by using the Renishaw software.

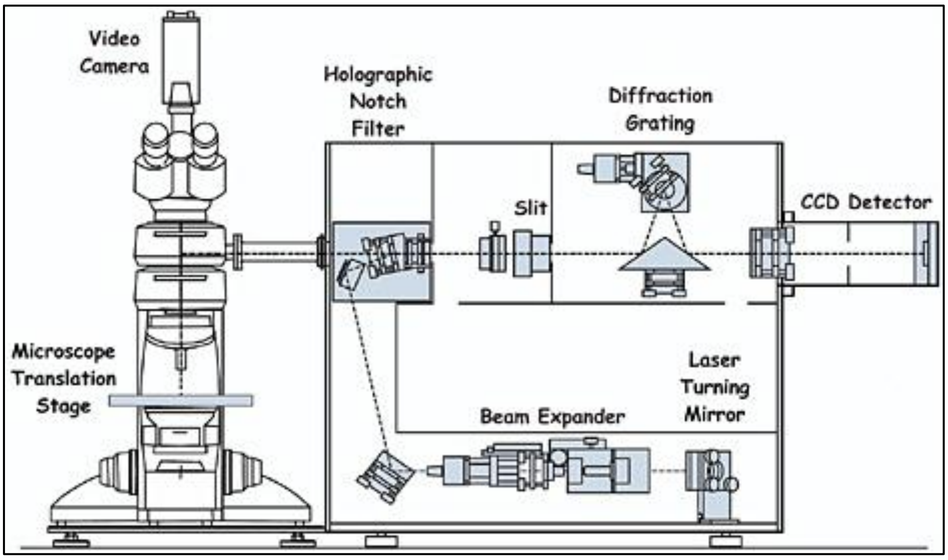

**Figure 3.8:** Schematic of Renishaw Raman-spectrometer (Clark, 2005)

### 3.5.6 Nitrogen adsorption-desorption measurement

Brunauer-Emmett-Teller (BET) analysis was used to determine the specific surface area of materials precisely. BET, the specific surface area, $S_{BET}$ was performed by Micrometrics ASAP 2010 sorptometer $N_2$ adsorption/ desorption isotherm measurements at -196 °C. Before determining the specific surface area of the sample, outgassing is needed in order to remove the gases and vapours that may physically adsorb into the surface after manufacture and during treatment. In this study, an amount of 1.0 sample was needed and degassed overnight at 200 °C under vacuum. After degassing, the sample was transferred to the analysis station where it was cooled in liquid nitrogen. Without degassing, molecules an intermediate area of the surface might cover with molecules of the previous adsorbed gas and caused the reduction of specific surface area. The specific surface area of materials is determined by physical adsorption of gas on the surface of the solid and the amount of adsorbed gas is calculated corresponding to a monomolecular layer on the surface. The adsorption isotherm was obtained by the measurement of the amount of nitrogen gas adsorbed over a range of partial pressure at a single temperature while the measurement of the quantities of nitrogen gas desorbed from the sample as the relative pressure was lowered was known as desorption isotherm. Data acquisition was then obtained from computer by using the TriStar II 3020 software.

### 3.5.7 Fourier transformed infrared (FT-IR) spectroscopy

FTIR technique was used to determine the functional groups and types of chemical bonds of the pristine and purified MWCNTs. In this study, the sample preparation for FTIR analysis was carried out using potassium bromide (KBr) pellet method. A small amount of sample was ground with KBr and the mixture was pressed into thin pellet form. Then, the pellet was placed on the sample holder before putting into the FT-IR spectrophotometer. In this study, the FTIR analysis was carried out by FTIR Bruker Vertex 80/80v, the wavelength range from 4000 to 400 $cm^{-1}$. An infrared spectroscopy system normally consists of five major components which included the source, interferometer, sample, detector and lastly the computer (Figure 3.9). The basic principle of Raman analysis is based on when an IR radiation passed through a sample, some of the IR radiation is absorbed by the sample while some of it is transmitted. The beam enters the interferometer where the source radiation can be separated into its different wavelength and goes to the sample. The beam that enters the surface of the sample is absorbed according to its chemical properties. The radiation that passes through the sample is collected and measured by the detector. The measured signal finally is sent to the computer and the infrared spectrum is then presented to the users.

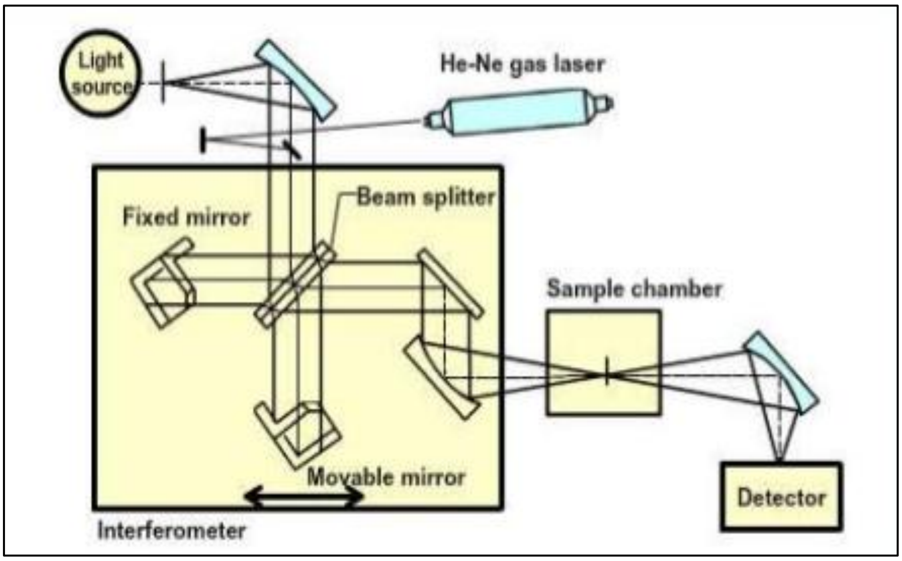

**Figure 3.9:** Schematic of FTIR Spectroscopy (Agrawal, 2016)

### 3.5.8 Thermo gravimetric (TGA) analysis

Thermo gravimetric analysis was used to study the thermal stability and the oxidation weight loss conditions of the samples. In this study, a small amount of sample was heated from room temperature to 1000 °C at a heating rate of 10 °C/min and in the presence of air flow rate of 20 ml/min. The TGA was conducted under air gas using a Perkin Elmer STA 6000 thermal analyser to evaluate the mass change of a sample as a function of temperature.

### 3.5.9 Ultraviolet-Visible Spectroscopy (UV-Vis)

#### 3.5.9.1 UV-Vis Absorption Spectroscopy

UV-Vis Absorption Spectroscopy was used to measure the absorption values of UV and visible radiation as it passes through a sample solution. Different molecules absorb radiation at different wavelengths corresponding to the changes in the energy states of electron (σ, π, free electron pairs, orbital splitting) in the energy states of electron. Apparently, the absorbance of a solution will increase as the attenuation of the beam increases. According to Beer's law (Equation 3.6), absorbance is directly proportional to the path length, b, and the concentration, c of the absorbing species.

$$A = \varepsilon bc \qquad \textbf{(3.6)}$$

where A is absorbance, ε is the molar absorbitivity, b is the path length of the sample and c is the concentration of the compound in solution.

In this study, the absorbance and concentration measurement of DMPEs was performed using UV-Vis spectrophotometer (Shidmadzu UV-2500). The broad scan of the UV-Vis spectrum was measured in the region of 200 – 500 nm. Additionally, the analysis was also performed using a single wavelength mode at 204 nm to measure the concentration of different amount of DMPEs.

#### 3.5.9.2 UV-Vis Diffuse Reflectance Spectroscopy (UV-Vis DRS)

UV-vis diffuse reflectance spectroscopy (UV-vis DRS) was used to determine the optical properties and the band gap energies of the solid materials. In this study, the samples were ground in an agate mortar and then placed in quartz cells evenly before putting into spectrophotometer. DRS were recorded on Shimadzu UV-2700 UV-vis Spectrophotometer and DRS measurements were done in wavelength range of 200 to 800 nm using an integrating sphere. Before carrying out the DRS measurement for the samples, a barium sulfate standard was used as a reference spectrum (Figure 3.10). Since the light cannot penetrate opaque solid samples, it is reflected in the surface of the samples and the relative change in the amount of reflected light off of the surface of the samples is measured by DRS. The optical band gap the samples were determined using the Kubelka-Munk expression with the transformation of diffuse reflectance spectra according to the following Equation 3.7:

$$[F(R)h\nu]^{1/2} = A(h\nu - Eg) \quad \textbf{(3.7)}$$

where F(R), h, Eg, ν and A are the Kubelka-Munk function, Planck's constant, band gap and a constant respectively.

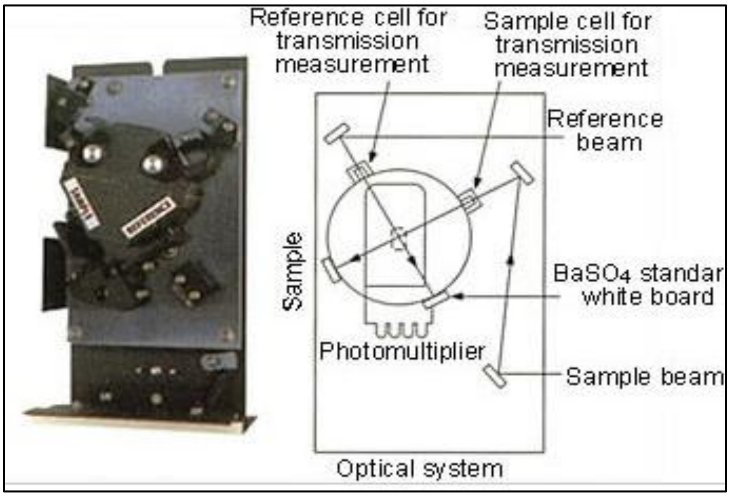

**Figure 3.10:** Picture of integrating sphere attached on DRS (Shimadzu, 2016)

### 3.5.10 Photoluminescence (PL) analysis

Photoluminescence analysis is a very useful tool to investigate the possibility of charge carrier trapping, immigration and to understand the transfer, separation and fate of photogenerated electron-hole pairs in semiconductor. In this study, the sample preparation for PL analysis was initiated with a small amount of sample in the powder form was placed on the top of the glass slide before putting it into microscope. The recombination in the samples was characterized using Renishaw inVia (United Kingdom) Raman Microscope with 325 nm wavelength monochromatic beam and the photoluminescence were recorded in the range of 350 nm to 650 nm. In PL, a sample is illuminated with a light source that having energy greater than the band gap energy, the photons being absorbed and the electrons are excited to a higher energy state then the photons is emitted and return to a lower energy state. The difference in energy levels between the two electrons states involved in the transition between the excited and equilibrium state was known as the energy of the emitted photons (photoluminescence). The level of recombination is closely related to the intensity of photoluminescence and the level of photoexcitation (Figure 3.11).

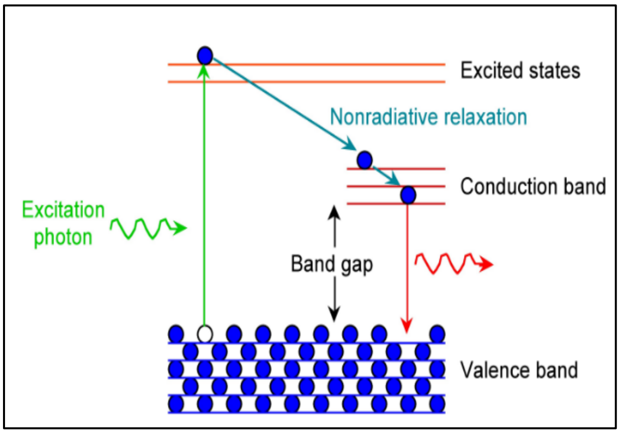

**Figure 3.11:** Emission luminescence of semiconductor (Gullapalli & Barron, 2010)

### 3.5.11 X-ray photoelectron spectroscopy (XPS)

X-ray photoelectron spectroscopy is a surface sensitive technique that used to determine the surface chemical composition, oxidation and chemical bonding states of elements in the samples. It has a probing depth from top 2 atomic layers to 15-20 layers (<50Å) and the area analysed can be as large as 1 cm x 1 cm or small as 70 µm x 70 µm. All elements except hydrogen and helium can be identified by XPS. In this study, the sample was initially pressed into pellet and ultra-high vacuum (UHV) was set before and during the measurement. The XPS measurements were performed by a PHI Quantera II with Spherical Capacitor Analyzer (SCA) and a monochromatic Al Kα (1486.6 eV) source. The C 1s line of spurious carbon located at binding energy of 284.8 eV was used as the reference to correct the binding energies for the charge shift. Survey scans in the range of 0-1200 eV were recorded and narrow scan were obtained for C 1s, O 1s and Ti 2p regions. The working principle of XPS is based on when a sample surface is excited with monoenergetic Al Kα x-rays, the photoelectrons will be emitted from the sample surface. The determination of an elemental identity, chemical state, and quantity of a detected element can be done from the binding energy and intensity of a photoelectron peak.

### 3.5.12 High Performance Liquid Chromatography (HPLC) Analysis

High Performance Liquid Chromatography is an analytical technique which was used to separate each component in a mixture. The chromatographic analysis was perfomed on a HPLC system equipped with a series of 1100 Autosampler, UV detector model with diode array detector (DAD) and the separation was performed by an isocratic elution on $C_{18}$ (250 x 4.6 mm, 10 µm) from Agilent Technologies, Palo Alto, CA,U.S.A. A mixture of acetronitrile and water (60:40, v/v) was used as the mobile phase with a flow rate of 0.5 ml/min. An injection volume of 20 µL was used and the UV detection at 204 nm. The HPLC instrument normally consistes of four componenets which includes a sampler, pump, a column and detector (Figure 3.12). The working principle of HPLC is based on an injection of a small volume of liquid sample into a tube packed with tiny particles in diameter known as stationary phase. An individual components of the sample are moved down the column with a mobile solvents forced through the column by high pressure delivered by a pump. Then, these components are separated from one another by the column packing and finally these separated components are detected at the exit of the column by a detector. A liquid chromatogram is an output from the detector. The DMPEs photoproducts were further identified by ultra high performance liquid chromatography(UHPLC) coupled with high resolution Orbitrap Mass Spectrometry(MS) from Thermo Fisher Scientific, San Jose, CA, U.S.A.

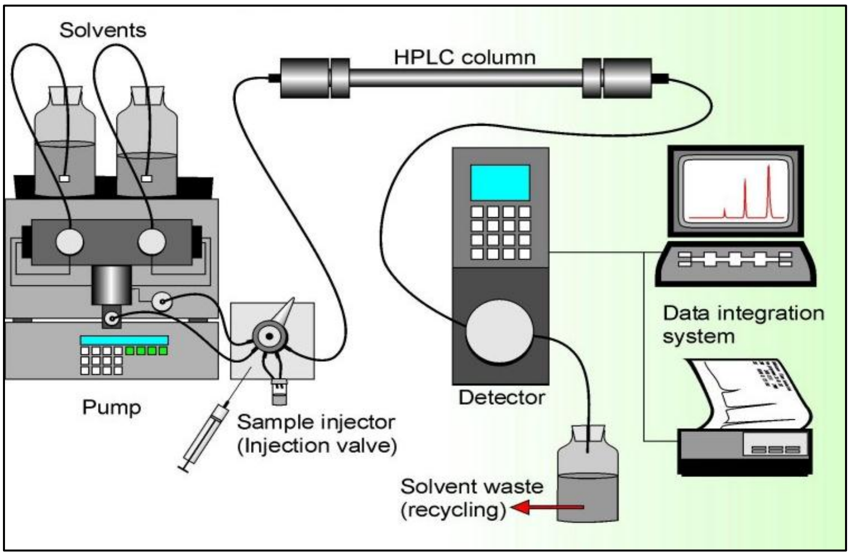

**Figure 3.12:** Schematic of HPLC system (Stormann, 2003)

### 3.5.13 Ultra High Performance Liquid Chromatography Coupled With High Resolution Orbitrap Mass Spectrometry (UHPLC/ Orbitrap/MS)

LC/MS analysis is performed with the liquid chromatography equipment connect to Thermo Scientific Orbitrap Fusion which enhance the separation of unknown compounds and enable high-throughput workflows. The unique Orbitrap mass analyzers equipped with a quadrupole mass filter, linear ion trap and Orbitrap mass analyzers from Thermo Fisher Scientific, San Jose, CA, U.S.A. provide the high-resolution, accurate-mass performance and identify the compounds more quickly. In this study, the separation was performed by an isocratic elution on RRHD SB-$C_{18}$ (150 x 2.6 mm, 1.8 µm) A mixture of acetronitrile and water (20:80, v/v) was used as the mobile phase with a flow rate of 0.3 ml/min. An injection volume of 10 µL was used and the UV detection at 204 nm. The working principle of Orbitrap mass analyzer is based on trapping of ions in electrostatic field. When an ions around a central spindle electrode are trapped after they are ejected from the C-Trap (a curved quadrupole ion trap between the linear trap quadrupole and orbitrap that injects ions into the orbitrap), the Mass/charge (m/z) value are derived from the harmonic oscillation frequencies of the trapped ions as they move across the trap spindle.

### 3.5.14 Total Organic Carbon (TOC) analysis

Total organic carbon (TOC) analyser is a useful tool to detect and measure the concentration of organic matter and compounds in water samples. The TOC analysis was performed on Ol Analytical Aurora 1030 TOC analyser equipped with 1088 Autosampler. Liquid samples were aspirated from vials via the autosampler and each sample aliquot was transferred to a TOC analyser for analysis. The operating principle of TOC analysis is based on heated persulfate wet oxidation technique which maintains the low system background necessary for high sensitivity TOC measurements. TOC was determined by removing inorganic carbon under acidic conditions, while organic carbon was digested by sodium persulfate and sulphuric acid to form carbon dioxide ($CO_2$). The measurement of the $CO_2$ released from the simultaneous dissociation and oxidation of carbon compounds present in the sample is quantified by the non-dispersive infrared (NDIR) detector and reported in concentration values (Visco et al., 2005).

# CHAPTER 4: RESULTS AND DISCUSSION

In this chapter, the results obtained in the present study followed by an explanation and discussions on the photocatalytic activity of the synthesized MWCNTs/$TiO_2$ nanocomposites for effective degradation of Dimethyl phthalate esters (DMPEs) are presented. The results are presented in four main sections on the subject of the consecutive of the work done to convey a better understanding of an ideal flow for the study. The first section presented in Chapter 4 is dealing with the information in respect to the formation of purified MWCNTs after the pre-treatment step of pristine MWCNTs with concentrated nitric acid and the synthesis of anatase $TiO_2$ nanoparticles. Again, the efficiency of DMPEs removal using synthesized $TiO_2$ nanoparticles will also be compared to MWCNTs/$TiO_2$ nanocomposites. The second section in this chapter presents the formation of MWCNTs/$TiO_2$ nanocomposites by a simple modified sol-gel method. The effects of MWCNTs content, pH and calcination temperature on resultant MWCNTs/$TiO_2$ nanocomposites are investigated in detail. Meanwhile, the influence of these synthesis parameters studies on the photocatalytic removal of DMPEs under UV irradiation are analyzed thoroughly for effective degradation of DMPEs. The third section in this chapter is associated with the performance evaluation of MWCNTs/$TiO_2$ nanocomposites in photodegradation of DMPEs under detail reaction parameter i.e. irradiation time, the initial concentration of DMPEs, catalyst dosage, solution pH and $H_2O_2$ dosage. The last section in this chapter will illustrate a proposed degradation pathway along with the possible intermediate products shown.

## 4.1 Pristine MWCNTs Vs Purified MWCNTs

### 4.1.1 Characterizations of pristine MWCNTs Vs. purified MWCNTs

A set of experiment was conducted by adopting optimum condition for purification of pristine MWCNTs based on preliminary studies, which favored the formation of purified MWCNTs. The characterizations of pristine and purified MWCNTs were conducted to reveal their properties such as surface morphology, elemental composition, functional groups, and carbon defects.

#### 4.1.1.1 Surface Morphology and Elemental Analysis

The possible MWCNTs fragmentation occurred during treatment and the possible morphological changes on MWCNTs were examined using FESEM analysis (Figure 4.1). Figure 4.1(a) shows that the pristine MWCNTs formed large agglomerates with a high degree of entanglement, varying from 100 µm to several hundreds of micrometers, respectively. It was basically due to their high aspect ratio and van der Waals forces. In addition, straight tubes were hardly observed and the ends of the pristine nanotubes appeared to be carbon protective caps (Figure 4.1 b). Both tips of MWCNTs usually have closed and the ends are capped by dome-shapped half fullerene molecules which help in closing of the tube at the two ends. Basically, the commercial pristine MWCNTs are synthesized by chemical vapour deposition (CVD) containing carbonaceous impurities and metal catalyst particles (Djokić et al., 2014, Kumar and Ando, 2010). In CVD processing, a substrate was prepared and processed using a layer of metal catalyst particles (i.e. cobalt, and manganese) in combination with a catalyst support such as MgO or $Al_2O_3$ to develop the surface area for the higher by-product of the catalytic reaction of pure carbon. Depending on the adhesion and attachment between the substrate and the catalyst particle, the catalyst can remain at the nanotube base during growth and expansion. Thus, after the treatment with concentrated $HNO_3$, the tube length of MWCNTs considerably became shorter and the functional groups of carboxyl groups were formed along the sidewalls (Liang et al., 2016). The treatment of MWCNTs with strong acid causes severe etching of the graphitic surface of the material, leading to tubes in shorter length with a large population of disordered sites.

From Figure 4.1(c), it can be observed that the purified MWCNTs were interwined with each other and an individual of MWCNTs showed a tubular-like structure with an average diameter of 20 nm (Datsyuk et al., 2008, Karimifard and Moghaddam, 2016) Liu, Gao, Sun & Wang, 2010 (Liu et al., 2010). As shown in Figure 4.1(d), the chemical modification leads to the removal of catalyst from the carbon nanotubes and the opening of the tube caps (red circle), followed by an oxidative etching along the walls with the concomitant release of carbon dioxide. The final products are nanotube fragments where ends and sidewalls are decorated with an oxygen containing groups (mainly carboxyl groups) (Datsyuk et al., 2008,Tseng et al., 2010, Wepasnick et al., 2011). During the purification, the tips of MWCNTs are opened up, and followed by producing defects at the MWCNTs neck. Amorphous and metal particles (including those entrapped between MWCNTs layers) are dissolved by acid and leave defect on the MWCNTs sidewall. Those defects are then being oxidized and attached by carboxyl groups (Figure 4.2) (Atieh et al., 2011). TEM analysis (Figure 4.1(e)) shows the purified MWCNTs exhibited long and straight tubular structure. Furthermore, MWCNTs consist of two or more concentric cylindrical shells of graphene sheets coaxially arranged around a hollow core with van der Waals forces between the adjacent layers.

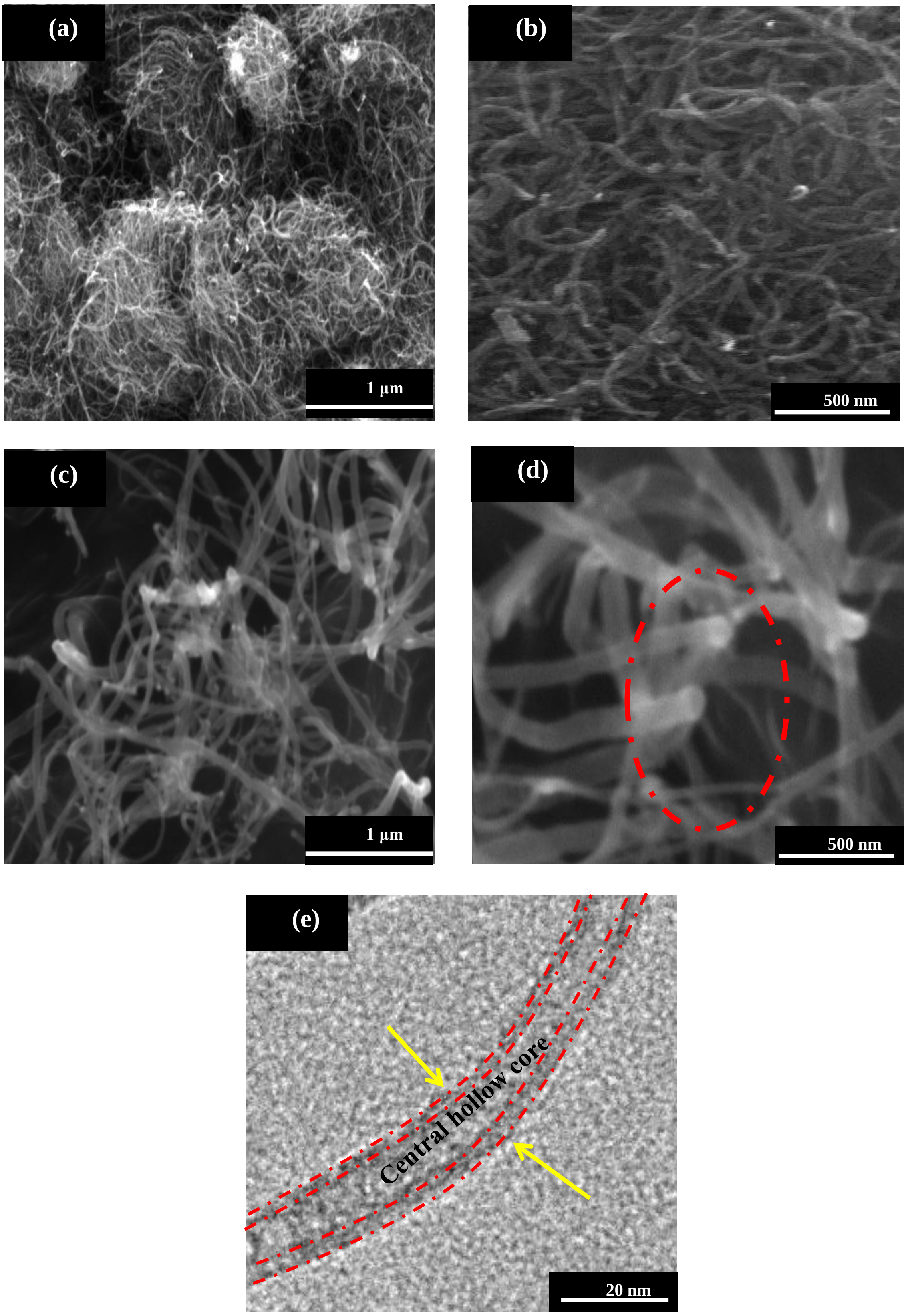

**Figure 4.1:** FESEM images of Pristine MWCNTs (a) low magnification and (b) high magnification, Purified MWCNTs with (c) low magnification and (d) high magnification, and (e) TEM image of Purified MWCNTs

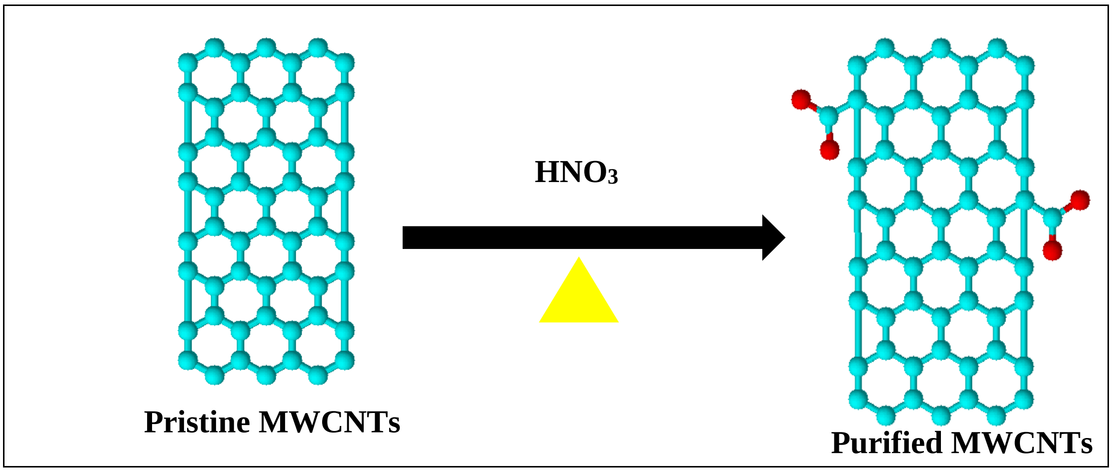

**Figure 4.2:** Pre-treatment oxidation of MWCNTs at 100 °C for 2h (Atieh et al., 2010)

The quantitative elemental analysis of pristine MWCNTs and purified MWCNTs was carried out by FESEM-EDX at a three different spot on the catalsyst. The presence of C, O, Mg, Al, Mn and Co elements in pristine MWCNTs are because of the MWCNTs were synthesized through a catalytic (CVD) method where a layer of metal catalyst particles (i.e. nickel, cobalt, and manganese) in combination with a catalyst support such as MgO or $Al_2O_3$ for producing higher by-product of the catalytic reaction of pure carbon (Tseng et al., 2010). It is necessary to remove these impurities as these residual metal-oxide particles significantly decrease their adsorption efficiency. The critical drawbacks of CNTs in many applications are because of the poor dispersibility and bundling between CNTs as affected by the attractive van der Waals interactions among themselves. On the other hand, only C and O presented in purified MWCNTs and no other trace impurities were found. The weight percentage of each element was presented in Table 4.1.

**Table 4.1**: EDX elemental analysis (Weight %) of Pristine MWCNTs and Purified MWCNTs

| Element | Pristine MWCNTs (wt%) | Purified MWCNTs (wt%) |
|---|---|---|
| C | 91.77 | 93.58 |
| O | 6.67 | 6.42 |
| Mg | 0.36 | - |
| Al | 0.43 | - |
| Mn | 0.41 | - |
| Co | 0.37 | - |

#### 4.1.1.2 FT-IR spectra

Figure 4.3 depicts the FT-IR spectra of pristine MWCNTs and purified MWCNTs. It can be seen that the pristine MWCNTs show two broad peaks at 3445 and 1563 cm $^{-1}$, which ascribed to the O-H stretch of the hydroxyl group and the carboxylate anion stretch mode. Meanwhile, the IR spectra of purified MWCNTs show the seven major peaks, located at 3759, 3425, 2914, 2388, 1724, 1575 and 1087 cm$^{-1}$. The peak at 3759 cm$^{-1}$ is associated with the free hydroxyl groups while the peak at 3425 cm$^{-1}$ is attributed to the O-H stretch from carboxyl groups (O=C-OH and C-OH). In addition, the peak at 2914 cm$^{-1}$ (Figure 4.3b) is attributed to the H-C stretch modes of H-C=O in the carboxyl group. Meanwhile, the peak at 2388 cm$^{-1}$ is assigned to hydrogen bonding due to the COOH groups present. The addition of $HNO_3$ leads to the formation of a carboxyl group (1724 cm$^{-1}$) in purified MWCNTs due to the oxidation of some carbon atoms on the surfaces of the MWCNTs (Ahmed et al., 2013). The broad peak at 1085 cm$^{-1}$ is assigned to the C-O stretching vibration indicated –COOH is introduced onto the surface of MWCNTs. The purified MWCNTs are treated with concentrated acid and the catalytic metals are possibly eliminated during the purification process with the cutting of the nanotube cap (Datsyuk et al., 2008, Karimifard and Moghaddam, 2016, Tseng et al., 2010).

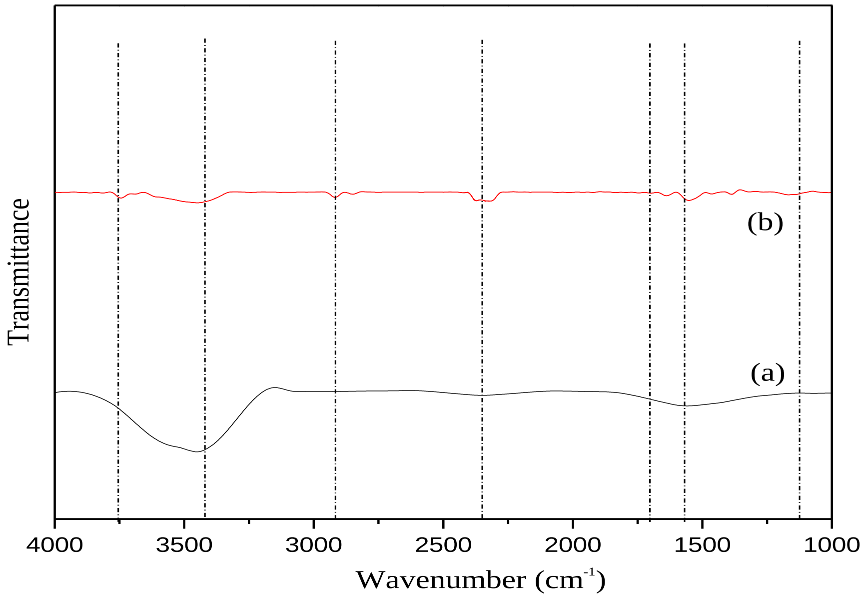

**Figure 4.3:** FTIR spectra for the (a) Pristine MWCNTs and (b) Purified MWCNTs

### 4.1.1.3 Raman analysis

The Raman spectra of the pristine and purified MWCNTs are shown in Figure 4.4. The changes in the surface chemistry of the MWCNTs before and after the acid treatment were also examined from the Raman shifts. Both sample spectra exhibit two characteristic bands: D-band ~1338 cm$^{-1}$ (sp$^2$ carbon consists of impurities or other symmetry-breaking defects) and G-band ~1580 cm$^{-1}$ (high degree of ordering and well-structured carbon based structures), respectively (Turgunov et al., 2014, Yudianti et al., 2011). From the results presented in Figure 4.4 (b), one can observe that intensity of the D band in the acid treated MWCNTs increased due to the purification leads to a high density of defects on the tube walls. The purification of MWCNTs typically involves oxidation using acids, causing carboxyl groups to functionalize the defects at the end of the MWCNTs. Those defects are oxidized and carboxyl groups are attached on MWCNTs. Additionally, the left shift of the Raman response of the purified MWCNTs can be ascribed to the electron transfer from the MWCNTs to the covalently attached functional groups on the CNTs surface. It is also revealed that upshifting of the G-band occurs during the acid treatment step when the electrons are transferred from the MWCNTs to the covalent bonded (-COOH) groups on the MWCNTs surface. The purification of MWCNTs can be divided into two categories based on the type of bonds, namely non-covalent or covalent bonding between the CNTs and the functional groups. The covalent bonding depends on the chemical reaction between the carbon atoms of CNTs and conjugation of hydrophilic organic molecules on the surface of CNTs. The chemical treatment of pristine MWCNTs with most widely used strong oxidative agents (concentrated $HNO_3$) generates the oxygenated groups such as carboxylic at “end and defects” sites and side walls of CNTs. An indication of the quality of CNTs and the chemical modification of MWCNTs or degree of “graphitization” can be depicted by the D and G mode intensity ratio ($I_D/I_G$) (Edwards et al., 2011). In addition, the extents of defects and impurities in the CNTs can also be indicated by the ratio of intensities of the characteristic peaks ($I_D/I_G$). The $I_D/I_G$ ratio decreases in the case of the purified samples which are mainly attributed to the removal of amorphous carbon from pristine MWCNTs and these results demonstrate the amount of defects and other carbonaceous phases are reduced. The treatment with nitric acid, while producing functional carboxylic groups, the amorphous carbon are being generated by shortening the MWCNTs and, causing increase in both the defects sites (Paunović et al., 2009, Turgunov et al., 2014, Yudianti et al., 2011).

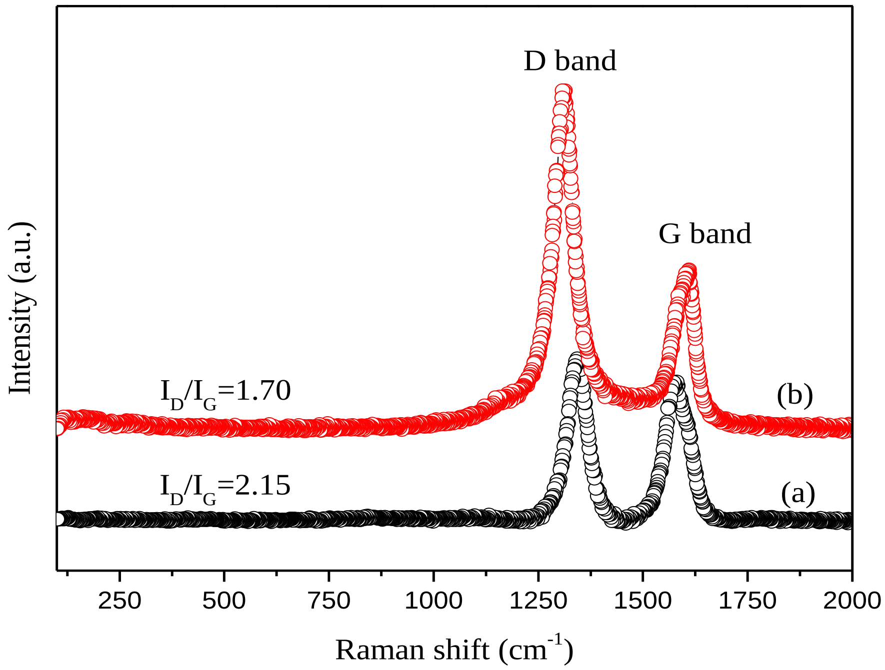

**Figure 4.4:** Raman spectra for the (a) Pristine MWCNTs and (b) Purified MWCNTs

#### 4.1.1.4 Summary

This study investigated the purification of MWCNTs in acid solutions in order to remove the carbonaceous impurities and metal catalyst particles on MWCNTs as proved by Energy Dispersive X-ray analysis. The presence of the only C and O elements after purification can also be determined by X-ray photoelectron spectroscopy as discussed further in Section 4.6. During the purification, the tips of MWCNTs are opened up and defects are produced at the MWCNTs neck. Amorphous and metal particles (including those entrapped between MWCNTs layers) are dissolved by acid and leave defect on the MWCNTs sidewall. Those defects are then oxidized and carboxyl groups are attached. It was necessary to remove these impurities as these residual metal-oxide particles significantly decrease their adsorption efficiency. The critical difficulty in applying CNTs for applications is because of the poor dispersibility and bundling between CNTs as affected by the attractive van der Waals interactions among themselves. During the acid treatment, the long nanotubes are broken into shorter ones and the opening of the tube caps as shown in the FESEM image, followed by an oxidative etching along the walls with the concomitant release of carbon dioxide which increased the available surface area associated with the CNTs edge planes. Moreover, the acid treatment also introduced the chemical groups on the MWCNTs surface as investigated by FTIR analysis which may facilitate the adsorption of organic pollutants and to be good supports to be decorated with nanoparticles. MWCNTs' surface groups take an important role in the way they link to $TiO_2$ and consequently, these functional groups are contributing to the formation of Ti-O-C bonds, as in esterification reactions between the carboxylic acid groups of MWCNTs and the hydroxyl groups existent at the surface of $TiO_2$ as being described in details in the section of the formation of MWCNTs/$TiO_2$ nanocomposites. Raman analysis further verified the increased of carbon defects on the purified MWCNTs due to length shortening after oxidation with nitric acid under reflux conditions. The amorphous carbon is generated by shortening the MWCNTs, causing an increase in both the defects sites. Therefore, it was necessary to carry out the purification of MWCNTs before it can be further added with titanium precursor for the synthesis of MWCNTs/$TiO_2$ nanocomposites.

## 4.2 $TiO_2$ Nanoparticles

The preparation methods of titania precursors as a form of sol or powder were diverse from article to article. Therefore, it is hard to compare the reported results in various articles and to tell the effect of control parameters explicitly. There are several factors in determining important properties in the performance of $TiO_2$ for photodegradation studies such as particle size, crystal phase as well as defect structures on its surface and in bulk. For example, the anatase crystal phase has been generally known for having a higher photoactivity than the rutile and brookite phase due to its better electronic and surface chemistry properties. The larger band gap of anatase $TiO_2$ reduces the light that can be absorbed which may raise the valence band maximum to higher energy levels relative to redox potentials of adsorbed molecules. Thus, the oxidation 'power' of electrons is increased and the electron is facilitated transfer from the $TiO_2$ to adsorbed molecules. Basically, the amorphous $TiO_2$ particles have no considerable photocatalytic activity due to many defects in the bulk. Among the various synthetic techniques, the sol-gel method provides a simple and easy way to prepare $TiO_2$ nanoparticles at low temperatures and excellent chemical homogeneity.

### 4.2.1 Characterizations of $TiO_2$ Nanoparticles

Based on the aforementioned discussion, $TiO_2$ nanoparticles were successfully synthesized via sol-gel techniques. Therefore, in the following studies, anatase $TiO_2$ nanoparticles were synthesized in the two steps: (i) the hydrolysis/ condensation and (ii) crystallization/ phase transformation to study the physicochemical properties of $TiO_2$ nanoparticles. The characterizations of $TiO_2$ nanoparticles were conducted to reveal their properties such as surface morphology, elemental composition, phase structure and optical property. This study will not focus much on the preparation parameters of $TiO_2$

nanoparticles but instead it would focus primarily on the use of the $TiO_2$ nanoparticles as a comparison with MWCNTs/$TiO_2$ nanocomposites in the next section.

#### 4.2.1.1 Formation of $TiO_2$ Nanoparticles

Sol-gel processing of $TiO_2$ nanoparticles has been extensively investigated, the hydrolysis of the titanium tetraisopropoxide (TTIP) combined with acetic acid and ethanol with subsequent annealing at 450 °C has led to the formation of anatase $TiO_2$ nanoparticles. Synthesis of anatase $TiO_2$ nanoparticles has been reported for a large variety of experimental conditions. According to literature, the phase pure anatase $TiO_2$ nanoparticles with diameters ranging from 6-30 nm are basically prepared from titanium (IV) isopropoxide and acetic acid with the optimal condition for calcination temperature of 450 °C. Typically, in sol –gel method, the sol-gel derived precipitates are amorphous in nature. Thus, it is required for further heat treatment to induce crystallization. In this work, anatase $TiO_2$ nanoparticles are formed by reaction in aqueous solutions of weak acids. The stronger acids used in the reactions gain a fraction of the products consists of brookite $TiO_2$ nanoparticles (Behnajady et al., 2011, Reyes-Coronado et al., 2008). Furthermore, the formation of rutile phase is promoted by higher acidity while the lower acidity leads to the formation of anatase phase (Ibrahim and Sreekantan, 2010). The sol-gel synthesis of $TiO_2$ nanoparticles can be described by an alcoholic permutation reaction, hydrolysis, and condensation of titanium alkoxides in aqueous media to form oxopolymers, which are transformed into a metal oxide. These reactions can be schematically represented in Equation (4.1-4.3) as follows:

**Alcoholic permutation**:

$$Ti(OR)_z + xR'(OH) \leftrightarrow Ti(OR)z\text{-}x(OR')x + xROH \qquad \textbf{(4.1)}$$

**Hydrolysis**:

$Ti(OR)_4 + 4H_2O \leftrightarrow Ti(OH)_4 + 4ROH$ **(4.2)**

**Condensation reactions**:

$Ti(OH)_4 \rightarrow TiO_{2x}H_2O + (2\text{-}x)H_2O$ **(4.3)**

During the hydrolysis, alkoxide was hydrolyzed with the presence of water results in a sol where the alkoxide groups (-OR) are replaced via the nucleophilic attack of the oxygen atom of a water molecule and give rise to the formation of a metal hydroxide. However, with the presence of an excess of water, the hydrolysis reaction can occur rapidly and completed within seconds; thus, alkoxides are usually diluted in ethanol prior to mix with water in order to moderate the high reactivity. The water to titanium molar ratio ($r=[H_2O]/[Ti]$) is important in determining the size, stability, and morphology of the sols produced from titanium alkoxides. Basically, the acid is used to restrain the hydrolysis process and consequently, to control the grain growth. The drying of the sol (heat treatment at 80 °C for 24 h) lead to gelation due to destabilization of the sols by evaporation of the alcohol. After drying, the yellowish transparent gels were obtained and this color is believed to be a result of the presence of alkoxy groups captured inside the gel (Mahshid et al., 2006, Nadzirah et al., 2015, Sayilkan et al., 2006).

#### 4.2.1.2 Surface Morphology and Elemental Analysis

Figure 4.5 shows the FESEM images of $TiO_2$ nanoparticles calcined in air at 450 ºC for 2 h. The calcination process is used to convert the amorphous structure of $TiO_2$ nanoparticles to the crystalline phase. It can be seen that the synthesized $TiO_2$ nanoparticles were spherical in shape with average size (15nm) and it showed that smaller particles likely to aggregate. The distance between the adjacent lattice fringes were found to be 0.35 nm (Figure 4.5(c)), which supported by the d-spacing of $TiO_2$ from HRTEM image was matched complementary with the d-spacing of $TiO_2$ lattice anatase plane in XRD result (Nadzirah et al., 2015, Valencia et al., 2010).

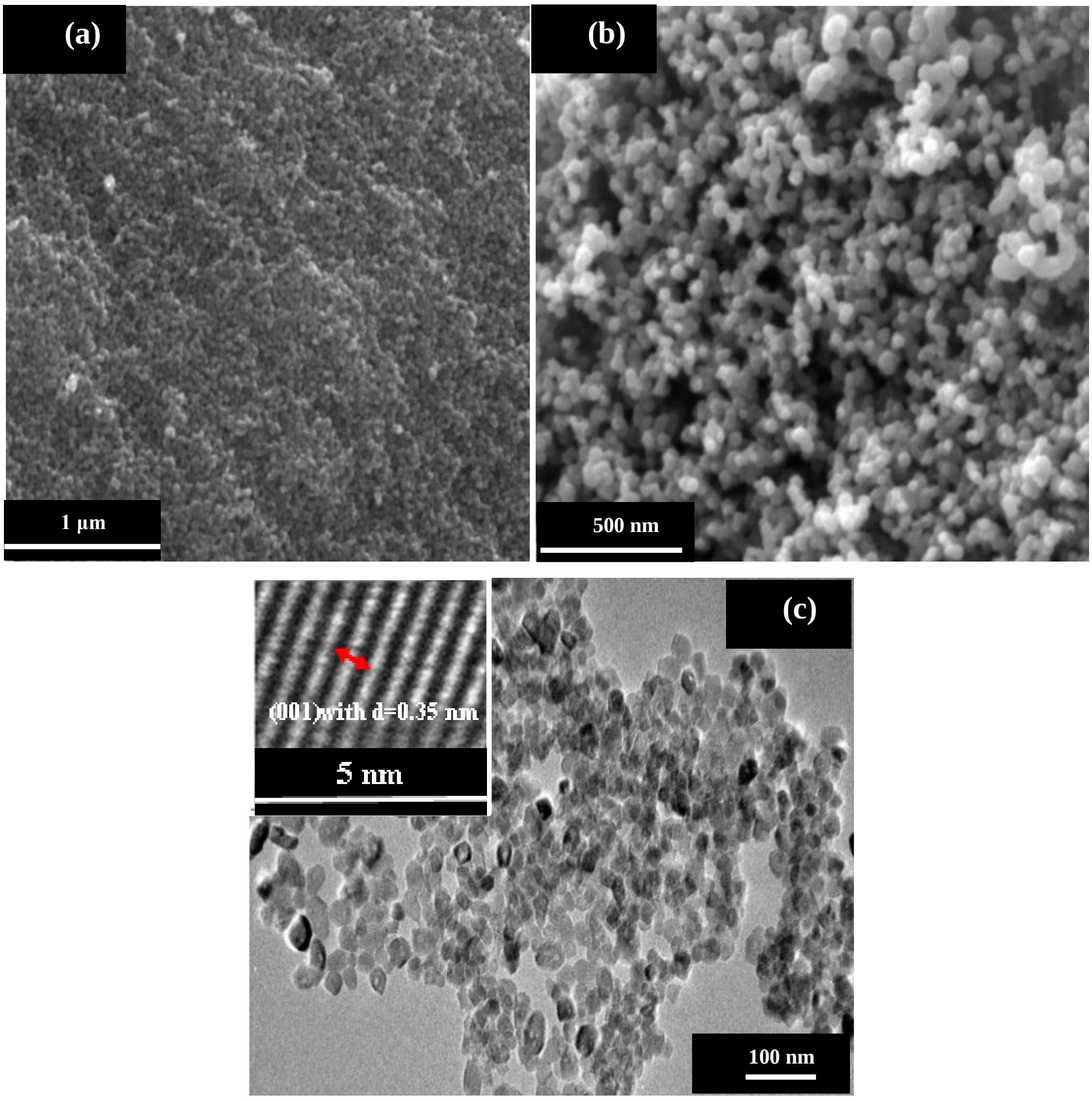

**Figure 4.5:** FESEM images of $TiO_2$ nanoparticles with (a) low magnification and (b) high magnification, and (c) HRTEM image of $TiO_2$ nanoparticles

The $TiO_2$ nanoparticles essentially remained stable after annealing at 450 °C for 2h in air. The elemental composition and distribution of the nanoparticles were visualized using EDX mapping as shown in Figure 4.6, which shows the typical mapping images of titanium and oxygen, confirming the presence of Ti and O element. The elemental mapping images indicate that Ti and O are evenly distributed on the spherical surface of

$TiO_2$ nanoparticles. The EDX was employed to estimate the relative compositions in $TiO_2$ nanoparticles. Although the EDX data are not completely reliable due to several factors such as surface, elements, and the specimen features, however, a reasonable reliable elemental composition particularly for insoluble inorganic materials like $TiO_2$ are provided by the technique (Yoo et al., 2016). Weight percentages of Ti and O of the $TiO_2$ nanoparticles were obtained directly from the EDX data based on the spot of three different area of the sample.

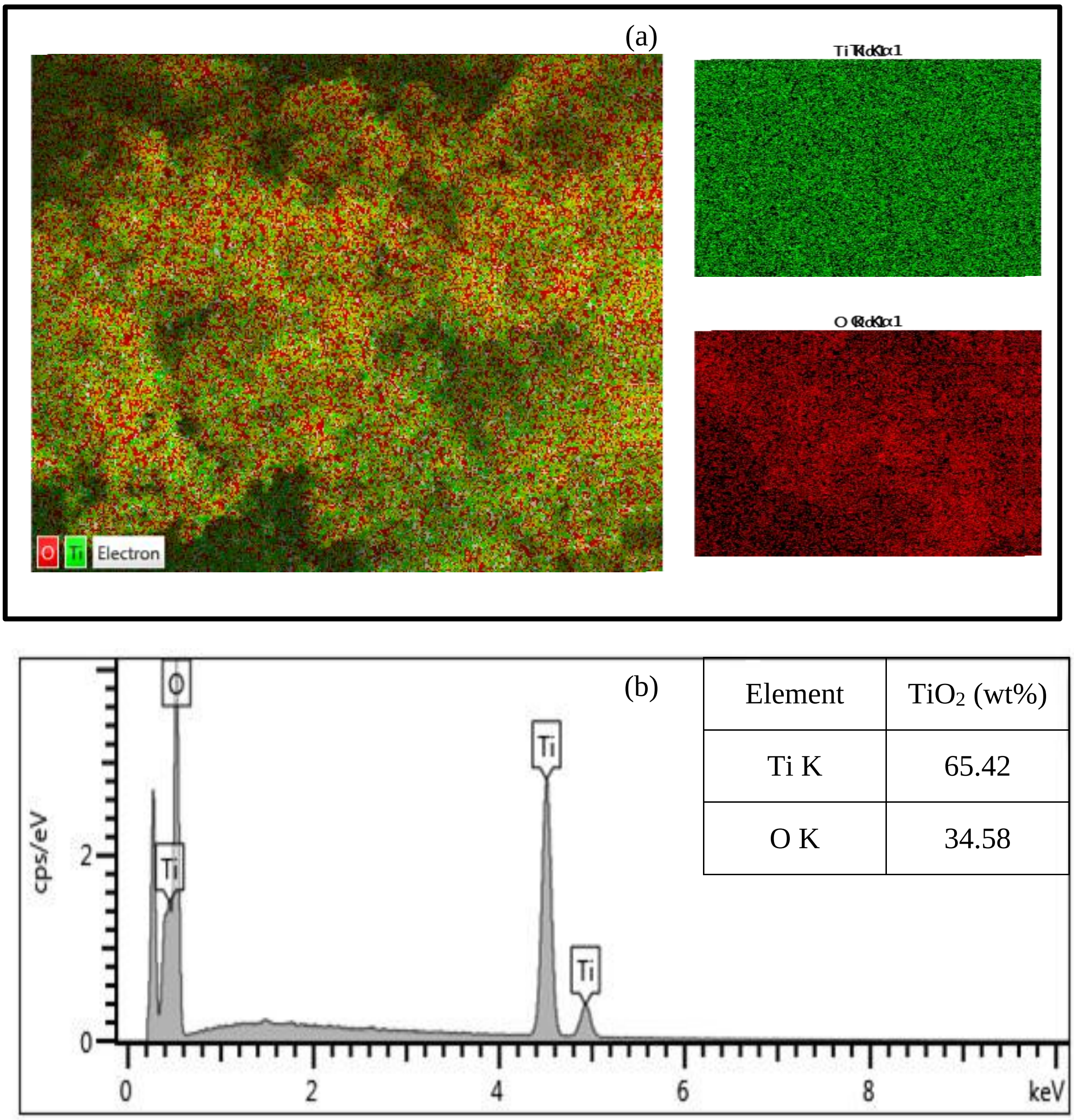

| Element | $TiO_2$ (wt%) |
|---|---|
| Ti K | 65.42 |
| O K | 34.58 |

**Figure 4.6**: (a) Elemental mapping and (b) EDX spectrum and composition of $TiO_2$ nanoparticles (calcined in air at 450 °C for 2h)

#### 4.2.1.3 Phase Structure and Raman analysis

According to literature, the preparation of the phase pure anatase $TiO_2$ nanoparticles with diameters ranging from 6-30 nm from titanium (IV) isopropoxide and acetic acid with the optimal condition for calcination temperature of 450 °C (Reyes-Coronado et al., 2008). The XRD patterns for annealing $TiO_2$ nanoparticles at 450 °C for 2 h under air condition are shown in Figure 4.7. The calcination process is used to convert the amorphous structure of $TiO_2$ nanoparticles to crystalline phase. The characteristic peaks in the pattern at 25.2 (101), 37.9 (004), 48.3 (200), 53.9 (105), 55.0 (211), 62.7 (204), 68.9 (116), 70.1 (220) and 75.5 (215) are corresponding to $TiO_2$ crystalline anatase phase, compatible with those shown in the JCPDS No. 21-1272. The crystallite size of the $TiO_2$ was calculated by the well-known Scherer's formula. The calculation is based on the measurement of full-width at half-maximum (FWHM) values in the corresponding XRD pattern. In the present study, the crystallite size of the $TiO_2$ prepared by sol-gel technique was found to be 12.9 nm which is smaller than the particle size determined. This is because one particle can be constituted by several crystalline domains and thus, this explained why particle size was normally bigger than the crystallize size (Hamid et al., 2014).

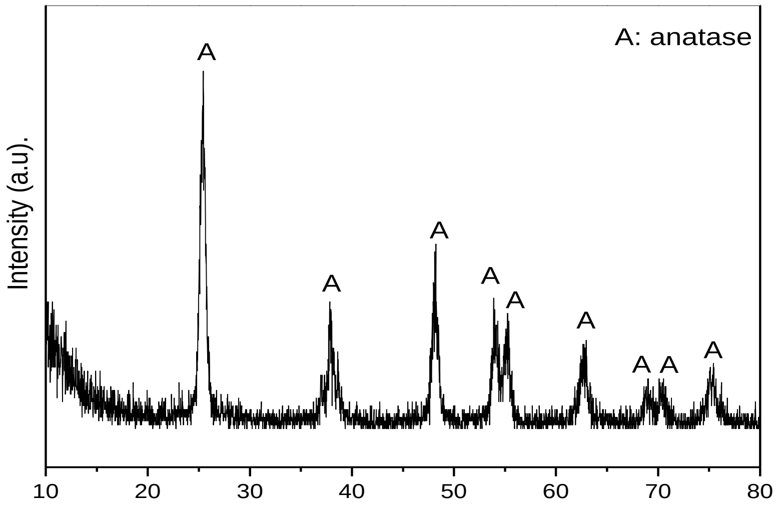

**Figure 4.7:** XRD spectra of $TiO_2$ nanoparticles calcined in air at 450 °C for 2 h

The Raman spectra of $TiO_2$ nanoparticles are shown in Figure 4.8. Bulk anatase has tetragonal structure (space group *$I4_1/ amd$*) containing twelve atoms per unit cell with lattice parameters a= 3.784 Å and c= 9.514 Å. The existence of 15 optical modes can be indicated via factor group analysis with the following irreducible representation of normal vibrations: $1A_{1g} + 1A_{2u} + 2B_{1g} + 1B_{2u} + 3E_g + 2E_u$. The modes of $A_{1g}$, $B_{1g}$, and $E_g$ are Raman active and those of $A_{2u}$ and $E_u$ are infrared active. According to factor group analysis, anatase $TiO_2$ has five Raman active modes (141.85, 198.15, 396.53, 517.12 and 641.86 $cm^{-1}$) in Raman spectrum indicates the presence of anatase mode as $E_{g\ (1)}$, $E_g$, $B_{1g\ (1)}$, $A_{1g}$ and $E_{g(2)}$ respectively. The Raman results further confirm the presence of anatase phase in the sample (Hamid et al., 2014, Sekiya et al., 2001).

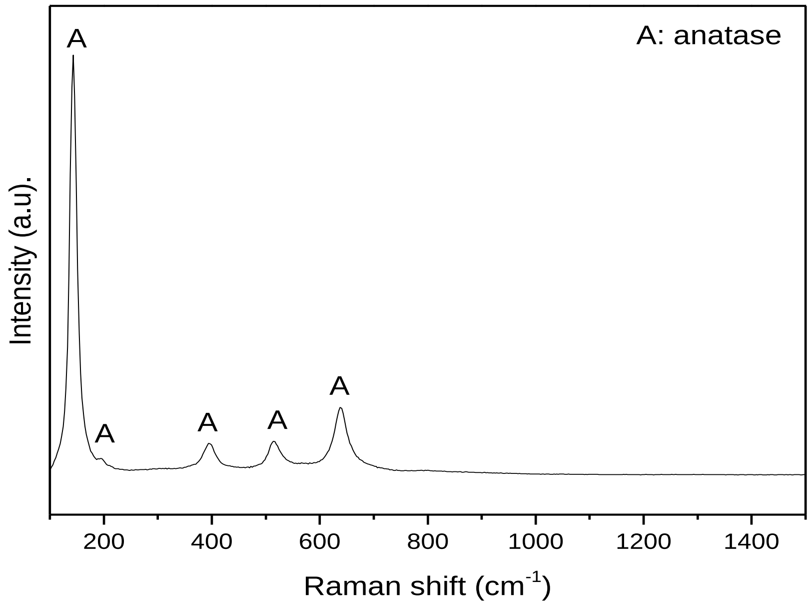

**Figure 4.8:** Raman spectra of $TiO_2$ nanoparticles calcined in air at 450 °C for 2 h

### 4.2.1.4 Optical properties

For the study of the optical properties of the synthesized $TiO_2$ nanoparticles, the band gap and the type of electronic transitions were determined. When $TiO_2$ absorbs photon of energy larger than the gap of the semiconductor, an electron is transferred from the valence band to the conduction band where there occurs an abrupt increase in the absorbency of the material to the wavelength corresponding to the band gap energy. The optical properties of the $TiO_2$ nanoparticles are shown in Figure 4.9. A typical absorption with an intense transition in the UV region of the spectra have been shown in the sample, therefore indicating the intrinsic band gap absorption of $TiO_2$ due to the electron transitions from the valence band into the conduction band ($O_{2p} \rightarrow Ti_{3d}$). The valence band mainly consist of O 2p states and a few Ti 3d states, indicating the strong p-d hybridizations between O 2p and Ti 3d states, which form bonding states in the valence band region. Moreover, the conduction bands are primarily consisting of Ti 3d states, mixed with a few O 2p and Ti 3p states. The hybridization broadens the valence bands and the transfers of photogenerated holes are promoted. The optical band gap of $TiO_2$ was determined by using the Kubelka-Munk expression with the transformation of diffuse reflectance spectra. The majority of authors have determined that in $TiO_2$ the anatase has an indirect band gap. The estimated band gap of anatase $TiO_2$ was 3.23 eV (Hamid et al., 2014, López and Gómez, 2012).

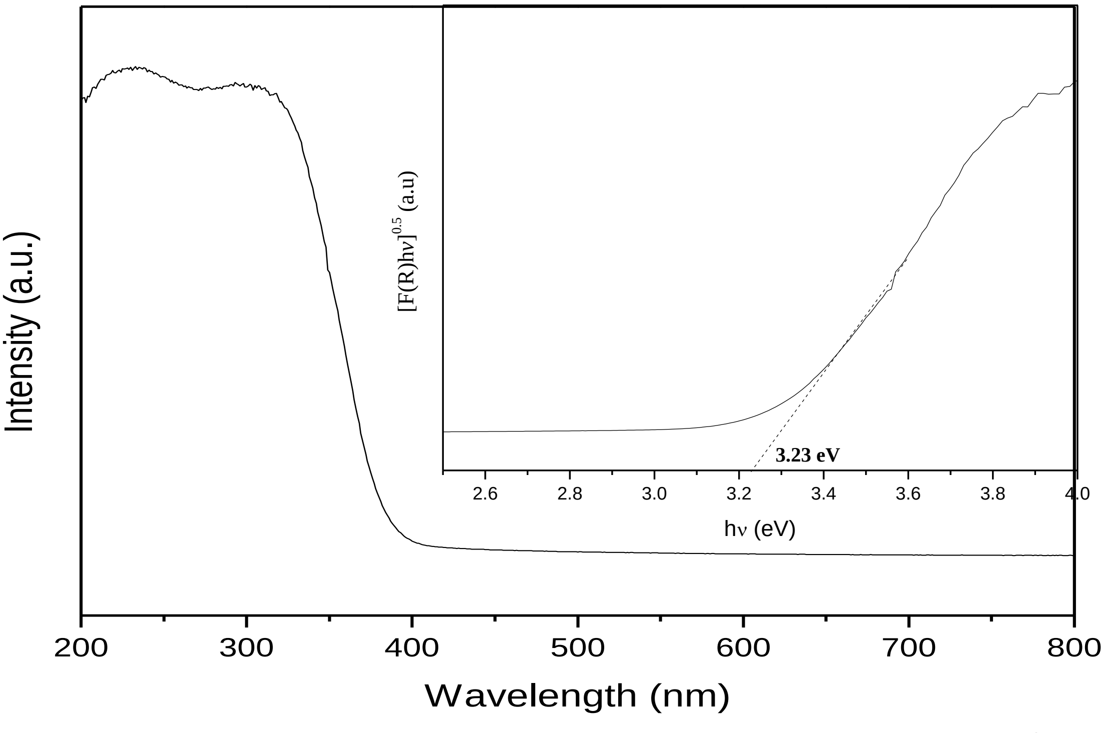

**Figure 4.9:** UV-vis diffuse reflectance spectra (Inset is a variation of $(\alpha h\nu)^2$ versus photon energy (hν) of $TiO_2$)

#### 4.2.1.5 Summary

Single phase anatase $TiO_2$ nanoparticles were successfully synthesized using the simple sol-gel technique by the hydrolysis of titanium-isopropoxide alcoholic solution. The results of the characterization of the $TiO_2$ nanoparticles by FESEM and HRTEM demonstrated that $TiO_2$ nanoparticles with spherical-shaped anatase form were obtained and it showed that smaller $TiO_2$ particles likely to aggregate. The XRD and Raman analysis shows that well-crystallized anatase $TiO_2$ obtained at 450 °C. Basically, the amorphous $TiO_2$ particles have no considerable photocatalytic activity due to many defects in the bulk. Thus, it is required for further heat treatment to induce crystallization. Generally, anatase displays much higher photocatalytic activities than both rutile and brookite. Although anatase has lower absorbance ability towards solar light than rutile due to the larger band gap than of rutile, the photocatalytic activity of anatase is obviously superior to that of rutile. The calculated band gap energy of anatase $TiO_2$ nanoparticles from the UV-DRS analysis has been found to be 3.23 eV. Indirect band gap anatase exhibits a longer lifetime of photoexcited electrons and holes than direct band gap rutile and brookite because the direct transitions of photogenerated electrons from the conduction band to valence band is impossible. Furthermore, anatase has the lightest average effective mass of photogenerated electrons and holes as compared to rutile and brookite. The lightest effective mass suggests the fastest migration of photogenerated electrons and holes from the interior surface of anatase $TiO_2$ nanoparticles, thus resulting in the lowest recombination rate of photogenerated charge carriers within anatase $TiO_2$. The structural, electronic and morphology properties of the synthesized anatase $TiO_2$ nanoparticles as well as its photocatalytic activity are bringing forward to compare with the synthesized MWCNTs/$TiO_2$ nanocomposites in the following section.

## 4.3 The Effect of MWCNTs loading

In the present study, MWCNTs/$TiO_2$ nanocomposites were fabricated using modified sol-gel technique. To the best of our knowledge, reports on the effect of MWCNTs loading on $TiO_2$ and its photocatalytic performance on DMPEs are not available. Therefore, the first part of the present study aims to determine the optimum MWCNTs loading in order to achieve the desired MWCNTs/$TiO_2$ nanocomposites for the high efficient photocatalytic performance. In addition, detailed studies on physicochemical properties of MWCNTs/$TiO_2$ nanocomposites via modified sol-gel method for photodegradation of DMPEs are lacking too. Thus, the current study aims to obtain the desired MWCNTs with a suitable amount of MWCNTs for the best photocatalytic performance.

### 4.3.1 Characterizations of MWCNTs/$TiO_2$ nanocomposites

The characterizations of the effect of various MWCNTs loading on MWCNTs/$TiO_2$ nanocomposites were conducted to reveal their properties such as surface morphology, elemental composition, phase structure and optical properties. Different amounts of MWCNTs had different effects on photodegradation efficiency which highly depend on the significant role of MWCNTs and the intimate contact between MWCNTs and $TiO_2$ nanoparticles.

#### 4.3.1.1 Surface Morphology and Elemental Analysis

The ratio of $TiO_2$ nanoparticles on MWCNTs is controlled by the initial concentrations of the metal ions. The mass ratio of MWCNTs and $TiO_2$ plays an important role in the combination of MWCNTs with $TiO_2$ in the way they link to $TiO_2$ nanoparticles and consequently, in the electronic and photocatalytic performance of the MWCNTs/$TiO_2$ composite. Figure 4.10 (a-d) shows the FESEM images of MWCNTs/$TiO_2$ nanocomposites with different weight percentage (3 wt to 15 wt %) of MWCNTs to $TiO_2$. All samples displayed that the incorporation of $TiO_2$ nanoparticles onto the surface of MWCNTs.

Generally, the synthesis method involving three main steps: i) The oxidation treatment of MWCNTs with concentrated $HNO_3$ introduced negative charged functionality –COOH onto the surface of MWCNTs; (ii) The hydrolysis of titanium isopropoxide produce titanium ions that adsorb on the surface of MWCNTs. The formation of Ti-O-C bonds between the carboxylic acid groups of MWCNTs and the hydroxyl groups existent at the surface of $TiO_2$ during an esterification reactions, contribute to a synergistic effect due to the creation of an electronic interphase interaction between MWCNTs and $TiO_2$ phases and iii) The formation of anatase $TiO_2$ nanoparticles on the surface of MWCNTs after the heat treatment. The heat treatment process is used to convert the amorphous structure of $TiO_2$ nanoparticles to crystalline anatase phase (Da Dalt et al., 2013, Gui et al., 2014b, Kim et al., 2012, Zhao et al., 2013).

As mentioned previously, the $TiO_2$ nanoparticles may undergo aggregation due to the instability of the nanosized particle and their dangling bonds. Additionally, it is worth mentioning that the high ratio of $TiO_2$ would result in the agglomerating of the nanoparticles on the nanotubes. From Figure 4.10 (a), it can be observed that large agglomeration of $TiO_2$ nanoparticles was formed on the surface of MWCNTs indicated that $TiO_2$ nanoparticles do not have close contact with the surface of MWCNTs. With the increasing amount of MWCNTs up to 10 wt-%, the smaller sizes of $TiO_2$ nanoparticles were attached on the surface of MWCNTs with less agglomeration. The uniformity of the $TiO_2$ varies according to the preparation method and the surface reactions between CNTs with $TiO_2$ nanoparticles. 10 wt-% of MWCNTs/$TiO_2$ nanocomposites showed a complete coverage of the MWCNTs by $TiO_2$ nanoparticles. In this manner, the role of MWCNTs acts as a “dispersing template or support” for photocatalytically active materials to form MWCNTs/$TiO_2$ composite photocatalyst. Basically, the functional groups present on the surface of MWCNTs promote the anchoring of the $TiO_2$ nanoparticles as well as avoiding agglomeration and subsequently increasing the surface area of the resulting MWCNTs/$TiO_2$ composite. However, non-uniform and large agglomerations of clumpy $TiO_2$ structure were spotted with 15 wt-% of MWCNTs/$TiO_2$ nanocomposites. This was probably due to the excessive loading of MWCNTs during the synthesis process. The excess amount of MWCNTs may cause aggregation of $TiO_2$ grains as the crystallinity of the $TiO_2$ decrease which may inhibit the transport of electrons and increase the probability of electron trapping by the crystal defects (Hamid et al., 2014, Kim et al., 2012, Zhao et al., 2013).

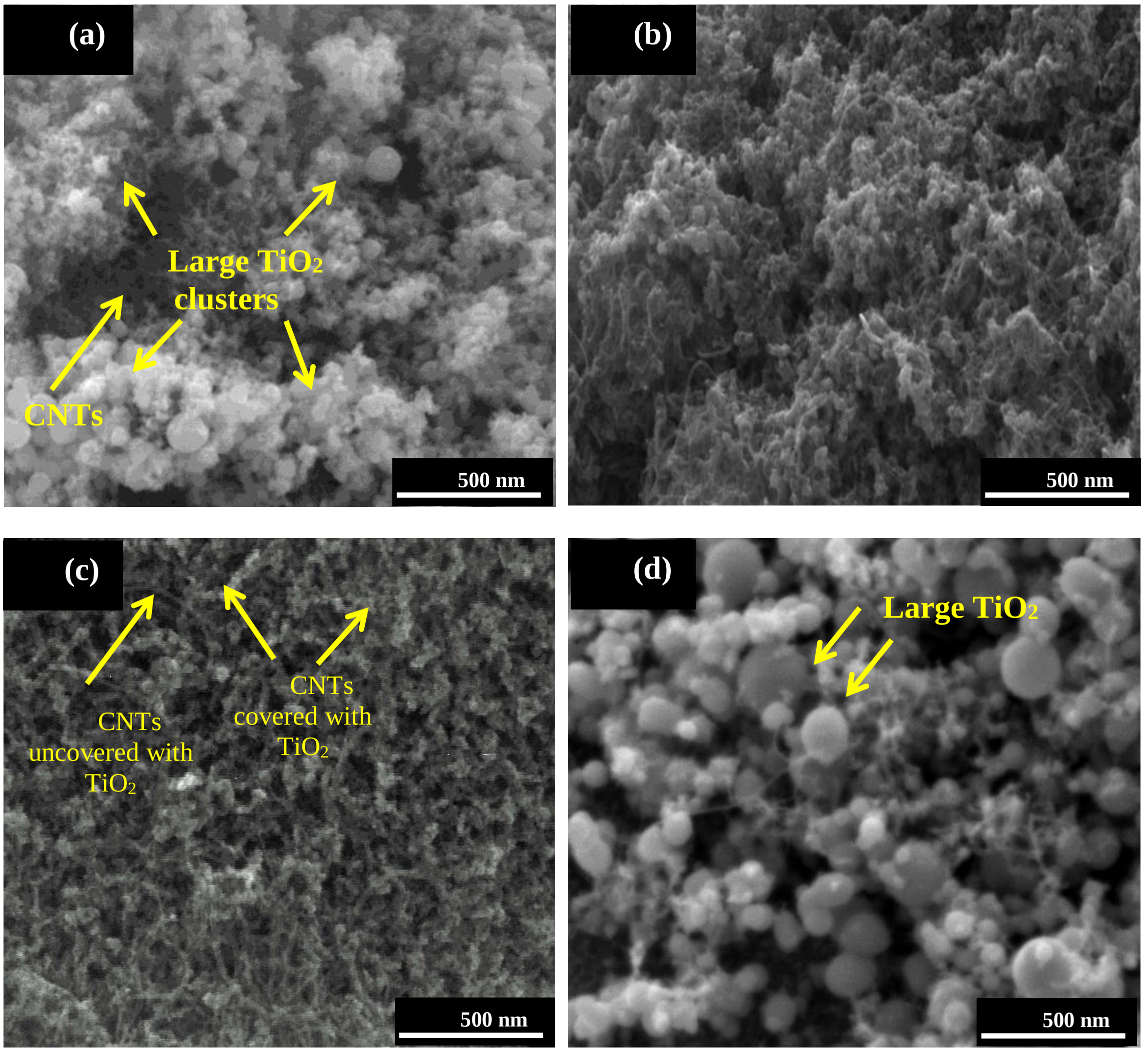

**Figure 4.10:** FESEM images of (a) 3 wt%, (b) 5 wt%, (c) 10 wt % and (d) 15 wt % of MWCNT/$TiO_2$ nanocomposites

TEM images of (3-15 wt-%) of MWCNTs/$TiO_2$ nanocomposites was displayed in Figure 4.11. It was observed that the formation of non-uniform and bigger agglomeration of $TiO_2$ clusters was formed with 3 wt-% and 5 wt-% MWCNTs/$TiO_2$ nanocomposites, respectively. On the other hand, 10 wt-% MWCNTs/$TiO_2$ nanocomposites unveiled the relatively uniform $TiO_2$ nanoparticles wrapping the entire surface of MWCNTs, indicating the intimate interaction between the MWCNTs and $TiO_2$. Furthermore, more MWCNTs appears that displays favorable electrostatic interactions that prevent agglomeration of $TiO_2$ particles, increase interactions between

$TiO_2$ and MWCNTs, thereby promoting reasonably good dispersion. A good dispersion of $TiO_2$ nanoparticles in the MWCNTs/$TiO_2$ composite attributed to the functionalization of MWCNTs with nitric acids leads to the creation of large amounts of carboxylic acid and phenol groups at the surface of the MWCNTs. MWCNTs provide large number of nucleation centers available on its surface for receiving the nanoparticles and preventing their agglomeration. However, the agglomeration of the bulk $TiO_2$ nanoparticles on the surface of MWCNTs was found in 15 wt-% of MWCNTs/$TiO_2$ nanocomposites due to an excessive amount of MWCNTs. Figure 4.11 (e) is a high magnification of the 10 wt % of $TiO_2$/MWCNTs which shows the obtained composites comprise of small spherical $TiO_2$ nanoparticles with less apparent aggregation of MWCNTs. The crystallographic morphology and crystal structure of the composites can be investigated through the measurement of the lattice fringe by HRTEM analysis in Figure 4.11 (f). The good contact between MWCNTs and $TiO_2$ nanoparticles can be confirmed by HRTEM image.The anatase (101) phase of $TiO_2$ nanoparticles in MWCNTs/$TiO_2$ nanocomposites is confirmed with the lattice spacing of 0.35 nm while the (002) graphitic plane of the MWCNTs is assigned with the lattice spacing of 0.33 nm, revealing the heterojunction between MWCNTs-$TiO_2$ (Kuvarega et al., 2012, Oh et al., 2009, Saleh and Gupta, 2012, Tian et al., 2011, Xia et al., 2007).

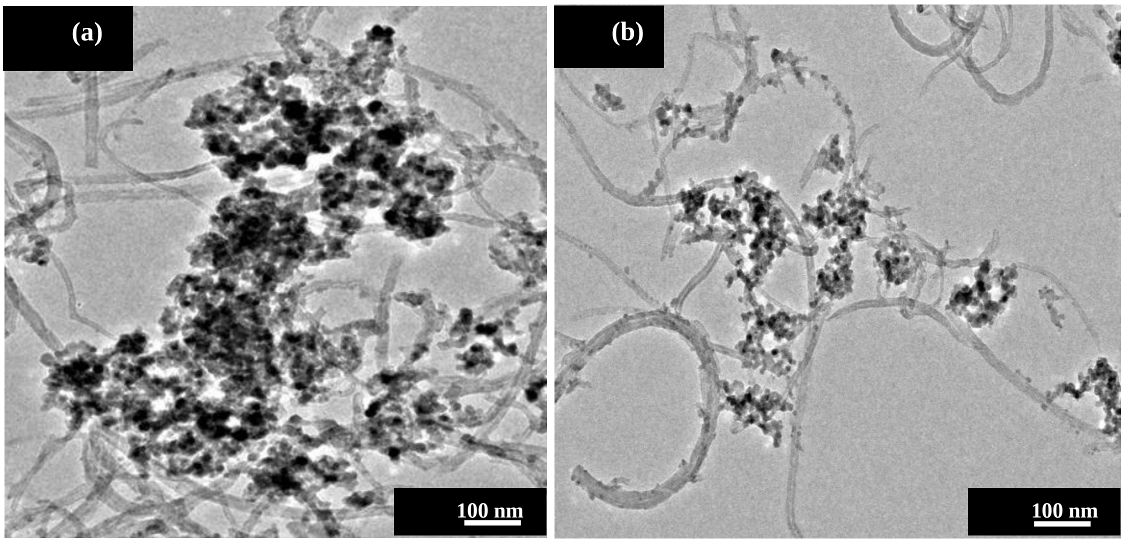

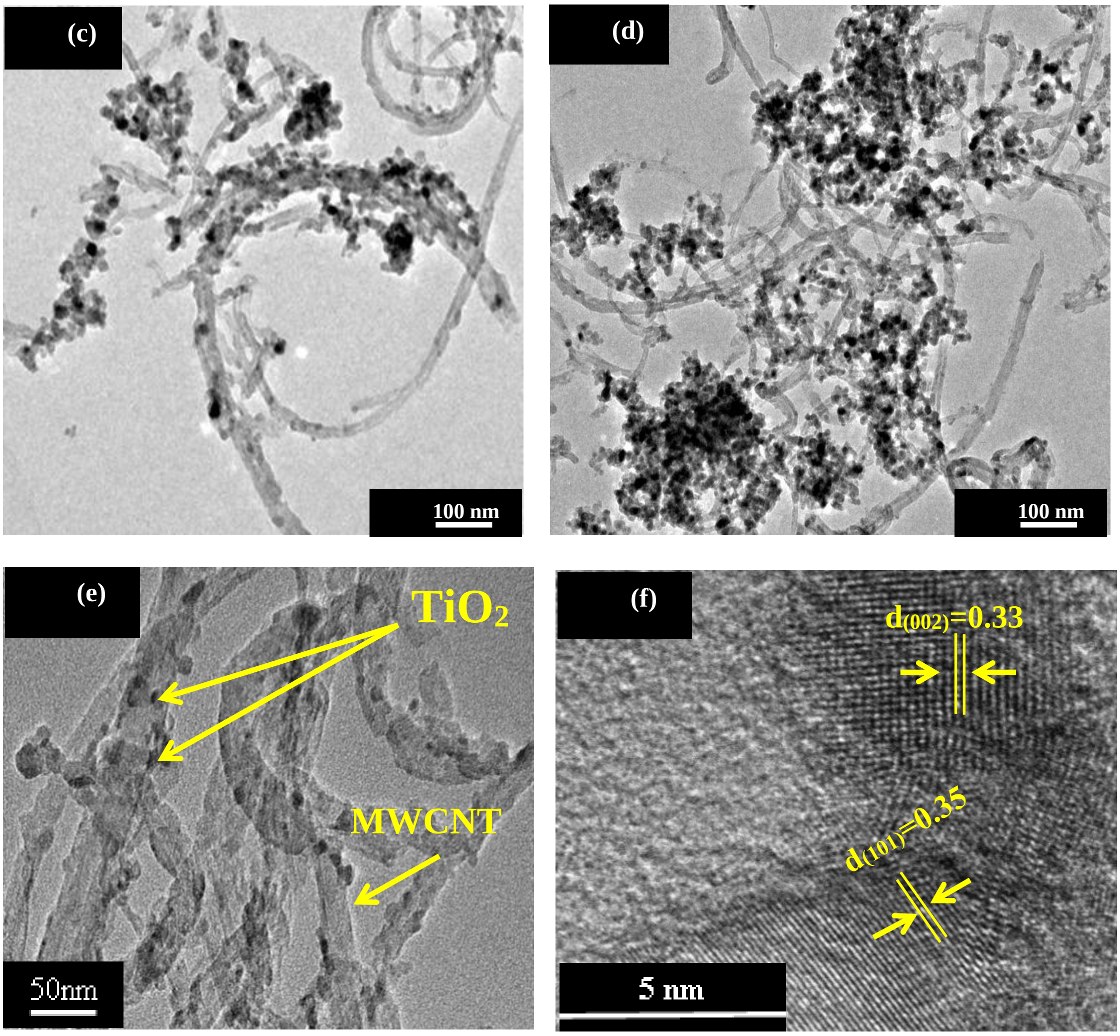

**Figure 4.11:** HRTEM images of (a) 3 wt%, (b) 5 wt%, (c) 10 wt % and (d) 15 wt % of MWCNT/$TiO_2$ nanocomposites, (e) high resolution of 10 wt % of MWCNT/$TiO_2$ and (f) lattice fringe of MWCNT/$TiO_2$ nanocomposites

The elemental composition of MWCNTs/$TiO_2$ nanocomposites prepared with different MWCNTs loadings was determined. The weight percent of Ti, C and O are tabulated in Table 4.2. From the table, all of the MWCNTs/$TiO_2$ nanocomposites showed the presence of Ti, C and O elements. The EDX data confirm that the carbon weight percentage in the samples increased and the amount of Ti decreased with an increasing loading of MWCNTs in the MWCNTs/$TiO_2$ nanocomposites.

**Table 4.2**: Elemental composition of (a) 3 wt %, (b) 5 wt %, (c) 10 wt % and (d) 15 wt % of MWCNTs/ $TiO_2$ nanocomposites

| **Element** | **3 wt % MWCNTs/$TiO_2$** | **5 wt % MWCNTs/$TiO_2$** | **10 wt % MWCNTs/$TiO_2$** | **15 wt % MWCNTs/$TiO_2$** |
|---|---|---|---|---|
| Ti | 61.68 | 60.38 | 56.87 | 49.52 |
| O | 35.34 | 36.35 | 35.08 | 34.52 |
| C | 2.97 | 5.27 | 10.05 | 15.96 |

The elemental distributions of the lower weight % of MWCNTs and higher weight % of MWCNTs on MWCNTs/$TiO_2$ nanocomposites were obtained using EDX mapping (Figure 4.12). The EDX mapping was carried out on these two samples to illustrate the obvious distribution between MWCNTs and $TiO_2$. The bright field image of Ti K-edge, O K-edge and C K-edge was shown in the below images respectively. It can be seen that the Ti, O and C signals are determined throughout the nanocomposites. With the increasing amount of MWCNTs in nanocomposites, the areas of the spectrum were filled with greener colour of C signal. This represents more C signal exists with the portions filled with big interconnected nanoparticles structures (Chen et al., 2009).

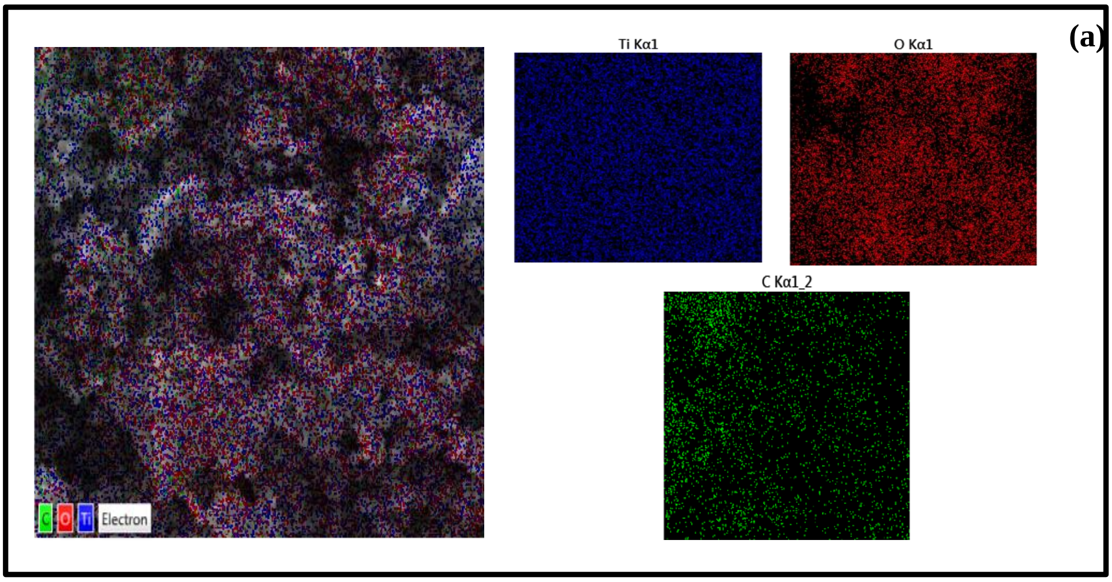

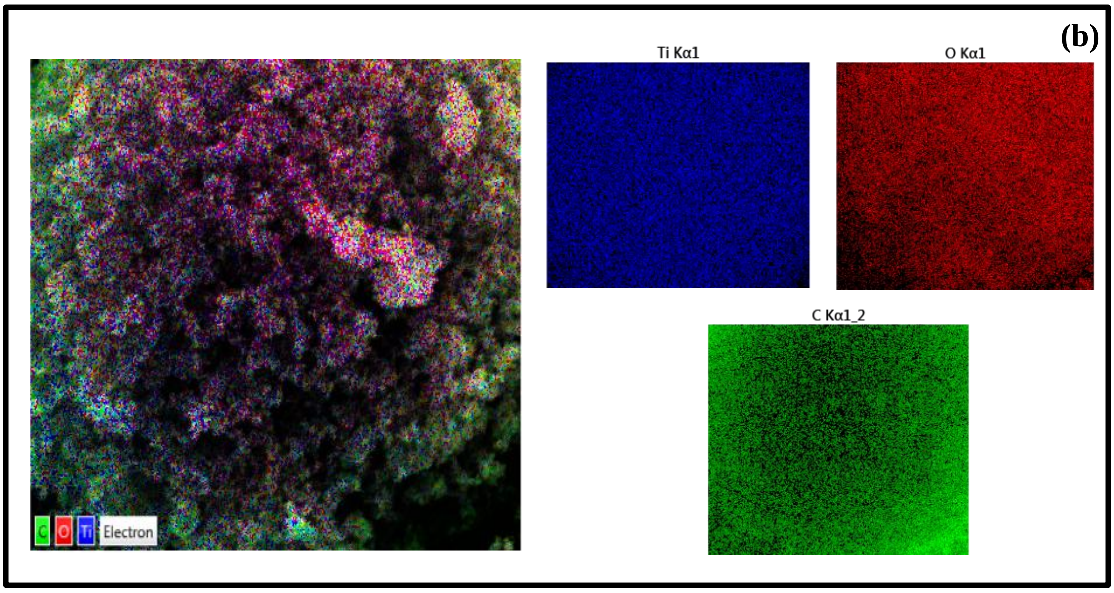

**Figure 4.12:** Elemental mapping of (a) 3 wt% and (b) 15 wt% of MWCNTs/ $TiO_2$ nanocomposites

#### 4.3.1.2 Phase Structure and Crystalinity

In this part of the experiment, XRD analysis was used to investigate the effect of MWCNTs loading on the crystallization and phase transition of MWCNTs/$TiO_2$ nanocomposites. The result clearly shows that the crystal structure of MWCNTs/$TiO_2$ nanocomposites is dependent on the MWCNTs loading. The XRD diffraction profiles exhibit identical patterns for all of the samples and only anatase phase of $TiO_2$ can be observed in the $TiO_2$/MWCNTs nanocomposites. The formation of anatase phase can be obtained via the calcination process. The diffraction peaks at $2\theta = 25.9$ and 43.2 corresponding with the (002) and (100) diffractions of the hexagonal graphite structure for MWCNTs samples. However, the peak at $2\theta = 25.9$ cannot be seen for MWCNTs/$TiO_2$ nanocomposites due to the peak was overlapped by the strong anatase $TiO_2$ peak at $2\theta= 25.2°$. The MWCNTs is shielded by the peaks of anatase $TiO_2$ where the peak intensity of $TiO_2$ showing higher crystallinity than MWCNTs. The characteristic peaks in the pattern at 25.2 (101), 37.9 (004), 48.3 (200), 53.9 (105), 55.0 (211), 62.7 (204), 68.9 (116), 70.1 (220) and 75.5 (215) corresponded to $TiO_2$

crystalline anatase phase, compatible with those shown in the JCPDS No. 21-1272. As shown in Figure 4.13, the diffraction peak intensity decreases and the peak width becomes broader with increasing concentration of MWCNTs. This was due to the increased of MWCNTs that give rise to the smaller grain sizes and the degree of crystallinity. The presence of MWCNTs in the composite restrict the direct contact of grains and induce the small grain of $TiO_2$ nanoparticles in the MWCNTs/$TiO_2$ nanocomposites (Da Dalt et al., 2013, Dai et al., 2014, Gui et al., 2014a, Hamid et al., 2014, Kim et al., 2012).

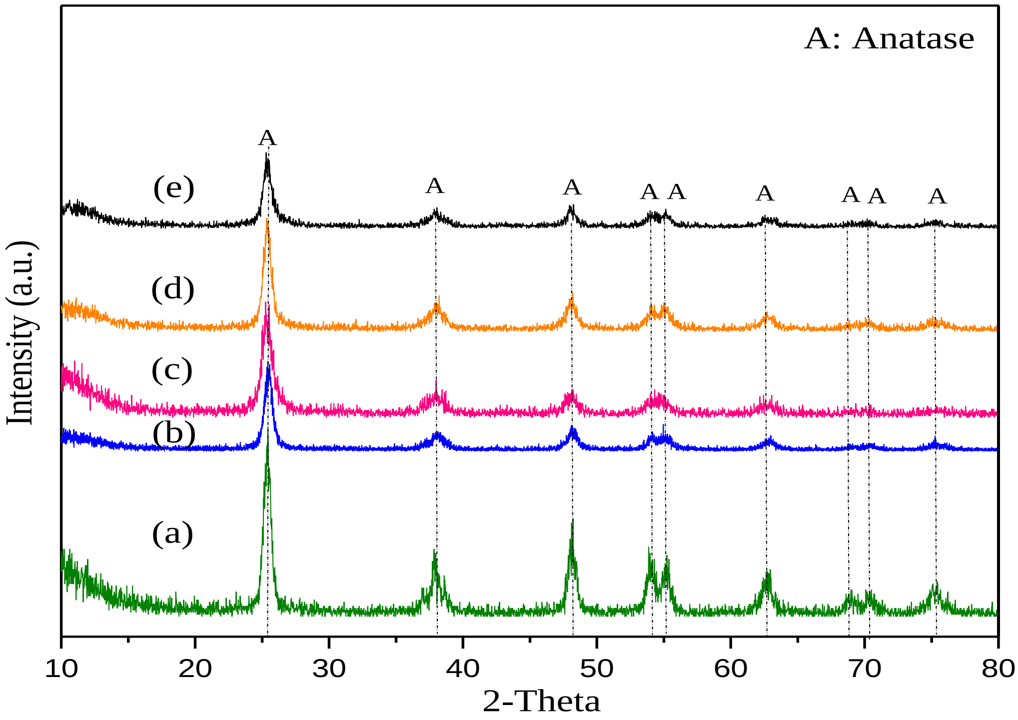

**Figure 4.13:** XRD spectra of (a) $TiO_2$ nanoparticles, (b) 3 wt%, (c) 5 wt%, (d) 10 wt% and (e) 15 wt% of MWCNTs/ $TiO_2$ nanocomposites

Table 4.3 presents the crystallite size, BET surface area and band gap energy of $TiO_2$ nanoparticles and MWCNTs/$TiO_2$ nanocomposites with various MWCNTs content. There was a correlation between crystallite size and surface area which revealed that the smaller the crystallize size, the larger the surface area. The crystallite size of the samples was calculated by the well-known Scherer's equation (Djokić et al., 2014). For MWCNTs/$TiO_2$ nanocomposites, the crystallite size was found to decrease with increasing MWCNTs content. Typically, the full width at half maximum (FWHM) of the anatase peaks for MWCNTs/$TiO_2$ nanocomposites are slightly broadened with an increasing amount of MWCNTs, indicating a decrease in the size of anatase crystallite. This result suggests that the presence of the MWCNTs in the MWCNTs/$TiO_2$ nanocomposites hinders the anatase crystallite growth. Moreover, the crystallinity of $TiO_2$ in the MWCNTs/$TiO_2$ nanocomposites is impaired by loading MWCNTs, especially with higher content (Da Dalt et al., 2013).

The BET results based on nitrogen sorption measurement showed the surface area of $TiO_2$ nanoparticles and MWCNTs/$TiO_2$ nanocomposites. The surface area of MWCNTs is 231 $m^2/g$. As shown in Table 4.3, the combination of MWCNTs with $TiO_2$ showed an increase in the $S_{BET}$ as compared to the pure $TiO_2$ nanoparticles which may lead to an increase of the capability for adsorbing pollutants. The adsorption capacity of CNTs is very fast, which is mainly due to the highly accessible adsorption sites and the short intraparticle diffusion distance, which is related to their large specific surface area. As a result, MWCNTs acts as supporting roles and strong adsorbent for enhancing the photocatalytic performance with the increasing of surface properties. The oxygen functional groups such as hydroxyl and carboxyl are introduced onto the CNT's surface during the synthesis and purification process. These functional groups can influence the maximum adsorption capacity of CNTs and make them more hydrophilic and suitable for the adsorption (Gao et al., 2008, Hamid et al., 2014, Wu et al., 2013). The surface area of the MWCNTs/$TiO_2$ nanocomposites increased with the MWCNTs content. This phenomenon may be caused by the separation of $TiO_2$ crystalline particles due to the introduction of MWCNTs, and the consequently formation of a structure of high porosity. Moreover, the significant change of the $TiO_2$ crystallite size may also explain the increase in the specific area of the nanocomposites. Smaller particles or crystalline sizes are well known generally to result in large surface area of the materials, increasing the photocatalytic activity. Also, as the crystalline size decreases, the number of active surface sites may increase.

The optical band gap of $TiO_2$ and MWCNTs/$TiO_2$ nanocomposites with various MWCNTs content was determined using the Kubelka-Munk expression and the estimated band gap is shown in Table 4.3. There is a correlation between the MWCNTs loading and absorption changes in the UV-Vis spectra. The increase amounts of MWCNTs obviously enhance the light absorption, owing to its good dispersion between $TiO_2$ and MWCNTs. The further details of the effect of MWCNTs content on band gap energy of MWCNTs/$TiO_2$ nanocomposites will be discussed in Section 4.3.1.4.

**Table 4.3:** Effect of various MWCNTs content on crystallite size, BET surface area and band gap energy of MWCNTs/ $TiO_2$ nanocomposites

| Sample name | Crystallite size, nm | BET surface area ($m^2/g$) | Band gap energy (eV) |
|---|---|---|---|
| $TiO_2$ | 12.9 | 75 | 3.23 |
| 3 wt% | 10.8 | 80 | 3.10 |
| 5 wt% | 9.1 | 96 | 3.06 |
| 10 wt% | 8.9 | 108 | 2.48 |
| 15 wt% | 7.5 | 163 | 2.34 |

#### 4.3.1.3 Raman Analysis

In this study, Raman analysis has been used to determine and understand the structural changes of MWCNTs/$TiO_2$ nanocomposites. Figure 4.14 shows the Raman spectra of the pure $TiO_2$ and $TiO_2$/MWCNTs nanocomposites (3-15 wt %) which confirmed the presence of MWCNTs, even at the low concentrations. Five obvious Raman modes are present at 143 $cm^{-1}$, 198 $cm^{-1}$, 395 $cm^{-1}$, 517 $cm^{-1}$ and 639 $cm^{-1}$, which are belong to the $E_g$ anatase vibration mode, $E_g$ mode, $B_{1g}$ mode, $B_{1g}$ + $A_{1g}$ mode and weak $E_g$ mode, respectively. This result clear to show that anatase phase is predominantly in both $TiO_2$ and $TiO_2$/MWCNTs nanocomposites. The intensity of the anatase peaks in $TiO_2$/MWCNTs nanocomposites is lower than that of $TiO_2$, which revealed the decrease of crystallinity and the energy of lattice vibration. In $TiO_2$/MWCNTs samples, the peak at 1315 $cm^{-1}$ was assigned to the structural disorder of the wall of the nanotubes (D-band) while the peak at 1594 $cm^{-1}$ was associated with the tangential vibrational mode (G-band). The intensity of the D and G-band increased with increasing MWCNTs concentrations, showing an interaction between $TiO_2$ and MWCNTs due to the creation of an electronic interphase interaction between MWCNTs and $TiO_2$ phases which enhanced the charge transfer from $TiO_2$ to the MWCNTs. On the contrary, the intensity of $E_g$ anatase mode decrease and the peak width becomes broadened with higher amount of MWCNTs, which is attributed to the abrupt reduction in $TiO_2$ percentage (Da Dalt et al., 2013, Gui et al., 2014a, Hamid et al., 2014, Kim et al., 2012, Zhao et al., 2013). The $E_g$ anatase mode of $TiO_2$ in the nanocomposites was blue-shifted to a higher wavenumber as compared with the pure $TiO_2$ anatase, indicating different compressive stresses on the atoms of $TiO_2$ nanoparticles. It is basically due to the strength of the bonding between $TiO_2$ and the MWCNTs (Ti-O-C bond) and thus, different vibrational wavenumbers were produced. The quality of MWCNTs or degree of “graphitization”, originated from defects associated with the amount of $sp^3$ hybridization after purification of the MWCNTs. It was indicated by the intensity ratio of D band to G band ($I_D/I_G$) as shown in Table 4.4. The $I_D/I_G$ ratio of the $TiO_2$/MWCNTs nanocomposites was increased with increasing amount of MWCNTs (Figure 4.15). An increased of the $I_D/I_G$ ratio was due to the nucleation of $TiO_2$ on the surface of MWCNTs and also attributed to the transfer of electrons from $TiO_2$ to MWCNTs. CNTs have an excellent electron transfer ability with a high electrical conductivity during photoexcitation, and transfer the electron away from the $TiO_2$ particles after photoexcitation. Additionally, it is noted that the D-band is red-shifting indicated a close interaction between MWCNTs with $TiO_2$ and the formation of C-O-Ti bonds stretches the in-plane covalent bonds. However, it is renowned that excessive amount of MWCNTs created more defects and increased the disorder of MWCNTs caused by Ti-C bonds in the interface. The formation of Ti-C bonds shows a determinant role in charge transfer enhancement. Substantially, XRD and Raman analysis confirmed the presence of anatase phase in the samples (Hamid et al., 2014).

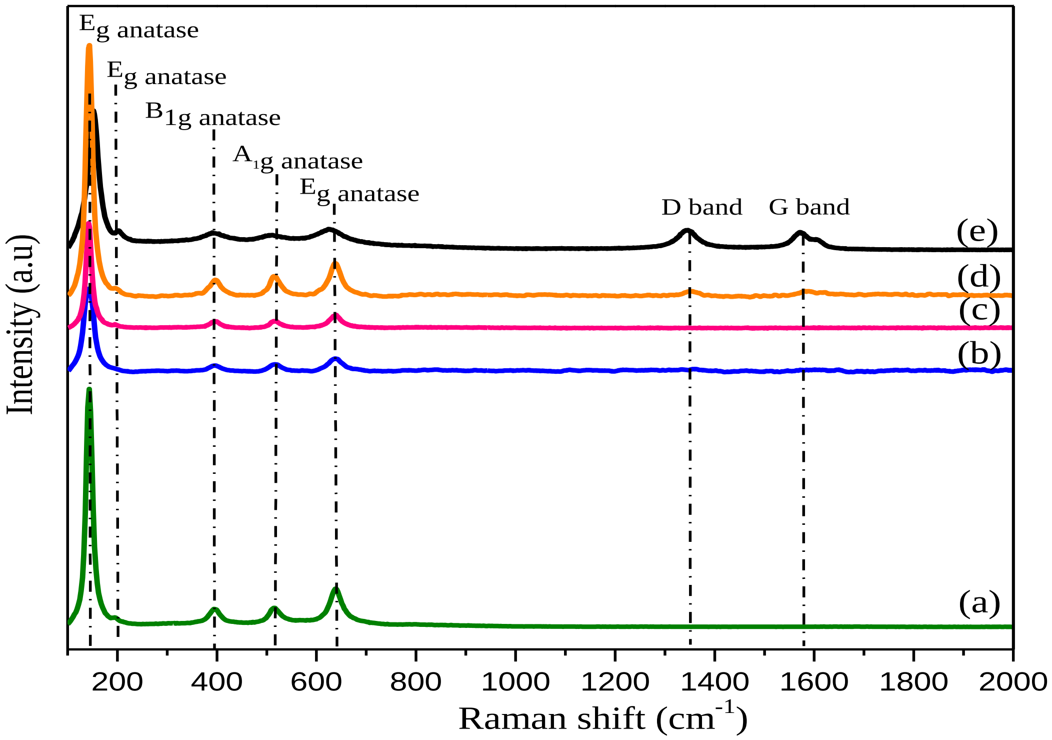

**Figure 4.14:** Raman spectra of (a) $TiO_2$, (b) 3 wt%, (c) 5 wt%, (d) 10 wt% and (e) 15 wt% of MWCNTs/ $TiO_2$ nanocomposites

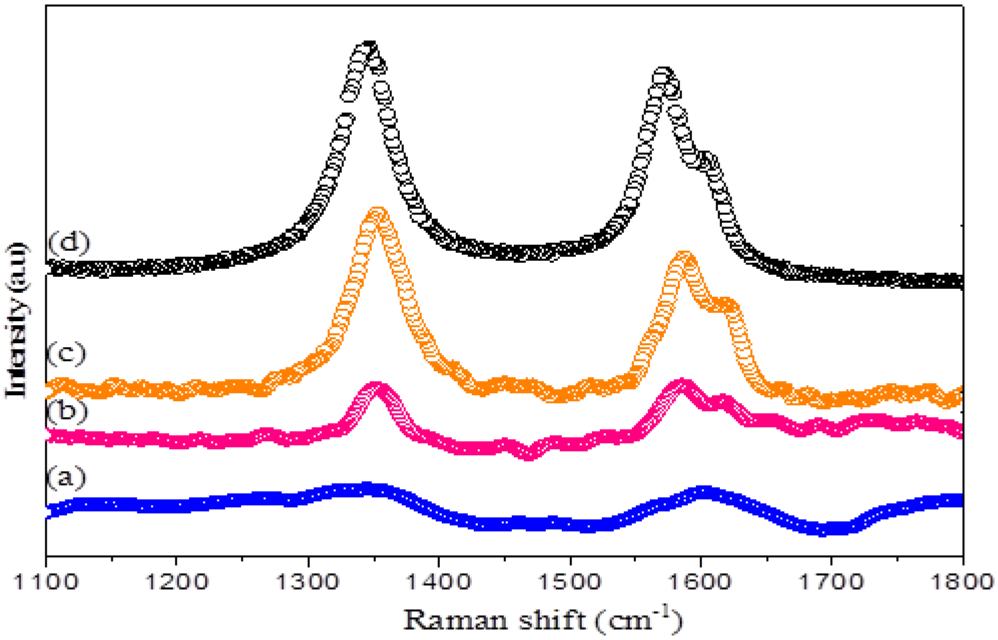

**Figure 4.15:** Raman shifts of the D band and G band of (a) 3 wt%, (b) 5 wt%, (c) 10 wt% and (d) 15 wt% of MWCNTs/ $TiO_2$ nanocomposites

**Table 4.4:** $I_D/I_G$ ratio of (3-15) wt% of MWCNTs/$TiO_2$

| **Sample** | **$I_D/I_G$ ratio** |
|---|---|
| 3 wt% MWCNTs/$TiO_2$ | 0.75 |
| 5wt% MWCNTs/$TiO_2$ | 0.94 |
| 10 wt% MWCNTs/$TiO_2$ | 1.10 |
| 15 wt% MWCNTs/$TiO_2$ | 1.33 |

### 4.3.1.4 Light absorption and photoluminesce (PL) properties

The PL spectroscopy has been widely used to provide information such as charge carrier trapping, immigration, and charge transfer. The optical properties of the as-prepared MWCNTs/$TiO_2$ nanocomposites with various MWCNTs content together with pure $TiO_2$ nanoparticles have been measured by UV-vis diffuse reflectance spectra in the range of 200-800 nm. $TiO_2$ shows light absorption under UV region (200-400 nm), while MWCNTs can absorb light in both UV and visible regions (200-700 nm). As displayed in Figure 4.16, the absorption spectra of MWCNTs/$TiO_2$ nanocomposites was shifted towards longer wavelength (red shift) as compared to that of pure $TiO_2$ nanoparticles, which is in agreement with the colour changing from white to dark grey. The presence of MWCNTs could reduce the necessary energy to electron transition between bands and contribute to the quantumn effciency during photocatalysis. These results revealed that MWCNTs enhance the light absorption of the entire UV-vis range because MWCNTs are good light absorptive materials. MWCNTs can act as a metal to accept a photogenerated electron and the charge recombination are decreased. As a result, the reduction in the band gap energies of $TiO_2$ nanoparticles able to enhance the catalytic activity. The band gap energies $E_g$ value was determined using the Kubelka-Munk function of optical absorption for allowed indirect transitions as shown in Table 4.3. The indirect band gap energy for 3 wt % MWCNTs/$TiO_2$, 5 wt % MWCNTs/$TiO_2$, 10 wt % MWCNTs/$TiO_2$ and 15 wt % MWCNTs/$TiO_2$ were 3.1, 3.06, 2.48 and 2.34 eV, respectively, this enhancement of absorption increases with the enhancement of the MWCNTs contents. It can be attributed to the enhancement of the surface electric charge of the $TiO_2$ in the nanocomposites because of the introduction of MWCNTs, which leads to the possible electronic transitions between the orbital of $TiO_2$ and MWCNTs. The great improvement in the light absorption and the reduced energy band gap can influent on the fundamental process of the photogenerated carrier formation and separation in the photocatalytic process (Da Dalt et al., 2013, Gui et al., 2014a, Hamid et al., 2014, Kim et al., 2012, Zhao et al., 2013).

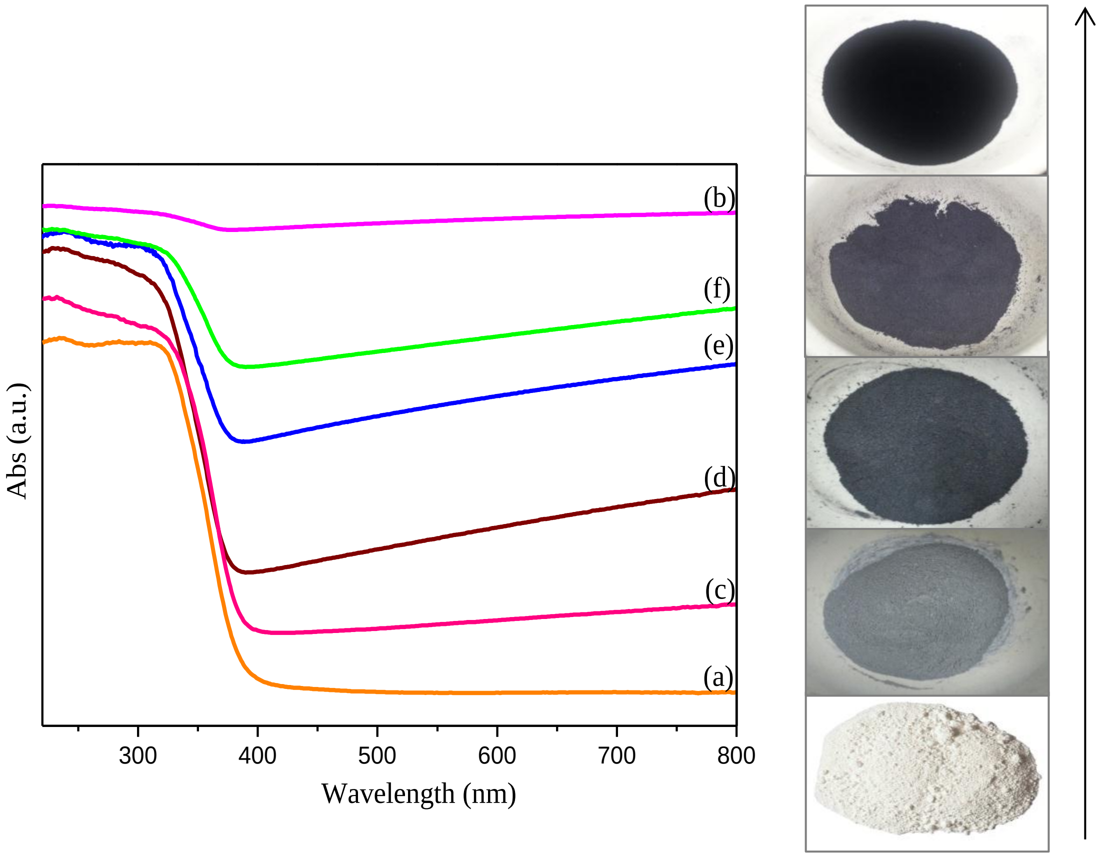

**Figure 4.16:** UV spectra of (a) $TiO_2$ nanoparticles, (b) Purified MWCNTs, (c) 3 wt%, (d) 5 wt%, (e) 10 wt% and (f) 15 wt% of MWCNTs/ $TiO_2$ nanocomposites

One of the factors limiting the photocatalytic performance of the $TiO_2$ photocatalyst is the fastest recombination of the photogenerated electron holes pairs besides the wide band gap phenomenon. During the photocatalysis process, the emission of photons prompts to PL in virtue of electron hole/pairs recombination. This is attributed to the reverse radiative deactivation from the excited-state of the Ti species. The PL spectra of the $TiO_2$ and MWCNTs/$TiO_2$ nanocomposites were presented in Figure 4.17. As anticipated, $TiO_2$ nanoparticles display a broad PL emission band and higher PL intensity, indicating highest charge recombination rate. Obviously, the MWCNTs / $TiO_2$ nanocomposites show diminished PL intensity as compared to the pure anatase $TiO_2$ nanoparticles. This indicates that the electron-hole recombination rate of self-trapped excitation in $TiO_2$ is reduced by the introduction of MWCNTs. Figure 4.17 indicates the effect of the MWCNTs content on the recombination rate of the electron holes/pairs. Basically, MWCNTs have a variety of electronic properties; it may also possess metallic conductivity as one of the many possible electronic structures. MWCNTs have a large electron-storage capacity which acts as an electron reservoir for trapping electrons, particularly generated from the photoexcitation of $TiO_2$ nanoparticles. The recombination time for the photogenerated electron-hole pairs has the order of $10^{-9}$ s while the time scale for the chemical interaction with adsorbed pollutant species was in the ranges of $10^{-8}$ to $10^{-3}$ s (Woan et al., 2009). The intensity of PL decreased with increasing in MWCNTs loading. This implies a suppression of charge recombination in the presence of MWCNTs (Da Dalt et al., 2013, Gui et al., 2014a). Several studies have proved that MWCNTs would act as scavengers of the photogenerated electrons arisen from the immobilization $TiO_2$ nanoparticles and thus, the fast electron transfer at the interface between the carbon and the $TiO_2$ layers are improved. The mixing of the delocalized p state of the carbon with O 2p orbital in the valence band of $TiO_2$, which in turn shift the valence band edge of $TiO_2$ upwards to narrow down the band-gap of $TiO_2$ significantly. Besides, there is a correlation between the PL intensity with the agglomeration of particles. According to the literature, the surface recombination traps is increased and the quantum yield is decreased by agglomeration along with the decrease in the value of the PL peak. When the MWCNTs are homogeneously covered with $TiO_2$ nanoparticles, it is expected that the PL signal of the composite will be higher than the MWCNTs alone, due to the presence of $TiO_2$ particles with stronger PL signal (Kim et al., 2012, Zhao et al., 2013).

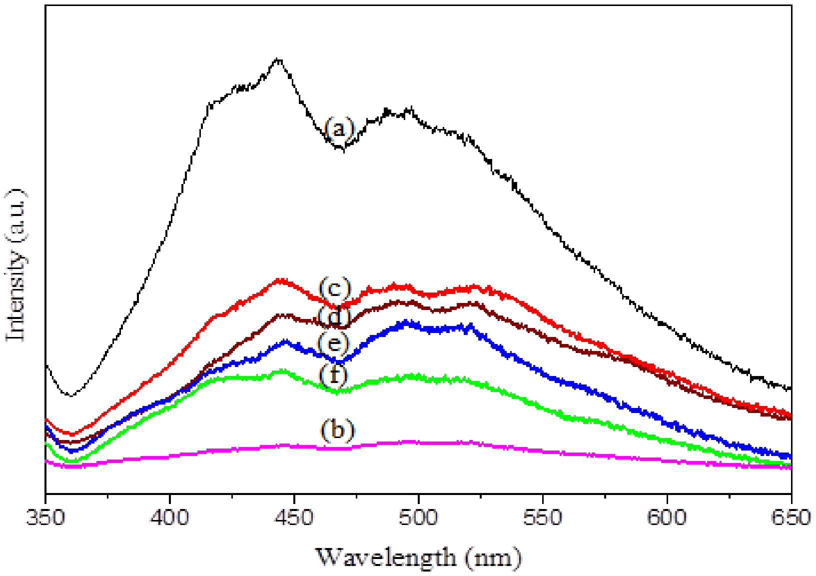

**Figure 4.17:** PL spectra of (a) $TiO_2$, (b) Purified MWCNTs, (c) 3 wt%, (d) 5 wt%, (e) 10 wt% and (f)15 wt% of MWCNTs/ $TiO_2$ nanocomposites

The photocatalytic activities of the synthesized MWCNTs/ $TiO_2$ were evaluated by photodegradation of DMPEs under 96 W UV lamp. The UV-Visible spectrum of DMPEs (Figure 4.18) consists of three maximum absorption peaks, an intense peak at 204 nm due to ($\pi \rightarrow \pi^*$) electronic transition, and two absorption peaks at 227 nm and 280 nm are attributed to ($n \rightarrow \pi^*$) electronic transition. The energy gap for an $n \rightarrow \pi^*$ transition is smaller than the $\pi \rightarrow \pi^*$ transition and thus the $n \rightarrow \pi^*$ peaks is at a longer wavelength. In addition, $n \rightarrow \pi^*$ transitions are weaker (less light absorbed) than those due to $\pi \rightarrow \pi^*$ transitions (Yuan, Li & Graham, 2008). The concentration of DMPEs in the test solution was determined at $\lambda_{max}$= 204 nm. The concentration of DMPEs was 1 mg/L.

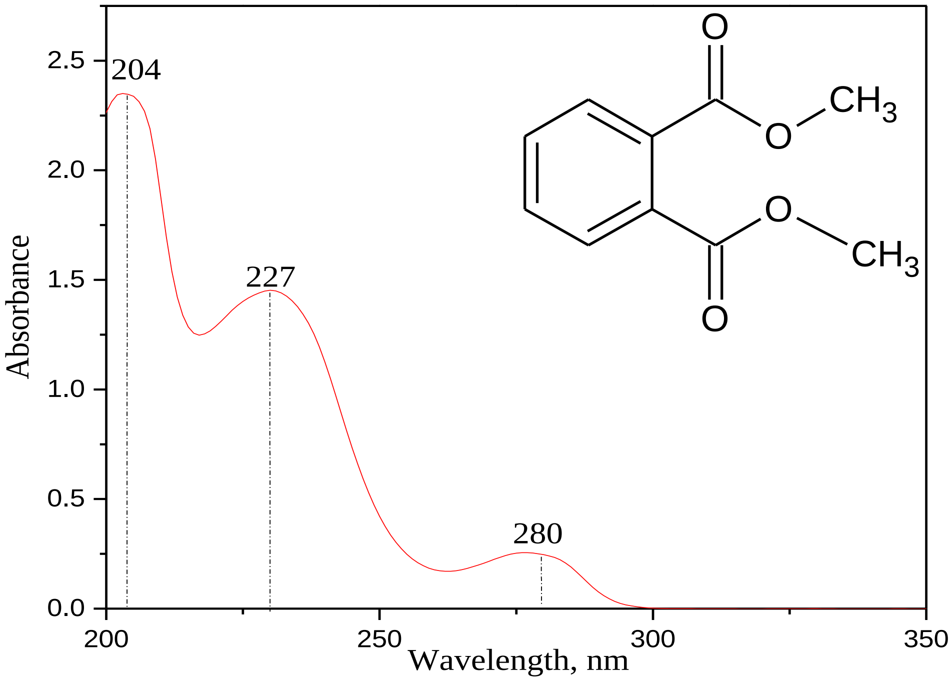

**Figure 4.18:** UV-visible spectrum of DMPEs

The photocatalytic efficiency of $TiO_2$/MWCNTs (97 %) is higher than $TiO_2$ (71 %) due to the MWCNTs acting as electron sinks and thereby hinders the recombination rate of the electron-hole pairs. The photogenerated holes are captured by MWCNTs/$TiO_2$ nanocomposites and transform to hydroxyl radicals, which are the main reactive species involved in decomposition of organic pollutants. There are more hydroxyl radicals being produced by MWCNTs/$TiO_2$ nanocomposites, which greatly improve the photocatalytic degradation rate (Hamid et al., 2014, Kim et al., 2012). The photocatalytic degradation studies of DMPEs were carried out by (3 wt % - 15 wt %) of MWCNTs/$TiO_2$ to further investigate their photocatalytic performance (Figure 4.19). As can be seen from Figure 4.19, the photodegradation of DMPEs during the 3 h photoreactions increase upon enhancing the MWCNTs contents from 3 to 10 wt % but decrease with a further enhancement to 15 wt %. The reason is that MWCNTs can act as electron acceptors and transfer channels and improve the charge separation efficiency. Once the amount of MWCNTs are larger than 10 wt %, especially for 15 wt % of

MWCNTs/$TiO_2$ nanocomposites, the photodegradation of DMPEs decrease. When the amount of MWCNTs increases, photon absorption would also increase, but increased adsorption capacity could not counteract the influence of fewer active sites. It can be seen that 10 wt % of MWCNTs exhibited an optimal photocatalytic activity among the samples, although the absorbance is continuously increased with the enhancement of the MWCNTs loadings. Basically, the presence of MWCNTs in the nanocomposites can lead to the decrease in the relative amount of $TiO_2$ in the photocatalyst and then to the decrease of the photogenerated carriers. This is because the same amount of photocatalyst was added for the photoreaction, and hence, the photodegradation of DMPEs decreases especially for the nanocomposites containing MWCNTs larger than 10 wt %. In addition, an apparent enhancement of visible light absorption was observed for MWCNTs/$TiO_2$ nanocomposites, this was mainly attributed to the introduction of more MWCNTs and does not necessarily mean an improved photoactivity of $TiO_2$ (Da Dalt et al., 2013, Zhao et al., 2013). Thereby, it has been shown that an optimal amount of MWCNTs to incorporate in the composite is needed to obtain good improvement in the catalyst efficiency. Furthermore, several authors have made similar observation that little $TiO_2$ or excessive CNTs addition shielded the $TiO_2$ and reduced the UV intensity, due to photon scattering by the nanotubes. However, a high $TiO_2$ content was found to be ineffective in suppressing exciton recombination due to the large distance between the titania and the nanotubes. Based on this study, it is clear that the MWCNTs/$TiO_2$ composite provides high surface area which is beneficial for photocatalytic activity, as it provides high concentration of target organic substances around sites activated by UV irradiation (Da Dalt et al., 2013, Gui et al., 2014a).

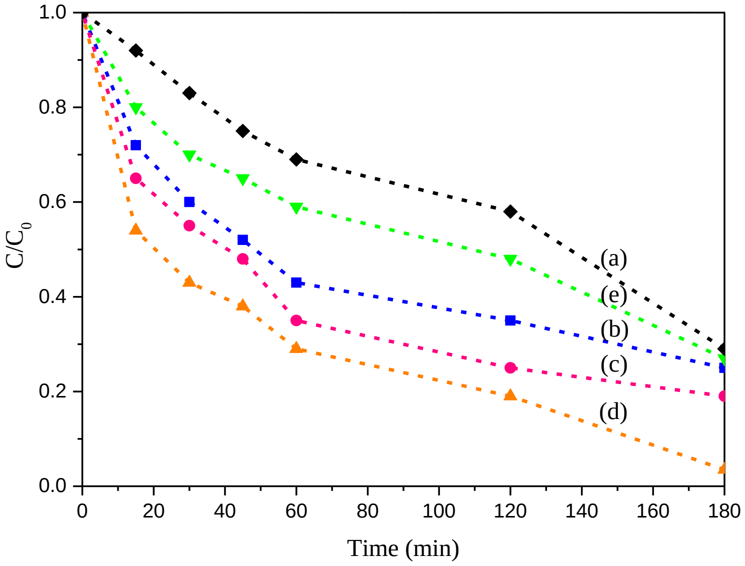

**Figure 4.19:** Photocatalytic activity of a) $TiO_2$, b-e) 3, 5, 10, 15 wt% of MWCNTs / $TiO_2$ to degradation DMPEs

The photocatalytic degradation process normally follows Langmuir-Hinshelwood kinetics and is a pseudo first order reaction (Yu et al., 2005). The kinetics of photocatalyzed degradation of DMPEs is illustrated in Figure 4.20. The linearity of the curves suggested that the photocatalytic degradation of DMPEs could be described by the pseudo first order kinetic model, ln $(C_0/C) = kt$, where $C_0$ is the initial concentration and C is the concentration at time t. The plots of the concentration data provided a straight line. The results of fitting experimental data to first-order kinetics are tabulated in Table 4.5. The result indicates that MWCNTs/$TiO_2$ nanocomposites has much higher photoactivity than that of $TiO_2$ nanoparticles with the irradiation of UV light. This enhanced photoactivity is attributed to unique structure and a variety of favorable properties by MWCNTs which harvest the full solar spectrum more effciency. The rate constant increases with increasing amount of MWCNTs up to 10 wt-% and then decreases with higher MWCNTs content. Based on the kinetic plots, this showed that the MWCNTs/$TiO_2$ with 10 wt % of MWCNTs demonstrated the highest rate constant and a higher degradation rate of 97 % at 3 h irradiation time. There is a strong interaction between the $TiO_2$ nanoparticles and MWCNTs and the roles of the

MWCNTs in tailoring the morphological structure of the MWCNTs/$TiO_2$. Meanwhile, the acceleration of the electrontransfer can be achieved by a long range π electronic conjugation of MWCNTs. Therefore, the photogenerated electrons of $TiO_2$ can be transferred quickly to MWCNTs under light irradiation. In addition, the increase in the amount of MWCNTs up to 10 wt % was accompanied by a rapid increase in the degradation rate, probably as a consequences of the overall increase of the number of active sites, which in turn increases the number of hydroxyl and superoxide radicals.

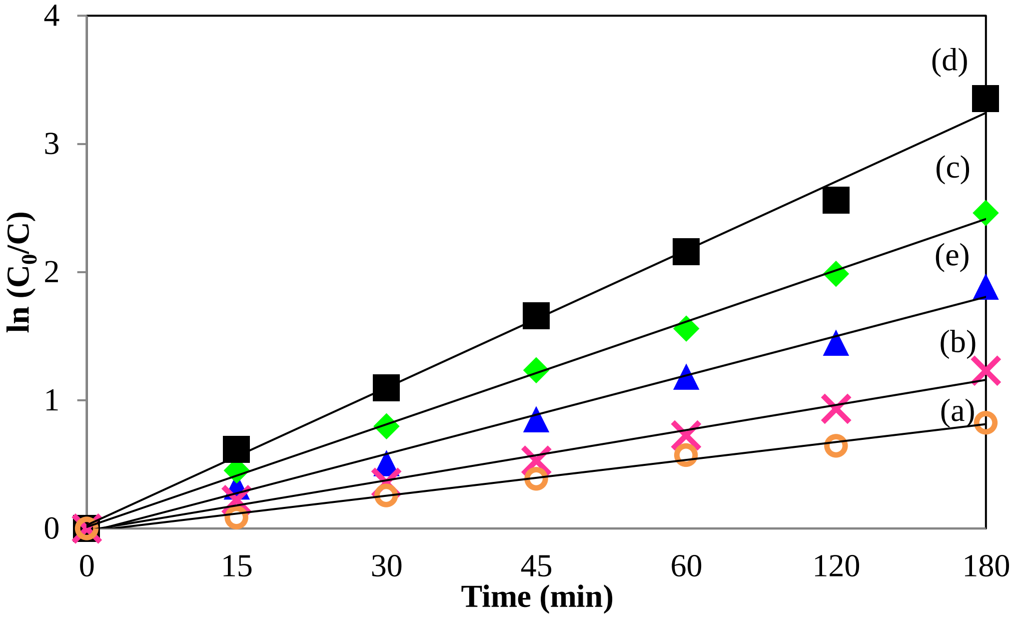

**Figure 4.20**: First-order kinetics for DMPEs photodegradation using of a) $TiO_2$, b-e) 3, 5, 10, 15 wt% of MWCNTs/$TiO_2$ nanocomposites

**Table 4.5:** Rate constants for catalytic photodegradation of DMPEs

| **Samples** | **Rate constant (k)** | **$R^2$** |
|---|---|---|
| $TiO_2$ | 0.0070 | 0.9928 |
| 3 wt% | 0.0167 | 0.9928 |
| 5 wt% | 0.0234 | 0.9982 |
| 10 wt% | 0.0317 | 0.9953 |
| 15 wt% | 0.0109 | 0.9891 |

#### 4.3.1.5 Summary

A series of MWCNTs/$TiO_2$ nanocomposites with different MWCNTs contents were successfully synthesized via incorporation of $TiO_2$ nanoparticles on the purified MWCNTs surface by a modified sol-gel method. The experiment results demonstrate that most of MWCNTs/$TiO_2$ nanocomposites show higher photoactivity than pure $TiO_2$ and 10 wt % MWCNTs/$TiO_2$ nanocomposites showed the maximum photocatalytic DMPEs degradation efficiency because of its fast carrier separation. The functional group (-COOH) on the MWCNTs surface would help the achievement of direct chemical bonding between MWCNTs and the $TiO_2$ nanoparticles, resulting in the synergistic effect of MWCNTs and $TiO_2$. XRD and Raman analysis proved that the desired, photocatalytically active anatase MWCNTs/$TiO_2$ nanocomposites have been successfully synthesized. Anatase $TiO_2$ shows much higher photocatalytic activity than rutile due to its higher surface area than rutile, leading to enhanced adsorption capability and much more active sites were generated. The UV-vis spectra of the samples showed extended absorption edge when increasing the amount of MWCNTs. In addition, the PL results divulged that 15 wt % have the lowest electron recombination rates as divulged by the PL results, however, this sample not showed the best photocatalytic efficiency. The apparently contradictory findings could be partially explained because of the presence of MWCNTs in the nanocomposites can lead to the decrease in the relative amount of $TiO_2$ in the photocatalyst and then to the decrease of the photogenerated carriers. This is because the same amount of photocatalyst was added for the photoreaction as mentioned above, and hence, the photodegradation of DMPEs decreases especially for the nanocomposites containing an excess amount of MWCNTs.

## 4.4 Effect of pH

Based on the aforementioned discussion, 10 wt % of MWCNTs/$TiO_2$ nanocomposites was synthesized via modified sol-gel method and subsequently annealed at 450 °C exhibited the best photocatalytic performance. A maximum photodegradation rate was achieved. Since pH of the resultant play an important role in determining the photocatalytic activity of MWCNTs/$TiO_2$ nanocomposites. Therefore, optimization of the pH during the sol-gel synthesis for MWCNTs/$TiO_2$ nanocomposites is crucial in improving the photocatalytic efficiency. Therefore, in the following studies, MWCNTs/$TiO_2$ nanocomposites were synthesized in such condition mentioned above to study the effect of pH on MWCNTs/$TiO_2$ nanocomposites. The aim of this section is to improve the uniformity of $TiO_2$ nanoparticles on MWCNTs surface for the best photocatalytic performance.

### 4.4.1 Phase Structure and Crystallinity analysis

The uniformity of $TiO_2$ nanoparticles on MWCNTs surface was affected by the control of the final pH synthesis solution, therefore our attention has focused on the effect of various pH value conditions in this study. Figure 4.21 shows the XRD patterns of the 10 wt % MWCNTs/$TiO_2$ nanocomposites prepared in final synthesis solution with different pH value. It showed that all samples are crystalline and strong effects on the crystallite size and degree of crystallinity are observed for the nanocomposites synthesized under different pH values. The crystallite size was determined by Scherrer equation and summarized in Table 4.6. The XRD pattern of the MWCNTs/$TiO_2$ nanocomposites confirms the presence of pure $TiO_2$ with anatase phase. The diffraction peaks at 25.2 (101), 37.9 (004), 48.3 (200), 53.9 (105), 55.0 (211), 62.7 (204), 68.9 (116), 70.1 (220) and 75.5 (215) correspond to $TiO_2$ crystal planes of the anatase phase, respectively. The diffraction peaks at $2\theta = 25.9$ and 43.2 are corresponding with the

(002) and (100) diffractions of the hexagonal graphite structure for MWCNTs samples. However, the peak at 2θ = 25.9 could not be seen for MWCNTs/$TiO_2$ nanocomposites due to the peak was overlapped by the strong anatase $TiO_2$ peak at 2θ= 25.2°. It is noteworthy that as the increasing pH of the solution to pH 9, the crystallinity of the MWCNTs/$TiO_2$ nanocomposites increases as can be seen by the variation in anatase peak intensities in Figure 4.21. At pH 11, the decrease in the intensity of the anatase peaks can be attributed to processes such as coarsening and aggregation-recrystallization. In addition, it is suggested that higher pH likely leads to inferior crystal quality due to the mutual contact of surface hydroxyl groups between particles. Furthermore, it is proposed that the surface of $TiO_2$ is covered with a certain number of Ti-OH groups and the surface of $TiO_2$ is substantially hydroxylated. Therefore, with the increased number of hydroxyl groups, the more oxygen vacancies are formed on the surface of $TiO_2$ which will cause many defects that influence the crystallization of $TiO_2$. This morphological change can further be confirmed by the FESEM images shown in Section 4.4.1.2. These results indicate that alkaline medium at pH 9 are favourable for the formation of MWCNTs/$TiO_2$ nanocomposites (Da Dalt et al., 2013, Gui et al., 2014a, Hamid et al., 2014, Zhao et al., 2013).

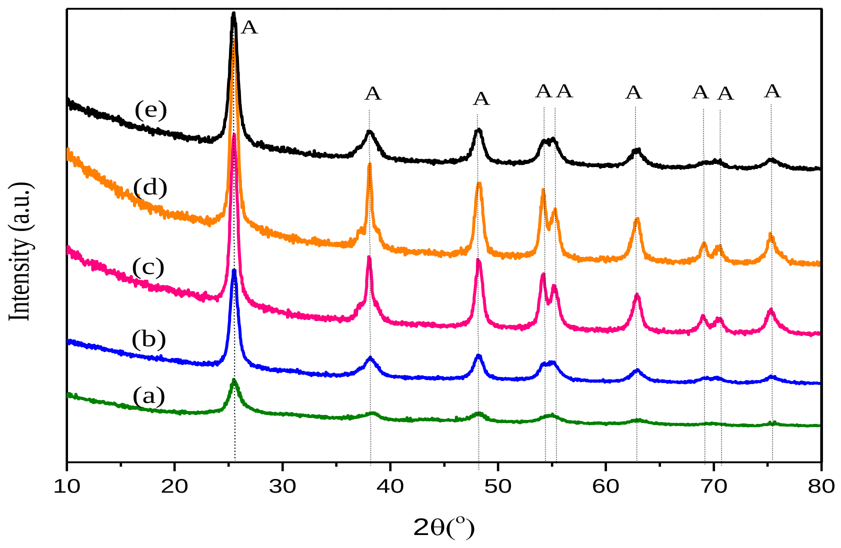

**Figure 4.21:** XRD spectra of of MWCNTs/ $TiO_2$ nanocomposites at (a) pH 3, (b) pH 5, (c) pH 7, (d) pH 9 and (e) pH 11

Table 4.6 presents the crystallite size, BET surface area and band gap energy of MWCNTs/$TiO_2$ nanocomposites with various pH value conditions. The crystallite size of the samples was calculated by the well-known Scherer's equation (Djokic et al., 2014). Typically, the FWHM of the anatase peaks for MWCNTs/$TiO_2$ nanocomposites are slightly sharpened with an increasing pH. It was obviously seen that, at the fixed amount of MWCNTs/$TiO_2$ composite, increasing pH resulted in increase of crystallite size of $TiO_2$. The results from both crystalline phase and crystallite size for synthesized MWCNTs/$TiO_2$ nanocomposites, suggest that photocatalytic activity of MWCNTs/$TiO_2$ is expected to be maximized at pH 9 since anatase crystallinity was greatest at pH 9 as compared to that at other pH conditions. The BET results based on the nitrogen sorption measurement showed the surface area of MWCNTs/$TiO_2$ nanocomposites with various pH value conditions. BET measurements showed that with increasing pH value, the surface area of the samples is decreasing, implying the formation of larger particle size as can be observed from the FESEM images. The optical band gap of $TiO_2$ and MWCNTs/$TiO_2$ nanocomposites with various pH value conditions were determined using the Kubelka-Munk expression and the estimated band gap was shown in Table 4.6. The further details of the effect of pH on band gap energy of MWCNTs/$TiO_2$ nanocomposites will be discussed in Section 4.4.4.

**Table 4.6:** Effect of various pH on crystallite size, BET surface area and band gap energy of MWCNTs/ $TiO_2$ nanocomposites

| **Sample name** | **Crystallite size, nm** | **BET surface area ($m^2/g$)** | **Band gap energy (eV)** |
|---|---|---|---|
| pH3 | 7.5 | 113 | 3.14 |
| pH5 | 9.8 | 110 | 3.00 |
| pH7 | 10.5 | 105 | 2.67 |
| pH9 | 12.8 | 95 | 2.49 |
| pH11 | 10.1 | 108 | 2.98 |

### 4.4.2 Morphological Studies

FESEM micrographs representing the effect of different pH from 3 to 11 on the MWCNTs/$TiO_2$ nanocomposites are shown in Figure 4.22. The amount of MWCNTs was fixed to 10 wt % was based on our previous study, which showed higher photocatalytic performance. The $TiO_2$ at pH 3 were observed with non-spherical particles and are widely separated clumped on the MWCNTs surface with high agglomeration. At pH 5, the as-prepared sample showed an irregular aggregation of $TiO_2$ particles attached on the surface of MWCNTs. It is clearly shown that the $TiO_2$ particles has a high degree of agglomeration caused by mutual interaction between particles which arises from some forces such as van der Waals forces, capillary forces and electrostatic forces. On the other hand, the FESEM image showed that MWCNTs/$TiO_2$ nanocomposites prepared at pH 7 consisted of spherical particles with poor agglomeration while the as-prepared nanocomposites at pH 9 showed that small particles of $TiO_2$ nanoparticles were homogeneously spread on the MWCNTs surface.

Furthermore, the MWCNTs tubes were also appeared to attach closely to the $TiO_2$ particles. This indicated that the MWCNTs/$TiO_2$ nanocomposites prepared at this pH displayed a favorable synergistic effect between the nanotube and $TiO_2$. $Ti^{4+}$ ions were attached on MWCNTs due to the coordination reaction between $Ti^{4+}$ ions and polar oxygenated functional groups in the sol-gel process. As a result, Ti nucleated heterogeneously via sol-gel technique because MWCNTs have prevented Ti from growing into aggregated nanoparticles. Furthermore, adding ammonia solution directly leads to a complete nucleation and growth in a few seconds that affects on agglomeration of particles. The agglomerated particles have regular distribution and the shapes of particles are similar and homogeneous. Lastly, the formation of large amounts of bigger $TiO_2$ particles was observed on the MWCNTs surface at pH 11. It should be noted that the influence of surface reaction on the suspension stabilization was considerable for dispersions of $TiO_2$ particles on MWCNTs surface. In general at low pH, the $TiO_2$ partially covers the individual MWCNTs and this increases with the change in pH until the maximum pH of 9 in complete coverage of individual MWCNTs. It can be concluded that the pH value of the synthesis conditions dramatically affects the surface morphology of the MWCNTs/$TiO_2$ nanocomposites during the sol-gel process. It is suggested that as particle size decreases, the curvature of nanoparticles approaches the same length as the hydrated ions, which enables the counterions to screen the surface sites from all directions rather than only one-half of the space in the case of a planar wall. However, the particle sizes are inconsistent because aggregates or agglomerates of crystals due to decreasing the pH and the particles contain several crystallite (Kuvarega et al., 2012, Oh et al., 2009, Saleh and Gupta, 2012, Tian et al., 2011, Xia et al., 2007).

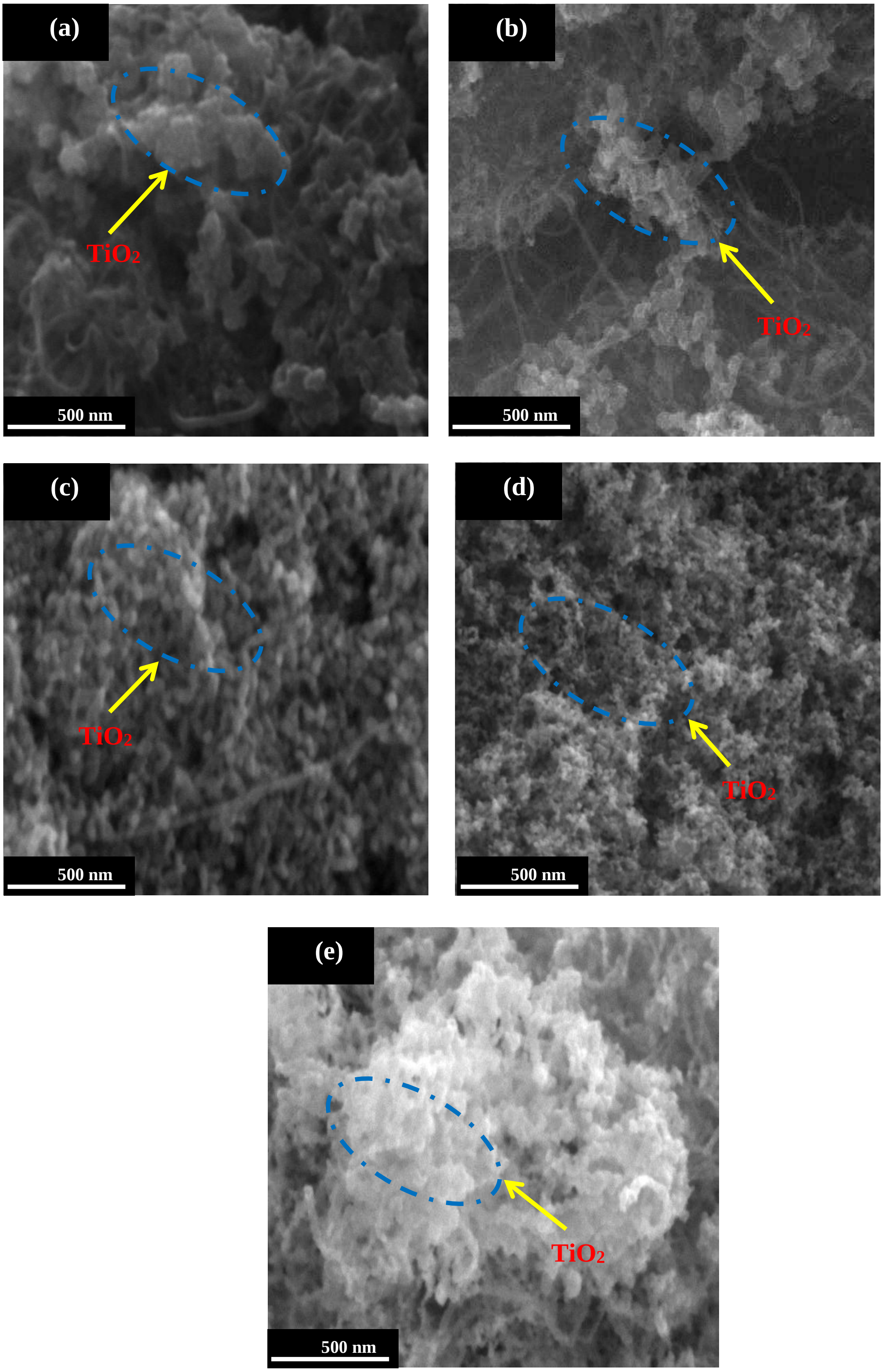

**Figure 4.22:** FESEM images of MWCNT/$TiO_2$ nanocomposites at (a) pH 3, (b) pH 5, (c) pH 7, (d) pH 9 and (e) pH 11

### 4.4.3 Raman Analysis

Figure 4.23 shows the Raman spectrum of MWCNTs/$TiO_2$ nanocomposites prepared at different pH value conditions. The presence of $TiO_2$ and MWCNTs in the nanocomposites was confirmed by Raman analysis. In MWCNTs/$TiO_2$ nanocomposites, two typical peaks of MWCNTs are observed at around 1314.95 and 1593.54 $cm^{-1}$. The band at 1314.95 $cm^{-1}$ is known as D-band which attributed to disorder $sp^3$ defects in the hexagonal framework of the carbon, whereas the other band at 1593.54 $cm^{-1}$ was known as G-band corresponding to ordered $sp^2$ carbon defects. The information on the extent of structural defects on the sidewalls of the carbon nanotubes can be determined via the $I_D/I_G$ ratios (Table 4.7). The $I_D/I_G$ ratios were calculated from the ratio of the intensity of the D and G band. MWCNTs/$TiO_2$ nanocomposites show the five Raman active fundamental modes (141.85, 198.15, 396.53, 517.12 and 641.86 $cm^{-1}$) in Raman spectrum indicated the presence of anatase mode as $E_g$ anatase vibration mode, $E_g$ mode, $B_{1g}$ mode, $B_{1g}$ + $A_{1g}$ mode and weak $E_g$ mode respectively. The positions and intensities of the five Raman characteristic modes correspond well with the anatase phase of $TiO_2$. The intensity of these Raman peaks increases with increasing pH value up to pH 9 in the nanocomposites. Higher intensity of peaks corresponds to higher crystallinity which in accordance with the previous XRD results shown. The $I_D/I_G$ ratios generally decreased with the increasing of pH value probably due to the number defects on MWCNTs walls and the amount of $TiO_2$ available to cover the defects sites. These values suggest decreased defects on MWCNTs resulting in decreased D-band intensity (Da Dalt et al, 2013; Gui et al., 2014; Hamid, et al., 2014; Kim et al., 2012; Zhao et al., 2013).

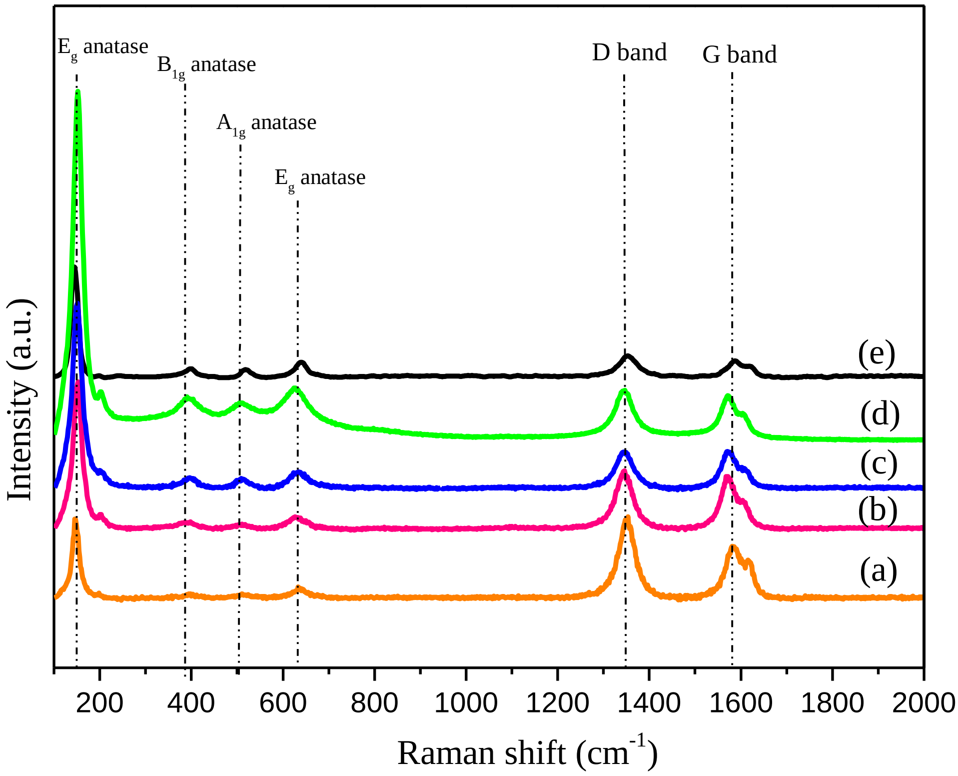

**Figure 4.23:** Raman spectra of MWCNT/$TiO_2$ nanocomposites at (a) pH 3, (b) pH 5, (c) pH 7, (d) pH 9 and (e) pH 11

**Table 4.7:** $I_D/I_G$ ratio of pH (3-11) of MWCNTs/$TiO_2$

| Sample | $I_D/I_G$ ratio |
|---|---|
| pH 3 | 1.56 |
| pH 5 | 1.34 |
| pH 7 | 1.15 |
| pH 9 | 1.08 |
| pH 11 | 0.98 |

### 4.4.4 Light absorption and photoluminesce (PL) properties

UV/Vis spectroscopy is routinely used in analytical chemistry for the quantitative determination of the band gap energy, and the light absorbance spectra of MWCNTs/$TiO_2$ samples are presented in Figure 4.24. All of the samples have intense absorption in the UV-vis range due to anatase $TiO_2$ in the region between 350 and 400 nm. There is a noticeable red shift in the absorption edge for MWCNTs/$TiO_2$ nanocomposites that can be correlated to the increase of pH value, indicating that pH enhanced the light absorption of the entire UV-vis range. The improvement in the light absorption can be attributed to the interaction of $TiO_2$ nanoparticles with the MWCNTs, which may modify the electron/hole pair recombination process under UV light irradiation. The band gap energy can be estimated from Kubelka-Munk function as reported in Table 4.6 and the estimated band gap energies were 3.14, 3.00, 2.67, 2.49 and 2.98 eV for MWCNTs/$TiO_2$ samples at pH 3, 5, 7, 9 and 11 respectively. By increasing the pH value from 3 to 9, the value of indirect band gap energy decreased from 3.14 eV to 2.49 eV due to increase or uniform coverage of MWCNTs in agreement with FESEM observations. The results demonstrate that there is a smaller band gap energy value for MWCNTs/$TiO_2$ nanocomposites synthesized at pH 9, which is useful for its photocatalytic activity under UV irradiation (Da Dalt, Alves & Bergmann, 2013; Gui, Chai, Xu & Mohamed, 2014; Hamid, Tan, Lai & Samsudin et al., 2014; Kim et al., 2012; Zhao, Yang, Chen & Wang, 2013).

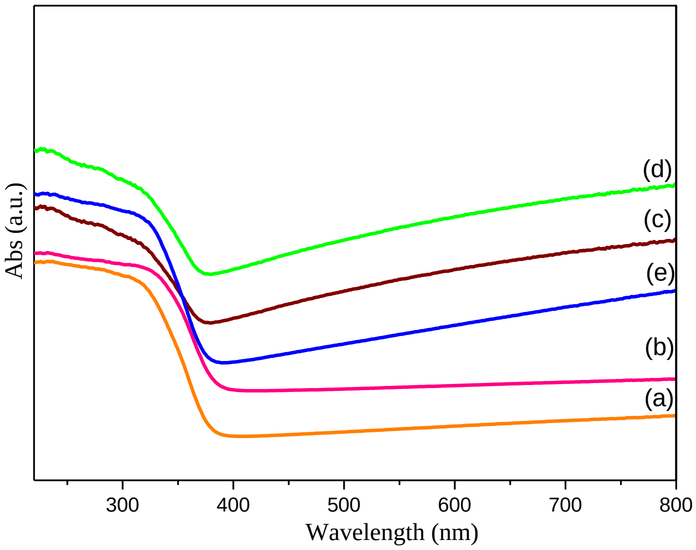

**Figure 4.24:** UV spectra of MWCNT/$TiO_2$ nanocomposites at (a) pH 3, (b) pH 5, (c) pH 7, (d) pH 9 and (e) pH 11

The radiative recombination of the self-trapped electrons upon photoexcitation of MWCNTs/$TiO_2$ nanocomposites were measured via PL analysis. Figure 4.25 shows the PL spectra of MWCNTs/$TiO_2$ nanocomposites with different pH value conditions as a function of wavelength. The recombination rates of $TiO_2$ have been reduced by MWCNTs through efficiently capturing and transporting generated electrons from the $TiO_2$ and thus suppressing recombination with generated holes. From Figure 4.25, it was observed that there were two peaks around 400 nm and 500 nm which is attributed to the recombination of electrons and holes on trap sites within the $TiO_2$. Moreover, the increase of the pH value reduced the intensity of the PL signal from $TiO_2$, which obviously implied a reduction in the recombination rate. This indicated direct contact and interaction between the MWCNTs and the $TiO_2$ at where the physical mixtures of MWCNTs and $TiO_2$ do not result in a significant decrease in the PL spectra. In addition, a correlation between the electrophoretic mobility and particle size was observed for MWCNTs/$TiO_2$ nanocomposites. The point of zero charge shifts toward a lower pH value with increasing particle size. Using a corrected Debye-Huckel theory and Monte Carlo simulation, it showed theoritically that such a size dependence of surface charge exits for metal oxide nanoparticles. Normally, a steep increase in nanoparticle owing to agglomeration process was found at pH>7 and stabilization was found for more alkaline pH. Thus, pH 9 yield an enhanced in PL intensity for MWCNTs/$TiO_2$ nanocomposites. MWCNTs/$TiO_2$ composite at pH 9 showed the CNTs are distributed well in the structure and are adhered tightly to a large number of $TiO_2$ nanoparticles, which have improves the electron collection and the bonding strength among $TiO_2$ particles increases. MWCNT probably prevents the recombination by bonding to $TiO_2$ nanoparticles (via the interaction of carboxylic acid group with hydroxyl group of $TiO_2$) (Da Dalt, Alves & Bergmann, 2013; Gui, Chai, Xu & Mohamed, 2014).

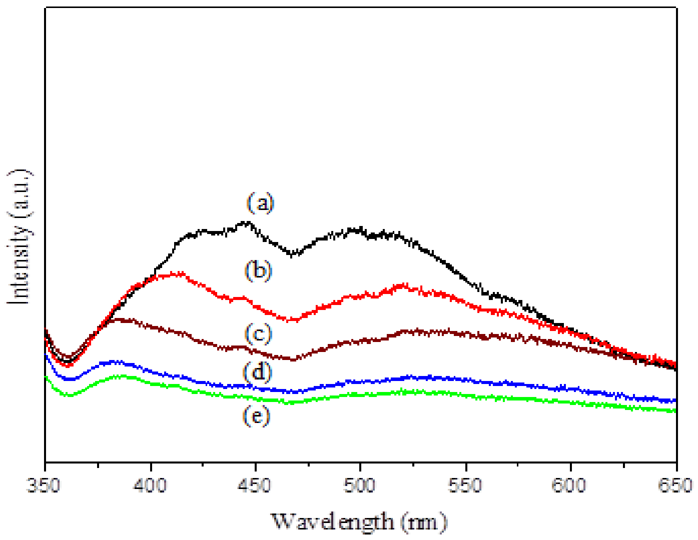

**Figure 4.25**: PL spectra of MWCNT/$TiO_2$ nanocomposites at (a) pH 3, (b) pH 5, (c) pH 7, (d) pH 9 and (e) pH 11

### 4.4.5 Photocatalytic activity On DMPEs

To examine the photocatalytic efficiency of MWCNT/$TiO_2$ nanocomposites prepared at various pH conditions, the photodegradation of DMPEs aqueous solution under 96 W UV irradiation was conducted and presented in Figure 4.26. The photocatalytic degradation of DMPEs solution is detected with UV-vis spectrophotometer and the characteristic absorption bands of DMPEs was located at 204 nm. The highest degradation efficiency under UV irradiation was observed for the MWCNTs/$TiO_2$ nanocomposites at pH 9 (97 %) for 3 h. There was an increase in the degradation efficiency of the nanocomposites with increasing pH value up to pH 9, with the pH 3, pH 5, pH 7 and pH 11 MWCNTs/$TiO_2$ nanocomposites showing values 55 %, 77%, 91% and 63% respectively. This trend correlates very well with the decrease in band gap observed as mentioned in Table 4.6. Furthermore, some studies reported that more OH groups existed on the surface of $TiO_2$, the greater photocatalytic activity appeared (Gui, Chai, Xu & Mohamed, 2014). However, the presence of high level of pH causes a decrease in DMPEs degradation efficiency probably due to the formation of large amounts of bigger $TiO_2$ particles on the MWCNTs surface as well as their aggregation. It is notable that $TiO_2$ particles tend to aggregate in acidic solution, leading to a decrease in substrate adsorption and photon absorption (Zhao, Yang, Chen & Wang, 2013; Da Dalt, Alves & Bergmann, 2013).

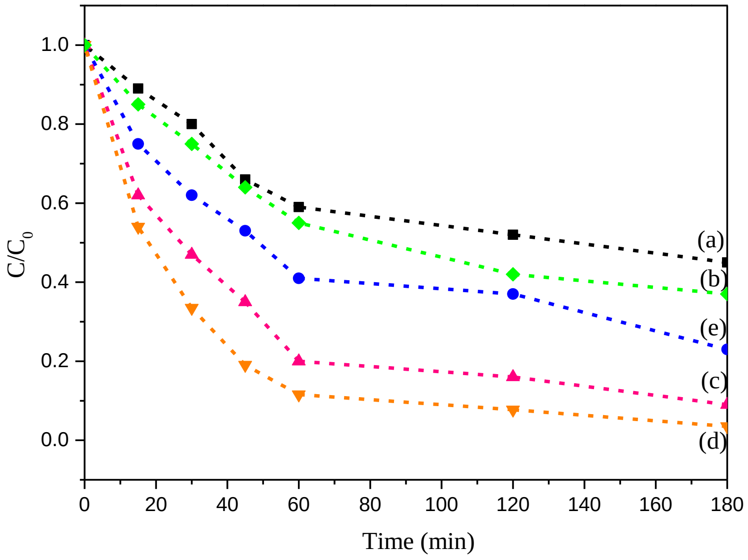

**Figure 4.26:** Photocatalytic activity of MWCNTs/$TiO_2$ at (a-e) pH 3, 5, 7, 9 and 11 for degradation of DMPEs

The photocatalytic activity of the MWCNTs/$TiO_2$ can also be quantitatively evaluated by comparing the apparent reaction rate constants. On the basis of previous reports, the photocatalytic activity of DMPEs is a pseudo-first order reaction when $C_0$ is low, and it's kinetic can be expressed as: $\ln (C_0/C) = kt$, where $C_0$ is the initial concentration and C is the concentration at time t. The plots of the concentration data gave a straight line. The results of fitting experimental data to first-order kinetics are tabulated in Table 4.8. The rate constant increased with increasing pH value up to pH 9 and then decreases with higher pH value, corresponding to the above mentioned changed in morphology. This showed that the MWCNTs/$TiO_2$ at pH 9 demonstrated the best photocatalytic activity for the degradation of DMPEs among the samples produced. The intimate contact between titania and MWCNTs at pH 9 allows for effective separation of charge carriers in the MWCNTs/$TiO_2$ nanocomposites, greatly reduces charge carrier recombination, increases the lifetime of the electron and holes and results in effective and possibly much more effcient pathway for the generation of radicals for the photodegradation of DMPEs. In addition, the photocatalytic activity of MWCNTs/$TiO_2$ nanocomposites increased with the increase of the degree of crystallinity, followed by decrease in the number of surface Ti defects sites which induced overall increase of photocatalytic activity. The decrease in photoactivity is related to the increased recombination rate of electron-hole pairs as a result of lower degree of crystallinity.

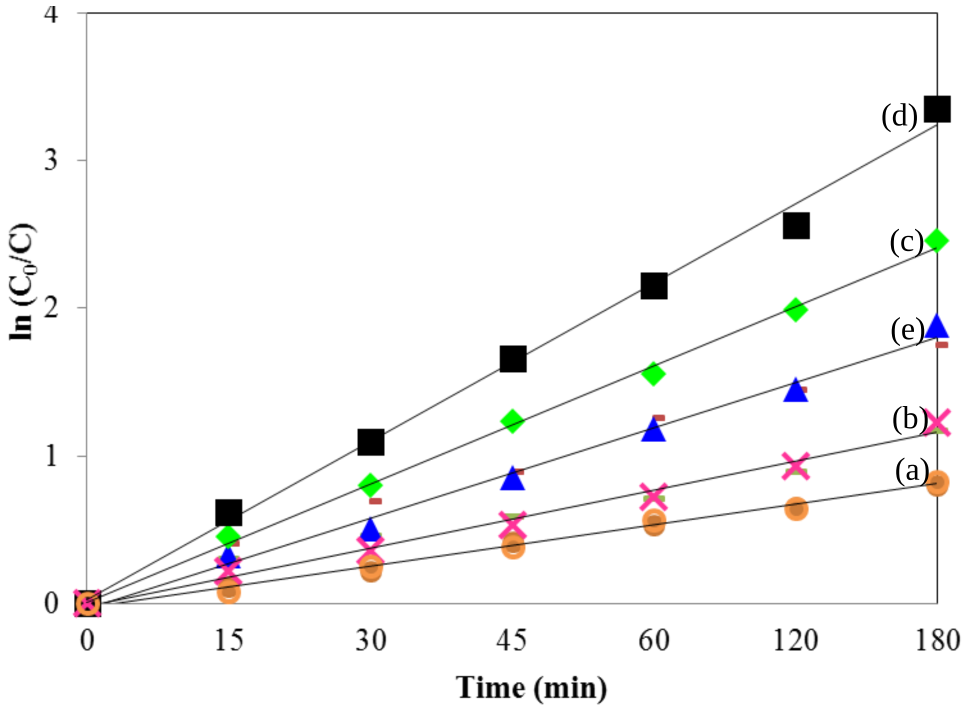

**Figure 4.27:** First-order kinetics for DMPEs photodegradation using MWCNTs/$TiO_2$ with different pH solution (a-e) pH 3, 5, 7, 9 and 11

**Table 4.8:** Rate constants for catalytic photodegradation of DMPEs using MWCNTs/$TiO_2$ nanocomposite

| **Samples** | **Rate constant (k)** | **$R^2$** |
|---|---|---|
| pH 3 | 0.0072 | 0.9956 |
| pH 5 | 0.0088 | 0.9749 |
| pH 7 | 0.0280 | 0.9903 |
| pH 9 | 0.0317 | 0.9953 |
| pH 11 | 0.01330 | 0.9750 |

### 4.4.6 Summary

The main aim of this work is to study the influence of the synthesis pH of the MWCNTs/$TiO_2$ solution in controlling the crystalline phases, the morphology and uniformity $TiO_2$ attached on the MWCNTs surface. In general at low pH, the $TiO_2$ partially covers the individual MWCNTs and this increases with the change in pH until the maximum pH of 9 in complete coverage of individual MWCNTs. It can be concluded that the pH value of the synthesis conditions dramatically affects the surface morphology of the MWCNTs/$TiO_2$ nanocomposites during the sol-gel process. It is noteworthy that as the increasing pH of the solution to pH 9, the crystallinity of the MWCNTs/$TiO_2$ nanocomposites increases as can be seen by the variation in anatase peak intensities in Figure 4.21. At pH 11, the decrease in the intensity of the anatase peaks can be attributed to processes such as coarsening and aggregation-recrystallization. In addition, it is suggested that higher pH likely leads to inferior crystal quality due to the mutual contact of surface hydroxyl groups between particles. The red-shift in UV-vis spectra occurred with the pH increasing up to pH 9 results in the lower band gap from 3.14 to 2.49 eV and this is attributed to the interaction of $TiO_2$ nanoparticles with the MWCNTs, which may modify the electron/hole pair recombination process under UV light irradiation. Thus, MWCNTs/$TiO_2$ nanocomposites at pH 9 gave the highest degradation efficiency of DMPEs among the samples.

## 4.5 Effect of Calcination Temperatures

Calcination is a key process during sol-gel preparation of MWCNTs/$TiO_2$ nanocomposites. The nanocomposites prepared at ambient temperature are normally in its amorphous state accompanied with crystalline imperfection. Thus, calcination at a certain temperature can lead to the formation of crystallite oxides.

### 4.5.1 Characterizations of MWCNTs/$TiO_2$ nanocomposites

Since crystallinity of the resultant MWCNTs/$TiO_2$ nanocomposites play an important role in determining the transportation of charge carrier. Therefore, optimization of the crystal structure during the heat treatment process for MWCNTs/$TiO_2$ nanocomposites is crucial in improving the photodegradation of DMPEs. The modified sol-gel method was duplicated for the preparation of MWCNTs/$TiO_2$ nanocomposites. The resultant MWCNTs/$TiO_2$ nanocomposites were then heat treated in the range of 350-750 °C in air atmosphere for 2 h at an interval of 100 °C.

#### 4.5.1.1 Phase Structure and Crystallinity analysis

Generally, $TiO_2$ possesses three different crystalline structures (e.g., orthorhombic brookite, tetragonal anatase and rutile). Specifically, rutile phase has been found to be the most stable structures and the amorphous MWCNTs/$TiO_2$ could be converted to crystalline anatase MWCNTs/$TiO_2$ during the calcination process. Accordingly, calcination temperature plays a critical role in determining the crystalline phases and sizes of MWCNTs/$TiO_2$. Figure 4.28 shows the XRD patterns of MWCNTs/$TiO_2$ calcined at different calcination temperatures ranging from 350 to 750 °C. Only anatase peak was observed for those MWCNTs/$TiO_2$ calcined at 350 ºC and the diffraction peaks were broad. This finding indicates that the crystallization is incomplete due to the presence of amorphous components on the grain boundary and thereby, the growth of the nanocrystallite is restricted. It is interesting to note the sharp anatase peaks and the increase in the intensity of these peaks by increasing the calcination temperature to 450 ºC. This designates the complete grain growth with improved crystallinity. Predominantly, there were only anatase peaks [i.e., 2θ=25.2 (101), 37.9 (004), 48.3 (200), 53.9 (105), 55.0 (211), 62.7 (204), 68.9 (116), 70.1 (220) and 75.5 (215)] detected in samples calcined at 350-650 ºC by referring to JCPDS reference pattern No. 21-1272. However, as shown in Figure 4.28 (e), it is noteworthy to mention that MWCNTs/$TiO_2$ illustrated the peak charateristics of both anatase and rutile phases when the calcination temperature was increased to 750 ºC. Specifically, the rutile peaks present at 2θ= 26.9 (110), 35.7 (101), 38.0 (200), 40.8 (111), 43.3 (210), 53.7 (211), 55.8 (220), 62.6 (200), 63.5 (310), 68.4 (301), 69.4 (112) and 74.9 (215). At 750 ºC, the rutile peaks became significant and the defects on the interface boundary were removed because of an increase in grain sizes. This was due to the cooperative movement of $Ti^{4+}$ and $O^{2-}$ ions involving the rupture of two of the six Ti-O bonds form new bonds of rutile at a higher temperature. Basically, the transformation involves the breaking and reforming of bonds (Hanaor and Sorrell, 2011). It is noteworthy that the conversion of minor fraction of anatase into rutile and the amount of anatase and rutile was calculated as 55 % and 45% in the mixed phase of MWCNTs/$TiO_2$ nanocomposites (An et al., 2014, Chen et al., 2009, Ouyang et al., 2013). The phase composition (rutile and anatase content) of 750 ºC-$TiO_2$/MWCNTs was calculated based on the following Equation 4.4:

$$X\mathrm{R} = 1 - [1 + 1.26\,(I\mathrm{R}/I\mathrm{A})]^{-1} \qquad \textbf{(4.4)}$$

where *X*R is the weight fraction of rutile in the mixture, and *I*R and *I*A are the peak intensities of the rutile (1 1 0) and anatase (1 0 1) diffractions, respectively. Accordingly, the crystallite size of MWCNTs/$TiO_2$ was found to increase with increasing of calcination temperatures. The diffraction peaks at 2θ = 25.9 and 43.2 corresponding with the (002) and (100) diffractions of the hexagonal graphite structure for MWCNTs samples. The peak at 2θ = 25.9 could not be seen for MWCNTs / $TiO_2$ nanocomposites due to the peak was overlapped by the strong anatase $TiO_2$ peak at 2θ= 25.2°. The MWCNTs is shielded by the peaks of anatase $TiO_2$ where the peak intensity of $TiO_2$ showing higher crystallinity than MWCNTs. However, the presence of MWCNTs in the composites could be further confirmed by Raman analysis as discussed later. The crystallite size of the $TiO_2$ anatase in MWCNTs/$TiO_2$ nanocomposites was calculated by the well-known Scherer's equation as tabulated in Table 4.9. The FWHM of the diffraction peaks decreased with increasing calcination temperature discloses that the average crystallite size is becoming bigger correspondingly.

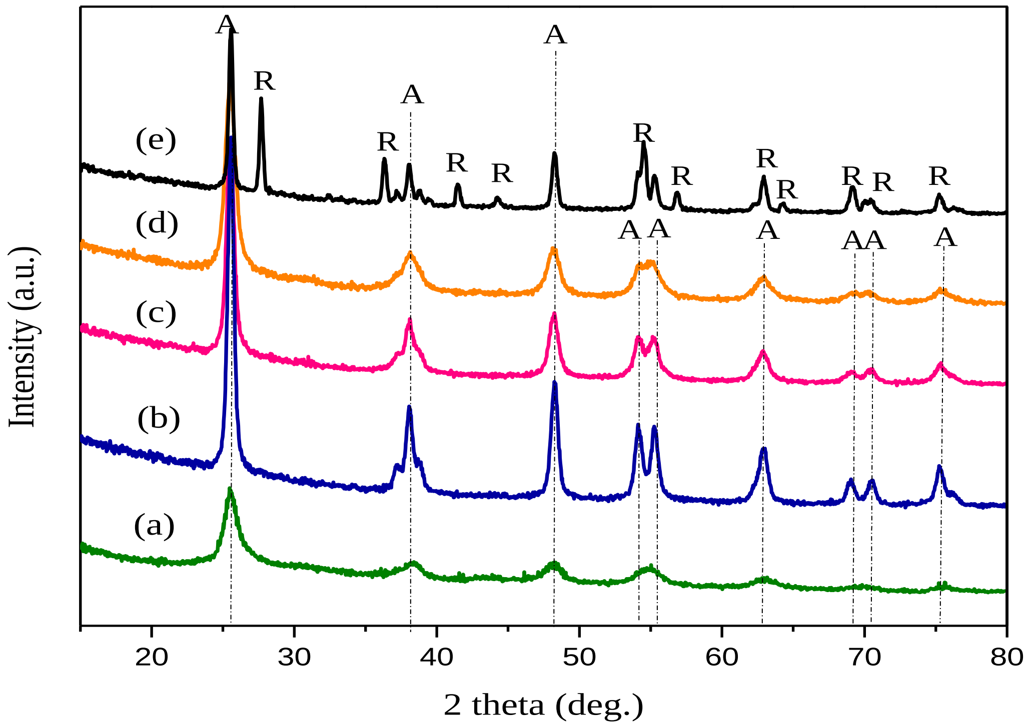

**Figure 4.28:** XRD spectra of MWCNTs/ $TiO_2$ nanocomposites calcined at (a) 350 °C, (b) 450 °C, (c) 550 °C, (d) 650 °C and (e) 750 °C

Table 4.9 summarizes the crystallite size, BET surface area and band gap energy of MWCNTs/$TiO_2$ nanocomposites with various calcination temperatures. It has been noticed that the width of peaks decreases with increasing of the calcination temperature due to the growth of crystals and construction to larger clusters. The slow increase of crystallite size in the early stage of calcination from 350 °C-450 °C, are due to the presence of water molecules and hydroxyl groups which prevent a rapid growth of crystals. Above 450 °C, the crystal growth increases rapidly with increasing in the calcination temperature which can be ascribed by more agglomerated crystals. The BET results based on the nitrogen adsorption measurements showed the MWCNTs/$TiO_2$ nanocomposites with various calcination temperatures. The BET surface area can be obtained from a linear portion of BET plot. Basically, a reduction of the surface area at higher temperatures can be associated to two effects: (i) sintering of $TiO_2$ nanoparticles as a result of the natural process to reach the lowest energy level of the particulate system and (ii) the decrease of the amount of MWCNTs in the sample due to thermal decomposition at higher temperature. It is noticeable that the surface area of MWCNTs/$TiO_2$ nanocomposites decrease with increasing in the calcination temperatures from 350 to 750 °C, indicating that the grain sizes increased with increasing calcination temperatures. This shows that the agglomeration of small grains to form larger grains at higher calcination temperature. It also can be attributed to the enhancement of nucleation and coalescence of grains. Rutile grains coarsen at the expense of neighboring anatase during coalescence until the large rutile grains begin to impinge in each other. Furthermore, a sharp decrease in specific areas for samples in the temperature range 450 °C to 750 °C are due to elimination of ammonia and chemically bonded water during development titania hydroxide to pure titania oxide. The high surface area of MWCNTs/$TiO_2$ composite at low calcination temperature lower than 450 °C suggests small size of particles.

The optical band gap of $TiO_2$ and MWCNTs/$TiO_2$ nanocomposites with various calcination temperatures were determined using the Kubelka-Munk expression and the estimated band gap was shown in Table 4.9. Heat treatment of MWCNTs/$TiO_2$ nanocomposites leads to changes in band gap energy. Among the series of catalysts, the MWCNTs/$TiO_2$ nanocomposites calcined at 350 °C showed the lowest band gap energy of 2.34 eV, while the MWCNTs/$TiO_2$ nanocomposites calcined at 750 °C showed the highest band gap energy of 2.93 eV. The different band gap energies might be attributed to the difference in the phase structure and surface microstructure in the MWCNTs/$TiO_2$ nanocomposites. The further details of the effect of MWCNTs content on band gap energy of MWCNTs/$TiO_2$ nanocomposites will be discussed in Section 4.5.1.4.

**Table 4.9:** Effect of various calcination temperatures on crystallite size, phase composition, surface area, and band gap energy of MWCNTs/ $TiO_2$ nanocomposites

| **Calcinations Temp. (ºC)** | **Crystallite size in XRD (nm)** | **Anatase (%)** | **Rutile (%)** | **Surface area, $m^2/g$** | **Band gap energy (eV)** |
|---|---|---|---|---|---|
| 350 | 7.5 | 100 | - | 252 | 2.45 |
| 450 | 8.9 | 100 | - | 108 | 2.48 |
| 550 | 12.9 | 100 | - | 91 | 2.64 |
| 650 | 18.7 | 100 | - | 54 | 2.65 |
| 750 | 24.3 | 55 | 45 | 23 | 2.93 |

### 4.5.1.2 Morphological Studies

The effects of calcination temperatures on the morphology of the MWCNTs/$TiO_2$ were studied. Figure 4.29 shows the FESEM micrographs of MWCNTs/$TiO_2$ calcined at various temperatures. Accordingly, it is clearly shown in Figure 4.29(a) that the MWCNTs/$TiO_2$ nanocomposites calcined at 350 ºC consist of small spherical $TiO_2$ particles adhered on the surface of MWCNTs; $TiO_2$ was found uniformly coated along the surface of MWCNTs with minimum agglomeration after calcinating the MWCNTs/$TiO_2$ at 450 ºC. From the literature, the particle with a lower sintering temperature had a higher agglomeration tendency, suggesting that the tendency of particle to sinter together was enhanced above the minimum sintering temperature. Basically, the functional groups (-COOH) present at the surface of MWCNTs promote the anchoring of the $TiO_2$ nanoparticles as well as avoiding agglomeration and subsequently increasing the surface area of the resulting MWCNTs/$TiO_2$ composite. Relatively bigger and irregular $TiO_2$ aggregates were detected on the surface of MWCNTs for those MWCNTs/$TiO_2$ calcined at 550 ºC. It is interesting to note that hollow tubular structure of MWCNTs disappeared when the calcination temperature was increased to 650 ºC. This is associated to the oxidation of MWCNTs at higher temperature as confirmed by the TGA thermogram. Additionally, it was found that the particle size of MWCNTs/$TiO_2$ increased with increasing calcination temperature from 350 to 750 ºC. Accordingly, the particle size of mixed phases (anatase + rutile) of the MWCNTs/$TiO_2$ calcined at 750 ºC was found to be the largest. This is in good agreement with the XRD data (Hamid et al., 2014, Mohammadi and Sabbaghi, 2014, Ouyang et al., 2013, Réti et al., 2014).

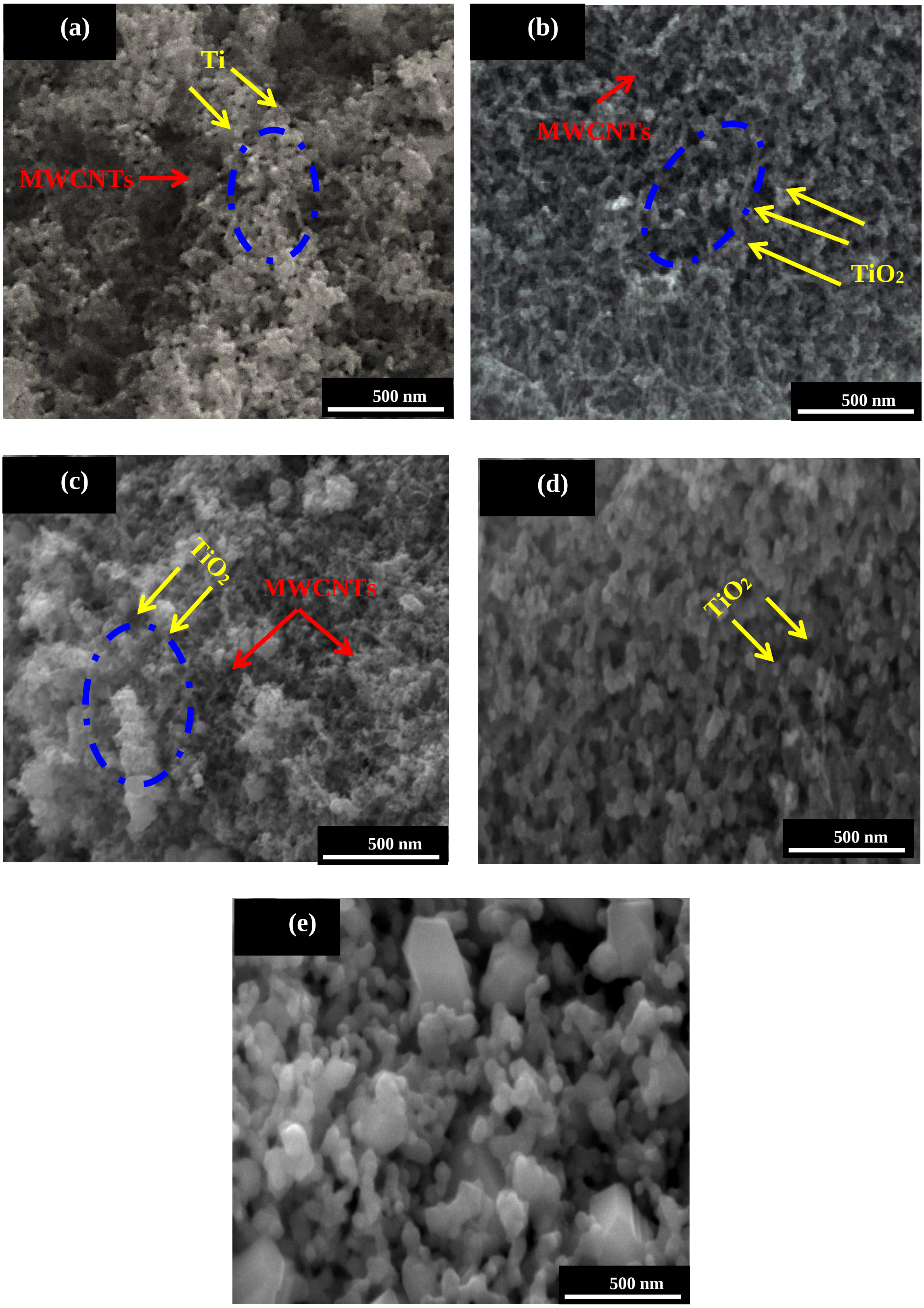

Figure 4.29: FESEM images of MWCNTs/ $TiO_2$ nanocomposites calcined at (a) 350 °C, (b) 450 °C, (c) 550 °C, (d) 650 °C and (e) 750 °C

#### 4.5.1.3 Raman analysis

Figure 4.30 illustrates the Raman spectra of MWCNTs/$TiO_2$ calcined at different temperatures. It is noteworthy that all samples calcined at various temperatures ranging from 350-750 ºC exhibit Raman peaks corresponding to the anatase phase of $TiO_2$ (143 $cm^{-1}$ ($E_g$ anatase vibration mode), 198 $cm^{-1}$($E_g$ mode), 395 $cm^{-1}$($B_{1g}$ mode), 517 $cm^{-1}$($B_{1g}$ + $A_{1g}$ mode) and 639 $cm^{-1}$ (weak $E_g$ mode)), and the presence of D band (1315 $cm^{-1}$) and G bands (1594 $cm^{-1}$) in the samples of 350-550 ºC. D and G bands were only observed on those samples calcined at 350-550 ºC. At 350 °C, relatively low intensity of Eg mode was present ascribed to the oxygen defects that give rise to the broadening and shifting of the entire peaks. The intensity of anatase Eg mode at 144 $cm^{-1}$ was found to increase with increasing the calcination temperatures. This is due to the fact that the increase of the calcination temperatures tends to transform the anatase phase to rutile, increasing the crystallite size, decreasing the oxygen defects and thus shifting the peak. For those samples calcined at temperature 750 ºC, relatively low intensity of Eg anatase peak was detected and the sharp rutile peaks only appeared at 240, 450 and 620 $cm^{-1}$. Considering these facts, the positions of Raman peaks were found shifting along with the rearrangement of $TiO_6$ octahedral and the formation of the mixed phase at 750 ºC was in good agreement with the XRD result. Apart from that, it can be seen that both the D and G bands disappeared once the calcination temperature was increased exceeding 550 ºC. This can be explained by the thermal decomposition of MWCNTs at 637 °C (Hamid et al., 2014, Muduli et al., 2009, Réti et al., 2014).

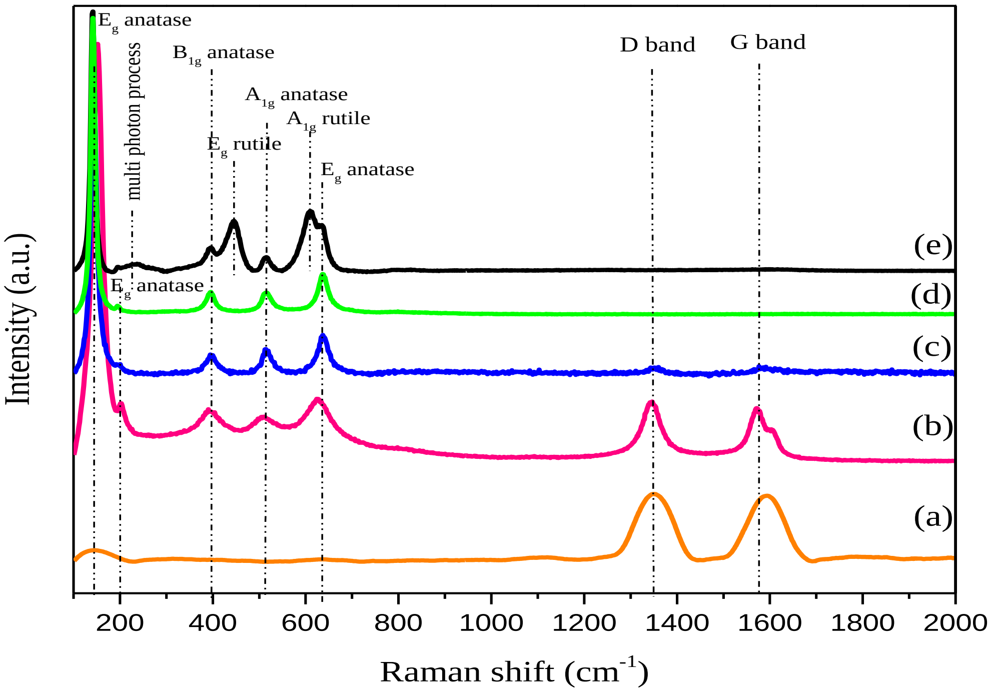

**Figure 4.30:** Raman spectra of MWCNTs/ $TiO_2$ nanocomposites calcined at (a) 350 °C, (b) 450 °C, (c) 550 °C, (d) 650 °C and (e) 750 °C

The thermal stability and the oxidation weight loss conditions of MWCNTs and MWCNTs/$TiO_2$ composites were determined via TGA (Figure 4.31). In the case of TGA of MWCNTs, it can be seen that the combustion points was found approximately at 654 °C due to the highest rate of weight loss, 86.8 % as reported in Figure 4.31 (a). For the MWCNTs, the thermal decomposition starts at 550 °C and quickly increase up to 654 °C, indicating there is no amorphous carbon in accordance with literature. For the 10 wt % of MWCNTs/$TiO_2$ nanocomposites, the initial weight loss was due to the water evaporation at around 100 °C and followed by the thermal decomposition of MWCNTs at 637 °C. Based on the literature, for TGA of CNT/metal oxide nanocomposites, it is expected to have the weight loss between 250 to 500 °C and can be attributed to condensation reactions of metal hydroxyl residual groups on the surface of the prepared nanocomposites materials.The total weight loss was determined as 25.8

% and it is indicated that $TiO_2$ becomes the major element after the combustion temperature of MWCNTs. (Hamid et al., 2014).

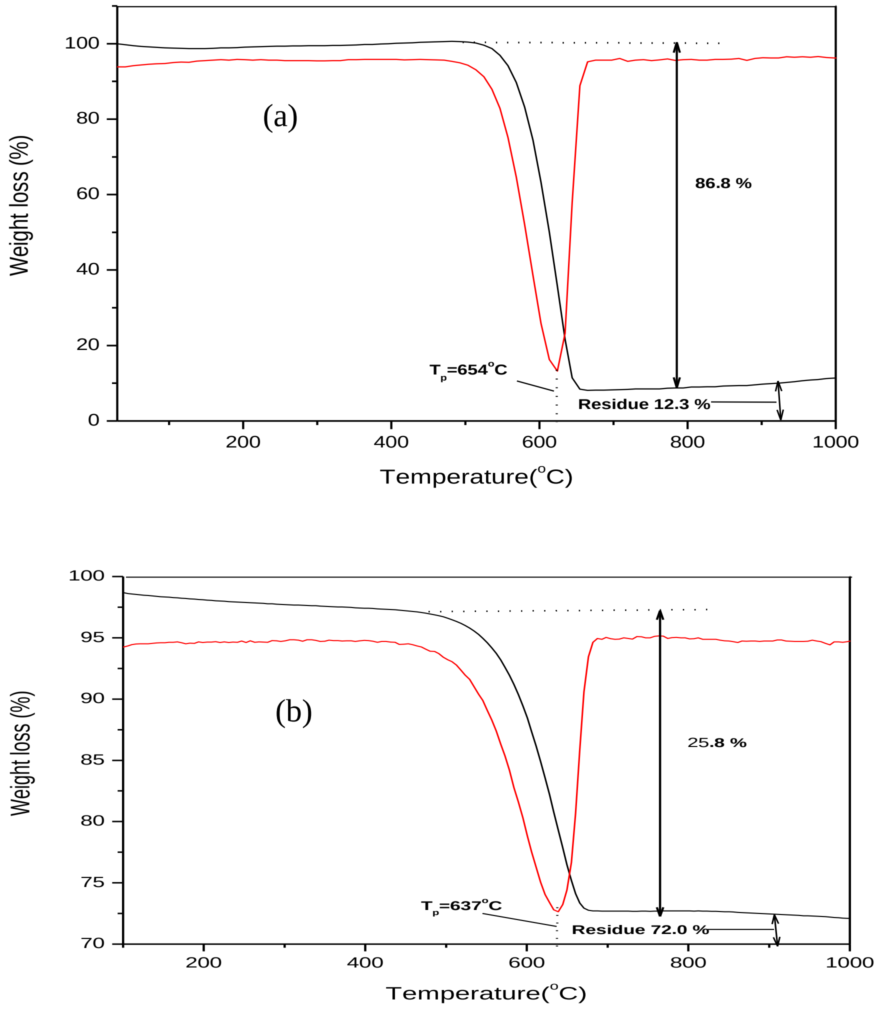

**Figure 4.31:** TGA curves of (a) Purified MWCNTs and (b)10 wt % MWCNTs/$TiO_2$ nanocomposites

#### 4.5.1.4 Light absorption and photoluminesce (PL) properties

UV-vis spectroscopy was used in the present study to determine the optical properties of the MWCNTs/$TiO_2$ calcinated at various temperatures. Figure 4.32 shows the light absorbance spectra of MWCNTs/$TiO_2$ samples. Noted that the band gap energy of the pure anatase $TiO_2$ is 3.2 eV, there was a significant shift towards the longer wavelengths in the presence of MWCNTs in MWCNTs/$TiO_2$. Accordingly, the absorption edge of MWCNTs/$TiO_2$ was found to have an inversely proportional relationship with the calcination temperature, in which the absorption edge shifted to the shorter wavelength with increasing calcination temperature. Specifically, the absorption edges of the sample calcined at 350, 450, 550, 650 and 750 °C were found to be 506, 500, 469, 468 and 423 nm, respectively. The reduction of light absorbance with calcination temperature with a decrease in the band gap energy could be ascribed to the decomposition of the carbon at relatively high calcination temperature. Thus, without the presence of MWCNTs in the nancomposites, there is no formation of Ti-O-C bond and thus the band gap energy increased. Table 4.9 tabulated the band gap energy of MWCNTs/$TiO_2$ estimated from the Kubelka-Munk functions. Among them, MWCNTs/$TiO_2$ calcined at 750 °C exhibited highest band gap energy. The increase of band gap energy may be due to the influences of surface morphology. High temperature calcination can lead to small specific surface area and thus the formation of larger agglomerate particles, since MWCNTs are burned off thoroughly at high temperature (Ouyang et al., 2013, Réti et al., 2014, Saleh and Gupta, 2012).

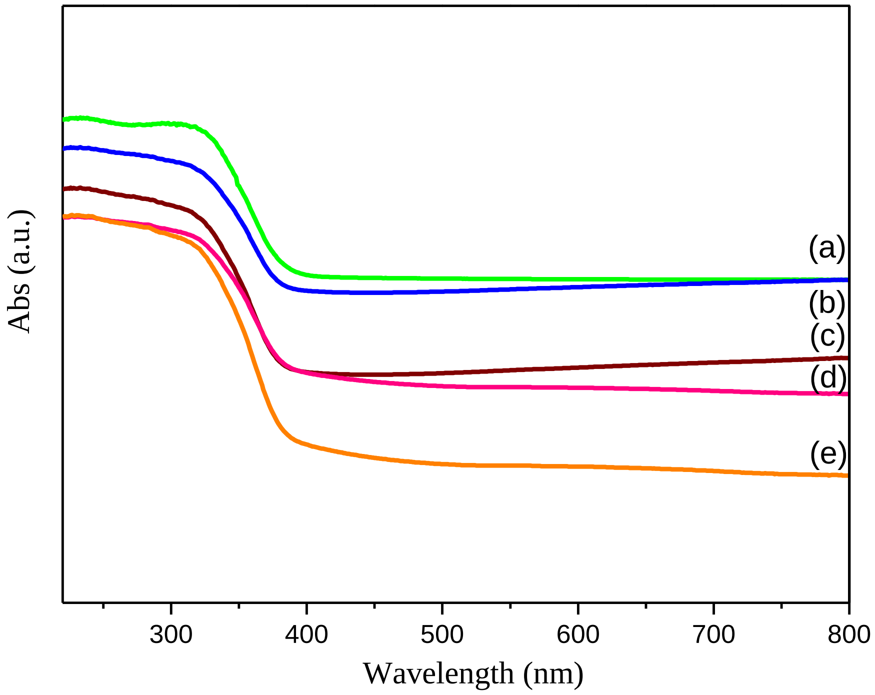

**Figure 4.32**:UV spectra of MWCNTs/ $TiO_2$ nanocomposites calcined at (a) 350 °C, (b) 450 °C, (c) 550 °C, (d) 650 °C and (e) 750 °C

PL analysis was used in the present study to investigate the possibility of charge carrier trapping and, immigration as well as to understand the transfer, separation and fate of the photogenerated electron-hole pairs in semiconductor. Figure 4.33 shows that the PL spectra of MWCNTs/$TiO_2$ nanocomposites calcined at various calcination temperatures. The overall sequence in the decreasing order of PL intensities was found to be 350°C > 450°C > 550°C > 650°C > 750 °C, also, the emission bands appeared between 425 nm and 433 nm could be attributed to self-trapped excitons, while the other emission peaks between 440 nm to 500 nm could be ascribed to the surface oxygen vacancies, impurities and defects present in MWCNTs/$TiO_2$. It is also noteworthy the PL intensity increased with increasing the calcination temperatures. This implies the increase in the recombination rate in MWCNTs/$TiO_2$ due to the decomposition of MWCNTs at relatively high calcination temperature. Adversely, at relatively low calcination temperature, MWCNTs/$TiO_2$ possessed comparatively lower PL intensity. This gives us a hint that MWCNTs acted as electron reservoir to trap electrons from the $TiO_2$ and thereby, significantly reduced the rate of recombination of the photo-induced electrons and holes in the MWCNTs/$TiO_2$. Additionally, the shift of peaks might be induced by electron trapping at the active site prior to recombination. In addition, the continuous growth of crystallite size with temperature, results in a continuous decrease of the surface-to-volume-ratio, which in turn reduces the luminescence quenching defects. In fact, the increase of the PL emission is associated to defects in $TiO_2$ structure, originating energy states or oxygen vacancies. An increase of the oxygen defects is caused by higher heat treatment temperatures, originating less photoactive composites (Gui et al., 2014a, Zhao et al., 2013).

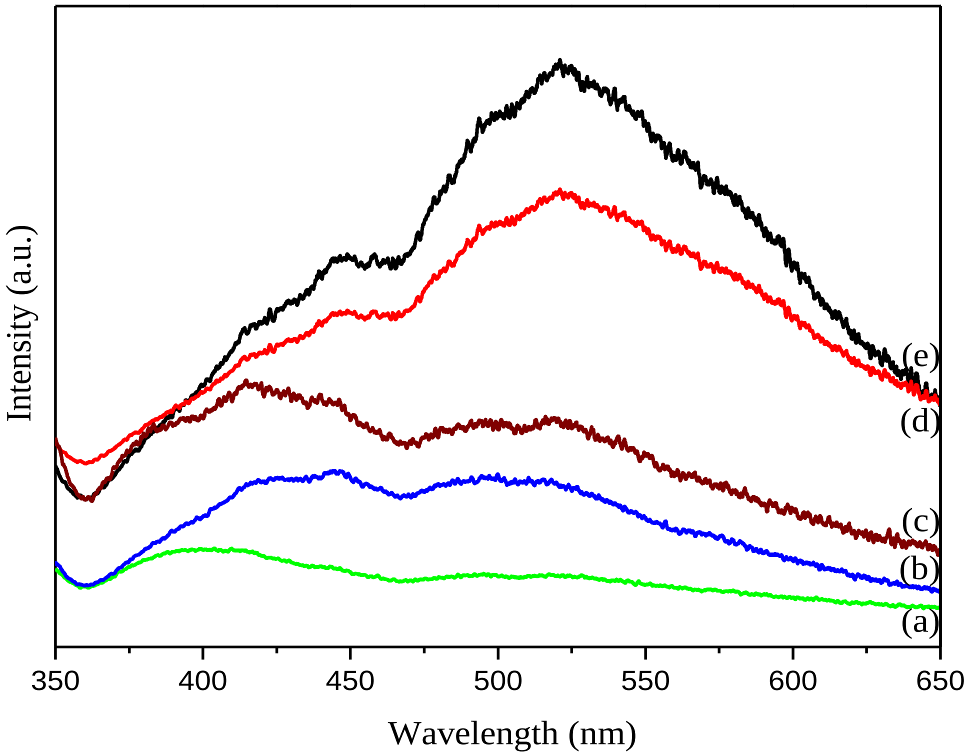

**Figure 4.33:** PL spectra of MWCNTs/ $TiO_2$ nanocomposites calcined at (a) 350 °C, (b) 450 °C, (c) 550 °C, (d) 650 °C and (e) 750 °C

#### 4.5.1.5 Photocatalytic activity On DMPEs

Figure 4.34 shows the effect of calcination temperatures on the photocatalytic activity of DMPEs. Accordingly, it is worth to mention that the degradation efficiency of DMPEs increased when the calcination temperature was increased from 350 to 450 ºC, after which there was a drop. In this respect, it can be concluded that MWCNTs/$TiO_2$ calcined at 450 ºC possessed the highest photocatalytic activity. This is probably ascribed to the increase in degree of crystallinity and a good interfacial contact between MWCNTs and $TiO_2$. Meanwhile, the photocatalytic activity of MWCNTs/$TiO_2$ calcined at 350 ºC was lower than that of those calcined at 450 ºC could be explained by the incomplete formation of crystallite oxides. It is interesting to note that, even though the intensity of anatase peaks increased with increasing the calcination temperature, the photocatalytic performance reduced with calcination temperature. This might be related to the formation of large crystallite size of titania at high calcination temperatures and reduced surface area of the MWCNTs/$TiO_2$ nanocomposites. Furthermore, the increase in particle size of MWCNTs/$TiO_2$ with increasing the calcination temperature (supported by the FESEM images) might induce a reduction in quantum size effects (An et al., 2013). It was also noticed that, the photocatalytic activity for those MWCNTs/$TiO_2$ calcined at high temperature (i.e., that is 750 ºC) was found to be the lowest. One possible explanation is the decomposition of MWCNTs during the calcination process. On top of that, literatures also reported that pure anatase of $TiO_2$ possesses a relatively higher photocatalytic activity than that of the rutile phase ascribed to its lower recombination rate. Anatase is the most active phase for photocatalysis which is ascribed to the higher density of localised states and consequent surface-adsorbed hydroxyl radicals and slower charge carrier recombination in anatase relative to rutile. As a result, higher levels of radicals adsorbed on the anatase surface give rise to significantly higher photoactivity than rutile (An et al., 2014, Chen et al., 2014, Da Dalt et al., 2013, Fujishima and Zhang, 2006). Also, the MWCNTs loss with calcination temperature increasing promoted the recombination of photogenerated holes and electron. These factors may result in the decrease in photocatalytic activity. Simultaneously, the larger-sized $TiO_2$ nanoparticles resulted from higher temperatures also gives raise to decrease in the photocatalytic performance of the composites.

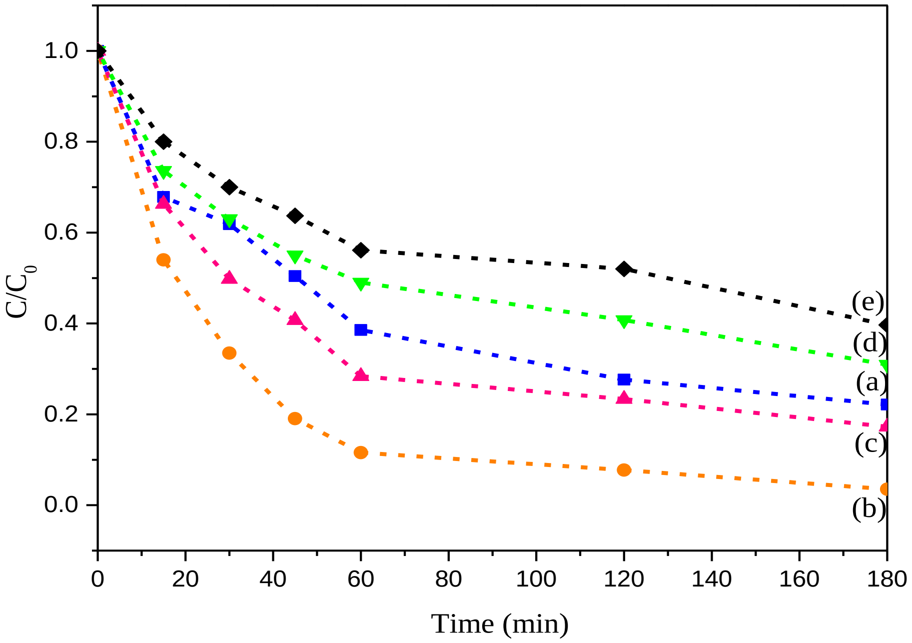

**Figure 4.34:** Photocatalytic activity of MWCNTs / $TiO_2$ calcined at (a) 350 °C, (b) 450 °C, (c) 550 °C, (d) 650 °C and (e) 750 °C for degradation of DMPEs

The kinetics for the degradation of DMPEs by titania-based photocatalysts has been well studied in the literature, and the data can be fitted using a pseudo first order kinetic equations, $\ln (C_0/C) = kt$, where $C_0$ is the initial concentration and C is the concentration at time t. The kinetics of photocatalyzed degradation of DMPEs is illustrated in Figure 4.35. The plots of the concentration data gave a straight line. The results of fitting experimental data to first-order kinetics are tabulated in Table 4.10. The rate constant increased with increasing calcination temperature up to 450 °C and then decreases with higher calcination temperature. This shows that the MWCNTs/$TiO_2$ calcined at 450 °C demonstrated the best photocatalytic activity for the degradation of DMPEs among the samples produced. This might be ascribed to the increased crystalline order that has the beneficial effects of decreasing the number of defects and reducing the band gap. The present results indicated that a suitable calcination temperature is crucial for optimizing the photocatalytic activity of MWCNTs/$TiO_2$ nanocomposites.

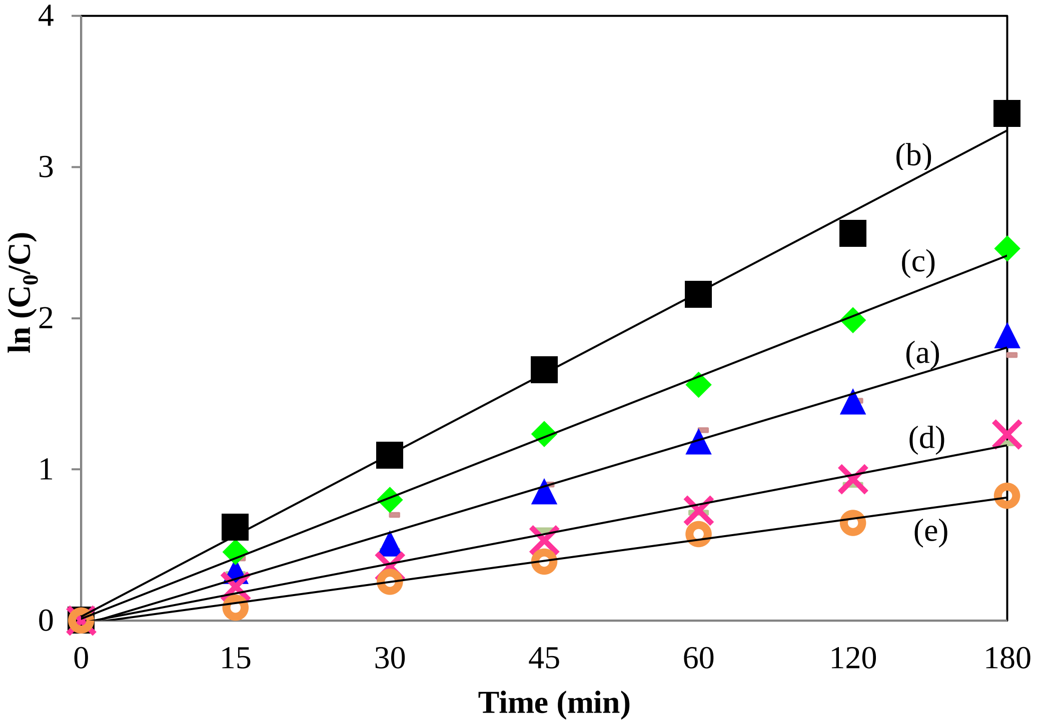

**Figure 4.35**: First-order kinetics for DMPEs photodegradation using MWCNTs/$TiO_2$ calcined at (a) 350 °C, (b) 450 °C, (c) 550 °C, (d) 650 °C and (e) 750 °C

**Table 4.10:** Rate constants for catalytic photodegradation of DMPEs

| **Samples** | **Rate constant (k)** | **$R^2$** |
|---|---|---|
| 350 | 0.0154 | 0.9928 |
| 450 | 0.0317 | 0.9928 |
| 550 | 0.0189 | 0.9891 |
| 650 | 0.0125 | 0.9982 |
| 750 | 0.0095 | 0.9953 |

### 4.5.1.6 Summary

In this study, calcination temperatures have a great influence on the photodegradation of DMPEs and the effect of calcination temperature on the structural, morphology and optical properties of MWCNTs/$TiO_2$ nanocomposites were investigated in detail. By the increasing temperature from 350°C to 750°C, the crystalline structure changes from anatase phase to mixed phase (anatase + rutile). Moreover, the $TiO_2$ nanoparticles size on MWCNTs surface became bigger by rising the calcination temperature from 350 to 750 °C as supported by FESEM images. This shows that the agglomeration of small grains to form larger grains at higher calcination temperature. It also can be attributed to the enhancement of nucleation and coalescence of grains. UV-vis spectroscopy indicated that the UV-vis absorption characteristics can be tuned by varying the calcination temperature. The blue-shift in UV-vis spectra occurred with the increasing of calcination temperature result in the larger band gap from 2.45 to 2.93 eV and this should be attributed to the decomposition of the carbon with increasing calcination temperature. From the result, increasing the calcination temperature from 350 to 450 ºC increases the degradation efficiency of DMPEs because of more crystallinity of $TiO_2$ with the presence of MWCNTs. MWCNTs/$TiO_2$ nanocomposites calcined at 450 ºC shows the highest photocatalytic performance and by increasing the calcination temperature, the photocatalytic activity decreases. Beyond 450°C, the photocatalytic activity of MWCNTs/$TiO_2$ decreased due to the formation of larger crystallite size that reduces the surface area of the nanocomposites and the decomposition of MWCNTs. This indicated that MWCNTs play an important role in the transfer and storage of photogenerated electrons and hereby increased the charge separation and the photocatalytic performance of the MWCNTs/$TiO_2$ nanocomposites.

## 4.6 Chemical State Analysis by XPS

Further information regarding the chemical and bonding environment of purified MWCNTs, $TiO_2$ and 10 wt % MWCNTs/$TiO_2$ nanocomposites calcined at 450 °C under pH 9 was ascertained from XPS studies. XPS analysis was performed to determine and have a better understanding of the interaction of MWCNTs with $TiO_2$ nanoparticles. The information of elements and the composition can be obtained from the survey scan spectrum of XPS. Figure 4.36 shows the survey spectra for $TiO_2$ nanoparticles as Ti LMM, O KLL Augers peaks and XPS spectra peaks of Ti and O were recorded for $TiO_2$. With reference to functionality grafting, XPS is one of the surface analytical techniques, which can provide useful information on the nature of the functional group (-COOH) and also on the presence of structural defects on the nanotube surface. The XPS survey scan of C1s and O1s peaks of the pre-treatment of CNTs with $HNO_3$ are presented. In addition, it shows only the presence of element C and O which indicated that the metal catalyst residue (i.e. nickel, cobalt, and iron) is removed from the sample during the pre-treatment step with $HNO_3$. Basically, the commercial pristine MWCNTs synthesized by CVD containing carbonaceous impurities and metal catalyst particles (Jiang et al., 2011, Tseng et al., 2010). Besides, the XPS survey scan of 10 wt % MWCNTs/$TiO_2$ clearly reveals that the main elements on the sample surface were Ti, C, and O elements.

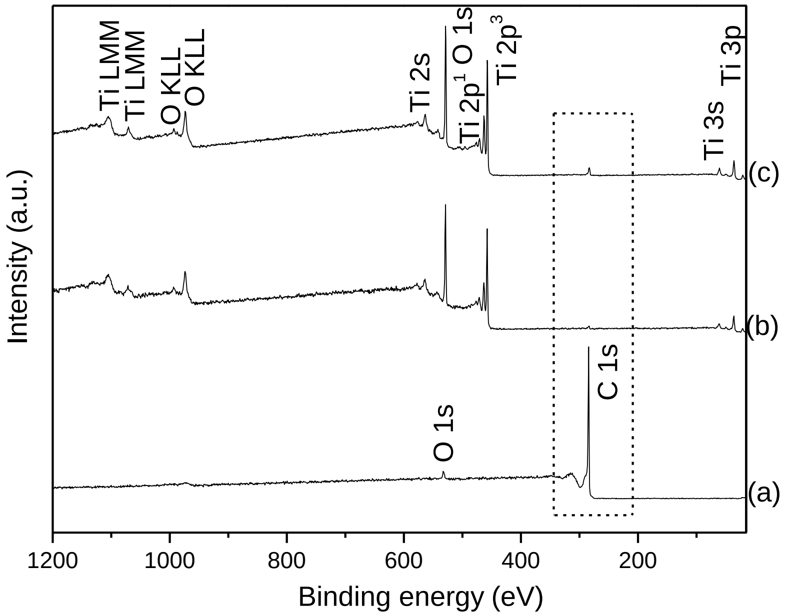

**Figure 4.36**: XPS survey spectra of 10 wt % MWCNTs/$TiO_2$ nanocomposites synthesized at pH 9 and calcined at 450 °C, $TiO_2$ and purified MWCNTs

Figure 4.37 shows the XPS narrow scan of $TiO_2$. Figure 4.37 (a) reveals that Ti $2p_{3/2}$ and Ti $2p_{1/2}$ have the binding energies of ~458.7 eV and ~464.5 eV, respectively, indicating the presence of $Ti^{4+}$ in $TiO_2$. This also implies that titanium atoms could react with any available oxygen to form the oxidized titanium. Figure 4.37(b) indicated that oxygen existed in two different forms as the core peak O1s in $TiO_2$. Specifically, the first band at 529.9.eV was attributed to a reduced form corresponding to oxygen atoms bound to the titanium atoms (Ti-O), while the another peak of O1s at 530.6 eV was assigned to the hydroxyl groups on $TiO_2$ (Tian et al., 2011, Zhao et al., 2013).

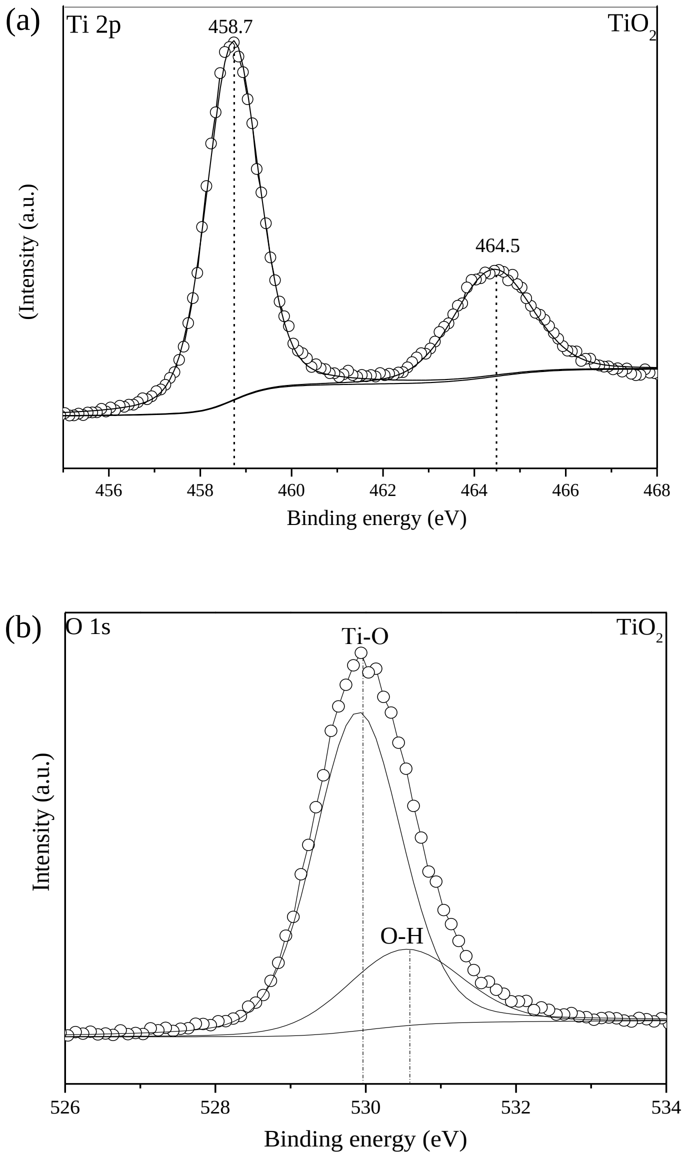

**Figure 4.37**: The XPS narrow scan of $TiO_2$ (a) Ti 2p and (b) O 1s

In Figure 4.38, the XPS narrow can of C1s and O1s peaks of the pre-treatment of CNTs with $HNO_3$ are presented. As shown in Figure 4.38a, the deconvolution of the C1s peak of the as-received MWCNTs showed a main peak at 284.8 eV. This is attributed to the graphitic structure of MWCNTs and is in agreement with the recent photoemission studies on MWCNTs. On top of that, the peak at 285.7 eV was assigned to defects on the nanotube structure, while, the peaks at 287.4 and 288.8 eV were corresponding to carbon atoms attached to different oxygen-containing moieties (An et al., 2014, Chen et al., 2014, Muduli et al., 2009). During the purification, the tips of MWCNTs are opened up and defects are produced at the MWCNTs neck. Amorphous and metal particles (including those entrapped between MWCNTs layers) will be dissolved by acid and leave defect on the MWCNTs sidewall. Those defects are oxidized and carboxyl groups are attached. Also, the π–π∗ transition loss peak was detected at 291.3 eV. As illustrated in Figure 4.38 (c), the deconvolution of XPS O1s peak at 533.3 eV and 531.9 eV confirmed the presence of some carboxylic and hydroxyl functions on the surface of CNT surface.

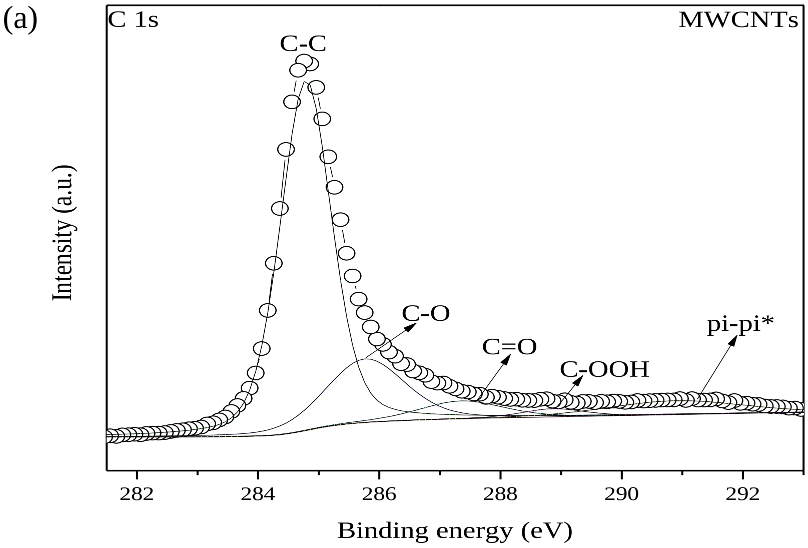

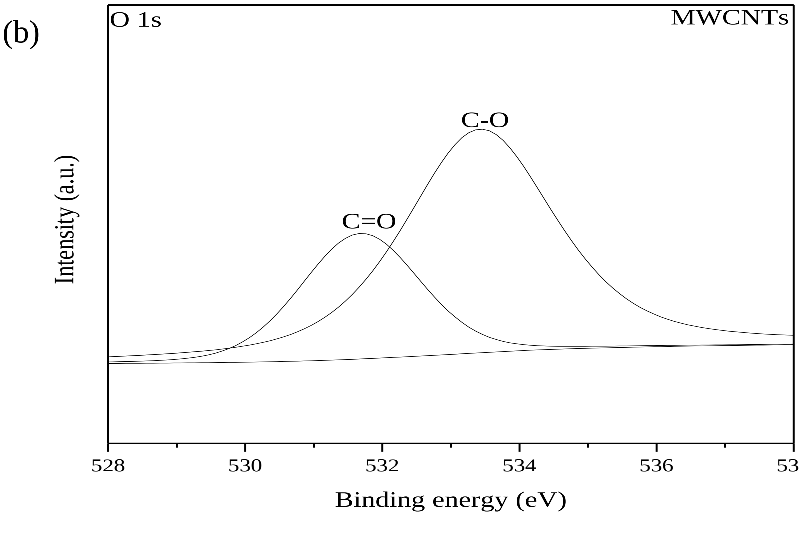

**Figure 4.38:** The XPS narrow scan of MWCNTs (a) C 1s and (b) O 1s

In order to study the formation of the chemical bonds between Ti-O-C and Ti-C after loading $TiO_2$ with MWCNTs, the interaction between $TiO_2$ with MWCNTs was investigated by the analysis of XPS results as shown in Figure 4.39. Figure 4.39 (a) reveals the Ti ($2p_{3/2}$, $2p_{1/2}$) spectra, and the binding energies of Ti $2p_{3/2}$ and Ti $2p_{1/2}$ were found to be 458.7 and 464.4 eV, respectively. These findings indicate the presence of $Ti^{4+}$ in the $TiO_2$. Figure 4.39(b) shows the O1s spectra of the MWCNTs/$TiO_2$ sample (calcined at 450 °C). There were basically, four peaks observed. The O 1*s* peak at 529.9 eV correspond to Ti-O-Ti (lattice oxygen), while the higher binding energies of 530.6 eV are assigned to Ti-O-C bond respectively. The other peaks centered at 531.8 eV and 532.11 eV are attributed to Ti-OH and C-O groups for MWCNTs/$TiO_2$ composites. Figure 4.39(c) displays the C 1s spectra of the MWCNTs/$TiO_2$ sample. Five peaks were observed in the C 1s spectra after peak fitting. The main peak located at 284.7 eV was associated with graphitic carbon and C–C bonds from MWCNTs. The second peak at 286.1 eV was attributed to C–O bonds, and the broad peaks located at 287.4 eV and 289.1 eV represented the C=O and COOH bonds, respectively. The presence of new peak at about 283.7 eV further supported the formation of titanium-carbide bond. It is thereby concluded that the Ti–O and C–O bonds that present in the C 1*s* and O 1*s* XPS spectra after the peak fitting led to the anticipation of intimate connection between MWCNTs and $TiO_2$ through Ti–O–C bonds. The formation of Ti-O-C bonds between the carboxylic acid groups of MWCNTs and the hydroxyl groups existent at the surface of $TiO_2$ during an esterification reactions, contribute to a synergetic effect due to the creation of an electronic interphase interaction between MWCNTs and $TiO_2$ phases. The binding of MWCNTs and $TiO_2$ may be advantageous for the transport of electrons through the MWCNTs/$TiO_2$ composites (Bergmann and Machado, 2015, Chen et al., 2014, Da Dalt et al., 2013, Leary and Westwood, 2011).

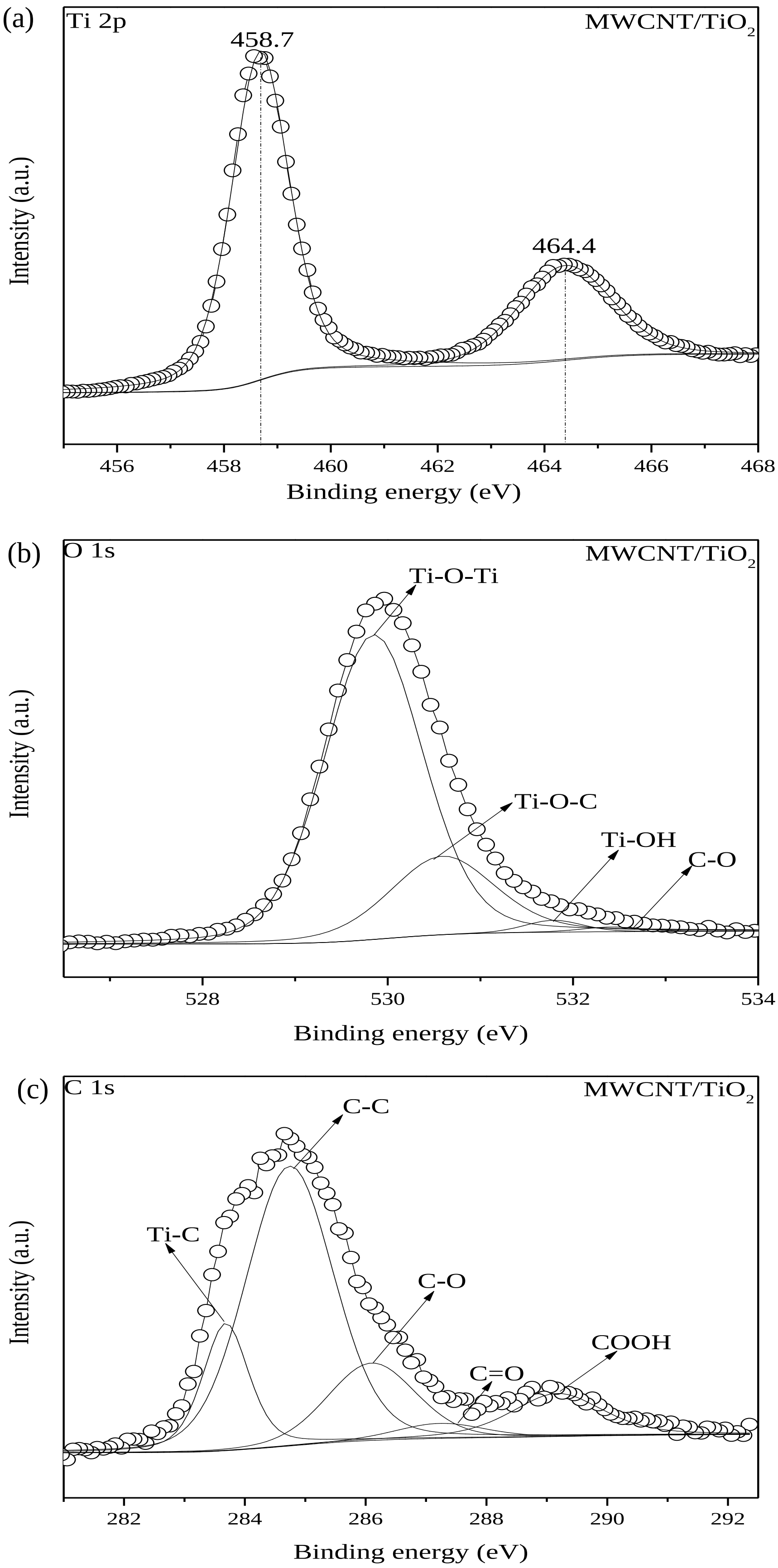

**Figure 4.39:** The XPS narrow scan of MWCNTs/TiO$_2$ nanocomposites (a) Ti 2p, (b) O 1s and (c) C 1s

## 4.7 Parameter studies in photocatalytic degradation process

Based on the aforementioned discussion, 10 wt% of MWCNTs/$TiO_2$ nanocomposites was synthesized via modified sol-gel method under pH 9 and subsequently annealed at 450 °C exhibited the best photocatalytic performance. A maximum photodegradation rate was achieved. Since process variables, such as irradiation time, solution pH, initial concentration of DMPEs, catalyst dosage and $H_2O_2$ dosage play an important role in determining the photocatalytic activity of MWCNTs/$TiO_2$ nanocomposites. Therefore, in the following studies, MWCNTs/$TiO_2$ nanocomposites were synthesized in such condition mentioned above to study the effect of irradiation time, solution pH, initial concentration of DMPEs, catalyst dosage and $H_2O_2$ dosage, on the photodegradation of DMPEs. Most of the research work reported recently are limited to the removal of DMPEs at higher concentration; however, the concentrations of PAEs in highly industrialized Klang Valley, Malaysia have found varying concentrations of PAEs ranging from 0.1 to 64.3 µg/L in the river water (Sin et al., 2011). In this research works, a higher concentration of DMPEs, 1 mg/L, was chosen. According to the parameters reported in the literature, the other operating parameters were fixed at pH 6 of solution pH and 3 h of reaction time before each of the parameter was selected (Zhu and Jiang, 2014).

### 4.7.1 Effect of irradiation time

The effect of irradiation time on the photocatalytic degradation of DMPEs from its aqueous solution was investigated from 0 to 240 min, at 1 mg/L DMPEs concentration, 0.5 g/L catalyst concentration and pH= 6.0. Figure 4.40 presents the degradation efficiency of DMPEs under various experimental conditions. It can be seen that only small changes in concentration were observed when the experiment was performed either with UV only (4 %) or with a photocatalyst in the darkness (8 %), indicating the stability of the DMPEs. This result confirms that degradation of the DMPEs in the presence of photocatalyst, but without light irradiation is insignificant. The reason is that no electron-hole pair could be generated in the semiconducting material without the assistance of light irradiation. The removal percentage of DMPEs increased dramatically in the presence of MWCNTs/$TiO_2$ nanocomposites and UV light, which confirms the synergistic effect between the catalyst and UV irradiation for efficient degradation. It is worth to mention that the MWCNTs/$TiO_2$ exhibits higher degradation efficiency (97 %) for 240 min compared to $TiO_2$ (75 %), for the same irradiation time which could be attributed to the high surface area of MWCNTs that favour the adsorption of DMPEs on the photocatalyst surface. The adsorption capacity of CNTs is very fast, which is mainly due to the highly accessible adsorption sites and the short intraparticle diffusion distance, which is related to their large specific surface area. This study shows that CNTs possess good structural integrity and chemical inertness support with relatively high oxidation stability which could endow CNTs more excellent performances as support for photocatalytic active (Liao and Wang, 2009, Zhao et al., 2013). For the $TiO_2$ or MWCNTs/$TiO_2$ nanocomposites, the photodegradation efficiency increases with time, up to 180 min, and thereafter, there is no noticeable change (Table 4.11). The result indicates that when the time of irradiation increases, the percentage of degradation increases and reaches a maximum at three hour irradiation. As time increases, more and more light energy falls on the catalyst surface which increases the formation of photoexcited species and enhances the photocatalytic activity. This indicates that photocatalytic degradation of DMPEs with catalyst for 180 min is the ideal irradiation time and it was adopted to investigate the effects of other parameters in the following studies.

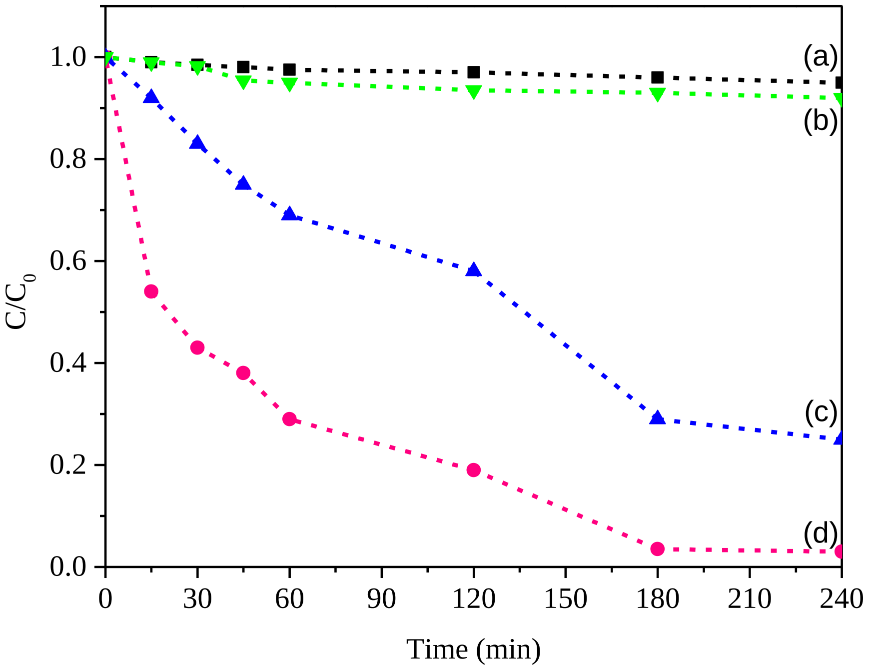

**Figure 4.40:** Effect of irradiation time of (a) photolysis, (b) dark adsorption, (c) nanocomposites photocatalysis with $TiO_2$ nanoparticles and (d) photocatalysis with MWCNTs/$TiO_2$ on the photocatalytic degradation of DMPEs

**Table 4.11:** Effect of irradiation time on the photocatalytic degradation of DMPEs

| **Sample (%)** | **UV irradiation time, min** | | | | | | |
|---|---|---|---|---|---|---|---|
| | 15 | 30 | 45 | 60 | 120 | 180 | 240 |
| Photolysis | 1 | 1.5 | 2 | 2 | 3 | 4 | 4 |
| Dark adsorption | 1 | 1.8 | 4.6 | 5.0 | 6.5 | 7 | 8 |
| MWCNTs/$TiO_2$ | 46 | 57 | 62 | 71 | 81 | 96.5 | 97 |
| $TiO_2$ | 8 | 17 | 25 | 31 | 42 | 71 | 75 |

### 4.7.2 Effect of pH

The pH of the solution is an important parameter controlling the photocatalytic degradation taking place on MWCNTs/$TiO_2$ surface since the surface charge properties of the photocatalyst is dictated. The effect of pH on the degradation of DMPEs was investigated at 1 mg/L DMPEs concentration, 0.5 g/L catalyst concentration under 180 min irradiations and varying the initial pH of the DMPEs solution from 2 to 10 as shown in Figure 4.41. The point of zero charge (pzc) of sol-gel $TiO_2$ was reported to be of 6.4. It was found that the $TiO_2$ surface is negatively charged ($TiO^-$) when the pH value higher than the $pH_{pzc}$ while the surface of $TiO_2$ is positively charged at pH below $pH_{pzc}$ and it should be neutral at $pH_{pzc}$ according to the Equation (4.5) to (4.7).

$$Ti^{4+}–OH + OH^- \leftrightarrow Ti^{4+}–O^- + H_2O \ (pH > pH_{pzc}) \qquad \textbf{(4.5)}$$

$$Ti^{4+}–OH + H^+ \leftrightarrow Ti^{4+}–OH_2^+ \ (pH < pH_{pzc}) \qquad \textbf{(4.6)}$$

$$TiO_2 + H_2O \leftrightarrow Ti^{4+}–OH + H^+ \qquad \textbf{(4.7)}$$

During sol-gel synthesis of MWCNTs/$TiO_2$ nanocomposites, there was a linkage between the hydroxyl groups from $TiO_2$ with the carboxylic groups present at the MWCNTs surface which is expected to the decrease in the $pH_{pzc}$ of the resulting composite material (Wang et al., 2009). A good dispersion of $TiO_2$ nanoparticles in the MWCNTs/$TiO_2$ composite attributed to the functionalization of MWCNTs with nitric acids leads to the creation of large amounts of carboxylic acid and phenol groups at the surface of the MWCNTs. It was observed that the degradation of DMPEs increases from 72 %, 78 % and 97% respectively for a solution pH 2, 4 and 6 and then decreased from 81 % and 73 % for a solution pH 8 and 10 (Table 4.12). This result indicated an ideal pH of approximately 6 for the enhancement in the photocatalytic degradation of DMPEs time and it was adopted to investigate the effects of other parameters in the following studies. The experimental results revealed that the solution pH influenced the amount of hydroxyl radicals formation on $TiO_2$. In addition, it could also show that the adsorption of organic pollutant is quite well at pH near the pzc of photocatalyst. Moreover, it was reported that model compound could be decomposed at higher alkaline pH due to alkaline-induced ester hydrolysis (Sin et al., 2011, Mohammadi and Sabbaghi, 2014, Muneer et al., 2001, Tseng et al., 2010).

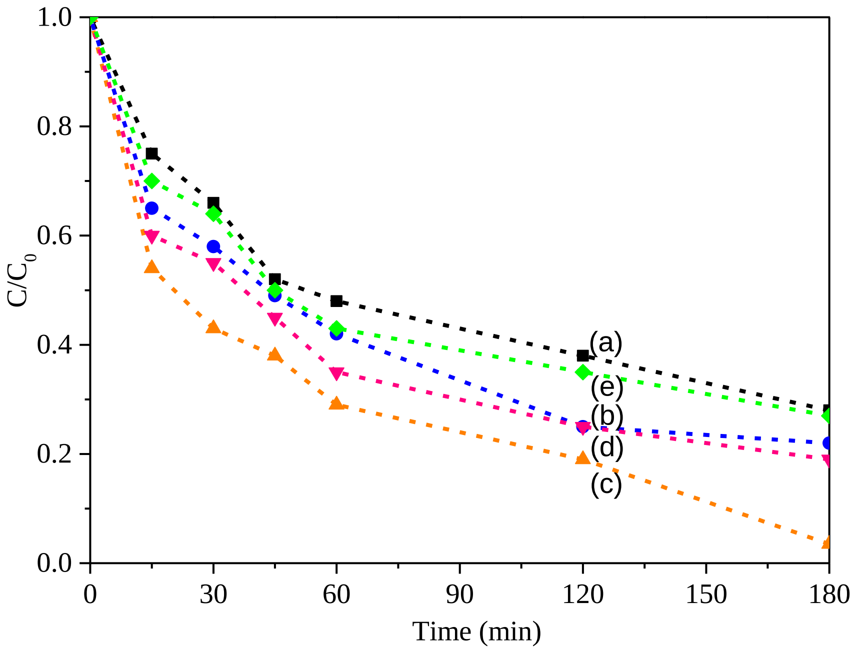

**Figure 4.41:** Effect of pH (a) pH =2, (b) pH =4, (c) pH =6, (d) pH =8 and (e) pH =10 on the photocatalytic degradation of DMPEs

**Table 4.12:** Effect of pH value on the photocatalytic degradation of DMPEs

| **pH (%)** | **UV irradiation time, min** | | | | | |
|---|---|---|---|---|---|---|
| | 15 | 30 | 45 | 60 | 120 | 180 |
| 2 | 25 | 34 | 48 | 52 | 62 | 72 |
| 4 | 35 | 42 | 51 | 58 | 75 | 78 |
| 6 | 46 | 57 | 62 | 71 | 81 | 97 |
| 8 | 40 | 45 | 55 | 65 | 75 | 81 |
| 10 | 30 | 36 | 50 | 57 | 65 | 73 |

### 4.7.3 Effect of Initial DMPEs Concentration

The effect of DMPEs concentration on degradation efficiency was investigated by varying the concentrations from 1 to 3 mg/L under 180 min irradiations with a fixed pH 6 and catalyst concentration 0.5 g/L. The results are presented in Figure 4.42. It has been observed that the degradation efficiency decreases with the increasing concentration of DMPEs. When the initial DMPEs concentration was 1 mg/L, the degradation efficiency was 96 % in 180 min. However, when the initial DMPEs concentration increased to 3 mg/L, the degradation efficiency declined to 65 %. Thus, the photocatalytic degradation efficiency of DMPEs was inversely proportional to the initial concentration of DMPEs. At higher concentration, more and more molecules of DMPEs are adsorbed on the surface MWCNTs/$TiO_2$ nanocomposites photocatalyst, which has hindered the photogeneration of •OH, and caused the decreasing rate of photodegradation reaction of the catalyst. The generation of •OH which was the main oxidant in this process was limited to oxidize the DMPEs. As a result, the degradation efficiency of DMPEs are reduced by the competitive adsorption of DMPEs molecules and reaction with •OH on the surface of the catalyst. Thus, much longer time is required to reach the complete degradation of higher concentration of DMPEs as compared to the low concentration of the DMPEs. These results are confirmed with the Beer- Lambert law: as the initial DMPEs increases, the path length of photons entering the solution is decreasing (Table 4.13). As a result, lower photon absorption on the catalyst particles is observed, and consequently reduced the photocatalytic reaction rate at higher concentration of DMPEs (Liao and Wang, 2009, Sin et al., 2011, Muneer et al., 2001, Tseng et al., 2010). Thus, the 1 mg/L of the the initial concentration of DMPEs was adopted to investigate the effects of others parameters in the following studies.

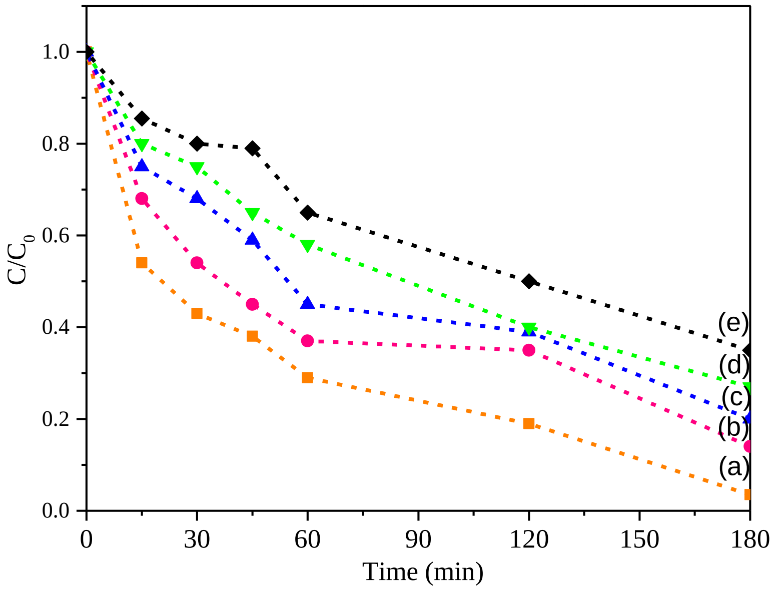

**Figure 4.42:** Effect of initial DMPEs concentrations (a) 1 mg/L, (b) 1.5 mg/L, (c) 2 mg/L, (d) 2.5 mg/L and (e ) 3 mg/L on the photocatalytic degradation of DMPEs

**Table 4.13:** Effect of initial DMPEs concentrations on the photocatalytic degradation of DMPEs

| **Initial [DMPEs], mg/L (%)** | **UV irradiation time, min** | | | | | |
|---|---|---|---|---|---|---|
| | 15 | 30 | 45 | 60 | 120 | 180 |
| 1 | 44 | 59 | 60 | 73 | 81 | 96 |
| 1.5 | 32 | 44 | 55 | 63 | 65 | 86 |
| 2 | 25 | 31 | 41 | 55 | 61 | 80 |
| 2.5 | 20 | 25 | 35 | 42 | 60 | 73 |
| 3 | 14.4 | 20 | 21 | 38 | 50 | 65 |

### 4.7.4 Effect of Catalyst Dosage

The degradation efficiency of the photocatalytic reaction is greatly influenced by the concentration of the catalyst in the reaction in order to avoid the use of an excess catalyst and ensure total absorption of efficient photons. The photocatalytic degradation efficiency of DMPEs was proportional with the concentration of the catalyst. Figure 4.43 shows a series of experimental conducted by varying the MWCNTs/$TiO_2$ dosage starting from 0.1 g/L to 0.7 g/L in order to obtain the ideal MWCNTs/$TiO_2$ catalyst dosage to give the highest photocatalytic degradation efficiency of DMPEs. It can be seen that the degradation efficiency increased from 65 % to 97 % with increasing MWCNTs/$TiO_2$ dosage from 0.1 g/ L to 0.5 g/L and then decreased slightly at higher loading (Table 4.14). Thus, the ideal dosage of MWCNTs/$TiO_2$ catalyst was 0.5 g/L. It is suggested that the increase in the amount of MWCNTs/$TiO_2$ would provide more available active sites for the generation of hydroxyl and superoxide radicals for the oxidation of DMPEs molecule. However, when the amount of MWCNTs/$TiO_2$ overdosed, it shows a detrimental effect because of the excess particles that hinder the optimum generation •OH free radical on the surface of the catalyst and thus decreased light penetration into the solution (Liao and Wang, 2009). Moreover, the increase of catalyst concentration beyond the optimum may result in the agglomeration of the catalyst particle, hence decrease the number of active sites available on the photocatalyst surface and the exposed surface area also decreases. Similar results have been reported in photocatalytic reaction of di-nbutyl phthalate (DBP) and 1, 2- diethyl phthalate (DEP) (Sin et al., 2011, Mohammadi and Sabbaghi, 2014, Muneer et al., 2001, Wang et al., 2009).

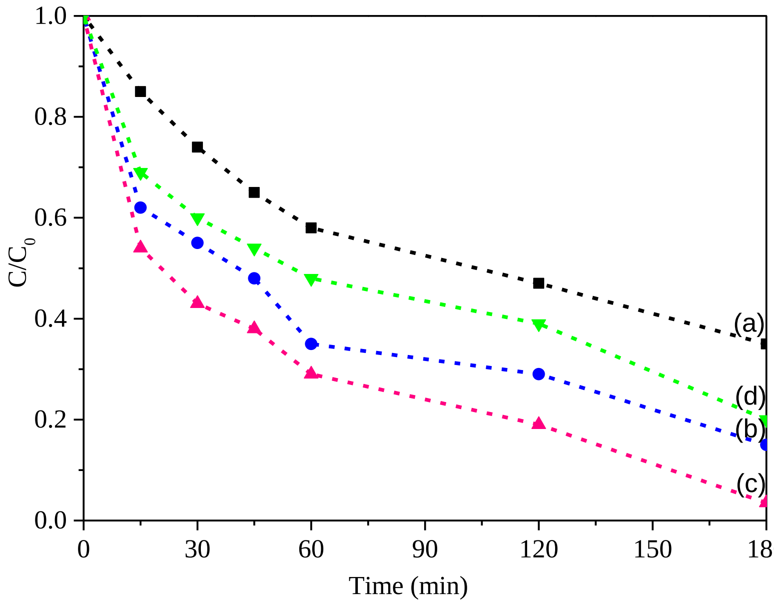

**Figure 4.43:** Effect of MWCNTs/$TiO_2$ dosage (a) 0.1 g/L, (b) 0.3 g/L, (c) 0.5 g/L and (d) 0.7 g/L on the photocatalytic degradation of DMPEs

**Table 4.14:** Effect of MWCNTs/$TiO_2$ dosage on the photocatalytic degradation of DMPEs

| **Catalyst dosage, g/L (%)** | **UV irradiation time, min** | | | | | |
|---|---|---|---|---|---|---|
| | 15 | 30 | 45 | 60 | 120 | 180 |
| 0.1 | 15 | 26 | 35 | 42 | 53 | 65 |
| 0.3 | 38 | 45 | 52 | 65 | 71 | 85 |
| 0.5 | 46 | 57 | 62 | 71 | 81 | 97 |
| 0.7 | 31 | 40 | 46 | 52 | 61 | 80 |

### 4.7.5 Effect of $H_2O_2$ amount

The photocatalytic degradation of organic pollutants was greatly influenced by the oxidizing agents such as hydrogen peroxide which act as an electron acceptor to prevent electron-hole recombination and thus increase the photocatalytic efficiency. The $H_2O_2$ would come into contact with the hydroxylated $TiO_2$ particles in aqueous solution and trap the photoinduced electron. Without electron acceptors, the limitation attributes to the recombination of electron hole pairs would decrease the photocatalytic efficiency.

Hence, the effect of the addition of hydrogen peroxide ($H_2O_2$) in the efficiency of the photocatalytic degradation of Dimethyl phthalate esters (DMPEs) was studied by varying the concentration of $H_2O_2$ from 5 mg/L to 20 mg/L. It was found that the degradation of DMPEs increased from to when the $H_2O_2$ concentration was increased from 5 to 15 mg/L (Table 4.15). However, there was a decrease in the degradation at a higher level of $H_2O_2$ concentration as shown in Figure 4.44. The enhancement of the degradation efficiency of DMPE with the addition of $H_2O_2$ could be explained in terms of the generated •OH radicals and the capture of the •OH radicals as presented by Equation (4.8-4.11).

$$H_2O_2 + e^{-} \rightarrow \bullet OH + OH^{-} \qquad \textbf{(4.8)}$$

$$H_2O_2 + O_2^{\bullet -} \rightarrow \bullet OH + OH^{-} + O_2 \qquad \textbf{(4.9)}$$

$$H_2O_2 + \bullet OH \rightarrow H_2O + OH_2^{\bullet} \qquad \textbf{(4.10)}$$

$$HO_2\bullet + \bullet OH \rightarrow H_2O + O_2 \qquad \textbf{(4.11)}$$

It is well-known that the photoinduced $e^-$ can be trapped by $H_2O_2$ for stabilizing the $e^-$-$h^+$ pairs. As a result, the degradation efficiency of DMPEs increase with more •OH generated in this study provided more chances to attack the organic compounds. However, the excess of $H_2O_2$ could trap the •OH radicals leading to form weaker $HO_2$• radicals. This $H_2O_2$ may compete with DMPEs for the active sites of $TiO_2$ to restrain the photodegradation of DMPEs (Sin et al., 2011, Tseng et al., 2010).

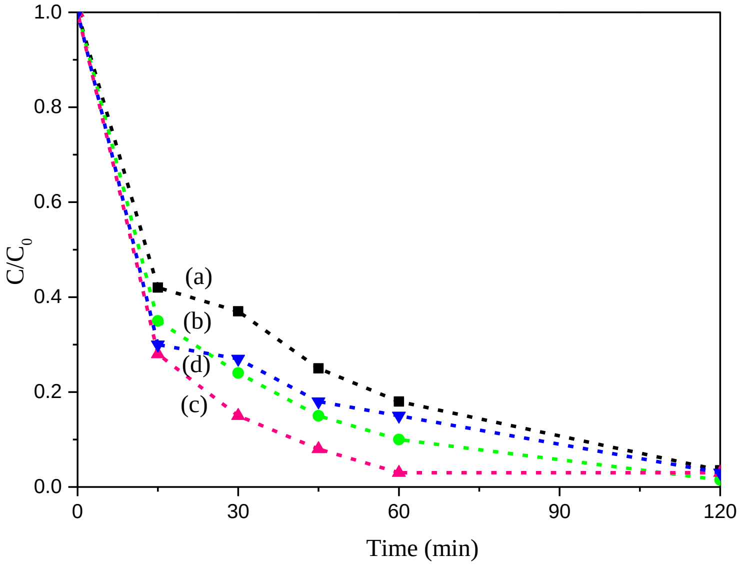

**Figure 4.44:** Effect of $H_2O_2$ amount (a) 5 mg/L, (b) 10 mg/L, (c) 15 mg/L and (d) 20 mg/L on the photocatalytic degradation of DMPEs (MWCNTs/$TiO_2$ dosage= 0.5 g/L, [DMPEs] = 1 mg/L, pH =6)

**Table 4.15:** Photodegradation of DMPEs in solution at different $H_2O_2$ concentrations within 120 min

| **[$H_2O_2$] (mg/L)** | **Degradation efficiency (%)** |
|---|---|
| 5 | 88 |
| 10 | 92 |
| 15 | 99 |
| 20 | 90 |

### 4.7.6 Reusability of MWCNTs/$TiO_2$ nanocomposites

Considering the potentially of using MWCNTs/$TiO_2$ nanocomposites for environmental application, the reusability of MWCNTs/$TiO_2$ nanocomposites was investigated by evaluating its catalytic performance for five cycles and results are shown in Figure 4.45. After the completion of the degradation, MWCNTs /$TiO_2$ nanocomposites catalyst at the end of the cycle was collected and utilized for the next cycle for the same initial concentration of DMPEs. Noticeably, it was found that after five consecutive cycling runs, DMPEs removal could still reach 96 % within 180 min, indicating that the reduction of catalytic activity of MWCNTs/$TiO_2$ was significant.

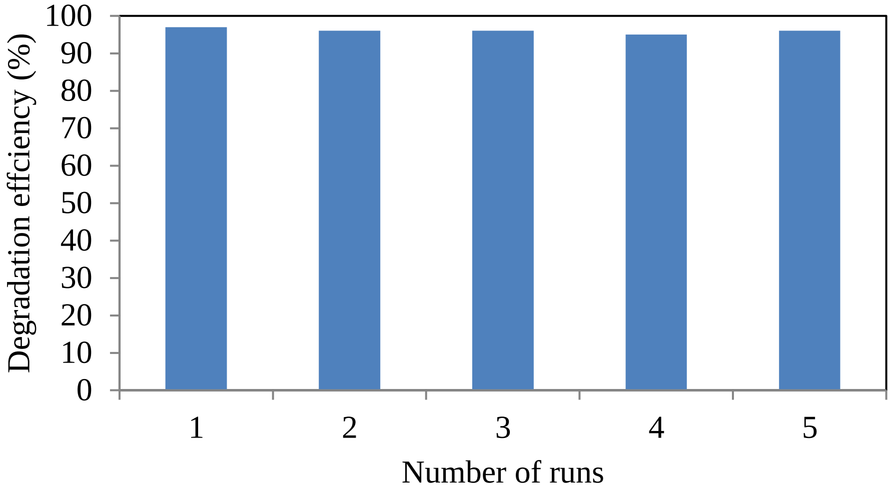

**Figure 4.45:** Reusability data over 10 wt % MWCNTs/$TiO_2$ nanocomposites in the degradation of 1mg/L DMPEs, over 0.5g/L catalyst, for 3 h irradiation under 96 W UV irradiation

Figure 4.46 illustrates the possible photodegradation mechanisms of DMPEs by MWCNTs/$TiO_2$ photocatalyst. Accordingly, the photocatalytic degradation process initiated via the absorption of photon by the $TiO_2$ semiconductor. Under such conditions, the electrons from valence band would be excited to the conduction band of $TiO_2$ creating the electron-hole pairs on the catalyst surface. The photogenerated electrons were then transferred to MWCNTs, (act as the electron acceptor). The trapped electrons would then react with the dissolved oxygen to form the reactive oxygen species, followed by, suppresses the rate of electron-hole recombination. In the meantime, the photogenerated electrons on the $TiO_2$ surface tended to reduce the dissolved oxygen to form superoxide anion, which may subsequently react with the adsorbed water to form the hydroxyl radicals. The hydroxyl radicals (acted as a primary oxidant in the photocatalytic system) then reacted with DMPEs molecules and mineralized the DMPEs into $CO_2$, $H_2O$ and mineral acids. The recombination rate of electron-hole pairs would be retarded gradually as more and more electrons being transferred from $TiO_2$ to MWCNTs (Hamid, Tan, Lai & Samsudin, 2014; Quyang, Xie & Ma, 2013; Reti, Mogyorosi, Dombi & Hemadi, 2014; Tian, Ye, Deng & Zan, 2011; Yu, Ma & Liu, 2011).

The mechanism reactions are shown as below:

$$TiO_2/MWCNTs \xrightarrow{h\nu} TiO_2\ (h^+) - MWCNTs\ (e^-) \tag{4.12}$$

$$MWCNTs\ (e^-) + O_2 \rightarrow MWCNTs + O_2^{\bullet -} \tag{4.13}$$

$$TiO_2\ (h^+) + H_2O/OH^- \rightarrow TiO_2 + {}^{\cdot}OH \tag{4.14}$$

$${}^{\cdot}OH + DMPEs \rightarrow CO_2 + H_2O + \text{mineral acids} \tag{4.15}$$

Technically, the synergistic effect of MWCNTs and $TiO_2$ in MWCNTs/$TiO_2$ composites leads to the formation of a space charge region, namely the Schottky barrier (Bergmann and Machado, 2015, Hamid et al., 2014, Leary and Westwood, 2011). Naturally, the electrons tends to migrate from a higher to a lower Fermi level at the interface of the $TiO_2$ and MWCNTs. Typically, $TiO_2$ is an n-type semiconductor; yet, the $TiO_2$ was turned into p-type semiconductor in the presence of MWCNTs, (acting as the electron sinks) due to the flow of photogenerated electrons in the space charge region to the MWCNTs surface. As a result, the positively charged holes would react with the adsorbed water to produce hydroxyl radicals, and subsequently degrade the DMPEs (Gui et al., 2014a).

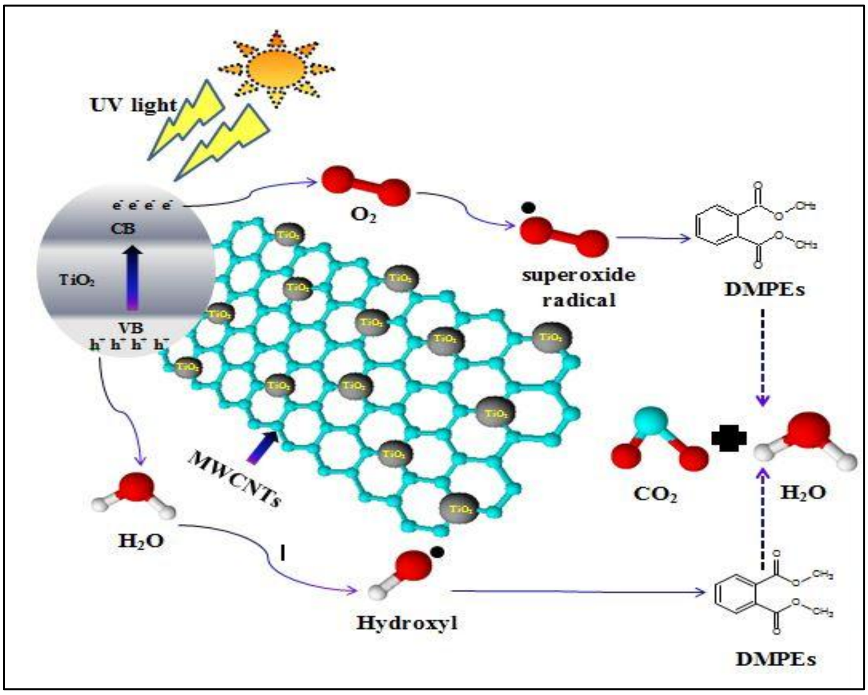

**Figure 4.46:** Photocatalytic mechanism of MWCNTs/$TiO_2$ nanocomposites

## 4.8 Photocatalytic Degradation Intermediates and DMPEs Degradation Mechanisms

Figure 4.47 13 shows the primary degradation intermediates of DMPEs detected using the HPLC (UV detector). It is clear that DMPEs showed retention time of about 8.9847 min, and 4 primary photo-products which possessed higher polarity than that of the DMPEs were observed during the early stage of photodegradation. As the irradiation time increased, it was determined that the peak intensity of DMPEs reduced, while the peaks intensity of the photoproducts increased. Accordingly, the retention times of these four main intermediates products were 3.991, 4.772, 6.452 and 7.013 min, respectively after 3-hour irradiation. The degraded products were further identified by UHLPC/Orbitrap/MS analyser and the degradation mechanism of DMPEs by the MWCNTs/$TiO_2$ was proposed thereafter.

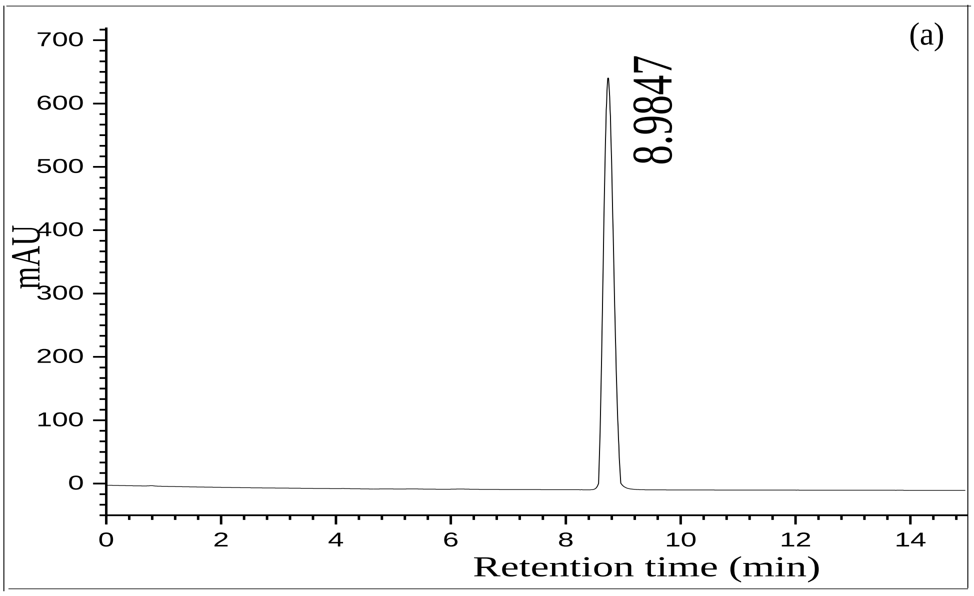
(a)
8.9847
mAU
700
600
500
400
300
200
100
0
0
2
4
6
8
10
12
14
Retention time (min)

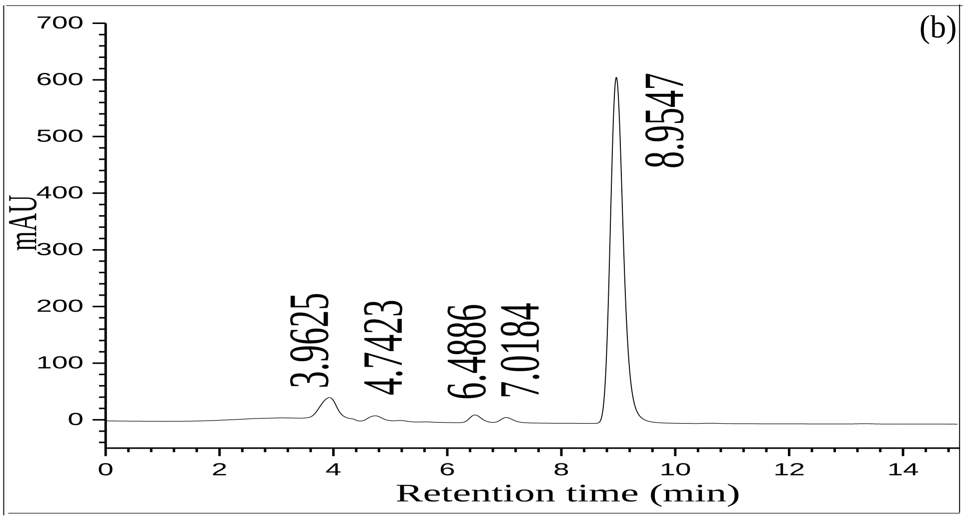
(b)
8.9547
3.9625
4.7423
6.4886
7.0184
mAU
700
600
500
400
300
200
100
0
0
2
4
6
8
10
12
14
Retention time (min)

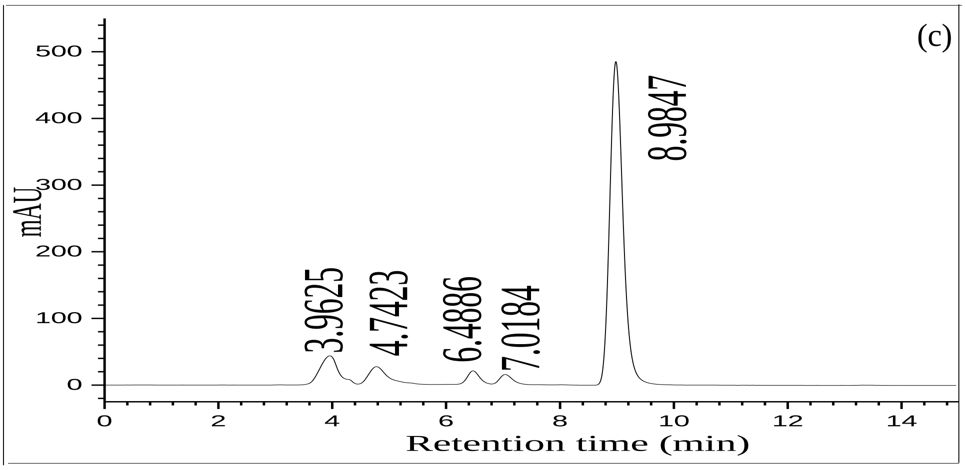
(c)
8.9847
3.9625
4.7423
6.4886
7.0184
mAU
500
400
300
200
100
0
0
2
4
6
8
10
12
14
Retention time (min)

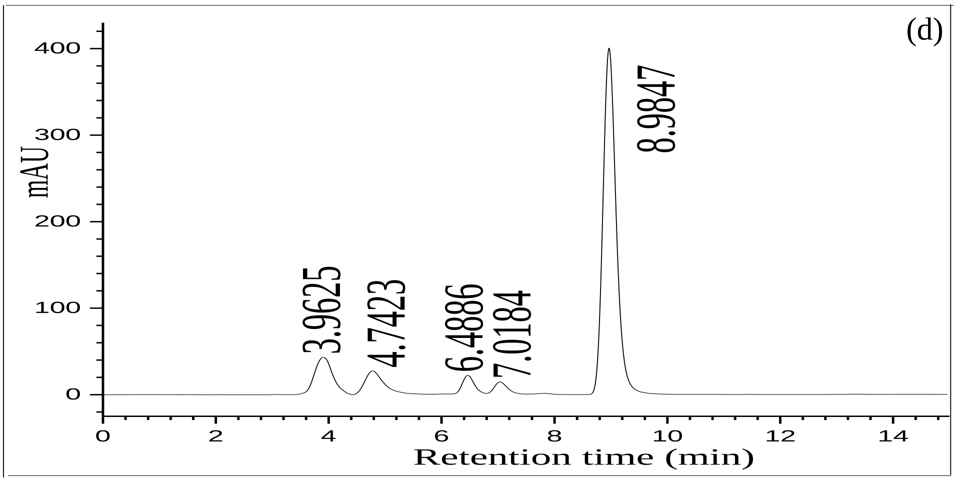
(d)
mAU
400
300
200
100
0
3.9625
4.7423
6.4886
7.0184
8.9847
0
2
4
6
8
10
12
14
Retention time (min)

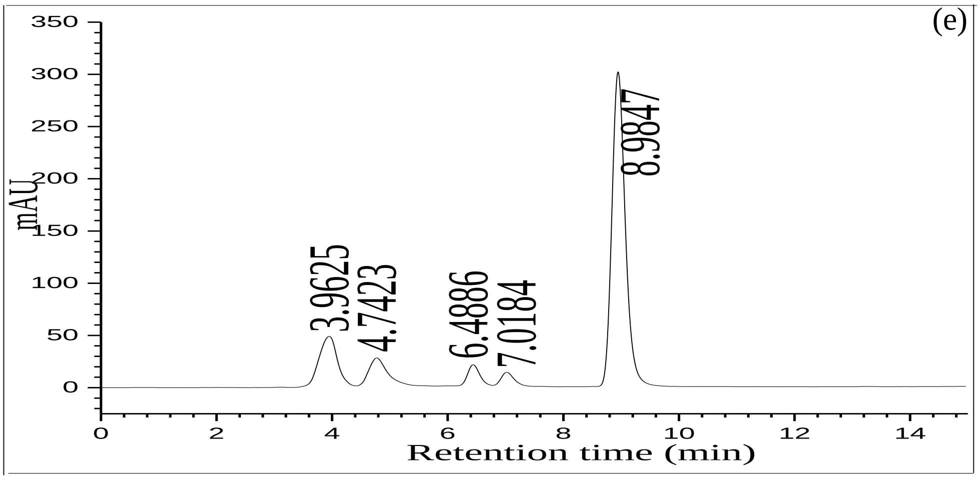
(e)
mAU
350
300
250
200
150
100
50
0
3.9625
4.7423
6.4886
7.0184
8.9847
0
2
4
6
8
10
12
14
Retention time (min)

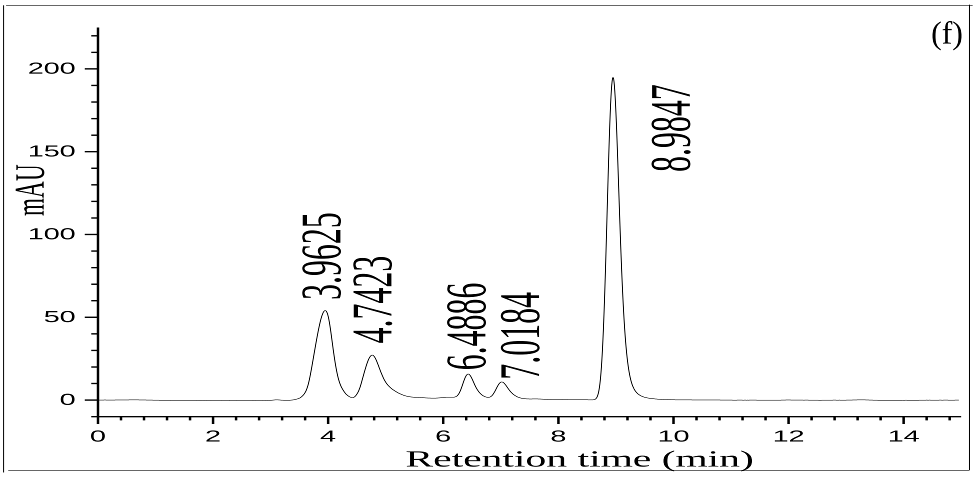
(f)
mAU
200
150
100
50
0
3.9625
4.7423
6.4886
7.0184
8.9847
0
2
4
6
8
10
12
14
Retention time (min)

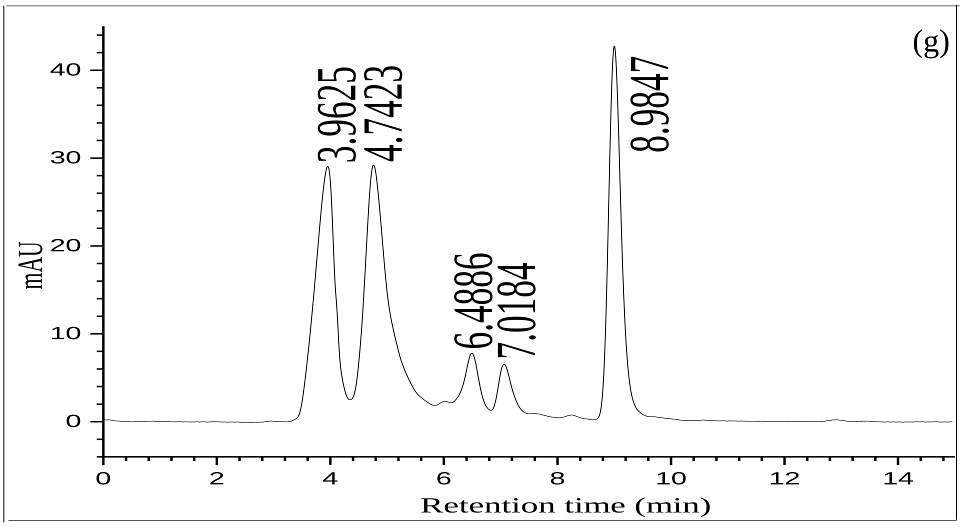

**Figure 4.47:** HPLC chromatogram of DMPEs at (a) 0h, (b) 15 mins, (c) 30 mins, (d) 45 mins, (e) 60 mins, (f) 120 mins, and (g) 180 mins irradiation time

The identification and characterization of the photoproducts during the photodegradation of DMPEs have been of great interest among the people working in this area around the world. In the present research work, the intermediate photoproducts formed during the photodegradation of DMPEs were tentatively identified and the reaction pathways were proposed according to the intermediates generated. Accordingly, the intermediate photoproducts in the solution were analyzed by UHPLC/Orbitrap/MS/MS analysis with the aim to identify the intermediate photo-products formed during the photocatalytic degradation of DMPEs. A total of eighteen products were identified; the molecular ions and fragment peaks obtained were then compared with the UHPLC/ Orbitrap/ MS library data as (Table 4.16). In general, this approach tends to provide accurate mass measurements of ions (m/z values) of different compounds formed. The HPLC-Orbitrap-MS chromatograms of photoproducts from DMPEs degradation are shown in Appendix A.

During the photocatalytic degradation of DMPEs, there are basically two possible sites for the attack of •OH, i.e., the aromatic ring and the aliphatic chain. Based on the identified primary intermediates, the degradation of DMPEs was initiated by different reaction pathways as shown in Figure 4.48, in which the major reaction attack occurred involving: (a) the hydroxylation of the aromatic ring, (b) the oxidation of the aliphatic chain. Accordingly, the degradation of DMPEs induced by the excitation of MWCNTs/$TiO_2$ involves the attack of the •OH radicals on the pollutant, where they were commonly reported according to their decrease molecular weight. However, based on all previously published studies on the photocatalytic degradation of DMPEs, there is no alcohol intermediate arising from the primary alkyl chain been detected; only dicarbonic acid (COOH) was reported in all reaction mechanisms published up to date, to the best of our knowledge.

In general, in the present research work, there are 5 pathways proposed for the photocatalytic degradation of DMPEs. In the first pathway, the photoproduct underwent a single cleavage of methoxy group, giving rise to product 2. Product 2 then experienced a further single cleavage of ester group and was reduced to product 7 by the attack of •H radical. The resulting primary alcohol intermediate (product 7) could be oxidized to product 11, followed by decarbonylation to form product 15.

In the second pathway, the photoproduct underwent an addition of •OH radicals on the aromatic rings to form product 3. The attack of the OH radicals led to the formation of hydroxyl-DMP photoproducts on the aromatic ring, followed by the loss of a hydrogen atom. Accordingly, compound 8 possessed two possible hydroxylated derivatives (12 and 13) of DMPEs and such products had been reported in photocatalytic degradation of DMPEs in the early references (Liao and Wang, 2009, Xu et al., 2013a, Yuan et al., 2008b). Next, dimethyl hydroxyphthalate underwent the subsequent removal of two methoxy group forming the final product 16 containing two aldehyde functional group. Another possible pathway for dimethyl hydroxyphthalate was the cleavage of the –$COOCH_3$ group to generate product 17, i.e., hydroxyl–methyl benzoates. The resulting intermediate product 17 could also be further cleavaged into product 18, i.e., phenol compound.

In the third pathway, the organic species 4 lost one of its methoxy groups and then underwent an addition reaction with the •OH radicals forming the product 9 (i.e., monomethyl phthalate, MMP). Next, the resultant product underwent a further cleavage of the C-C bond, followed by connecting the $COOCH_3$ group to the aromatic ring leading to the formation of the product 14, i.e., benzoic acid. Under the reductive conditions, the product 14 was reduced to form product 19, i.e., phenyl methanol. It is worth to mention that this photoproduct has not been previously reported during the photocatalytic degradation of DMPEs, benzoic acid was detected instead of phenyl methanol as the final photoproduct based on the published studies.

In the fourth pathway, DMPEs tended to loss its methoxy group, followed by experiencing an addition reaction with the •OH radicals on the different position of the ester group forming the product 5. This was followed by the decarbonylation process and reduced to generate product 14. Under the reductive condition, the carboxylic group of DMPEs could be further reduced to phenol (product 18).

Apart from the •OH radical, the •H radical could be obtained by the reaction of H+ with electron. In the fifth pathway, the •H radical attacked the aliphatic chain of DMPEs and generated the product 6. Next, the product 6 experienced the removal of two methoxy groups forming product 10. The intermediate products (e.g., 10, 15, 16, 17, 18 and 19) could be further decomposed to $CO_2$ and $H_2O$. Previous studies have shown that hydroxyl photoproducts (hydroxylated on the aromatic rings) could be formed by the attack of hydroxyl radicals on the phthalates containing shorter alkyl chains like dimethyl and diethyl. Considering this fact, the results obtained in this study was in good agreement with the previous research studies, indicating the importance of the chemical structure of the pollutant as the site for the •OH radical attack (Sin et al., 2012).

**Table 4.16:** Possible products of the degradation of DMPEs

| **Symbol** | **Compound name** | **Structure Formula** | **Molecular formula** | **Molecular weight (m/z)** |
|---|---|---|---|---|
| 1 | Dimethyl phthalate | $C_{10}H_{10}O_4$ | 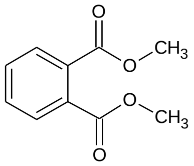 | 194.184 |
| 2 | methyl 2-formylbenzoate | $C_9H_8O_3$ | 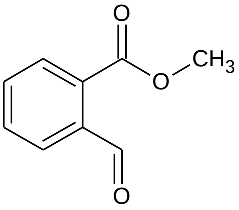 | 164.15802 |
| 3, 8 | Hydroxyl-DMPEs | $C_{10}H_{11}O_5$ | 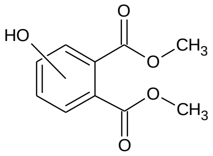 | 211.19134 |
| 5 | 2-formylbenzoic acid | $C_8H_6O_3$ | 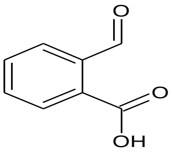 | 150.13144 |
| 6 | methyl 2-[hydroxy(methoxy)methyl] benzoate | $C_{10}H_{12}O_4$ | 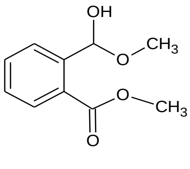 | 196.19988 |

**Table 4.16 (to be continued)**

| | | | | |
|---|---|---|---|---|
| 7 | 2-(hydroxymethyl)benzaldehyde | $C_8H_8O_2$ | 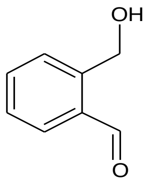 | 136.14792 |
| 9 | Monomethyl phthalate, MMP | $C_9H_8O_4$ | 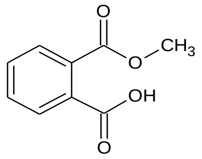 | 180.15742 |
| 10 | 2-(dihydroxymethyl)benzaldehyde | $C_8H_8O_3$ | 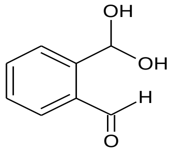 | 152.14732 |
| 11 | benzene-1,2-dicarbaldehyde | $C_8H_6O_2$ | 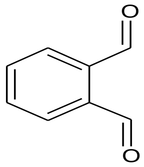 | 134.13204 |
| 12 | 3-hydroxyl-DMP | $C_{10}H_{10}O_5$ | 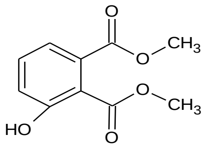 | 210.1834 |
| 13 | 4-hydroxyl-DMP | $C_{10}H_{10}O_5$ | 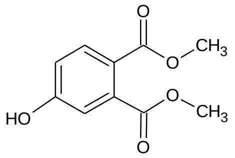 | 210.1834 |
| 14 | Benzoic acid | $C_7H_6O_2$ | 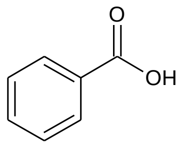 | 122.12134 |
| 15 | Benzaldehyde | $C_7H_6O$ | 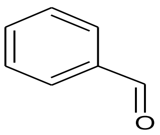 | 106.12194 |

**Table 4.16 (to be continued)**

| | | | | |
|---|---|---|---|---|
| 16 | 4-hydroxyl-1,2-dibenzoic acid | $C_8H_6O_3$ | 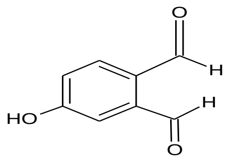 | 150.1314 |
| 17 | Hydroxyl-methyl benzoates | $C_8H_6O_3$ | 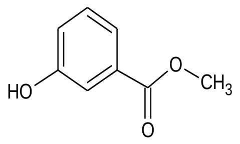 | 152.14732 |
| 18 | Phenol | $C_6H_6O$ | 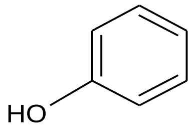 | 94.11124 |
| 19 | phenyl methanol | $C_7H_8O$ | 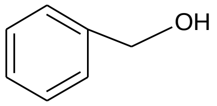 | 108.13782 |

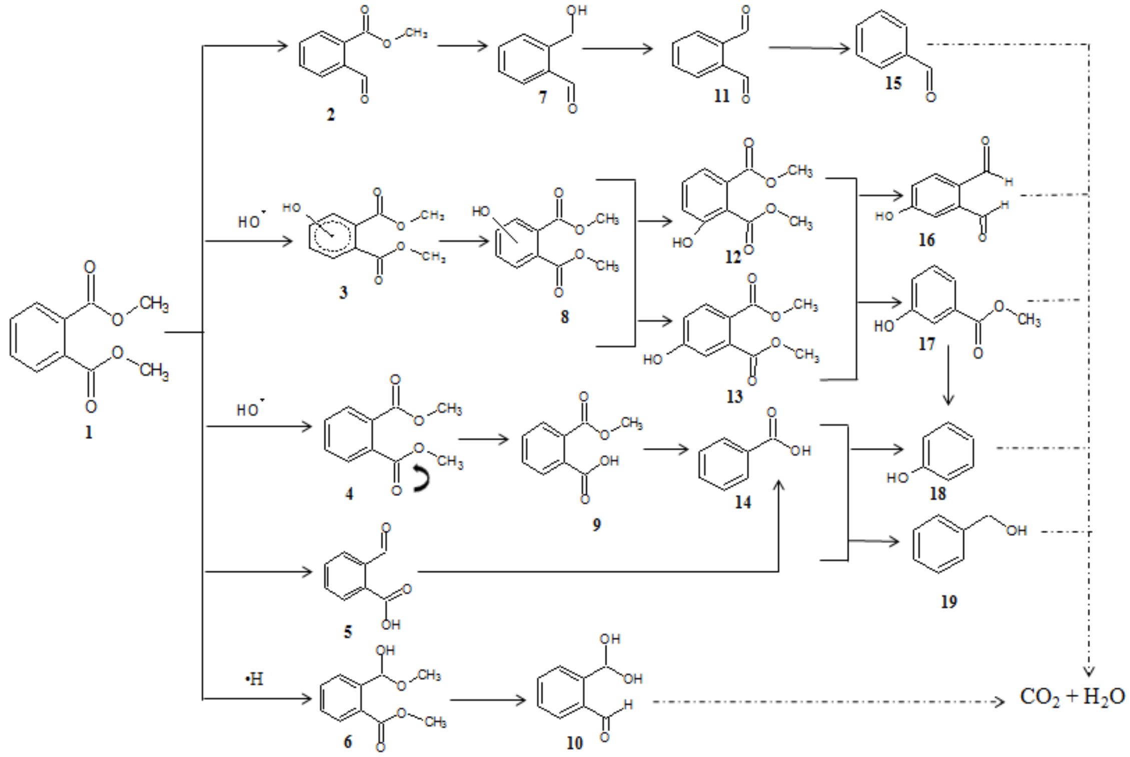

**Figure 4.48**: Proposed degradation pathways of DMPEs in photocatalytic reaction. The identified products are shown with solid arrows while the dotted black arrows are undefined pathways.

## 4.9 Mineralization of DMPEs

In addition to Dimethyl Dimethyl phthalate esters (DMPEs) removal, the Total organic carbon (TOC) analysis is important to investigate the extent of mineralization rather than just transformation of DMPEs. Figure 4.49 shows the depletion in TOC as a function of time on irradiation of an aqueous solution of DMPEs (1 mg/L) in the presence of MWCNTs/$TiO_2$ nanocomposites photocatalyst (0.5 g/L). At the end of the photodegradation runs (3 h of irradiation), it can be seen that 48 % of TOC removal of its initial value for DMPEs. The TOC removal efficiency increased proportionally with the irradiation time. This can be explained by the fact that, with time, the DMPEs gets hydrolyzed and oxidized to lower molecular weight compounds so the TOC content was observed to decrease with time. However, TOC values remain high even at the end of the degradation run and this imply that some organic intermediates (phthalic acid and monomethyl phthalate) are produced during the course of DMPEs degradation and this is in agreement with Xu et al. (2010) who reported that the TOC was found to remain at high value even with the high photodegradation efficiency.

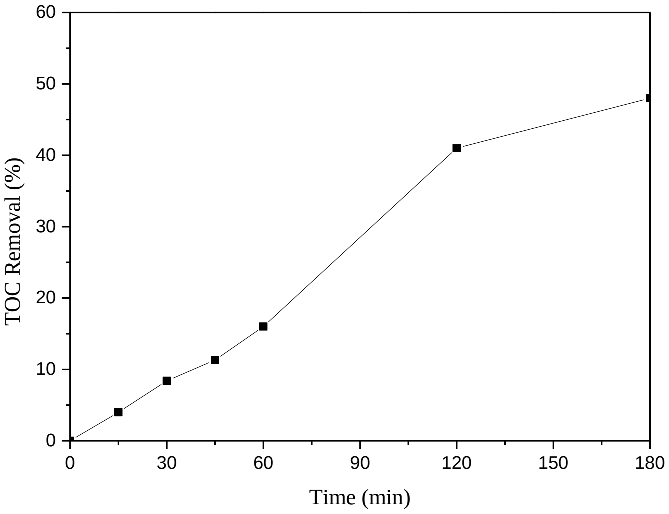

**Figure 4.49:** Percentage removal of TOC of DMPEs by MWCNTs/$TiO_2$ nanocomposites

# CHAPTER 5: CONCLUSION & FUTURE WORK RECOMMENDATIONS

## 5.1 Conclusion

Photodegradation of POPs by $TiO_2$ nanoparticles has attracted increasing attention in the past decades. However, there are some drawbacks by using $TiO_2$ nanoparticles alone as photodegradation catalysts. In this study, MWCNTs with large specific surface area, inertness, stable in all pH range, and tunable surface chemistry, were coupled with $TiO_2$ nanoparticles. This inclusion of MWCNTs phases with $TiO_2$ have induced beneficial effects on the photocatalytic performance of $TiO_2$ nanoparticles. Generally, this effect is attributed to the decrease of the band gap energy of this composite catalysts, leads to an enhancement of adsorptive properties as well as charge separation and transportation properties. The first objective in my study was to synthesize MWCNTs/ $TiO_2$ nanocomposites by using acid catalyzed sol-gel route. This synthesis techniques involved a hydrolysis step during the addition of MWCNTs, followed by the polycondensation of titanium alkoxides. The final MWCNTs/$TiO_2$ nanocomposites were obtained after calcination at 450 °C. In short, the first objective of this study was achieved. One-dimensional MWCNTs/$TiO_2$ nanocomposites were successfully synthesized by optimising the synthesis conditions including different loading of MWCNTs, pH of solution and calcination temperature. The removal effciency of DMPEs using MWCNTs/$TiO_2$ nanocomposites were also compared to $TiO_2$ nanoparticles. The conclusions attained after achieved the objective are as follows:

- The incorporation of MWCNTs lead to an significant increase in the photocatalytic effciency towards the degradation of DMPEs under 96 W UV irradiation as compared to $TiO_2$ nanoparticles. This was attributed to a synergistic effect by creating of an electronic interphase interaction between MWCNTs and $TiO_2$ phases. The functional group (-COOH) on the surface of MWCNTs has promoted the anchoring of the $TiO_2$ nanoparticles as well as their dispersion by avoiding agglomeration and subsequently increased the surface area of the MWCNTs/$TiO_2$ nanocomposites. The combination of MWCNTs with $TiO_2$ showed an increase in the $S_{BET}$ as compared to the pure $TiO_2$ nanoparticles which may lead to an increase of the capability for adsorbing pollutants. The formation of Ti-C bonds (as proved in the XPS result) at the interphase between MWCNTs and $TiO_2$ nanoparticles has enhanced the light absorption of MWCNTs/$TiO_2$ nanocomposites, led to a higher photocatalytic activity. The photocatalytic efficiency of $TiO_2$/MWCNTs (97 %) is higher than $TiO_2$ (71 %) due to the MWCNTs acting as electron sinks and hereby hinders the recombination rate of the electron-hole pairs.

- For the effect of MWCNTs loading (3 wt % to 15 wt %), the results showed that the surface area of MWCNTs/$TiO_2$ nanocomposites has increased when the MWCNTs loading was increased up to 15 wt %. In addition, the PL results divulged that the 15 wt % of MWCNTs/$TiO_2$ showed the highest electron charge efficiency with the lowest electron recombination rates. The suitable loading of MWCNTs appeared to be highly dependent on the morphology of the MWCNTs/$TiO_2$. The apparently contradictory findings could be partially explained because of $TiO_2$ is the photoactive phase while MWCNTs is acting as an electron sink, it is beneficial to incorporate higher percentages of $TiO_2$ to promote exposed $TiO_2$ surface area. The higher loadings of MWCNTs (>10 wt%) has caused the blockage of $TiO_2$ active sites, and thus, lower the photocatalytic activity of MWCNTs/$TiO_2$ nanocomposites. Besides, excess MWCNTs has caused aggregation of $TiO_2$ nanoparticles (as observed in the FESEM result), leading to a decreased in amount of DMPEs being adsorbed on the surface of MWCNTs/$TiO_2$

nanocomposites. Nevertheless, 10 wt% MWCNTs/$TiO_2$ nanocomposites was found to be the optimum loading as it has showed the highest photocatalytic efficiency among the samples.

- The influence of pH on the morphological and electronic properties of MWCNTs/$TiO_2$ nanocomposites were discussed and correlated to the photocatalytic effciency of DMPEs. With the increasing of pH value to pH 9, the particle size has increased and well-dispersion of highly uniform $TiO_2$ on MWCNTs according to FESEM analysis. Besides, red-shifting in UV-vis spectra occurred with increasing pH up to pH 9 resulted from lowering band gap from 3.14 to 2.48 eV. This should be attributed to the interaction of $TiO_2$ nanoparticles with the MWCNTs, which may modify the electron/hole pair recombination process under UV light irradiation. Combining all these factors, favourable interactions between $TiO_2$ and MWCNTs at pH 9 has resulted in highest degradation efficiency of DMPES.
- It had been proven that the increasing calcination temperature has caused the sintering of $TiO_2$ nanoparticles into bigger crystals; detachment of $TiO_2$ nanoparticles from the surface of MWCNTs was also observed and the formation of rutile phase. MWCNTs/$TiO_2$ calcined at 450°C exhibited the highest photocatalytic activity (96 %) due to the high crystallinity and uniform coating of $TiO_2$ along the MWCNTs with minimum agglomeration. Basically, the functional groups (-COOH) present at the surface of MWCNTs promote the anchoring of the $TiO_2$ nanoparticles as well as avoiding agglomeration and subsequently increasing the surface area of the resulting MWCNTs/$TiO_2$ composite. Beyond 450°C, the photocatalytic activity of MWCNTs/$TiO_2$ has decreased due to the formation of larger crystallite size and decomposition of MWCNTs at 637 °C. It is noticeable that the surface

area of MWCNTs/$TiO_2$ nanocomposites has decreased with increasing calcination temperatures from 350 to 750 °C, indicating that the grain sizes increased and the agglomeration of small grains to form larger grains at higher calcination temperature. It also can be attributed to enhancement of nucleation and coalescence of grains.

In the second part, the effect of reaction parameter i.e. irradiation time, initial concentrations of DMPEs, catalyst dosages, pH of the solution and $H_2O_2$ dosages were studied in order to investigate the photocatalytic efficiency of DMPEs. Furthermore, the degradation mechanism of DMPEs by MWCNTs/$TiO_2$ was then been proposed. The conclusions attained in this part of the research are as follow:

- Most of the research works reported recently are limited to the removal of DMPEs at higher concentration; however, the concentrations of PAEs in highly industrialized Klang Valley, Malaysia have found varying concentrations of PAEs ranging from 0.1 to 64.3 µg/L in the river water. In this research works, lower concentration of DMPEs, 1 mg/L, was chosen. According to the parameters reported in literature, the other operating parameters were fixed at pH 6 of solution pH and 3 h of reaction time before each of the parameter was selected. The high removal efficiency of DMPEs was obtained when the MWCNTs/$TiO_2$ nanocomposites dosage was 0.5 g/L, the initial concentration of DMPEs was 1 ppm, the initial pH of DMPEs was 6, and irradiation time was 3 h.
- It was found that the degradation of DMPEs increased from to when the $H_2O_2$ concentration was increased from 5 to 15 mg/L. As a result, the degradation efficiency of DMPEs has increased with amount of •OH generated. However,

excess amount of $H_2O_2$ could trap the •OH radicals leading to form weaker $HO_2$• radicals. This $H_2O_2$ may compete with DMPEs for the active sites of $TiO_2$ to restrain the photodegradation of DMPEs.

- The possible photoproducts formed in the photocatalytic degradation of DMPEs were analysed using reversed phase UHPLC/Orbitrap/MS analysis. All the intermediates detected in this study had shorter retention times than DMPEs, implying a higher polarity than their mother compound. The degradation of DMPEs involved the hydroxylation of the aromatic ring and the oxidation of the aliphatic chain due to the attack of •OH. The intermediates of monomethyl phthalate (MMP) and phthalic acid have been reported to be less toxic than DMPEs.

## 5.2 Suggestions and Recommendations

Despite various exploitations and extensive studies of this MWCNTs/$TiO_2$ nanocomposites have been undertaken, a number of great challenges still remain and require attention in the future works. In order to bring this technology to practical applications, further studies and developments are required. A few suggestions for further studies were proposed:

- The underlying mechanism of the photocatalytic enhancement by MWCNTs/$TiO_2$ nanocomposites is not fully understood and need to be examined in details to gain the clear understanding and to prove guidelines for future water treatment design based on photocatalysis. Generally, this enhancement is ascribed to the extended absorption and improved charge transfer in the hybrids. Although some studies have suggested a different mechanism in the literature, the possible mechanism of photocatalytic reaction may depend on the interfacial status of MWCNTs/$TiO_2$ nanocomposites, type of bonding, phase of $TiO_2$, type of CNTs, functionalization, surface area and so forth. Thus, all these aspects in the fundamental processing-structural-developments will need to be better understood and controlled.

- In this work, the use of MWCNTs/$TiO_2$ nanocomposites in the photocatalytic removal of DMPEs was achieved using UV lamp as the source of energy. Thus, the study of using MWCNTs/$TiO_2$ nanocomposites in the photocatalytic removal of DMPEs under solar irradiation will be a good suggestion for further studies.
- The optimization of the reaction parameter i.e. irradiation time, initial concentrations of DMPEs, catalyst dosages, pH of the solution using design of experiment will be good suggestion for future studies in order to study the effect on a response variables due to one or more factors.
- A complete photodegradation of DMPEs by the photocatalysts is still difficult to be achieved. More studies shall be carried out with the aim of enhancing the reactivity of photocatalysts. Additionally, it is necessary to explore the possibility of combined use of MWCNTs/$TiO_2$-based technologies with other technologies (e.g., biological means and electrodynamics) to expand the scope of application.
- Broader environmental applications on this MWCNTs/$TiO_2$ nanocomposite shall be explored. For instance, the photocatalytic degradation of persistent organic pollutants that hardly found in the literature shall be investigated, which important to the environmental protection and human health. Although it is still in the infancy, a widespread and great progress in this area can be expected in the future.

- The hydrolysis intermediates products, such as MMP and phthalic acid, still remain in aqueous solution as potential organic pollutants and need further removal.
- The previous work mainly focused on a batch scale of photocatalytic degradation for pollutant removal, but the lack of application in a larger scale. Thus, there is a need for the design of a prototype for the convenience of photocatalytic degradation of organic pollutants so that it can be applied in real practice.

# REFERENCES

Aazam, E. S. (2014). Visible light photocatalytic degradation of thiophene using Ag–$TiO_2$/multi-walled carbon nanotubes nanocomposite. *Ceramics International,* 40**:** 6705-6711.

Agrawal, A. (2016). Fourier Transform Infrared (FTIR) Spectrophotometry. Retrieved 15 May 2016, from http://www.slideshare.net/AniketAgrawal9/ftirfourier-transformed-infrared-spectroscopy

Ahmed, D. S., Haider, A. J., & Mohammad, M. (2013). Comparesion of functionalization of multi-walled carbon nanotubes treated by oil olive and nitric acid and their characterization. *Energy Procedia,* 36**:** 1111-1118.

Al-Saleh, I., & Elkhatib, R. (2016). Screening of phthalate esters in 47 branded perfumes. *Environmental Science and Pollution Research,* 23**:** 455-468.

Amin, M. T., Alazba, A. A., & Manzoor, U. (2014). A Review of Removal of Pollutants from Water/Wastewater Using Different Types of Nanomaterials. *Advances in Materials Science and Engineering,* 2014**:** 24.

An, H., Cui, H., Zhou, D., Tao, D., Li, B., Zhai, J., & Li, Q. (2013). Synthesis and performance of Pd/$SnO_2$–$TiO_2$/MWCNT catalysts for direct formic acid fuel cell application. *Electrochimica Acta,* 92**:** 176-182.

An, X., & Yu, J. C. (2011). Graphene-based photocatalytic composites. *RSC Advances,* 1**:** 1426-1434.

An, Y., Yang, L., Hou, J., Liu, Z., & Peng, B. (2014). Synthesis and characterization of carbon nanotubes-treated Ag@$TiO_2$ core–shell nanocomposites with highly enhanced photocatalytic performance. *Optical Materials,* 36**:** 1390-1395.

Atalay, S., & Ersoz, G. (2016). Introduction. *Novel Catalysts in Advanced Oxidation of Organic Pollutants.* Springer.

Atieh, M. A., Bakather, O. Y., Al-tawbini, B., Bukhari, A. A., Abuilaiwi, F. A., & Fettouhi, M. B. (2011). Effect of carboxylic functional group functionalized on carbon nanotubes surface on the removal of lead from water. *Bioinorganic chemistry and applications,* 2010.

Bagheri, S., Muhd Julkapli, N., & Bee Abd Hamid, S. (2014.) Titanium Dioxide as a Catalyst Support in Heterogeneous Catalysis. *The Scientific World Journal,* 2014**:** 21.

Bao, L.-J., Maruya, K. A., Snyder, S. A., & Zeng, E. Y. (2012). China's water pollution by persistent organic pollutants. *Environmental Pollution,* 163**:** 100-108.

Barberio, M., Barone, P., Imbrogno, A., Ruffolo, S. A., La Russa, M., Arcuri, N., & Xu, F. (2014). Study of band gap of carbon nanotube-titanium dioxide heterostructures. *Journal of Chemistry and Chemical Engineering,* 8**:** 36.

Begg Cousland Envirotec Limited. (2015-2016). Gas cleaning active carbon systems. Retrieved 15 May 2016, from http://beggcousland.co.uk/products/gas-cleaning/active-carbon-systems/

Behnajady, M., Eskandarloo, H., Modirshahla, N., & Shokri, M. (2011). Investigation of the effect of sol–gel synthesis variables on structural and photocatalytic properties of $TiO_2$ nanoparticles. *Desalination,* 278**:** 10-17.

Bergmann, C. P., & Machado, F. M. (2015). *Carbon Nanomaterials as Adsorbents for Environmental and Biological Applications*, Springer.

Bessegato, G. G., Guaraldo, T. T., & Zanoni, M. V. B. (2014). Enhancement of photoelectrocatalysis efficiency by using nanostructured electrodes. *Modern Electrochemical Methods in Nano, Surface and Corrosion Science***,** 271-319.

Bui, T. T., Giovanoulis, G., Cousins, A. P., Marner, J., Cousins, I. T., & De Wit, C. A. (2016). Human exposure, hazard and risk of alternative plasticizers to phthalate esters. *Science of the Total Environment,* 541**:** 451-467.

Buzzle. (2016). Light microscope Vs. electron microscope: A detailed comparison. Retrieved 20 May 2016, from http://www.buzzle.com/articles/light-microscope-vs-electron-microscope.html

Cao, X. L. (2010). Phthalate esters in foods: sources, occurrence, and analytical methods. *Comprehensive reviews in food science and food safety,* 9**:** 21-43.

Caserta, D., Bordi, G., Ciardo, F., Marci, R., La Rocca, C., Tait, S., Bergamasco, B., Stecca, L., Mantovani, A., & Guerranti, C. (2013). The influence of endocrine disruptors in a selected population of infertile women. *Gynecological Endocrinology,* 29**:** 444-447.

Cases, V., Alonso, V., Argandona, V., Rodriguez, M., & Prats, D. (2011). Endocrine disrupting compounds: A comparison of removal between conventional activated sludge and membrane bioreactors. *Desalination,* 272**:** 240-245.

Çecen, F., & Aktas, Ö. (2011). Fundamentals of Adsorption onto Activated Carbon in Water and Wastewater Treatment. *Activated Carbon for Water and Wastewater Treatment.* Wiley-VCH Verlag GmbH & Co. KGaA.

Cesaro, A., & Belgiorno, V. (2016). Removal of Endocrine Disruptors from Urban Wastewater by Advanced Oxidation Processes (AOPs): A Review. *The Open Biotechnology Journal,* 10.

Chabot, V., Higgins, D., Yu, A., Xiao, X., Chen, Z., & Zhang, J. (2014). A review of graphene and graphene oxide sponge: material synthesis and applications to energy and the environment. *Energy & Environmental Science,* 7**:** 1564-1596.

Chan, S. H. S., Yeong Wu, T., Juan, J. C., & Teh, C. Y. (2011). Recent developments of metal oxide semiconductors as photocatalysts in advanced oxidation processes (AOPs) for treatment of dye waste-water. *Journal of Chemical Technology and Biotechnology,* 86**:** 1130-1158.

Chen, J., Luo, H., Shi, H., Li, G., & An, T. (2014). Anatase $TiO_2$ nanoparticles–carbon nanotubes composite: Optimization synthesis and the relationship of photocatalytic degradation activity of acyclovir in water. *Applied Catalysis A: General,* 485**:** 188-195.

Chen, J., Rao, A. M., Lyuksyutov, S., Itkis, M. E., Hamon, M. A., Hu, H., & Haddon, R. C. (2001). Dissolution of full-length single walled carbon nanotubes. The Journal of Physical Chemistry B, 105(13), 2525-2528.

Chen, M.-L., & Oh, W.-C. (2010). The Improved Photocatalytic Properties of Methylene Blue for V2O3/CNT/TiO2 Composite under Visible Light. *International Journal of Photoenergy,* 2010.

Chen, M.-L., Zhang, F.-J., & Oh, W.-C. (2009). Synthesis, characterization, and photocatalytic analysis of CNT/$TiO_2$ composites derived from MWCNTs and titanium sources. *New Carbon Materials,* 24**:** 159-166.

Chen, X., Jeyaseelan, S., & Graham, N. (2002). Physical and chemical properties study of the activated carbon made from sewage sludge. *Waste Management,* 22**:** 755-760.

Chen, X., & Mao, S. S. (2006). Synthesis of titanium dioxide ($TiO_2$) nanomaterials. *Journal of nanoscience and nanotechnology,* 6**:** 906-925.

Chen, X., & Selloni, A. (2014). Introduction: titanium dioxide ($TiO_2$) nanomaterials. *Chemical reviews,* 114**:** 9281-9282.

Chen, Y.-F., Lee, C.-Y., Yeng, M.-Y., & Chiu, H.-T. (2003). The effect of calcination temperature on the crystallinity of $TiO_2$ nanopowders. *Journal of crystal growth,* 247**:** 363-370.

Cheung, J. K. H., Lam, R. K. W., Shi, M. Y., & Gu, J. D. (2007). Environmental fate of endocrine-disrupting dimethyl phthalate esters (DMPE) under sulfate-reducing condition. *Science of The Total Environment,* 381**:** 126-133.

Choi, K. J., Kim, S. G., Kim, C. W., & Park, J. K. (2006). Removal efficiencies of endocrine disrupting chemicals by coagulation/flocculation, ozonation, powdered/granular activated carbon adsorption, and chlorination. *Korean Journal of Chemical Engineering,* 23**:** 399-408.

Chu, L., Wang, J., Dong, J., Liu, H., & Sun, X. (2012). Treatment of coking wastewater by an advanced Fenton oxidation process using iron powder and hydrogen peroxide. *Chemosphere,* 86**:** 409-414.

Clark, R. J. H. (2016). Raman microscopy in the identification of pigments on manuscripts and other artwork. Retrieved 20 Jun 2016, from http://www.nap.edu/read/11413/chapter/13

Da Dalt, S., Alves, A. K., & Bergmann, C. P. (2013). Photocatalytic degradation of methyl orange dye in water solutions in the presence of MWCNT/TiO2 composites. *Materials Research Bulletin,* 48**:** 1845-1850.

Dai, K., Zhang, X., Fan, K., Zeng, P., & Peng, T. (2014). Multiwalled Carbon Nanotube-$TiO_2$ Nanocomposite for Visible-Light-Induced Photocatalytic Hydrogen Evolution. *Journal of Nanomaterials,* 2014**:** 8.

Dai, L., Chang, D. W., Baek, J.-B., & Lu, W. (2012). Carbon Nanomaterials for Advanced Energy Conversion and Storage. *Small,* 8**:** 1130-1166.

Datsyuk, V., Kalyva, M., Papagelis, K., Parthenios, J., Tasis, D., Siokou, A., Kallitsis, I., & Galiotis, C. (2008). Chemical oxidation of multiwalled carbon nanotubes. *Carbon,* 46**:** 833-840.

De Angelis, F., Di Valentin, C., Fantacci, S., Vittadini, A., & Selloni, A. (2014). Theoretical studies on anatase and less common $TiO_2$ phases: bulk, surfaces, and nanomaterials. *Chemical reviews,* 114**:** 9708-9753.

De Volder, M. F., Tawfick, S. H., Baugman, R. H., & Hart, A. J. (2013). Carbon nanotubes: present and future commercial applications. *Science,* 339**:** 535-539.

Deblonde, T., Cossu-Leguille, C., & Hartemann, P. (2011). Emerging pollutants in wastewater: a review of the literature. *International journal of hygiene and environmental health,* 214**:** 442-448.

Ding, X., An, T., Li, G., Chen, J., Sheng, G., Fu, J., & Zhao, J. (2008). Photocatalytic degradation of dimethyl phthalate ester using novel hydrophobic $TiO_2$ pillared montmorillonite photocatalyst. *Research on Chemical Intermediates,* 34**:** 67-83.

Djokic, V. R., Marinkovic, A. D., Ersen, O., Uskokovic, P. S., Petrovic, R. D., Radmilovic, V. R., & Janackovic, D. T. (2014). The dependence of the photocatalytic activity of $TiO_2$/carbon nanotubes nanocomposites on the modification of the carbon nanotubes. *Ceramics International,* 40**:** 4009-4018.

Eatemadi, A., Daraee, H., Karimkhanloo, H., Kouhi, M., Zarghami, N., Akbarzadeh, A., Abasi, M., Hanifehpour, Y., & Joo, S. W. (2014). Carbon nanotubes: properties, synthesis, purification, and medical applications. *Nanoscale Res Lett,* 9**:** 393.

Edwards, E. R., Antunes, E. F., Botelho, E. C., Baldan, M. R., & Corat, E. J. (2011). Evaluation of residual iron in carbon nanotubes purified by acid treatments. *Applied Surface Science,* 258**:** 641-648.

Farlex. (2003-2016). X-ray diffraction. Retrieved 5 Jun 2016, from http://encyclopedia2.thefreedictionary.com/x-ray+diffraction

Fei. (2003). Quanta SEM. Retrieved 14 Jun 2016, from https://www.fei.com/products/sem/quanta-sem/

Fisher, J. S. (2004). Are all EDC effects mediated via steroid hormone receptors? *Toxicology,* 205**:** 33-41.

Frye, C., BO, E., Calamandrei, G., Calza, L., Dessi-Fulgheri, F., Fernandez, M., Fusani, L., Kah, O., Kajta, M., & Le Page, Y. (2012). Endocrine disrupters: a review of some sources, effects, and mechanisms of actions on behaviour and neuroendocrine systems. *Journal of neuroendocrinology,* 24**:** 144-159.

Fujishima, A., Rao, T. N., & Tryk, D. A. (2000). Titanium dioxide photocatalysis. *Journal of Photochemistry and Photobiology C: Photochemistry Reviews,* 1**:** 1-21.

Fujishima, A., & Zhang, X. (2006). Titanium dioxide photocatalysis: present situation and future approaches. *Comptes Rendus Chimie,* 9**:** 750-760.

Gao, B., Peng, C., Chen, G. Z., & Puma, G. L. (2008). Photo-electro-catalysis enhancement on carbon nanotubes/titanium dioxide (CNTs/$TiO_2$) composite prepared by a novel surfactant wrapping sol–gel method. *Applied Catalysis B: Environmental,* 85**:** 17-23.

Gao, D.-W., & Wen, Z.-D. (2016). Phthalate esters in the environment: A critical review of their occurrence, biodegradation, and removal during wastewater treatment processes. *Science of The Total Environment,* 541**:** 986-1001.

Ghosh, T., & Oh, W.-C. (2012). Carbon based titania photocatalysts. *Asian Journal of Chemistry,* 24**:** 5419.

Geim, A. (2013). The wonder material graphene. Retrieved 25 Jun 2016, from http://www.33rdsquare.com/2012/10/the-wonder-material-graphene.html

Gui, M. M., Chai, S.-P., Xu, B.-Q., & Mohamed, A. R. (2014a). Enhanced visible light responsive MWCNT/$TiO_2$ core–shell nanocomposites as the potential photocatalyst for reduction of $CO_2$ into methane. *Solar Energy Materials and Solar Cells,* 122**:** 183-189.

Gui, M. M., Chai, S.-P., Xu, B.-Q., & Mohamed, A. R. (2014b). Visible-light-driven MWCNT@$TiO_2$ core-shell nanocomposites and the roles of MWCNTs on the surface chemistry, optical properties and reactivity in $CO_2$ photoreduction. *RSC Advances,* 4**:** 24007-24013.

Gullapalli, S., & Barron, A. R. (2010). Optical characterization of group (12-16) (II-VI) semiconductor nanoparticles by fluorescence spectroscopy. *Open Stax-CNX.*

Guo, Y., & Kannan, K. (2012). Challenges encountered in the analysis of phthalate esters in foodstuffs and other biological matrices. *Analytical and bioanalytical chemistry,* 404**:** 2539-2554.

Guo, Y., Wang, L., & Kannan, K. (2014). Phthalates and Parabens in Personal Care Products From China: Concentrations and Human Exposure. *Archives of Environmental Contamination and Toxicology,* 66**:** 113-119.

Gupta, S. M., & Tripathi, M. (2011). A review of $TiO_2$ nanoparticles. *Chinese Science Bulletin,* 56**:** 1639-1657.

Hamid, S. B. A., Tan, T. L., Lai, C. W., & Samsudin, E. M. (2014). Multiwalled carbon nanotube/$TiO_2$ nanocomposite as a highly active photocatalyst for photodegradation of Reactive Black 5 dye. *Chinese Journal of Catalysis*, 35**:** 2014-2019.

Hanaor, D. A. H., & Sorrell, C. C. (2011). Review of the anatase to rutile phase transformation. *Journal of Materials Science,* 46**:** 855-874.

Hansen, K. M., Christensen, J. H., Geels, C., Silver, J., & Brandt, J. (2015). Modelling the impact of climate change on the atmospheric transport and the fate of persistent organic pollutants in the Arctic. *Atmospheric Chemistry and Physics,* 15**:** 6549-6559.

Herrmann, J.-M. (1999). Heterogeneous photocatalysis: fundamentals and applications to the removal of various types of aqueous pollutants. *Catalysis today,* 53**:** 115-129.

Hsieh, C.-T., & Teng, H., (2000). Influence of mesopore volume and adsorbate size on adsorption capacities of activated carbons in aqueous solutions. *Carbon,* 38**:** 863-869.

Hu, J.-H., Feng, T., Li, W.-L., Zhai, H., Liu, Y., Wang, L.-Y., Hu, C.-L., & Xie, M.-X. (2014). Surface molecularly imprinted polymers with synthetic dummy template for simultaneously selective recognition of nine phthalate esters. *Journal of Chromatography A,* 1330**:** 6-13.

Huang, K.-C.， & Chien, S.-H. (2013). Improved visible-light-driven photocatalytic activity of rutile/titania-nanotube composites prepared by microwave-assisted hydrothermal process. *Applied Catalysis B: Environmental,* 140–141**:** 283-288.

Huang, X., Qi, X., Boey, F., & Zhang, H. (2012). Graphene-based composites. *Chemical Society Reviews,* 41**:** 666-686.

Hubinger, J. C. (2009). A survey of phthalate esters in consumer cosmetic products. *Journal of cosmetic science,* 61**:** 457-465.

Hung, H., Katsoyiannis, A. A., & Guardans, R. (2016). Ten years of global monitoring under the Stockholm Convention on Persistent Organic Pollutants (POPs): Trends, sources and transport modelling. *Environmental Pollution*.

Ibhadon, A. O., & Fitzpatrick, P. (2013). Heterogeneous photocatalysis: recent advances and applications. *Catalysts,* 3**:** 189-218.

Ibrahim, S. A., & Sreekantan, S. Effect of annealing atmosphere towards $TiO_2$ nanoparticles on their photocatalytic performance in aquoues phase. Enabling Science and Nanotechnology (ESciNano), 2010 International Conference on, 2010. IEEE, 1-2.

Jiang, G., Lin, Z., Chen, C., Zhu, L., Chang, Q., Wang, N., Wei, W., & Tang, H. (2011). $TiO_2$ nanoparticles assembled on graphene oxide nanosheets with high photocatalytic activity for removal of pollutants. *Carbon,* 49**:** 2693-2701.

Jing, Y., LI, L., Zhang, Q., Lu, P., Liu, P., & Lu, X. (2011). Photocatalytic ozonation of dimethyl phthalate with $TiO_2$ prepared by a hydrothermal method. *Journal of Hazardous Materials,* 189**:** 40-47.

Jo, W.-K., & Kim, K.-H. (2012). Feasibility of Carbonaceous Nanomaterial-Assisted Photocatalysts Calcined at Different Temperatures for Indoor Air Applications. *International Journal of Photoenergy,* 2012**:** 9.

Kamrin, M. A. (2009). Phthalate risks, phthalate regulation, and public health: a review. *Journal of Toxicology and Environmental Health, Part B,* 12**:** 157-174.

Karimifard, S., & Moghaddam, M. R. A. (2016). Enhancing the adsorption performance of carbon nanotubes with a multistep functionalization method: Optimization of Reactive Blue 19 removal through response surface methodology. *Process Safety and Environmental Protection,* 99**:** 20-29.

Khan, M. M., Adil, S. F., & Al-Mayouf, A. (2015). Metal oxides as photocatalysts. *Journal of Saudi Chemical Society,* 19**:** 462-464.

Kim, J. H., Zhang, X. H., Kim, J. D., Park, H. M., Lee, S. B., Yi, J. W., & Jung, S. I. (2012). Synthesis and characterization of anatase $TiO_2$ nanotubes with controllable crystal size by a simple MWCNT template method. *Journal of Solid State Chemistry,* 196**:** 435-440.

Kumar, M., & Ando, Y. (2010). Chemical vapor deposition of carbon nanotubes: a review on growth mechanism and mass production. *Journal of nanoscience and nanotechnology,* 10**:** 3739-3758.

Kuvarega, A. T., Krause, R. W., & Mamba, B. B. (2012). Multiwalled carbon nanotubes decorated with nitrogen, palladium co-doped $TiO_2$ (MWCNT/N, Pd co-doped TiO2) for visible light photocatalytic degradation of Eosin Yellow in water. *Journal of Nanoparticle Research,* 14**:** 1-16.

Leary, R., & Westwood, A. (2011). Carbonaceous nanomaterials for the enhancement of $TiO_2$ photocatalysis. *Carbon,* 49**:** 741-772.

Lee, D.-H., Porta, M., Jacobs JR, D. R., & Vandenberg, L. N. (2014). Chlorinated persistent organic pollutants, obesity, and type 2 diabetes. *Endocrine reviews,* 35**:** 557-601.

Liang, D.-W., Zhang, T., Fang, H. H., & He, J. (2008). Phthalates biodegradation in the environment. *Applied microbiology and Biotechnology,* 80**:** 183-198.

Liang, S., Li, G., & Tian, R. (2016). Multi-walled carbon nanotubes functionalized with a ultrahigh fraction of carboxyl and hydroxyl groups by ultrasound-assisted oxidation. *Journal of Materials Science,* 51**:** 3513-3524.

Liao, W., & Wang, P. (2009). Microwave-assisted photocatalytic degradation of dimethyl phthalate using a microwave discharged electrodeless lamp. *Journal of the Brazilian Chemical Society,* 20**:** 866-872.

Tan, T. L., Hamid, S. B. A., & Lai, C. W. (2015). Modification of Multi-walled Carbon Nanotubes with Nanoparticles for High Photocatalytic Activity. *Current Nanoscience,* 11**:** 504-508.

Liu, Y., Chen, Z., & Shen, J. (2013). Occurrence and Removal Characteristics of Phthalate Esters from Typical Water Sources in Northeast China. *Journal of Analytical Methods in Chemistry,* 2013**:** 419349.

Liu, Y., Gao, L., Sun, J., & Wang, Y. (2010). Functionalization of carbon nanotubes for nanoparticle attachment. *J Ceram Process Res,* 11**:** 120-122.

Lopez, R., & Gomez, R. (2012). Band-gap energy estimation from diffuse reflectance measurements on sol–gel and commercial $TiO_2$: a comparative study. *Journal of Sol-Gel Science and Technology,* 61**:** 1-7.

Luttrell, T., Halpegamage, S., Tao, J., Kramer, A., Sutter, E., & Batzill, M. (2014). Why is anatase a better photocatalyst than rutile?-Model studies on epitaxial $TiO_2$ films. *Scientific reports,* 4.

Mahshid, S., Ghamsari, M. S., Askari, M., Afshar, N., & Lahuti, S. (2006). Synthesis of $TiO_2$ nanoparticles by hydrolysis and peptization of titanium isopropoxide solution. *Semiconductor Physics, Quantum Electronics & Optoelectronics,* 9**:** 65-68.

Maqbool, F., Mostafalou, S., Bahadar, H., & Abdollahi, M. (2016). Review of endocrine disorders associated with environmental toxicants and possible involved mechanisms. *Life sciences,* 145**:** 265-273.

Market Research Store. (2016). Plasticizers (low phthalate, high phthalate and non phthalate) market for floor wall & coverings, wires & cables, consumer goods, film & sheets and other application: Global industry perspective comprehensive analysis, size, share, growth, segment, trends and forecast, 2014-2020. Retrieved 22 Jun 2016, from http://www.marketresearchstore.com/report/plasticizers-market-z59107

Martins-Junior, P., Alcantara, C., Resende, R., & Ferreira, A. (2013). Carbon nanotubes directions and perspectives in oral regenerative medicine. *Journal of dental research***,** 0022034513490957.

Matsumoto, M., Hirata-Koizumi, M., & Ema, M. (2008). Potential adverse effects of phthalic acid esters on human health: a review of recent studies on reproduction. *Regulatory Toxicology and Pharmacology,* 50**:** 37-49.

Medellin-Castillo, N. A., Ocampo-Perez, R., Leyva-Ramos, R., Sanchez-Polo, M., Rivera-Utrilla, J., & Mendez-Diaz, J. D. (2013). Removal of diethyl phthalate from water solution by adsorption, photo-oxidation, ozonation and advanced oxidation process ($UV/H_2O_2$, $O_3/H_2O_2$ and $O_3$/activated carbon). *Science of the total environment,* 442**:** 26-35.

Minnesotacorn Research & Promotion Council (2014). Marketplace opportunities for integration of biobased and conventional plastics. Retrived 25 May 2016, from http://www.auri.org/

Mohammadi, M., & Sabbaghi, S. (2014). Photo-catalytic degradation of 2, 4-DCP wastewater using MWCNT/TiO 2 nano-composite activated by UV and solar light. *Environmental Nanotechnology, Monitoring & Management,* 1**:** 24-29.

Muduli, S., Lee, W., Dhas, V., Mujawar, S., Dubey, M., Vijayamohanan, K., Han, S.-H., & Ogale, S. (2009). Enhanced conversion efficiency in dye-sensitized solar cells based on hydrothermally synthesized TiO2− MWCNT nanocomposites. *ACS applied materials & interfaces,* 1**:** 2030-2035.

Muneer, M., Theurich, J., & Bahnemann, D. (2001). Titanium dioxide mediated photocatalytic degradation of 1,2-diethyl phthalate. *Journal of Photochemistry and Photobiology A: Chemistry,* 143**:** 213-219.

Nadal, M., Marques, M., Mari, M., & Domingo, J. L. (2015). Climate change and environmental concentrations of POPs: A review. *Environmental research,* 143**:** 177-185.

Nadzirah, S., Foo, K., & Hashim, U. (2015). Morphological reaction on the different stabilizers of titanium dioxide nanoparticles. *Int J Electrochem Sci,* 10**:** 5498-5512.

Nakata, K., & Fujishima, A. (2012). $TiO_2$ photocatalysis: Design and applications. *Journal of Photochemistry and Photobiology C: Photochemistry Reviews,* 13**:** 169-189.

Odling, G., & Robertson, N. (2015). Why is Anatase a Better Photocatalyst than Rutile? The Importance of Free Hydroxyl Radicals. *ChemSusChem,* 8**:** 1838-1840.

Oh, W.-C., Zhang, F.-J., & Chen, M.-L. (2009). Preparation of MWCNT/TiO2 composites by using MWCNTs and Titanium (IV) alkoxide precursors in Benzene and their photocatalytic effect and bactericidal activity. *Bulletin of the Korean Chemical Society,* 30**:** 2637-2642.

Oloibiri, V., Ufomba, I., Chys, M., Audenaert, W. T., Demeestere, K., & Van Hulle, S. W. (2015). A comparative study on the efficiency of ozonation and coagulation–flocculation as pretreatment to activated carbon adsorption of biologically stabilized landfill leachate. *Waste Management,* 43**:** 335-342.

Ong, Y. T., Ahmad, A. L., Zein, S. H. S., & Tan, S. H. 2010. A review on carbon nanotubes in an environmental protection and green engineering perspective. *Brazilian Journal of Chemical Engineering,* 27**:** 227-242.

Osman, B., Özer, E. T., Demirbel, E., Gucer, Ş., & Besirli, N. (2013). Synthesis and characterization of L-tryptophan containing microbeads for removal of dimethyl phthalate from aqueous phase. *Separation and Purification Technology,* 109**:** 40-47.

Oturan, M. A., & Aaron, J.-J. (2014). Advanced oxidation processes in water/wastewater treatment: principles and applications. A review. *Critical Reviews in Environmental Science and Technology,* 44**:** 2577-2641.

OuYang, K., Xie, S., & Ma, X. O. (2013). Photocatalytic activity of $TiO_2$ supported on multi-walled carbon nanotubes under simulated solar irradiation. *Ceramics International,* 39**:** 7531-7536.

Pariatamby, A., & Kee, Y. L. (2016). Persistent Organic Pollutants Management and Remediation. *Procedia Environmental Sciences,* 31**:** 842-848.

Paunovic, P., Dimitrov, A. T., Popovski, O., Slavcheva, E., Grozdanov, A., Lefterova, E., Petrusevski, G., & Jordanov, S. H. (2009). Effect of activation/purification of multiwalled carbon nanotubes (MWCNTs) on the activity of non-platinum based hypo-hyper d-electrocatalysts for hydrogen evolution. *Materials Research Bulletin,* 44**:** 1816-1821.

Pelaez, M., Nolan, N. T., Pillai, S. C., Seery, M. K., Falaras, P., Kontos, A. G., Dunlop, P. S., Hamilton, J. W., Byrne, J. A., & O'shea, K. (2012). A review on the visible light active titanium dioxide photocatalysts for environmental applications. *Applied Catalysis B: Environmental,* 125**:** 331-349.

Perreault, F., De Faria, A. F., & Elimelech, M. (2015). Environmental applications of graphene-based nanomaterials. *Chemical Society Reviews,* 44**:** 5861-5896.

Politakos, N., Zalakain, I., Fernandez Darlas', B., Eceiza, A., & Kortaberria, G. (2013). Optical, structural and electrical properties of polyaniline systems doped with C60 and small gap C60 fullerenes. *Materials Chemistry and Physics,* 142**:** 387-394.

Puma, G. L., Bono, A., Krishnaiah, D., & Collin, J. G. (2008). Preparation of titanium dioxide photocatalyst loaded onto activated carbon support using chemical vapor deposition: A review paper. *Journal of hazardous Materials,* 157**:** 209-219.

Rebecca, J., Priya, G., & Nicola, A. S. (2005). Transition metal-doped $TiO_2$ and ZnO—present status of the field. *Journal of Physics: Condensed Matter,* 17**:** R657.

Ren, A., Qiu, X., Jin, L., Ma, J., Li, Z., Zhang, L., Zhu, H., Finneli, R. H., & Zhu, T. (2011). Association of selected persistent organic pollutants in the placenta with the risk of neural tube defects. *Proceedings of the National Academy of Sciences,* 108**:** 12770-12775.

Reti, B., Mogyorosi, K., Dombi, A., & Hernadi, K. (2014). Substrate dependent photocatalytic performance of $TiO_2$/MWCNT photocatalysts. *Applied Catalysis A: General,* 469**:** 153-158.

Reyes-Coronado, D., Rodriguez-Gattorno, G., Espinosa-Pesqueira, M., Cab, C., De Coss, R. D., & Oskam, G. (2008). Phase-pure TiO2 nanoparticles: anatase, brookite and rutile. *Nanotechnology,* 19**:** 145605.

Riget, F., Vorkamp, K., Bossi, R., Sonne, C., Letcher, R., & Dietz, R. (2015). Twenty years of monitoring of persistent organic pollutants in Greenland biota. A review. *Environmental Pollution*.

Rivera-Utrilla, J., Ocampo-Perez, R., Mendez-Diaz, J. D., & Sanchez-Polo, M. (2012). Environmental impact of phthalic acid esters and their removal from water and sediments by different technologies–a review. *Journal of environmental management,* 109**:** 164-178.

Sajid, M., Basheer, C., Narasimhan, K., Buhmeida, A., Al Qahtani, M., & Al-Ahwal, M. S. (2016). Persistent and endocrine disrupting organic pollutants: advancements and challenges in analysis, health concerns and clinical correlates. *Nature Environment and Pollution Technology,* 15**:** 733.

Saleh, T. A., & Gupta, V. K. (2012). Photo-catalyzed degradation of hazardous dye methyl orange by use of a composite catalyst consisting of multi-walled carbon nanotubes and titanium dioxide. *Journal of Colloid and interface Science,* 371**:** 101-106.

Sauve, S., & Desrosiers, M. (2014). A review of what is an emerging contaminant. *Chemistry Central Journal,* 8**:** 1-7.

Sayilkan, F., Asilturk, M., Sayilkan, H., Önal, Y., Akarsu, M., & Arpac, E. (2006). Characterization of TiO_2 Synthesized in Alcohol by a Sol-Gel Process: The Effects of Annealing Temperature and Acid Catalyst. *Turkish Journal of Chemistry,* 29**:** 697-706.

Shimadzu. (2016). Diffuse Reflectance Measurement. Retrieved 11 May 2016, from http://www.shimadzu.com/an/molecular_spectro/uv/accessory/solidsample/solid.html

Schneider, J., Matsuoka, M., Takeuchi, M., Zhang, J., Horiuchi, Y., Anpo, M., & Bahnemann, D. W. (2014). Understanding $TiO_2$ Photocatalysis: Mechanisms and Materials. *Chemical Reviews,* 114**:** 9919-9986.

Sekiya, T., Ohta, S., Kamei, S., Hanakawa, M., & Kurita, S. (2001). Raman spectroscopy and phase transition of anatase $TiO_2$ under high pressure. *Journal of Physics and Chemistry of Solids,* 62**:** 717-721.

Serpone, N., & Emeline, A. (2002). Suggested terms and definitions in photocatalysis and radiocatalysis. *International Journal of Photoenergy,* 4**:** 91-131.

Sharma, B. M., Bharat, G. K., Tayal, S., Nilzzetto, L., Čupr, P., & Larssen, T. (2014). Environment and human exposure to persistent organic pollutants (POPs) in India: A systematic review of recent and historical data. *Environment international,* 66**:** 48-64.

Shpilevsky, E. M., Shpilevsky, M. E., Prylutskyy, Y. I., Matzuy, L. Y., Zakharenko, M. I., & Le Normand, F. (2011). Structure and properties of C60 fullerene films with titanium atoms.

Silva, C. G., & Faria, J. L. (2009). Anatase vs.rutile efficiency on the photocatalytic degradation of clofibric acid under near UV to visible irradiation. *Photochemical & Photobiological Sciences,* 8**:** 705-711.

Sin, J.-C., Lam, S.-M., Mohamed, A. R., & Lee, K.-T. (2011). Degrading Endocrine Disrupting Chemicals from Wastewater by $TiO_2$. *International Journal of Photoenergy,* 2012.

Sin, J.-C., Lam, S.-M., Mohamed, A. R., & Lee, K.-T. (2012). Degrading Endocrine Disrupting Chemicals from Wastewater by $TiO_2$ Photocatalysis: A Review. *International Journal of Photoenergy,* 2012.

Smart Economy. (2008). What come before DNA or RNA? Fullerenes and amino acids. Retrieved 14 Jun 2016, from http://smarteconomy.typepad.com/smart_economy/2008/01/what-came befor.html

Song, C., Wang, L., Ren, J., Lv, B., Sun, Z., Yan, J., Li, X., & Liu, J. (2016). Comparative study of diethyl phthalate degradation by UV/H2O2 and UV/TiO2: kinetics, mechanism, and effects of operational parameters. *Environmental Science and Pollution Research,* 23**:** 2640-2650.

Stormann, R. (2003). Scheme of a HPLC system. Retrieved 19 April 2016, form http://chem.uft.uni-bremen.de/Chromatography/chrom065.htm

Su, D. S., Perathoner, S., & Centi, G. (2013). Nanocarbons for the development of advanced catalysts. *Chemical reviews,* 113**:** 5782-5816.

Sun, J., Huang, J., Zhang, A., Liu, W., & Cheng, W. (2013). Occurrence of phthalate esters in sediments in Qiantang River, China and inference with urbanization and river flow regime. *Journal of hazardous materials,* 248**:** 142-149.

Talat-Mehrabad, J., Khosravi, M., Modirshahla, N., & Behnajady, M. A. (2016). Sol–gel preparation and characterization of Ag and Mg co-doped nano $TiO_2$: efficient photocatalytic degradation of C.I. Acid Red 27. *Research on Chemical Intermediates,* 42**:** 595-609.

Teh, C. M., & Mohamed, A. R. (2011). Roles of titanium dioxide and ion-doped titanium dioxide on photocatalytic degradation of organic pollutants (phenolic compounds and dyes) in aqueous solutions: A review. *Journal of Alloys and Compounds,* 509**:** 1648-1660.

Tessonnier, J.-P., Rosenthal, D., Hansen, T. W., Hess, C., Schuster, M. E., Blume, R., Girgsdies, F., Pfander, N., Timpe, O., & Su, D. S. (2009). Analysis of the structure and chemical properties of some commercial carbon nanostructures. *Carbon,* 47**:** 1779-1798.

Thomaidi, V. S., Stasinakis, A. S., Borova, V. L., & Thomaidis, N. S. (2015). Is there a risk for the aquatic environment due to the existence of emerging organic contaminants in treated domestic wastewater? Greece as a case-study. *Journal of hazardous materials,* 283**:** 740-747.

Tian, L., Ye, L., Deng, K., & Zan, L. (2011). $TiO_2$/carbon nanotube hybrid nanostructures: Solvothermal synthesis and their visible light photocatalytic activity. *Journal of Solid State Chemistry,* 184**:** 1465-1471.

Tiwari, D. K., Behari, J., & Sen, P. (2008). Application of Nanoparticles in Waste Water Treatment 1.

Tonejc, A. M. (2006). Hrtem Investigation of Nanocrystalline Materials. *Electron Crystallography,* 211: 443-453.

Tseng, Y.-H., Yen, C.-Y., Yen, M.-Y., & Ma, C.-C. (2010). Effects of the acid pretreated multi-walled carbon nanotubes on the photocatalytic capacity of TiO $_2$/multi-walled carbon nanotubes nanocomposites. *IET Micro & Nano Letters,* 5**:** 1-6.

Tullo. (2015). Plasticizer makers want a pierce of the phthalates pie. Retrieved 10 Jun 2016, from http://cen.acs.org/articles/93/i25/Plasticizer-Makers-Want-Piece-Phthalates.html

Turgunov, M. A., Oh, J. O., & Yoon, S. H. (2014). Surface Modification of Multiwall Carbon Nanotubes by Sulfuric Acid and Nitric Acid.

Valencia, S., Marin, J. M., & Restrepo, G. (2010). Study of the bandgap of synthesized titanium dioxide nanoparticules using the sol-gel method and a hydrothermal treatment. *Open Materials Science Journal,* 4**:** 9-14.

Visco, G., Bellanti, F., Campanella, L., Mazzella, T., & Nobili, V. (2005). Optimisation of a Photochemical Sensor for Total Organic Carbon Measurement. *Annali di Chimica,* 95**:** 185-198.

Wang, H., Wang, H.-L., Jiang, W.-F., & Li, Z.-Q. (2009). Photocatalytic degradation of 2, 4-dinitrophenol (DNP) by multi-walled carbon nanotubes (MWCNTs)/$TiO_2$ composite in aqueous solution under solar irradiation. *Water research,* 43**:** 204-210.

Wepasnick, K. A., Smith, B. A., Schrote, K. E., Wilson, H. K., Diegelmann, S. R., & Fairbrother, D. H. (2011). Surface and structural characterization of multi-walled carbon nanotubes following different oxidative treatments. *Carbon,* 49**:** 24-36.

Woan, K., Pyrgiotakis, G., & Sigmund, W. (2009). Photocatalytic carbon-nanotube-$TiO_2$ composites.

Wu, C.-H., Kuo, C.-Y., & Chen, S.-T. (2013). Synergistic effects between $TiO_2$ and carbon nanotubes (CNTs) in a $TiO_2$/CNTs system under visible light irradiation. *Environmental technology,* 34**:** 2513-2519.

Wu, M.-H., Liu, N., Xu, G., Ma, J., Tang, L., Wang, L., & Fu, H.-Y. (2011). Kinetics and mechanisms studies on dimethyl phthalate degradation in aqueous solutions by pulse radiolysis and electron beam radiolysis. *Radiation Physics and Chemistry,* 80**:** 420-425.

Xia, X. H., Jia, Z. J., Yu, Y., Liang, Y., Wang, Z., & Ma, L. L. (2007). Preparation of multi-walled carbon nanotube supported TiO2 and its photocatalytic activity in the reduction of $CO_2$ with $H_2O$.

Xie, Y., Heo, S. H., Kim, Y. N., Yoo, S. H., & Cho, S. O. (2009). Synthesis and visible-light-induced catalytic activity of $Ag_2S$-coupled $TiO_2$ nanoparticles and nanowires. *Nanotechnology,* 21**:** 015703.

Xing, B., Shi, C., Zhang, C., Yi, G., Chen, L., Guo, H., Huang, G., & Cao, J. (2016). Preparation of $TiO_2$/Activated Carbon Composites for Photocatalytic Degradation of RhB under UV Light Irradiation. *Journal of Nanomaterials,* 2016**:** 10.

Xu, B., Gao, N.-Y., Cheng, H., Xia, S.-J., Rui, M., & Zhao, D.-D. (2009a). Oxidative degradation of dimethyl phthalate (DMP) by UV/H2O2 process. *Journal of Hazardous Materials,* 162**:** 954-959.

Xu, B., Gao, N.-Y., Sun, X.-F., Xia, S.-J., Rui, M., Simonnot, M.-O., Causserand, C., & Zhao, J.-F. (2007). Photochemical degradation of diethyl phthalate with UV/H 2 O 2. *Journal of hazardous materials,* 139**:** 132-139.

Xu, L., Chu, W., & Graham, N. (2013a). A systematic study of the degradation of dimethyl phthalate using a high-frequency ultrasonic process. *Ultrasonics sonochemistry,* 20**:** 892-899.

Xu, L. J., Chu, W., & Gan, L. (2015). Environmental application of graphene-based CoFe2O4 as an activator of peroxymonosulfate for the degradation of a plasticizer. *Chemical Engineering Journal,* 263**:** 435-443.

Xu, W., Wang, X., & Cai, Z. (2013b). Analytical chemistry of the persistent organic pollutants identified in the Stockholm Convention: A review. *Analytica Chimica Acta,* 790**:** 1-13.

Xu, X.-R., Li, S.-X., Li, X.-Y., Gu, J.-D., Chen, F., Li, X.-Z., & Li, H.-B. (2009b). Degradation of n-butyl benzyl phthalate using TiO2/UV. *Journal of Hazardous Materials,* 164**:** 527-532.

Xu, Y.-J., Zhuang, Y., & Fu, X. (2010). New insight for enhanced photocatalytic activity of TiO2 by doping carbon nanotubes: a case study on degradation of benzene and methyl orange. *The Journal of Physical Chemistry C,* 114**:** 2669-2676.

Yang, R. T. (2003). Activated Carbon. *Adsorbents: Fundamentals and Applications.* John Wiley & Sons, Inc.

Yao, H., & Kimura, K. (2007). Field emission scanning electron microscopy for structural characterization of 3D gold nanoparticle superlattices. *Modern research and educational topics in microscopy*. Formatex, Badajoz.

Yoo, J. B., Yoo, H. J., Jung, H. J., Kim, H. S., Bang, S., Choi, J., Suh, H., Lee, J.-H., Kim, J.-G., & Hur, N. H. (2016). Titanium oxynitride microspheres with the rock-salt structure for use as visible-light photocatalysts. *Journal of Materials Chemistry A,* 4**:** 869-876.

Yu, Y., Yu, J. C., Chan, C. Y., Che, Y. K., Zhao, J. C., Ding, L., Ge, W. K., & Wong, P. K.. (2005). Enhancement of adsorption and photocatalytic activity of $TiO_2$ by using carbon nanotubes for the treatment of azo dye.

Yuan, B.-L., Li, X.-Z., & Graham, N. (2008a). Aqueous oxidation of dimethyl phthalate in a Fe (VI)-$TiO_2$-UV reaction system. *Water Research,* 42**:** 1413-1420.

Yuan, B.-L., Li, X.-Z., & Graham, N. (2008b). Reaction pathways of dimethyl phthalate degradation in $TiO_2$–UV–$O_2$ and $TiO_2$–UV–Fe(VI) systems. *Chemosphere,* 72**:** 197-204.

Yudianti, R., Onggo, H., Sudirman, Y. S., Iwata, T., & Azuma, J.-I. (2011). Analysis of functional group sited on multi-wall carbon nanotube surface. *Open Materials Science Journal,* 5**:** 242-247.

Zeng, F., Cui, K., Xie, Z., Wu, L., Liu, M., Sun, G., Lin, Y., Luo, D., & Zeng, Z. (2008). Phthalate esters (PAEs): emerging organic contaminants in agricultural soils in peri-urban areas around Guangzhou, China. *Environmental Pollution,* 156**:** 425-434.

Zhang, C., & Wang, Y. (2009). Removal of dissolved organic matter and phthalic acid esters from landfill leachate through a complexation–flocculation process. *Waste Management,* 29**:** 110-116.

Zhang, J., Zhou, P., Liu, J., & Yu, J. (2014a). New understanding of the difference of photocatalytic activity among anatase, rutile and brookite $TiO_2$. *Phys. Chem. Chem. Phys.*, 16**:** 20382-20386.

Zhang, X.-Y., Fan, X., Qiu, Y.-J., Li, C.-Y., Xing, S., Zheng, Y.-T., & Xu, J.-H. (2014b). Newly identified thermostable esterase from Sulfobacillus acidophilus: properties and performance in phthalate ester degradation. *Applied and environmental microbiology,* 80**:** 6870-6878.

Zhang, Y., Liang, Q., Gao, R., Hou, H., Tan, W., He, X., Zhang, H., Yu, M., Ma, L., Xi, B., & Wang, X. (2015). Contamination of Phthalate Esters (PAEs) in Typical Wastewater-Irrigated Agricultural Soils in Hebei, North China. *PLoS ONE,* 10**:** e0137998.

Zhao, D., Yang, X., Chen, C., & Wang, X., (2013). Enhanced photocatalytic degradation of methylene blue on multiwalled carbon nanotubes–$TiO_2$. *Journal of Colloid and Interface Science,* 398**:** 234-239.

Zhu, J., & Jiang, Z. (2014). Flocculation Behavior in Removal of Dimethyl Phthalate from Water using Cationic Flocculant P (AM-DAC-DMC). *Asian Journal of Chemistry,* 26**:** 1103.

List of Publications and Papers Presented

## ISI-Cited Publications:

1. **Tong Ling Tan**, Chin Wei Lai, Sharifah Bee Abd Hamid (2014). Nanocomposites of Multi-Walled Carbon Nanotubes with $TiO_2$ for High Photocatalytic Activity. *Advanced Materials Research*, 925, 13-17.

2. Sharifah Bee Abd Hamid, **Tong Ling Tan**, Chin Wei Lai, Emy Marlina Samsudin (2014). Nanohybrid of Multiwalled Carbon Nanotubes / $TiO_2$ as a Highly Active Photocatalyst for Photodegradation of Reactive Black 5 Dye. *Chinese Journal of Catalysis*, 35(12), 1-6.

3. **Tong Ling Tan**, Sharifah Bee Abd Hamid, Chin Wei Lai, Modification of Multi-walled Carbon Nanotubes with $TiO_2$ Nanoparticles for High Photocatalytic Activity (2015). *Current Nanoscience*, 11(4), 504-508.

4. Chin Wei Lai, Sharifah Bee Abd Hamid, **Tong Ling Tan**, Wai Hong Lee (2015). Rapid Formation of 1-D Titanate Nanotubes using Alkaline Hydrothermal Treatment and its Photocatalytic Performance. *Journal of Nanomaterials*, 2015, Article ID: 145360.

## Conference Proceedings:

1. **Tong Ling Tan**, Chin Wei Lai, Sharifah Bee Abd Hamid (2013). Nanocomposites of Multi-walled Carbon Nanotubes with $TiO_2$ for High Photocatalytic Activity, presented at *21st Joint International Conference on Nanoscience, Engineering and Management*, BOND 21, 2013, Bayview Beach Resort, Batu Feringgi, Penang, 19-21 Aug 2013.

2. **Tong Ling Tan**, Chin Wei Lai and Sharifah Bee Abd Hamid (2014). Modification of multi-walled carbon nanotubes with $TiO_2$ nanoparticles for high photocatalytic activity, presented at *Nano-Scitech 2014 & IC-Net 2014 Malaysia-Japan International Conference on Nanoscience, Nanotechnology and Nanoengineering 2014, Institute of Leadership and Quality Management* (ILQAM), Universiti Teknologi MARA(UITM), Shah Alam, Selangor, 28 Feb-3 March, 2014.

3. Chin Wei Lai, **Tong Ling Tan**, Syazwan Hanani Binti Meriam Suhaimi, Sharifah Bee Abd Hamid (2014). Formation of hybrid WO3-TiO2 Nanotube (WTNT) and Its Application to Conserve the Environment, presented at

*International Conference of Environmental and Occupational Health* (ICEOH 2014), Marriott Hotel, Putrajaya, 7-9 April 2014.

4. **Tong Ling Tan**, Sharifah Bee Abd Hamid, Kian Mun Lee and Chin Wei Lai (2016). Fabrication of TiO2 Nanoparticles on Large-Area Graphene Oxide Sheets as Promising Photocatalytic Material, presented at *2016 International Conference on Composite Materials and Materials Engineering*, ICCMME, 2016, Chateau de Bangkok, Thailand, 9-11 March 2016.

*Advanced Materials Research Vol. 925 (2014) pp 13-17*
*Online available since 2014/Apr/17 at www.scientific.net*
*© (2014) Trans Tech Publications, Switzerland*
*doi:10.4028/www.scientific.net/AMR.925.13*

# Nanocomposites of Multi-walled Carbon Nanotubes with $TiO_2$ for High Photocatalytic Activity

Tong Ling Tan[1], Chin Wei Lai [2], Sharifah Bee Abd Hamid [3]

Nanotechnology and Catalysis Research Center (NANOCAT), Institute of Graduate Studies,
University of Malaya, 50603 Kuala Lumpur, Malaysia
E-mail: [2]cwlai@um.edu.my; [3]sharifahbee@um.edu.my

**Keywords:** MWCNTs, $TiO_2$, Sol-gel, Rhodamine B

## Abstract

Multi-walled Carbon Nanotubes (MWCNTs) coupled with $TiO_2$ nanoparticles was successfully synthesized using sol-gel method at room temperature. Titanium isopropoxide and MWCNTs were selected as starting materials. The presence of anatase $TiO_2$ phase in the MWCNTs/$TiO_2$ composites was determined by XRD analysis. In addition, FTIR analysis was conducted to determine the chemical bonding of MWCNTs/$TiO_2$ composites. Interestingly, it was found that the shifting of absorption edges of $TiO_2$ nanoparticles towards to the visible-light region due to the incorporation of MWCNTs using UV-Visible spectroscopy. The photocatalytic activity of MWCNTs/$TiO_2$ nanocomposites was demonstrated by the Rhodamine B degradation.

## Introduction

In recent years, $TiO_2$ was known as one of the most popular semiconductors and had attracted a tremendous interest from the researchers and scientists all over the world [1]. It has a great performance in a broad range of applications such as in the fields of $H_2$ production, environmental remediation, gas sensors and photoeletrochemical cells. Nonetheless, $TiO_2$ has attracted considerable scientific interest due to its promising properties such as non-toxic, inexpensive, thermodynamically and chemically stable [2].

However, an obvious hindrance to the widespread use of $TiO_2$-based materials is its $TiO_2$ has a wide band gap energy (Eg = 3.2 eV for anatase) and thus can only absorb light with the wavelengths of 385nm and below. In the light of this, the poor visible light absorption and fast recombination of electron-hole pairs after photoexcitation will cause low quantum efficiency in photocatalytic reactions [1]. Hence, several methods have been attempted in order to modify or enhance the photoresponse of the $TiO_2$ to the visible region with the doping of metals, non-metals or transition elements, coupling with semiconductors and dye-sensitiztion [3]. In this present study, the nanocomposites of carbonaceous materials coupled with titanium dioxide ($TiO_2$) have attracted a significant attention owing to their remarkable structural and electrical properties. With the incorporation of carbonaceous materials, the band gap energy of $TiO_2$ reduced from 3.2 to 2.79 eV respectively. Among the carbonaceous materials, carbon nanotubes have become the major of interest due to its large specific surface area (>150 $m^2g^{-1}$), excellent mechanical properties and good electrical conductivity, which make them suitable for mitigating environmental pollutants [2, 5].

In this manner, Multi-walled carbon nanotubes (MWCNTs) play a vital role as an electron acceptor for photocatalytic $TiO_2$ through the modification of the band gap energy and the retardation of electron-hole recombination[6]. The dispersion of $TiO_2$ on MWCNTs surface may create more active sites for photon absorption from illumination and thus, MWCNTs can efficiently generate photo-excited electrons from $TiO_2$ for better photocatalytic activity. As a result, the MWCNTs-$TiO_2$ composites exhibit the better photocatalytic activity than pure $TiO_2$ [7].

Over the past ten years, several methods have been done to fabricate MWCNTs/$TiO_2$ composite materials including simple mixing, hydrothermal, sol-gel, electrophoretic deposition and chemical

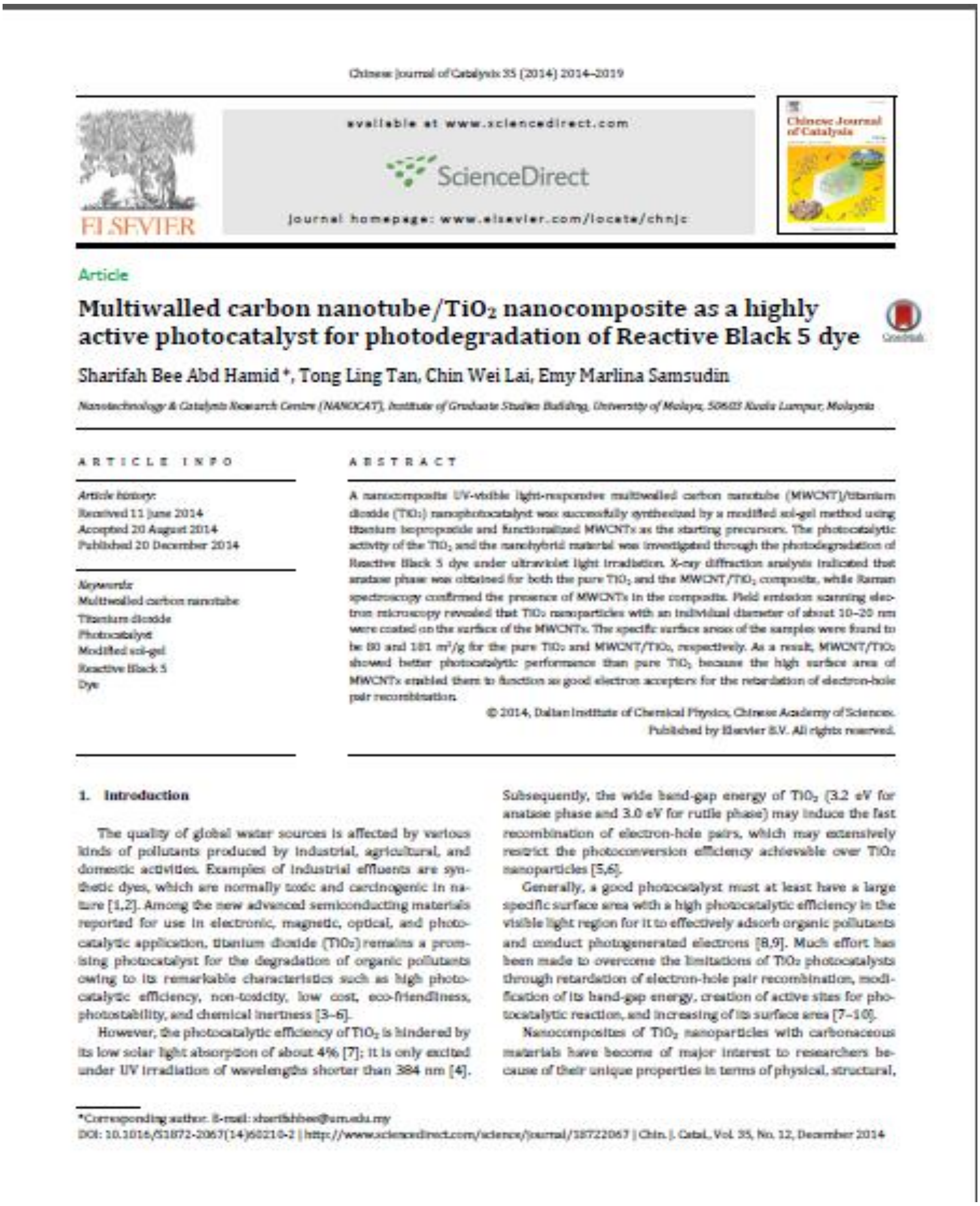

Chinese Journal of Catalysis 35 (2014) 2014–2019

available at www.sciencedirect.com

ScienceDirect

journal homepage: www.elsevier.com/locate/chnjc

Article

# Multiwalled carbon nanotube/$TiO_2$ nanocomposite as a highly active photocatalyst for photodegradation of Reactive Black 5 dye

Sharifah Bee Abd Hamid *, Tong Ling Tan, Chin Wei Lai, Emy Marlina Samsudin

*Nanotechnology & Catalysis Research Centre (NANOCAT), Institute of Graduate Studies Building, University of Malaya, 50603 Kuala Lumpur, Malaysia*

ARTICLE INFO

*Article history:*
Received 11 June 2014
Accepted 20 August 2014
Published 20 December 2014

*Keywords:*
Multiwalled carbon nanotube
Titanium dioxide
Photocatalyst
Modified sol-gel
Reactive Black 5
Dye

ABSTRACT

A nanocomposite UV-visible light-responsive multiwalled carbon nanotube (MWCNT)/titanium dioxide ($TiO_2$) nanophotocatalyst was successfully synthesized by a modified sol-gel method using titanium isopropoxide and functionalized MWCNTs as the starting precursors. The photocatalytic activity of the $TiO_2$ and the nanohybrid material was investigated through the photodegradation of Reactive Black 5 dye under ultraviolet light irradiation. X-ray diffraction analysis indicated that anatase phase was obtained for both the pure $TiO_2$ and the MWCNT/$TiO_2$ composite, while Raman spectroscopy confirmed the presence of MWCNTs in the composite. Field emission scanning electron microscopy revealed that $TiO_2$ nanoparticles with an individual diameter of about 10–20 nm were coated on the surface of the MWCNTs. The specific surface areas of the samples were found to be 80 and 181 $m^2/g$ for the pure $TiO_2$ and MWCNT/$TiO_2$, respectively. As a result, MWCNT/$TiO_2$ showed better photocatalytic performance than pure $TiO_2$ because the high surface area of MWCNTs enabled them to function as good electron acceptors for the retardation of electron-hole pair recombination.

## 1. Introduction

The quality of global water sources is affected by various kinds of pollutants produced by industrial, agricultural, and domestic activities. Examples of industrial effluents are synthetic dyes, which are normally toxic and carcinogenic in nature [1,2]. Among the new advanced semiconducting materials reported for use in electronic, magnetic, optical, and photocatalytic application, titanium dioxide ($TiO_2$) remains a promising photocatalyst for the degradation of organic pollutants owing to its remarkable characteristics such as high photocatalytic efficiency, non-toxicity, low cost, eco-friendliness, photostability, and chemical inertness [3–6].

However, the photocatalytic efficiency of $TiO_2$ is hindered by its low solar light absorption of about 4% [7]; it is only excited under UV irradiation of wavelengths shorter than 384 nm [4]. Subsequently, the wide band-gap energy of $TiO_2$ (3.2 eV for anatase phase and 3.0 eV for rutile phase) may induce the fast recombination of electron-hole pairs, which may extensively restrict the photoconversion efficiency achievable over $TiO_2$ nanoparticles [5,6].

Generally, a good photocatalyst must at least have a large specific surface area with a high photocatalytic efficiency in the visible light region for it to effectively adsorb organic pollutants and conduct photogenerated electrons [8,9]. Much effort has been made to overcome the limitations of $TiO_2$ photocatalysts through retardation of electron-hole pair recombination, modification of its band-gap energy, creation of active sites for photocatalytic reaction, and increasing of its surface area [7–10].

Nanocomposites of $TiO_2$ nanoparticles with carbonaceous materials have become of major interest to researchers because of their unique properties in terms of physical, structural,

---

*Corresponding author. E-mail: sharifahbee@um.edu.my

DOI: 10.1016/S1872-2067(14)60210-2 | http://www.sciencedirect.com/science/journal/18722067 | Chin. J. Catal., Vol. 35, No. 12, December 2014

*Current Nanoscience*, 2015, *11*, 000-000 1

# Modification of Multi-walled Carbon Nanotubes with Nanoparticles for High Photocatalytic Activity

Tong Ling Tan, Sharifah Bee Abd Hamid* and Chin Wei Lai

*Nanotechnology & Catalysis Research Centre (NANOCAT), 3$^{rd}$ Floor, Block A, Institute of Postgraduate Studies (IPS), University of Malaya, 50603 Kuala Lumpur, Malaysia*

**Abstract:** Titanium dioxide ($TiO_2$) nanoparticles were successfully attached to the outer surface of one dimensional oxidized multi-walled carbon nanotubes (MWCNTs) *via* sol-gel technique. It was well-established that calcination temperature played a critical role in controlling the crystallinity and phase of MWCNTs/$TiO_2$ composites. Thus, the effects of calcination temperature on the resulting MWCNTs/$TiO_2$ were illustrated. The phase transition of MWCNTs/$TiO_2$ composites was determined using XRD analysis. The photocatalytic activity evaluation of MWCNTs/$TiO_2$ composites was conducted under degradation of organic dye (methyl orange solution). The results revealed that annealed MWCNTs/$TiO_2$ composites showed significantly enhanced photocatalytic activity due to the highly crystalline anatase $TiO_2$ structures.

**Keywords:** Methyl orange, MWCNTs, Sol-gel, $TiO_2$.

## 1. INTRODUCTION

The discharges of organic dyes with carcinogenic, harmful and toxic properties into water systems have been gaining attention over the past decades [1, 2]. These organic pollutants are widely applied in domestic activities such as in textile, printing, food and pharmaceutical industries [3, 4]. For instance, methyl orange, a well-known anionic dye could subsequently lead to the serious water contamination problems and constitute negative impacts on human health when the effluents are discharged into water systems [1, 3]. Therefore, it is necessary to study the removal of methyl orange from the water streams in order to avoid any environmental threats.

Among the new emerging semiconducting materials for environmental remediation, gas sensors, solar cells, photocatalysis and other applications, Titanium dioxide ($TiO_2$) still remains a benchmark photocatalyst. This would be attributed to its promising properties such as non-toxic, inexpensive and thermodynamically and chemically stable [5, 6]. However, $TiO_2$ has a wide band gap energy of 3.2 eV (anatase) and it only shows photoactivity under the irradiation of ultraviolet (UV) light with wavelengths shorter than 385 nm [7-11]. Therefore, the photocatalytic activation of $TiO_2$ under visible light is being restricted due to its low utilization of solar energy in the visible region and the fast recombination of photogenerated electron-hole pair [8, 12].

Generally, several methods have been attempted in order to improve the photo efficiency of $TiO_2$ in the visible light region such as metal/non-metal doping, coupling with semiconductors and dyes sensitization [8-10]. In this present study, a one-dimensional oxide nanostructure is represented by the incorporation of $TiO_2$ nanoparticles into Multiwalled Carbon Nanotubes (MWCNTs) surface. Interestingly, the band gap energy of $TiO_2$ reduced from 3.2 to 2.79 eV with the incorporation of MWCNTs [9, 11].

In this study, a simple and cost-effective sol-gel method was used for the synthesis of uniform $TiO_2$ nanoparticles on MWCNTs surfaces. The effect of calcination temperature on the structural crystallinity and surface morphology of MWCNTS/$TiO_2$ was carried out. The photocatalytic activity of the MWCNTS/$TiO_2$ was studied using methyl orange dye. Calcined MWCNTS/$TiO_2$ showed better photocatalytic performance as compared to uncalcined MWCNTS/$TiO_2$.

## 2. MATERIALS AND METHODS

### 2.1. Materials

Multiwalled carbon nanotubes were supplied by Bayer Material Science AG (Germany) and the MWCNTs received had carbon purity higher than 95% with the diameter of 10-20 nm. Titanium isoproposide, TTIP (purchased from Aldrich), was used as a precursor without further purification.

### 2.2. Synthesis Procedures of MWCNTs-$TiO_2$ Nanocomposites

An appropriate amount of functionalized MWCNTs was dispersed in ethanol and mixed for 30 min to reach a uniform suspension. Next, a mixture of titanium tetraisopropoxide, ethanol and acetic acid underwent vigorous stirring for 30 min to form a clear solution. Then, the titanium solution was added dropwise into the as-prepared MWCNTs solution under vigorous stirring at room temperature for 2

---

*Address correspondence to this author at the Nanotechnology & Catalysis Research Centre (NANOCAT), 3rd Floor, Block A, Institute of Postgraduate Studies (IPS), University of Malaya, 50603 Kuala Lumpur, Malaysia; Tel/Fax: 603-79676960; E-mail: sharifahbee@um.edu.my

1573-4137/15 $58.00+.00

Hindawi Publishing Corporation
Journal of Nanomaterials
Volume 2015, Article ID 145360, 7 pages
http://dx.doi.org/10.1155/2015/145360

Research Article

# Rapid Formation of 1D Titanate Nanotubes Using Alkaline Hydrothermal Treatment and Its Photocatalytic Performance

**Chin Wei Lai, Sharifah Bee Abd Hamid, Tong Ling Tan, and Wai Hong Lee**

*Nanotechnology & Catalysis Research Centre (NANOCAT), University of Malaya, Institute of Graduate Studies Building, 50603 Kuala Lumpur, Malaysia*

Correspondence should be addressed to Chin Wei Lai; cwlai@um.edu.my

Received 11 December 2014; Revised 29 January 2015; Accepted 2 February 2015

Academic Editor: Cheol-Min Park

One-dimensional (1D) titanate nanotubes (TNT) were successfully synthesized using alkaline hydrothermal treatment of commercial $TiO_2$ nanopowders in a Teflon lined stainless steel autoclave at 150°C. The minimum time required for the formation of the titanate nanotubes was 9 h significantly. After the hydrothermal processing, the layered titanate was washed with acid and water in order to control the amount of $Na^+$ ions remaining in the sample solutions. In this study, the effect of different reaction durations in a range of 3 h to 24 h on the formation of nanotubes was carried out. As the reaction duration is extended, the changes in structure from particle to tubular shapes of alkaline treated $TiO_2$ were obtained via scanning electron microscope (SEM). Also, the significant impact on the phase transformation and crystal structure of TNT was characterized through XRD and Raman analysis. Indeed, the photocatalytic activity of TNT was investigated through the degradation of methyl orange aqueous solution under the ultraviolet light irradiation. As a result, TNT with reaction duration at 6 h has a better photocatalytic performance than other samples which was correlated to the higher crystallinity of the samples as shown in XRD patterns.

## 1. Introduction

Nowadays, various kinds of environmental contaminants are around all of us, especially organic and inorganic pollutants from industrial textile [1]. In fact, textile industry with the discharge of synthetic dyes-containing effluents into the water system can cause considerable environmental pollution which would gravely impact the quality of life of humans [2–4]. For instance, methyl orange acts as one of the major chemical classes of azo dyes that is normally carcinogenic, toxic, and mutagenic in nature [5, 6]. Thus, the treatments of such wastewater have become a major concern and it is urgent to develop a sustainable and cost-effective treatment technology to solve the discharge of toxic chemicals into water systems [6–8]. Lately, photocatalytic oxidation treatment has reason for using $TiO_2$ is mainly attributed to its ability to break down complex molecules in the pollutant into simple and non-toxic substances during the photocatalytic oxidation treatment; thus, no second treatment was involved for processing the sludge. Furthermore, the catalyst remains unchanged and can be reused which results in a significantly lower operating expense [7–9].

To date, designing one-dimensional (1D) nanostructure assemblies with precisely controllable nanoscale features has gained significant scientific interest, such as nanotubes, nanowires, and nanorods [11–15]. Of such properties, the large surface-to-volume ratio, good ion-changeable ability, and the tube-like structures of TNT have become the major interest of study [3, 8, 16–18]. In addition to this, a few studies showed that TNT exhibits a better photocatalytic

# APPENDIX

## APPENDIX A:

HPLC-Orbitrap-MS chromatogram of photoproducts from DMPEs degradation: